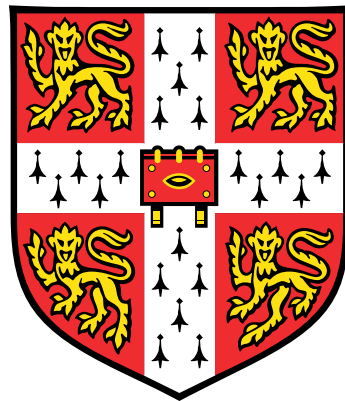


Numerical modelling of plasmas formed and magnetically controlled in hypersonic flows



Heather Alexandria Muir

Centre for Scientific Computing
Department of Physics
Cavendish Laboratory, University of Cambridge

This dissertation is submitted for the degree of
Doctor of Philosophy

Dedication-

To the family who were alongside me throughout my PhD years.
In the end, more were gained than was lost.

Mum & Dad

Lizzie, Chris, Joris, Kat & Jeanine

Declaration

I hereby declare that except where specific reference is made to the work of others, the contents of this dissertation are original and have not been submitted in whole or in part for consideration for any other degree or qualification in this, or any other university. This dissertation is my own work and conforms to the University of Cambridge's guidelines on plagiarism. Where reference has been made to other research this is acknowledged in the text and bibliography.

Heather Alexandria Muir
September 2022

Abstract

Title: Numerical modelling of plasmas formed and magnetically controlled in hypersonic flows

Author: Heather A. Muir

In high enthalpy hypersonic flows, the pressures and temperatures in the shock layer can become so extreme that dissociation and ionisation reactions produce a weakly ionised plasma. Owing to its elevated electrical conductivity, the plasma can be actively manipulated via magnetohydrodynamic (MHD) effect when a magnetic field is imposed upon the flow. The concept is of current research interest for its applications in spacecraft reentry, hypersonic flight control, and emerging aerospace plasma technologies. However, many challenges prevail in the numerical modelling of the complex and multiscale flow physics arising in a compressible, electrically conductive, magnetically influenced fluid.

This work makes advances in numerical modelling methodologies, combined with an advanced air-plasma equation of state, to permit the realistic and efficient simulation of hypersonically formed plasmas with imposed MHD effects. The dissertation wholly encompasses: the regime-specific mathematical modelling, the direct implementation and development of numerical algorithms within a high performance computing framework, and application of the numerical model to study the physics of hypersonic flows with imposed MHD effects.

A modularised approach is derived with problem-specific mathematical sub-models offering a high degree of generality (many types of fluid and plasma problems can be simulated) without compromising on efficiency. Key extensions are made to an advanced 19-species equilibrium air-plasma equation of state (EoS), meaning the EoS can be newly applied to the regime of hypersonically generated equilibrium air-plasmas, and makes improvements in the prediction of electric properties which underpin MHD forcing dynamics. A unique combination of numerical methods is employed. This includes: an original hypersonically stabilised numerical solver paired with a rigid body Ghost Fluid Method (GFM) for embedded geometries, with stable Lorentz forcing integration. The model is directly implemented within the AMReX framework, which facilitates block-structured parallelism and hierarchical adaptive mesh refinement (AMR).

The numerical methodology, combined with advanced EoS, is validated across a wide range of test problems. Quantitative agreement between simulation and experiment is

achieved for the first time for a hypersonic flow over a double-cone geometry with multiple shock interactions, augmented by an imposed magnetic field. Extended numerical studies of this problem configuration reveal insights into the detailed and coupled magneto-dynamic flow physics. The numerical studies demonstrate how an applied magnetic field not only influences shock *position*, but conditions are identified which predict a *topological adaptation* to the fundamental flow structure. Such predictions have technological consequence for emerging MHD control technologies.

The generality of the approach, as well as its specific advantages in simulating air-plasmas in compressible flows with complex shock interactions, means the developed numerical model can be applied to a wide set of problems. Application of the model to plasma generation via remote energy deposition is used as an example demonstration of extended model capabilities, and opens the door to future possibilities in aerospace plasma research.

Acknowledgements

It seems that a common response to telling people you are doing a PhD, is a curious look, a slight tilting of the head, and the simple muttering of “*why?*”. The pause before replying is at times short, and at times long.

To me it seemed a natural choice to pursue a PhD. It has always been an appealing idea to delve deeply into an academic problem, and to be afforded the time to sit and think, or, at times, just to sit. Of course as things evolve, they have their ups, their downs, and their ‘spurious oscillations’. The thing that has been, without a doubt, the most incredible part of my PhD years in Cambridge, has been the people I’ve had the privilege to meet, call friends, and with whom I have created a feeling of family so far away from home.

There are many people I would like to thank and acknowledge, both professionally and personally. To begin with the first- I would like to acknowledge Professor Nikos Nikiforakis for taking me on as a Masters student more than 4 years ago, and for his ongoing supervision since. It is amazing to see the work produced by other members of the LSC, and I have benefitted from discussions and input from Stephen Milmore, Louisa Michael, Nandan Gokhale, Philip Blakely and my office mates Tim Wallis, Miriam Aspley, and Maria Nikodemau. A dishonourable mention goes to Gilles Rodway-Gant for distracting me with fun coffee chats while I was trying hard to write-up.

A very sincere thank-you must go to Leo Christodoulou for his kind voluntary guidance and advice. Your words of wisdom and encouragement have been greatly valued.

I am indebted to the General Sir John Monash Foundation for providing the primary funding source of my PhD. However, the support of the foundation goes far beyond the funding. The foundation has connected me to other Monash Scholars who ultimately became many of my closest friends here in the UK. I would also like to thank the department of Physics for the top-up funding, and Mr Jerry Platt for the Masters Scholarship which enabled the start of the journey.

Other friends who have been a big support personally, as well as academically, include: Dante McGrath - for our weekly(ish) writing sessions at Stir which were valuable and motivating to get to the finish line, even more so when reflecting on leaving Brisbane, starting at Cambridge, and finishing our theses all in step.

A big note of appreciation goes to Viv Alligator Bone, who has been a go-to source for academic advice, as well wider academic and general chats. Lots of respect Viv, for being ridiculously clever and a loose unit at the same time.

I'd also like to say a big thanks to Kyri Tapinau, whose recent Zoom and Great Court chats were very illuminating. I have full faith in your KAMReX development.

In my first year in Cambridge, I had the extremely good fortune of being placed in the Sidney Sussex grad house 6 Park Parade. Along with Kat and Chris who occasionally crawled in through our kitchen window, this placed me with some of the best people I've had the pleasure of meeting. Even though our Masters mates (Chris, Nick and Brennan) broke our hearts by leaving after the first year, it was from within this Park Parade crew that formed our 'PhD family' at George Street.

Jeanine, despite your strange late-night operating schedule keeping me up chatting way too late into the evening, our friendship and discussions made some of my most valuable and enriching times in Cambridge. Thanks for bringing balance to a house where - "do they even read books?". There is no one I would rather be a 'Fen Ditton Girl' (minus the mud) or a 'positive possum' with.

Kat, thanks for being a constant source of fun, entertainment, and a reminder that life is for living (especially the ~8 weeks PhD holiday per year). It has been super inspiring to watch your journey from "moving into the maths department was an accident" to a no-corrections viva and Cambridge Fellowship. Proud is an understatement. Most of all, thank you for welcoming me into your family for three Christmases (stranded) in the UK.

To the Grayson family - Tina, Jo, Liz and Granny - I can't thank-you enough for warmly (radiator-depending) welcoming me into your beautiful family at Christmas time, and rescuing me from precarious journeys to Heathrow airport. At that time of year, it replaced home sickness with a lot of joy, which means a lot.

Joris, well well well, from start to finish in Cambridge, we've been through it all together! Thanks for being a constant source of support, a sense of calm, for your eloquent explanations about the universe, for matching my slowness of eating, and for your impeccably high quality memes. I couldn't have asked for a better housemate, and mate, through thick and thin.

One never could have predicted that life at Cambridge would quickly become centred so entirely in the home environment. But in the many months under lockdown it never felt like isolation. George street has been blessed with beautiful people through every season. Thanks to Leonie, Tim and Michael for the many good times, and adventures.

Amy, well, what a gift to the household. You are a profoundly special human, and I am beyond grateful for you to have graced our home. Thank-you for being a guide and a support through a particularly challenging time, and, for bringing a sense of spirit into the world, and yoga into my life. Namaste.

Bronte! Who would have thought that from getting constantly mixed up at football practise, we really would become twins. Pants and all! From our rescue picnics, to endless laughs, there are too many good memories to count. Thanks for bringing so much brightness into my final year in Cambridge and a reminder that when life gives you apples, make apple crumble (?).

Jessie and Cat, the both of you are endlessly inspiring women. I am constantly amazed at how you can be such bosses and yet so grounded at the same time. Hugh and I are your biggest fans. Speaking of whom, Hugh, thank you for being an absolute life saver through the crazy covid years, and on October holidays abroad. So happy to have you by my side in some of the best memories, and in all of my best photos. Ahmad, you were the first Monasher to come visit me in Cam, and have held a place in my heart ever since. You are a rare and special friend who I can rave about new science ideas with, or, just rave with. Both equally appreciated.

Steven, it didn't take too much rooftop Sangria before we realised that we were destined to be mates. There's nothing some good sports metaphors can't describe, nor distance too far for a jog home. From start to end of PhD, thanks for the constant reminders that we are the same person, except, fair to say, you've come out just a little bit ahead in every way. Very proud to watch you thrive over here, BNOC.

To my mates back home, Dylan and Harry, I don't know where I would be today without your persistent bullying spurring me into action and self-improvement. In moments of great uncertainty, I simply ask myself- "what would Dylan do?". It's been immensely heartening, and comforting to know I have you guys as mates whilst having been abroad for so long. I hope I've been able to generate an acceptable amount of goss for your consumption. And Ryan, what a surprise and a joy for you to rock up in Cambo. It's been amazing and rewarding to re-connect, even when ankle-deep in a field of mud.

And now, partner in all things life and podcasting, my constant source of awe, inspiration, and pure joy, miss Christine Carpenter. Thank you for being firmly aboard this crazy ride with me, and for sharing (or purely expressing) my outrage, and my elation. All of my love and gratitude.

Elisabeth Dumitriu, with all that's happened over the course of this PhD, I can say with certainty I would not have gotten to the finish line without you by my side. Through our 14 years of friendship, words cannot express my gratitude for you, and the strength and meaning you bring to my life.

Finally, Mum and Dad, and an unfathomable past few years we've had. We've made it through together, and I am beyond blessed and proud to have you as my parents. Completion of this thesis is a lot more than the product of 4 years at Cambridge. It is the product of 28 years of unwavering support, guidance and love. This work, the end of this chapter, and the start of the next, really is in dedication to the both of you. Thank-you.

Nomenclature

List of commonly used symbols and acronyms:

Symbol	Definition	Symbol	Definition
ρ	Density	ρ_c	Electric charge density
\mathbf{u}	Velocity vector	σ	Electrical conductivity
p	Pressure	ϕ	Electric potential
E	Total energy	η	Electrical resistivity
e	Internal energy	c	Speed of light in a vacuum
T	Temperature	Ma	Mach number
τ	Dynamic viscosity	V	Total velocity
ζ	Thermal conductivity	a	Acoustic wave speed
γ	Adiabatic index	L	Length
C_p	Specific heat at constant pressure	Re	Reynolds number
C_v	Specific heat at constant volume	Re_m	Magnetic Reynolds number
R	Specific gas constant	Q_{MHD}	Magnetic Interaction parameter
N_e	Electron number density	C_H or β	Hall coefficient
M_e	Mass of an electron	Da	Damköhler number
e	Electron charge	St	Strouhal number
ϵ_0	Permittivity of vacuum	Pr	Prandtl number
\mathbf{E}	Electric field vector	χ_e	Electron molar fraction
\mathbf{B}	Magnetic field density vector	S	Wave speed
\mathbf{J}	Electric current density vector		

Acronym	Definition
MHD	Magnetohydrodynamic
CFD	Computational Fluid Dynamics
GFM	Ghost Fluid Method
LTE	Local Thermodynamic Equilibrium
NEQ	Non Equilibrium chemistry
HPC	High Performance Computing
AMR	Adaptive Mesh Refinement
MPI	Message Passing Interface
EoS	Equation of State
NS	Navier-Stokes
CFL	Courant-Friedrichs-Lewy number
HLL	Harten Lax van Leer solver
HLLC	Harten Lax van Leer + contact wave solver
HLLC-HS	HLLC + Hypersonic Stabilisation solver
TVD	Total variation diminishing
MUSCL	Monotonic Upstream-centred Scheme for Conservation Laws
EB	Embedded Boundary
BC	Boundary Condition

Table of contents

Nomenclature	xiii
List of figures	xvii
List of tables	xix
1 Introduction	1
1.1 Background	2
1.1.1 Context and motivation	2
1.1.2 MHD flow control and emerging plasma technologies	3
1.1.3 Prevailing numerical modelling challenges	9
1.2 Thesis overview	13
1.2.1 Research objectives and novelty	13
1.2.2 Thesis outline	16
2 Mathematical modelling	17
2.1 Physics of fluids	18
2.1.1 Fundamental equations of fluid dynamics	18
2.1.2 Plasma- the fourth state of matter	19
2.1.3 Maxwell's equations for electromagnetism	21
2.1.4 MHD conservation equations	22
2.2 Modelling an aerospace plasma	24
2.2.1 Important dimensionless numbers	24
2.2.2 Order of magnitude analysis	25
2.2.3 Imposed magnetic field	30
2.2.4 Hall effect assessment	30
2.2.5 Electric field reduction	31
2.3 Model hierarchy	33
2.3.1 Full system model	33
2.3.2 Magnetic field reduction	35
2.3.3 Transport property reductions	35
2.3.4 Map of models	36

3	Equation of state for air-plasma	39
3.1	Air plasmas formed in hypersonic flows	40
3.1.1	Electrical conductivity models	45
3.1.2	Extent of LTE validity	48
3.2	Plasma19	51
3.2.1	Theory and development	51
3.2.2	Data structure of tabulated EoS	53
3.2.3	Property extensions	53
3.2.4	Computing electron molar fraction and number density	58
3.3	Computing electrical conductivity	61
3.4	Implementation advances	63
3.5	EoS comments	66
4	Numerical methods and algorithm development	69
4.1	Development designation	70
4.2	Mesh topology and the AMReX framework	71
4.2.1	Hierarchical adaptive mesh refinement	72
4.2.2	Refinement conditions	73
4.2.3	Parallelism and scalability	74
4.3	Numerical methods for inviscid compressible flows	75
4.3.1	Riemann solvers and finite volume methods	75
4.3.2	HLL and HLLC approximate Riemann solvers	77
4.3.3	High resolution extension	80
4.3.4	Numerical solution strategy	81
4.4	Embedded boundaries and the Ghost Fluid Method	82
4.4.1	Formulation	84
4.5	Hypersonically stable solver	88
4.5.1	In the literature	88
4.5.2	Proposed formulation	90
4.5.3	Solver performance	92
4.6	Numerical methods for compressible Navier-Stokes equations	93
4.6.1	Computing viscous fluxes	93
4.6.2	Numerical solution strategy	94
4.6.3	Time step with AMR considerations	96
4.7	Full system solution	97
4.7.1	MHD forcing terms	97
4.7.2	Numerical solution strategy	100

5	Validation of models	101
5.1	Ideal Euler model	102
5.1.1	2D Circular Sod Test	102
5.1.2	AMR configuration	103
5.1.3	Supersonic rigid body GFM tests	104
5.2	Hypersonically stable solver	108
5.2.1	Standardised tests	109
5.2.2	Performance assessment	115
5.3	Inviscid MHD model	116
5.3.1	Resistive MHD system under ideal gas law	116
5.4	Navier-Stokes fluid model	118
5.4.1	Subsonic flows	118
5.4.2	Supersonic flow tests	124
5.5	plasma19X real-flight EoS validation	135
5.5.1	Equilibrium validity for reentry regime	135
5.5.2	Reentry flight electron number density measurement	137
5.6	Hypersonic double cone tests	140
5.6.1	Non-reactive Nitrogen test	142
5.6.2	Reactive air test	143
5.7	Validation and performance comments	145
6	Hypersonic MHD applications	147
6.1	Spherical reentry vehicle with imposed B-field	148
6.1.1	Problem configuration and governing assumptions	148
6.1.2	Results	150
6.2	Hypersonic double cone with imposed magnetic field	155
6.2.1	Experimental conditions	155
6.2.2	LTE analysis	165
6.3	Studies of complex interactions in hypersonic flows with MHD effect	166
6.3.1	Effect of conical surface angle	168
6.3.2	Magnetic path dependence	173
6.3.3	Effect of magnetic field configuration	174
6.3.4	Magnetic replacement of surface actuation - an outlook	181
6.4	Conclusions	183
7	New and emerging plasma technologies	187
7.1	Background	188
7.2	Laser energy deposition modelling	189
7.2.1	Numerical modelling considerations	191
7.2.2	Validation: single pulse laser energy deposition over a blunt body	193

7.2.3	Validation: double pulse laser energy deposition over blunt body . .	197
7.3	Plasmoid generation via magnetocompressor	198
7.4	Plasma generation combined with MHD flow control	204
7.5	Model summary	211
8	Conclusions and future outlook	213
8.1	Thesis summary	213
8.2	Proposed future work	219
8.3	Applications and implications	224
	References	227
	Appendix A Computing electron molar fraction and number density - tables of coefficients	239

List of figures

1.1	MHD flow control concept diagram: velocity streamlines \mathbf{V} along which charged particles travel inside the shock layer (original bow shock position labelled). Charged particles passing through the magnetic field lines (two local tangential components of the larger dipole field shown as \mathbf{B}) induce a circumferential electric current \mathbf{J}_θ . Lorentz forcing therefore acts in the $\mathbf{J} \times \mathbf{B}$ direction, acting to push the bow shock position further out from the vehicle surface.	4
1.2	MHD assisted oblique shock control of scramjet inlet: left configurations shows ingested leading oblique shock when the system dynamic pressure is not exactly at on-design specification. This can be dynamically corrected for via application of an imposed magnetic field generated within the vehicle.	6
1.3	Comparison of magnetic actuation via MHD effect, and mechanical actuation via physical surface inclination, for a double cone geometry. Left) two different positions of magnetic dipole centre are shown, where resultant Lorentz forcing acts on the shock layer, and right) two different second surface inclination angles are depicted (θ_1 and θ_2), which similarly influences the shock position.	7
1.4	Example configuration of remote laser energy deposition experiment (optical lens of laser located in vehicle nose - surprising as it may seem, the laser system is housed entirely on-board). Energy is deposited by the laser upstream of the double cone geometry, with heated bounded volumes of gas then propagating over the vehicle.	9
2.1	Plasma: the fourth state of matter	20
2.2	Flow regimes as classified by Mach Number	24
2.3	2D profile for axisymmetric problem around z - quarter circle revolves to form half sphere	32
2.4	Map of mathematical models and associated underlying assumptions, with defined conditions on system reductions.	37

3.1	Peak temperature in the stagnation region of the shock layer for a blunt body reentry vehicle at 52 km altitude. Plot adapted from sketch by Fletcher [1]	41
3.2	Computed electron number density from three different 11-species non-equilibrium chemistry models for the RAM-C II geometry at 61 km travelling at Mach 23.9. Figure from Niu et al. [2]. a is a selected weighting factor of the forward vs backward ($b = 1 - a$) reaction rates (values $a=0.5-0.7$ debated in the literature).	45
3.3	FIRE II reentry capsule geometry diagram	49
3.4	Plot demonstrating regions of valid thermochemical assumptions, with overlaid reentry trajectories given by velocity-altitude coordinates. The zones of equilibrium states are as classified by Fujino <i>et. al.</i> [3], and the set of reentry trajectories is modelled from reference trajectory data [4] [5].	50
3.5	Tabulated equation of state data structure depiction, with ordered list of computed property spaces.	53
3.6	Temperature and electrical conductivity computed within existing plasma19 database over region: $[\rho = 10^{-3} - 10 \text{ kg/m}^3] \times [p = 1.013 \times 10^3 - 1.823 \times 10^7 \text{ Pa}]$ with 'switching' applied to ideal gas ($\gamma = 1.4$) over low density $[\rho = 10^{-5} - 10^{-3} \text{ kg/m}^3]$ and low pressure $[p = 7.55187 - 1.013 \times 10^3 \text{ Pa}]$ regions. Original plasma19 property borders shown in black. Supplementary conductivity model adopted for ideal EoS switching is as per equation 3.4 with exponent of $n=2$.	55
3.7	Left) colour plot of adiabatic index computed using the internal energy as a basis: $\gamma = 1 + \frac{p}{\rho \cdot e}$ with temperature contours overlaid in black. Right) Variational parameter of equation 3.13 computed through finite difference routines over the plasma19 property space, showing the relative ratio of partial derivative of γ with respect to pressure, scaled by partial derivative with respect to temperature.	56
3.8	Depiction of extension process: Boundary cells identified with indexing (p/ρ) stored, along with computed α coefficients for each corresponding property. Properties in cells of extension region are computed from the α variables identified from a projection along isotherms.	57
3.9	Left) computed sound speed, and right) computed temperature, over extended property space.	58
3.10	Left) computed total energy, and right) computed electrical conductivity, over extended property space.	58

3.11	Implementation of electron molar fraction for accurate computation over 50 K - 20,000 K (this work: coloured data points), validated against the results of D'Angola (solid black lines), for pressure values: 0.001 bar - 1000 bar. Linearly-scaled molar fraction shown for various pressures on left, and log-scaled molar fraction for $p=1.0$ bar shown on right.	60
3.12	Left) Original plasma19 electron number density property space, Right) new generated plasma19X N_e property space after implementing the extended formulation for computing electron number density.	61
3.13	Electrical conductivity across low air-plasma temperature range at pressure = 1 atm. Comparison of σ computed by plasma19X with other models currently used in the literature and to experimental measurements. Three sets of experimental measurements have been obtained from the works of Asinovsky et al. (1973) [6], Schreiber et al. (1971) [7] and Yos (1963) [8] where a low-temperature equilibrium plasma was generated via a stabilised DC arc applied to a column of air maintained at atmospheric pressure. Otsu [9] and Bush [10] use the simple analytic power law approximation defined in equation 3.4 with exponents 2 and 4 respectively. Solution to the Boltzmann equation is as per the solver developed by Weng and Kushner [11] for two different levels of resolution. EoS11 is an 11-species equilibrium model as implemented by Villa et al. [12].	62
3.14	Difference between bilinearly interpolated internal energy value (black e_*) and exact value (orange e_*) corresponding to input intensive properties (p, ρ).	65
4.1	Mathematical Bridge, as seen from the river bank at Queens' College, Cambridge. C.G. Harper, 1892 [13].	69
4.2	Three different mesh topologies demonstrated for a hypothetical bounded circular domain region	71
4.3	Block-structured AMR grid containing a hierarchy of nested refinement levels. Figure adapted from the image by [14].	72
4.4	1D space-time diagram: cells are refined spatially by a refinement factor $R^D = 2^1$, and corresponding temporal refinement factor $R = 2$ maintains global time equivalence with the base level after synchronised sub-cycled smaller time steps.	73
4.5	Block structured domain subdivided into sub-grids which retain ghost cells ($nG = 1$) populated via boundary cell communication, such that the sub-grids can be computed in parallel across nodes.	75
4.6	Finite volume discretisation with one spatial dimensional and one temporal axis.	76

4.7	Assumed two-wave and three-wave configuration for HLL and HLLC methods respectively. Constant states are separated in x-t space by computed wave speeds S_L , S_R , and S_* . The left and right waves may be a shock wave or a rarefaction wave, whereas the centre HLLC wave is always a contact wave.	78
4.8	The linear reconstruction is performed by replacing constant state variables ϕ_n^i by piecewise linear functions $\phi_i^n(x)$	80
4.9	Body-fitted computational meshes used in the spherical body re-entry simulations: left) Otsu & Abe [9], and right) Dias & Xisto [15]	83
4.10	Cartesian mesh configuration with two levels of hierarchical AMR. Blue borders show subdivision of the domain into ‘blocks’ which can be computed in parallel.	84
4.11	Two methods of fluid, boundary and rigid body cell identification. Left) The fluid sample point, denoted F, is determined from a projection from the cell normal, where bilinear interpolation of surrounding cells determines the mixture value, and is copied into boundary cell G. Right) left and right bordering fluid cells are identified, and bilinearly interpolated mixture value again copied to G.	86
4.12	Riemann based GFM: 1D problem constructed along the normal direction of the local problem geometry, with \mathbf{U}^* subsequently substituted (transformed back to x-y coordinates) into the boundary cell. Effective slip-boundary condition property state vectors are shown for the normal-tangential coordinate system in which the Riemann problem is solved.	86
4.13	Cell stencil for computed normal velocity increments	92
4.14	Finite difference stencils for computing the partial derivatives in the viscous flux vectors at cell boundaries.	93
4.15	Using the example of the flow conditions given in the supersonic wedge test of subsequent section 5.4.2, this plot shows the computed stable Δt (log-scaled) on the hyperbolic and diffusive fluxes for increasing AMR levels. As can be seen, up to the 7th AMR level the global time step is still hyperbolically restricted, however, by the 8th AMR level, the diffusive flux becomes restrictive. The corresponding cell size is also shown (exponential decrease with increasing AMR levels).	97
5.1	2D Circular Sod test at final time $t_f = 0.25$: plot of density with base level mesh patches shown, radial line for property trace shown in black	103
5.2	Primitive variable property traces along centre radial line, at $t_f = 0.25$: known exact solution in black [16], and computed result in red, discrete markers representing each cell along the radial line.	103

5.3	2D Circular Sod test at final time $t_f = 0.25$: plot of density with patches shown to mark the borders of the 2 AMR levels (radial line for property trace shown in black)	104
5.4	Primitive variable property traces along centre radial line, at $t_f = 0.25$: known exact solution in black [16], and computed result in red, note that the discrete markers are clustered represented the refined regions.	104
5.5	2D supersonic wedge test- initial Cartesian mesh shown with 2 additional levels of refinement shown around the triangular geometry and the incident normal shock wave, initialised at position $x=0.099$ m. AMR ‘blocks’ defined for parallel computation are shown with blue boundaries.	105
5.6	Upper) numerical Schlieren result of this work, and lower) experimental image obtained from Sivier [17]. Matching time frames 2 and 3.	105
5.7	Upper) numerical Schlieren result of this work, and lower) experimental image obtained from Sivier [17]. Matching time frames 4 and 6.	106
5.8	Left) comparison of numerical Schlieren of this work to Sivier [17], and right) comparison of final time frame to numerical result of Sambasivan et al. [18].	106
5.9	Final time mesh shown with mesh levels adaptively refined based on density gradient and geometry boundary.	106
5.10	Left) solution of this work, right) solution by Sambasivan et al. [18]	107
5.11	Left) solution of this work, right) solution by Sambasivan et al. [18]	107
5.12	Left) solution of this work, right) solution by Sambasivan et al. [18]	108
5.13	Adaptively refined mesh with two levels, as at the final time frame.	108
5.14	Plot of density with contours: left) HLLC solution, right) HLLC-HS steady-state solution	109
5.15	Plot of pressure with contours: left) HLLC, right) HLLC-HS	110
5.16	Plot of density with contours: top) HLLC, middle) HLLC-HS, bottom) HLL	111
5.17	Plot of internally computed ω values for: upper) G -flux sweep to detect strong vertically aligned shocks, and lower) F -flux sweep to detect strength of horizontally aligned shocks. Shown with AMR level boxes.	112
5.18	Plot of density with contours: upper left) HLLC, upper right) HLLC-HS. With HLLC-HS computed: lower left) G -flux ω , and lower right) F -flux ω	113
5.19	Plot of density with contours as computed by the different numerical solvers	114
5.20	Plot of internally computed ω values for: left) G -flux sweep and right) F -flux sweep. Shown with AMR level boxes.	114
5.21	Upper: Figure adapted from results of [19], pressure contours computed by Fujino et. al, validated in that study against Poggie & Gaitonde [20]. Lower: Pressure profiles with contours as computed in this work for $Q_{MHD} = 0$ and $Q_{MHD} = 6$	117

5.22	Quantitative comparison of shock stand-off distance for this work vs previous studies for $Q_{MHD} = 0 - 6$	118
5.23	Velocity profile through the boundary layer at varying distances along a flat plate. The boundary layer thickness doubles for every quadrupling of distance from the plate edge.	119
5.24	Comparison of velocity profile vs Blasius parameter for subsonic flat plate simulation vs known solution.	120
5.25	Domain configuration for the viscous cylinder test case. Base resolution of 192×96 with two levels of AMR, refined around boundary of embedded cylinder at T_0	121
5.26	Top) Density plot for inviscid simulation, bottom) density plot for viscous simulation	121
5.27	Comparison of plots of vorticity ($\nabla \times \mathbf{u}$) with contours during steady vortex shedding formation: upper result by Gokhale [21], and lower result is this work. The results show good structural similarity.	122
5.28	High resolution mesh with 4 AMR levels, producing effective resolution $\frac{D}{\Delta x} = 132$	122
5.29	Plot of vertical component of velocity v taken at a time interval when vortices have fully formed in the wake. A time trace of the vertical velocity at point P is taken to determine the vortex shedding frequency.	123
5.30	Supersonic flat plate test configuration matching that of Anderson [22]. . .	124
5.31	Pressure trace taking at the plate trailing edge ($x_L = 1 \times 10^{-5}$ m) through the boundary layer. Results of this work compared to Anderson [22] for both wall conditions: Fixed wall $T = 288.2$ K and an adiabatic wall.	125
5.32	Comparison of Navier-Stokes model numerical Schlieren (top) to the experimental Schlieren image (bottom).	126
5.33	Schlieren image captured in the experiments of Degrez et al. [23], showing steady state shock wave formation from a Mach 2.0 flow over a 3.09° angled wedge at the top of the test section which produces a 32.6° oblique shock wave impinging on the boundary layer of the lower flat plate at a distance of 0.05m from the leading edge where a secondary oblique shock has formed at an angle of 30°	128

- 5.34 The interaction of the impinging shock wave with the viscous boundary layer produces a separation region where there is a small amount of flow recirculation. The boundary layer (exaggerated in the diagram) becomes thickened along the plate surface downstream of the impingement point. The velocity profiles are depicted, with the impingement point resulting in a small recirculation region near the body surface. The reflected shock wave is split into two shock features separated by an expansion fan. The pressure along the surface of the plate exhibits a plateau beneath the separation region, whereas the inviscid solution only resolves a shock discontinuity at the surface. 128
- 5.35 Problem configuration and initial conditions for Oblique Shock BL interaction test. The flat plate depicted at the lower surface is configured with a no-slip boundary condition, where x_L is the plate length and x_i is the length from the leading edge to the shock impingement location. Free stream conditions denoted ∞ and post shock conditions labelled s 129
- 5.36 Top) numerical Schlieren of computed result, middle) density plot showing reduced-region for subsequent high resolution test, bottom) computational mesh with base resolution: x-direction - 1.28 cells per mm, y-direction - 2.13 cells per mm, and 2 levels of hierarchical AMR, giving effective resolutions of 5.12 cells per x -mm and 8.52 cells per y -mm 130
- 5.37 Top) numerical Schlieren of domain sub-section, bottom) x-component of velocity showing a negative minimum velocity which occurs inside the separation region where the flow recirculates 131
- 5.38 Comparison of computed property profiles to other numerical studies (num) and to the recorded experimental values (exp). Left) trace of pressure along surface of plate, distance from leading edge, right) x-direction velocity u through boundary layer, perpendicular to flat plate at shock impingement point $x=0.061$ m. The negative velocities through the boundary layer could not be measured experimentally, thus the flat series of red dots, however is known to occur phenomenologically. 131
- 5.39 Velocity profile through boundary layer showing separation and reattachment where the solid contour line traces $u = 0$. The white interior contours show a region of recirculation with negative u -velocity, and outer black contours are of positive velocity through the boundary layer. 132

5.40	Problem configuration including initial conditions for upstream gas (state 0) and post-shock gas (state 1). Gas constants for the problem are given on the left, and the Mach stem is depicted for the desired time evolution of $9.6 \mu s$. The length x_0 is the initial distance between the wedge and the normal shock at time = 0, and L_x is the 2D domain length. Both the 49° inclined wedge and the lower wall are viscous no-slip boundaries. Remaining domain boundaries are transmissive.	133
5.41	Left) inviscid solution, right) viscous solution, at time = $9.6 \mu s$	133
5.42	Numerical solution from Graves et al. [24] for the viscous case, at time = $9.6 \mu s$	134
5.43	Adaptively refined mesh for the viscous solution at time = $9.6 \mu s$	134
5.44	2D plot of pressure, and property profiles along the stagnation line, comparing the models of Damevin & Hoffmann (DH) to the chemistry model of this work for the 30km altitude Mach 18 test case.	136
5.45	Reentry trajectory and thermochemical assumptions map with known markers of blackout onset and recovery as reported by Savino et al. [25]. RAMC-II test point of this analysis also marked.	137
5.46	RAMC-II geometry with marked probe positions along vehicle surface . . .	138
5.47	Compiled results for peak N_e from different model in the literature, as listed. Literature results presented along log-scaled number lines in orange, with the computed results of this work for 41 km and 61 km altitude shown in green.	138
5.48	RAMC-II electron number density comparison of a collection of literature results: Equilibrium and non-equilibrium solution compared by Shang [26], a 7-species non-equilibrium result (USIM) computed by Kundrapu [27], the various 11-species equilibrium results of Gupta [28], Park [29] and Ozawa [30], compared with the plasma19X result of this work.	139
5.49	RAMC-II plot of computed steady state temperature and electron number density profiles for 61 km flight conditions.	140
5.50	Geometry specifications of the CUBRC 25/55 $^\circ$ double cone model	141
5.51	Top) schematic of features formed in hypersonic double cone flow, bottom) numerical Schlieren result of this work from test conditions of the CUBRC run 1 flow. Comparison shows complete feature formation captured by the full Navier-Stokes rigid body GFM model of this work for a hypersonic flow over a non-simple geometry.	141
5.52	3D rendered visualisation of the double cone flow for CUBRC run 1 conditions. Plot of density is shown with AMR block borders indicating regions of adaptive refinement.	142

5.53	Pressure trace along surface of double cone: CUBRC run 7 result of this work compared with experimental result and simulations of Nagata et al. [31] and Moss et al. [32].	143
5.54	Pressure trace along surface of double cone: left: CUBRC run 7 compared with experimental result and simulations of Nagata et al. [31] and Moss et al. [32], right: CUBRC run 43 compared with experimental result and simulations of Holloway [33] under different thermochemistry assumptions.	144
6.1	3D rendering of the configured dipole magnetic field around the defined spherical geometry: radial and z-components depicted respectively over each half plane. Mesh AMR blocks shown at time = 0.	149
6.2	Comparison of electrical conductivity profiles before the magnetic field is activated	150
6.3	Top) Temperature profiles at steady state in the absence of magnetic field for ideal gas and for plasma19X chemistry models. Bottom) Temperature profiles at steady state under imposed magnetic field of strength $B_0 = 1$ T.	150
6.4	Comparison of circumferential (θ -component) electric current density. NB: both simulations are run in the right half plane (plasma19X result as shown), whereas the ideal gas result is reflected across the z-axis of symmetry, however the electrical current is shown with its original sign/direction as per the right plane for mirrored comparison. Both peak negative currents circulate in the anti-clockwise direction around the z-axis.	152
6.5	Comparison of Lorentz forcing directional vectors (black arrows) and magnitude (colour map).	152
6.6	Comparison of Lorentz forcing vectors (black arrows) and magnitude of the magnetic interaction parameter (colour map): $Q_{MHD} = (\sigma \mathbf{B} ^2 R_0)/(\rho \mathbf{u})$	153
6.7	Comparison of: top) density field, and bottom) total velocity profile for each EoS.	153
6.8	Logarithmically scaled plot of electron number density N_e for the the $B_0 = 0$ T case (left) and the $B_0 = 1$ T case (right). 3D rendering to better represent true geometry and fluid profile.	154
6.9	Computed magnetic field from this work - configured to match the experimental condition. Key geometry points and features are labelled for reference. Dimensions in mm.	156
6.10	Left) Body fitted mesh employed by Nagata et al. [31], compared with right) adaptively refined Cartesian mesh employed in this work - resolved at the steady state solution time step once the flow has formed around the embedded double cone (embedded boundary shown in red.)	157

6.11	Left) pressure contours computed by Nagata et al. [31] for different magnetic field strengths as measured at the kink point of the double cone, and right) corresponding pressure traces along surface (projected distance along the z-axis).	158
6.12	Contours of pressure for the cases: without magnetic field, magnetic field initialised to experimental value $B_{ref} = 0.36$ T, and a stronger magnetic field of $B_{ref} = 1.5$ T intensity. Radial lines (along which property traces are taken) of 4 mm, 8 mm, 10 mm are marked.	159
6.13	Pressure trace along the surface of the model for the simulations of this work.	159
6.14	Brightness intensity rendering of the flow field for $\mathbf{B}=0$ and \mathbf{B} at the test condition for a given test run. Image by Wasai et al. [34].	160
6.15	Top) experimental result brightness intensity traces through radial lines 4 mm, 8 mm, and 10 mm, for a number of test runs by Wasai et al.[34]. Middle) pressure traces taken at the same radial lines from the numerical result of Nagata et al. [31]. Bottom) pressure traces taken at the same radial lines from the numerical result of this work. Experimental and Nagata traces are presented as total distance along the central z-axis (labelled X-axis in the experimental results), and simulation traces are shown more clearly as distance along the z-axis measured directly from the surface intersection point as $z=0$ for each case.	161
6.16	Comparison of steady state solution for electrical conductivity (σ) without magnetic field (left plane) and for the case of applied magnetic field of strength $B_{ref} = 1.5$ T. Regions of mesh refinement are shown by white block borders.	163
6.17	Comparison of steady state solution for electron number density (N_e) without magnetic field (left plane) and for the case of applied magnetic field of strength $B_{ref} = 1.5$ T.	163
6.18	Key electromagnetic properties- left: circumferential component of electric current density, and right: Lorentz forcing magnitude and directional vectors.	164
6.19	Full 3D rendering of computed steady state Mach number for case of imposed magnetic field strength $B_{ref} = 1.5$ T.	164
6.20	Left) magnetic interaction parameter: $Q = (\sigma B ^2 R_0)/(\rho \mathbf{u})$, compared with right) residence time indicator of regions approaching equilibrium: $\tau_r = \frac{L_0}{ V }$	166
6.21	Schematic of the known shock structure formed for the hypersonic flow over the previously studied hypersonic double cone test cases. All flow features are labelled, including sonic lines to depict the supersonic and subsonic regions of the flow. This flow structure is classified as CLASS A in the analysis to follow.	167

6.22	Schematic of the flow structures CLASS B and CLASS C. All flow features are labelled, including sonic lines ($M=1$) to depict the supersonic and subsonic regions of the flow.	167
6.23	Imposed dipole magnetic field configuration for the $\theta_2 = 55^\circ$ test case. . . .	169
6.24	Computed steady state electrical conductivity (colour-map) for the base case without magnetic field activation for each of the second surface angles. Mach number contours are overlaid in black with the $M=1.0$ sonic line contour additionally overlaid in white.	169
6.25	Computed steady state pressure contours for different second conical surface angles. Guide lines are added for reference: one perpendicular to the z-axis of symmetry, intersecting through the kink point, and two tangential guide lines running parallel to the second surface incline, one at the surface and one offset 2 mm from the vehicle surface.	170
6.26	Computed Q_{MHD} and Lorentz forcing vectors for each θ_2 surface angle. . . .	172
6.27	Numerical Schlieren (density gradient) contours at different time stages of the evolution of the steady state for the case $\theta_2 = 65^\circ$ with magnetic field activated from $t = 0$ s.	173
6.28	Resultant magnetic fields from varied dipole centre locations: intensity colour plot (colour bar shown in left figure holds for all plots) with magnetic field directional vectors scaled by magnitude. Magnetic dipole centre shown, with calculated B_0 in order for maximum B-strength in the fluid region to be equivalent at 2.25 T across all cases.	175
6.29	Steady state pressure contours for each magnetic field location.	176
6.30	Examining the effect of magnetic field location on separation region: steady state pressure contours in black with computed velocity streamlines (coloured by total velocity magnitude) shown for each magnetic dipole centre location.	177
6.31	Computed Q_{MHD} (logarithmically scaled between 0.1-10) and Lorentz forcing vectors (showing direction and relative magnitude) for each magnetic field location.	178
6.32	Mach number plots of $Z_{dist} = 19.5$ mm and $Z_{dist} = 30.0$ mm cases, with sonic line ($M = 1$) contour and key features labelled.	180
6.33	Plot of Mach number for the base flow case with declined second surface angle at $\theta_2 = 50^\circ$. The steady state flow is of CLASS C exhibiting a shock inflection point and fully supersonic detached shock layer. The sonic line ($M=1$) is overlaid in white.	182

- 6.34 Numerical Schlieren (density gradient) depicting two classes of emergent flow structures: Top) CLASS C, and Bottom) CLASS B. In each case an equivalence is drawn between: left) magnetic actuation effect, with contours of $|B|$ depicted in grey, and right) mechanical surface actuation via varied θ_2 angles of the geometry. 183
- 7.1 Multi-level procedure for time-step sub-cycling, depicted for 2 AMR levels. Chronological steps listed. Synchronisation steps between level integrations ensure that flux conservation is maintained between the finer cells and adjacent coarse cells. This is termed *re-fluxing* where the coarse data (lower accuracy) is modified in line with the fine data solution at the coarse-fine boundary. This figure is adapted from an image by A. Meyers, AMReX developer [35]. 192
- 7.2 Pressure over time, sampled at the stagnation point at the front of the spherical leading surface: comparing result of the full Navier-Stokes simulation closed with plasma19X EoS, and the inviscid Euler simulation closed with ideal gas EoS. 194
- 7.3 Numerical Schlieren result of this work (left column), compared with experimental Schlieren image from Adalgren et al. [36] (middle column), and the numerical results of Zheltovodov et al. [37] (right column) at equivalent times post single laser energy deposition: $20\mu s - 50\mu s$ 195
- 7.4 Numerical Schlieren result of this work (left column), compared with experimental Schlieren image from Adalgren et al. [36] (middle column), and the numerical results of Zheltovodov et al. [37] (right column) at equivalent times post single laser energy deposition: $60\mu s - 100\mu s$ 196
- 7.5 Experimental Schlieren from Schülein et al. experiments (left column) compared with numerical Schlieren result of this work (middle column), and the numerical results of Schülein et al. [37] (right column) at equivalent times post double pulse laser energy deposition. 198
- 7.6 Left) result of Znamenskaya et al. [38]. Plot of normalised density with contours, normalised time also shown. Ideal Euler model. Key features labelled (SW: shock wave, and CD: contact discontinuity). Right) Results of this work: ideal Euler model. Plot of density with contours (dimensional), at close to equivalent time frames as the Znamenskaya et al. result. 200
- 7.7 Left) result of Znamenskaya et al. [38] (non-dimensional). Right) Results of this work: ideal Euler model. Plot of density with contours (dimensional), at close to equivalent time frames, as the simulation evolves. 201
- 7.8 Results of this work: inviscid plasma19X model. Colour plot of electrical conductivity. With contours of density to show the shape of the bulk fluid flow. 202

7.9	Plot electron number density through plasmoid region, with density contours depicting broader flow structure.	203
7.10	3D rendered plot of temperature field midway through plasmoid evolution.	204
7.11	Static dipole magnetic field - absolute magnitude shown (colour map) with field line vectors shown in black. Rigid body geometry shown in white.	205
7.12	Steady state density field at 130 μs after simulation initialisation, with black density contours superimposed for shape visualisation.	206
7.13	Comparison of: left) base flow case (no magnetic field) with right) MHD affected case (magnetic field initialised). Evolution of density field (25 white contour lines), and generated plasma region shown via a colour plot of conductivity (colour map re-scaled for each time progression), with internal detail depicted through 15 overlaid black conductivity contour lines. Evolved solution over 135-160 μs after simulation initialisation	207
7.14	Comparison of: left) base flow case (no magnetic field) with right) MHD affected case (magnetic field initialised). Evolution of density field (25 white contour lines), and generated plasma region shown via a colour plot of conductivity (colour map re-scaled for each time progression), with internal detail depicted through 15 overlaid black conductivity contour lines. Evolved solution over 170-200 μs after simulation initialisation	208
7.15	For the magnetically affected case: plots of induced circumferential (\mathbf{J}_θ) electric current density, with Lorentz forcing directional vectors (direction only, magnitude not indicated), for the two time stages: 135 μs and 150 μs after simulation initialisation.	209
7.16	Density field at 130 μs after simulation initialisation, with black density contours superimposed for shape visualisation. Left) no magnetic field, right) with magnetic field.	210
7.17	3D revolved rendering of 2D axisymmetric result: numerical Schlieren scaled (function of density gradient) to depict more complex wave structures at play. Time progression shown: 153 μs . The borders of AMR refinement blocks are overlaid in white.	210
8.1	Modularised approach: map of mathematical sub-models, governing assumptions, and reductions.	214
8.2	Diagram depicting the topological adaptation which can arise due to imposed MHD effects - as identified for certain geometric and magnetic field problem configurations.	217
8.3	Coarse depiction of the full domain discretisation, whereby, a layer of finite conductivity is defined for the material substrate. Electric boundary conditions can be defined on the full domain boundary for ϕ	221
8.4	The way in which simulation and experiment reciprocally interact.	224

List of tables

5.1	Comparison of the result of this work to two recent numerical results by Gokhale [21] and Al-Marouf and Samtaney [39], as well as an established experimental result by Berger and Wille [40].	123
5.2	Comparison of R_M ratio between this work and reference sources: Gokhale [41], Al-Marouf and Samtaney [39], and Graves et al. [24].	135
6.1	Comparison of MHD shock stand-off enhancement prediction for the ideal vs plasma19X gas models	151
6.2	Comparison of MHD shock stand-off enhancement (increase in leading shock distance from surface) for the experimental conditions with magnetic field strength $B_{ref} = 0.36$ T: experimental result by Wasai et al. [34] (as measured from experimental graphs), and computed result from the model of this work (as measured from computed pressure traces along radial lines shown in Figure 6.15).	162
6.3	Collated in the table is the measured peak stand-off distances for $B_{max} = 2.25$ T case, with computed MHD stand-off distance calculated as a % enhancement from the base case: $enhancement(\%) = \frac{\delta_{MHD} - \delta_0}{\delta_0} \times 100\%$. . .	171

Chapter 1

Introduction

Over the course of producing this PhD thesis, the world has witnessed some remarkable feats on the frontiers of space science. Underlying many of the advances in aerospace technology, hypersonics, and fluid dynamics more broadly, is the rapid development of computational approaches.

This thesis is concerned with such computational advances: focussing specifically on numerical methodologies for the realistic and efficient simulation of weakly ionised plasmas formed in hypersonic flows, and ways in which they can be magnetically controlled. This dissertation wholly encompasses:

1. The problem-specific mathematical modelling of aerospace plasmas
2. The direct implementation and development of advanced numerical algorithms
3. Application of the numerical model to current and emerging plasma physics research problems

This Chapter introduces the broader context to the problems and technologies motivating the advancements in numerical simulation capabilities. A key interest area is specifically: magnetohydrodynamic (MHD) flow control. Some background to this concept and associated applications is offered accordingly. A number of the prevailing modelling challenges are examined from the literature, naturally introducing the objectives of this work.

The purpose and novelty of the dissertation is clearly designated in this Chapter, along with an outline of the contents to follow.

The thesis touches upon quite a broad set of topics and associated literature. Therefore, the finer details and relevant literature appears in the sections where those topics are directly addressed (e.g. equations of state, conventional numerical approaches, comparative simulations). This Chapter is intended, simply, to offer the *bigger picture*.

1.1 Background

1.1.1 Context and motivation

During hypersonic flight, the conversion of kinetic to thermal energy across the leading shock wave results in severe compression and heating of the gas surrounding the vehicle. Temperatures can become so extreme that dissociation and ionisation reactions produce a weakly ionised plasma. This plasma layer has properties which present both challenges and opportunities.

Perhaps one of the most challenging aerospace plasma environments occurs during spacecraft reentry into Earth's atmosphere. When the density of electrons around the vehicle is sufficiently high, the plasma reflects and attenuates radio-waves, resulting in a dangerous period of radio-blackout. Specifically, blackout occurs when the plasma frequency exceeds the frequency of the electromagnetic wave (radio-wave) [42], where the plasma frequency (ω_p) can be determined as a function of electron number density (N_e):

$$\omega_p = \sqrt{\frac{N_e e^2}{m_e \epsilon_0}} \quad (1.1)$$

Historically, manned and unmanned space missions including the Apollo missions, the Mars Pathfinder, and the failed 2018 Soyuz rocket launch (which returned plummeting back to earth without leaving the atmosphere) incurred communications blackout in the order of minutes. Just last year, the SpaceX crew dragon (manned) return to earth mission experienced radio blackout for a period of 6 minutes. Blackout not only leads to loss of connection to on-board persons and flight data, but to a loss of remote control and guidance. Several approaches for mitigating signal attenuation have been tested, including: satellite relay, aerodynamic shaping, electrophilic liquid injection, and the more recent, and perhaps most popular proposal of the "magnetic window" method [27]. The problem of communications blackout remains unresolved for most vehicle types.

During atmospheric reentry, temperatures in the post-shock layer reach as high as 7,000 K (for reference - the surface of the sun is approximately 5,780 K [43]). When the free electrons in the plasma medium recombine in an exothermic reaction, additional heat is added to the system [44], increasing heat flux to the vehicle amidst a flight period already sustaining very high thermal loads. Where historically, ablative heat shielding has been an effective and popular method of thermal protection, the recent push towards reusable space technologies has shifted the gaze of engineers towards the class of *active* thermal protection systems (i.e. non-ablative). February 2018 saw the impressive Falcon Heavy Demonstration mission, verified to be the most powerful rocket launch to date, which rather questionably launched Elon Musk's personal Tesla car into heliocentric orbit. Most critically, the demonstration mission saw reusable side boosters return to Earth, landing intact and in unison. This strongly signified the current shift in space industry objectives towards reusable

components and materials, and various technologies are currently being appraised for their efficacy as active thermal protection systems. Magnetic heat shielding is a strong candidate for active, non-ablative thermal protection [45].

The interesting part about the plasma formation, is that whilst it poses these challenges and dangers, it is also possible to leverage some of the properties of the plasma layer to combat these challenges. Plasma is characterised by heightened electrical conductivity, which enables the plasma layer to be actively manipulated via an electromagnetic effect. This active plasma manipulation is termed MHD flow control.

The MHD flow control concept was first proposed in the 1960's when manipulation of a partially ionized plasma flow via electromagnetic field effect was demonstrated experimentally by Kranc *et al.* [46]. These studies also showed that a strong magnetic field of the order of 1 T or more would be necessary to achieve a heat shielding effect sufficient for real reentry flight. At the time, this magnitude corresponded to a prohibitively heavy magnet system, stifling this line of research. Additionally, the very high cost of experimental studies for space technologies provided another significant barrier to testing and progress.

Fortunately, in the decades following these studies on electron manipulation within a plasma medium, we also saw electrons passed through logic gates for the first time. The rise of computing in the last ~ 70 years has seen computation emerge as a third mode of investigation in the sciences; after experimentation and theory. This has provided a means to affordably test space technologies via simulation.

Jumping forward to the end of the 1990's, the advancement of materials science has enabled magnetic fields of the order of 1 T to be generated within a practicable weight via the use of superconducting coils. And so, where advances in material science, exponential gains in computing power, and shifts in space industry objectives, reach a confluence - the MHD flow control concept is re-opened, this time with computational studies at the core of the research.

Whilst the reentry context is the classic example for MHD flow control, there are a number of viable applications of magnetically controlled plasma dynamics in emerging aerospace technologies. In fact this is presently one of the most active research areas in flow control [26], and a field foundationally driven by numerical modelling.

1.1.2 MHD flow control and emerging plasma technologies

A number of configurations have been proposed for the active manipulation of ionised gases via electromagnetic effect. Application of electric fields and imposed magnetic fields are able to exert forces on the charged particles of a plasma, and with sufficient collisionality these forces are imparted upon neutral particles, resulting in flow acceleration or deceleration on the macroscopic scale, as well as irreversible Joule heating. Both of these mechanisms can be leveraged for flow control of aerospace plasmas [47].

Atmospheric reentry

To explain the primary dynamics of the aforementioned reentry problem: a strong dipole magnetic field is first generated from within the vehicle and imposed upon the flow. As the charged particles of the shock layer flow through the magnetic field, an electric current is induced in the circumferential direction. That induced current crossing through the magnetic field then produces a Lorentz force which acts macroscopically on the fluid, augmenting the bow shock position by pushing the ionised shock layer further away from the vehicle. This is termed *shock layer enhancement* [48]. MHD flow control exhibits a collective mechanism of desirable properties: it increases shock stand-off distance, increases total drag force, reduces the heat flux and can locally reduce regions of electron number density (helping to mitigate the communications attenuation problem). This concept is depicted in Figure 1.1.

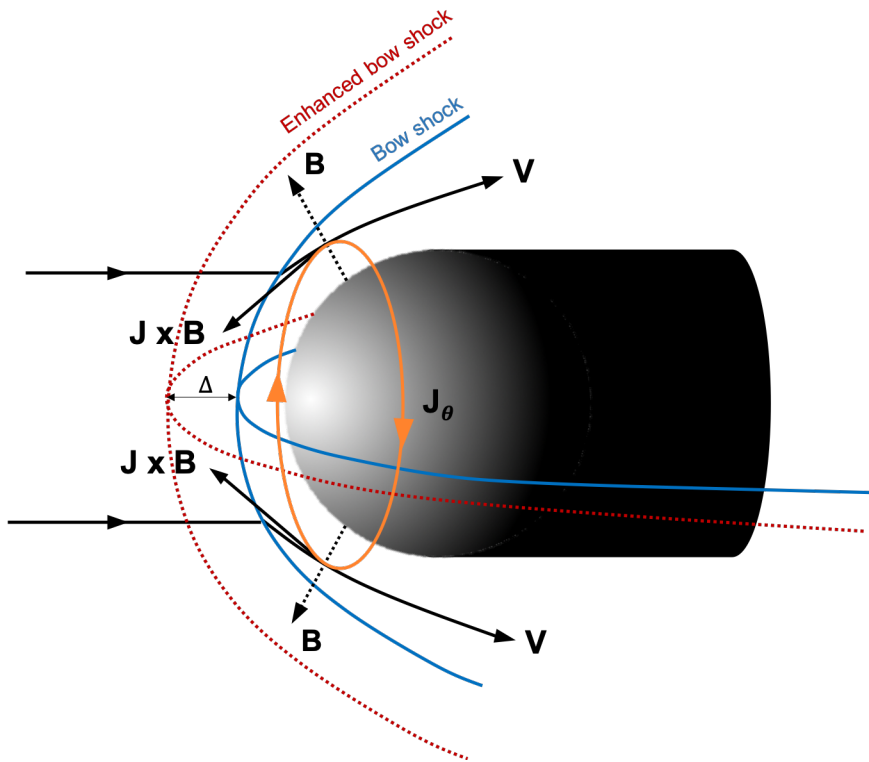


Fig. 1.1 MHD flow control concept diagram: velocity streamlines V along which charged particles travel inside the shock layer (original bow shock position labelled). Charged particles passing through the magnetic field lines (two local tangential components of the larger dipole field shown as B) induce a circumferential electric current J_θ . Lorentz forcing therefore acts in the $J \times B$ direction, acting to push the bow shock position further out from the vehicle surface.

This problem configuration is a primary application of interest for this work. Since this concept is yet to be tested in real atmospheric reentry flight [49], it is a problem configuration which was originally investigated through simplified theoretical analyses by Bush in 1958 [10] and Porter & Cambel in 1967 [50]. Given the preliminary feasibility suggested by the

theoretical analyses, many experimental wind tunnel tests have followed: [46, 51–54, 5] (most of which use Argon instead of air as the test gas due its lower ionisation potential).

Following confirmation of shock enhancement effects observed in experiments, numerical simulation has become a primary mode of investigation for MHD flow control for the reentry regime. Therefore, this problem configuration is the subject of extensive numerical investigations with the key focus on quantifying MHD effects in terms of shock position augmentation (increase in stand-off distance), and heat flux reduction. Fujino et al. conduct a number of 2D axisymmetric numerical studies which employ an 11-species non-equilibrium chemistry model for the plasma with a focus on real wall conductivity effects on MHD flow control [3, 55, 19]. These studies simulate the OREX flight experiment vehicle geometry and trajectory (in the high altitude range) with a hypothetically applied magnetic field. Li et al. also implement an 11-species model and conduct full 3 dimensional simulations of the OREX flight test, examining heat flux reductions as a result of different strengths of applied magnetic fields [56]. Additionally they examine the effects of varying expressions for electric current density, and magnetic field configurations to optimise the active heat shield system [45, 57]. Otsu and Abe conduct 2D axisymmetric simulations of simple spherical blunt bodies, whereby the model is closed with an ideal gas law with finite conductivity model in order to examine the relative influence of the Hall current (in the expansion of Ohm's law in the governing equations), and the effect of different surface treatments (fully insulative or fully conductive vehicle surface) [58, 9]. Dias & Xisto adopt a similar simplified ideal gas model to conduct studies on a slender sphere-cone geometry examining the effects of varying magnetic field orientation and strength on shock stand-off distance [15]. Poggie & Gaitonde explore the role of analytic gas conductivity equations adopted for simple gas MHD models [20].

Given the complexity of the magneto-fluid dynamics and numerical simulation constraints, at best, qualitative agreement has been achieved, where general flow behaviours (changes in shock position and surface properties) can be related to parameter variation (e.g. changes in magnetic field strength or manually defined fluid properties), however quantitative agreement between simulation and experiment has remained a research challenge [54].

This problem configuration motivates some of the studies conducted in Chapter 6 of this thesis, where the developed model is applied to concepts in MHD flow control for a realistic reentry regime.

While the focus of previous studies has been heat shielding and aerodynamic drag enhancement, other works are concerned with electron number density, in relation to the communications blackout problem. A number of studies conduct numerical simulations demonstrating how the electron plasma density can be locally reduced (around an antenna) via application of an electric cross magnetic field ($\mathbf{E} \times \mathbf{B}$ field) [49, 59] - the so-called "magnetic window" method. Other studies examine the communications attenuation problem by resolving and analysing the computed electron number density profile around the vehicle,

both with and without static magnetic field effects [60, 42, 27, 61, 62], among others. These studies are very difficult to validate given the difficulties in obtaining detailed experimental data on electron density.

MHD assisted inlet control

Another key application of magnetic flow control in hypersonic flight is scramjet inlet control. A scramjet engine can provide thrust to a vehicle flying above about Mach 3. The geometric configuration of the inlet determines at what precise dynamic pressure the engine is at *on-design* flight condition, where the leading oblique wave is positioned on the engine lip. MHD assisted control of the oblique shock offers the possibility of achieving on-design specification at off-design flight conditions.

Bitiyurin et al. conduct experimental studies on a wedge geometry with applied magnetic field [63], as well as 2D MHD simulations on ramjet and scramjet inlet configurations [63, 64, 52]. Kuranov [65] and Sheikin [66] also numerically investigated MHD assisted inlet control, conducting analysis for $M_\infty = 6$ and $M_\infty = 8$ free stream Mach numbers and magnetic field strength varied between $\mathbf{B} = 0 - 5$ T. Kuranov's modelling predicts that MHD influence is feasible to adjust oblique shock position at off-design conditions, thereby increasing engine specific impulse and thrust, and actively controlling air capture and flow compression. Sheikin further examines which magnetic field configurations can optimise performance. The concept is depicted in Figure 1.2.

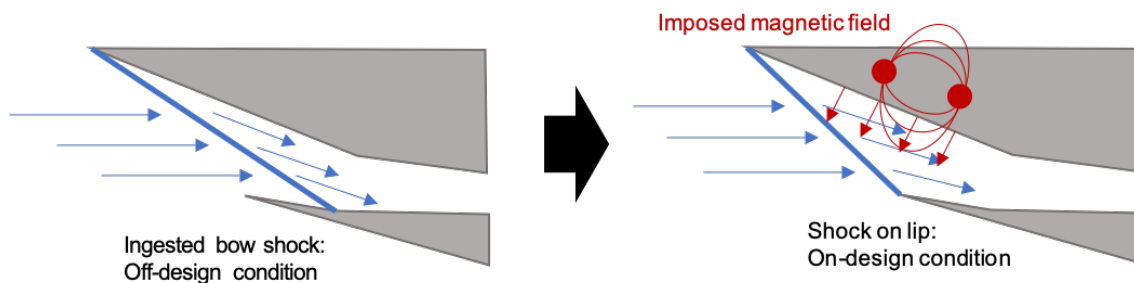


Fig. 1.2 MHD assisted oblique shock control of scramjet inlet: left configurations shows ingested leading oblique shock when the system dynamic pressure is not exactly at on-design specification. This can be dynamically corrected for via application of an imposed magnetic field generated within the vehicle.

Given that the ionisation degree behind the oblique shock is fairly low (therefore requiring very high magnetic field strength), MHD control can be supplemented by electron beam injection, as examined numerically by Shneider et al. [67–69] and Macharet et al. [70]. The use of electron beams is one form of *remote energy deposition*, an emerging concept for supplementing the electrical conductivity of aerospace plasma systems in order to enhance MHD control effects.

Magnetic actuation concepts

Another emerging mechanism under study is the use of plasma and magnetic actuators for hypersonic flow control. So-called plasma actuators typically refer to systems of electrodes most effectively employed in the boundary layer of hypersonic inlets or surfaces (where the fluid inertial forces are low and more easily augmented). The additional generation of a local electric field creates a supplementary mechanism in the Lorentz force, and the electromagnetic perturbation can amplify a viscous-inviscid interaction in order to actively manipulate the flow [71]. Such concepts are currently being explored through numerical simulation, including recent studies (2020) on wedge shock wave control by surface MHD actuation include Gong et al. [72], and Jiang et al. [73].

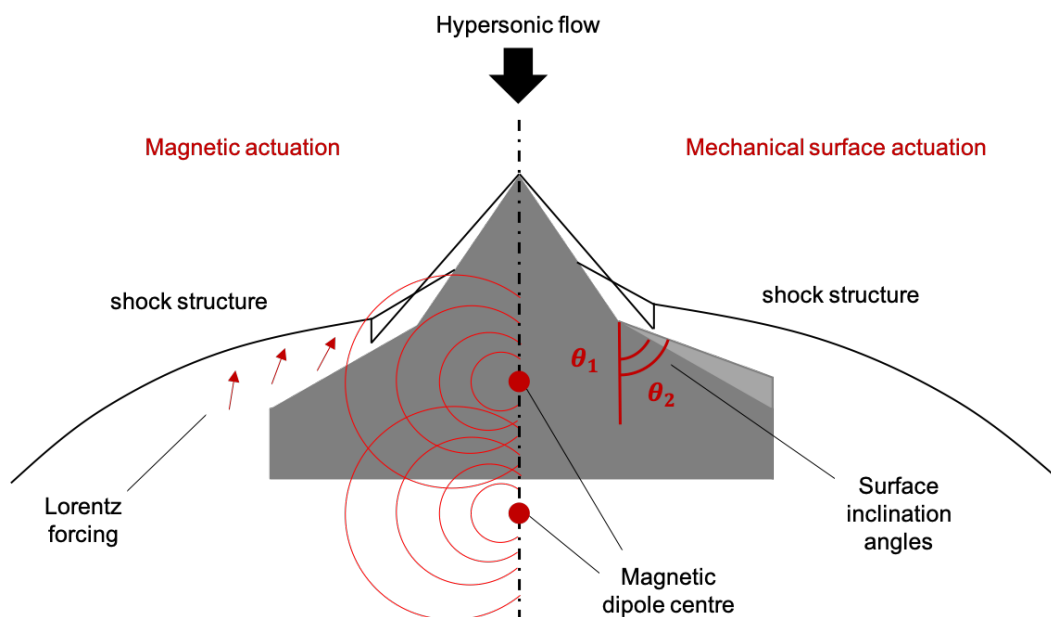


Fig. 1.3 Comparison of magnetic actuation via MHD effect, and mechanical actuation via physical surface inclination, for a double cone geometry. Left) two different positions of magnetic dipole centre are shown, where resultant Lorentz forcing acts on the shock layer, and right) two different second surface inclination angles are depicted (θ_1 and θ_2), which similarly influences the shock position.

In hypersonic flows where a sufficiently high level of electrical conductivity is generated via direct impact of the freestream with the vehicle body, an imposed magnetic field can directly influence the flow [63] - as is the focus of this work. Purely magneto-aerodynamic control (magnetic field only) has shown to be able to affect separation regions with the possibility of altering shock-boundary layer interactions in hypersonic flows over non-simple geometries [71].

The possibility of replacing mechanical control surfaces via *magnetic actuation* is an enticing prospect in hypersonic flight, due to the extreme loads and multiple moving parts involved in physical surface actuation. The double cone is considered a highly useful

test geometry since the resultant flow exhibits all of the relevant features of common 3D internal engine geometries or generic aerodynamic control surfaces. Figure 1.3 depicts the comparison between shock structure control via imposed MHD effect and traditional mechanical surface actuation.

While the magnetic actuation concept is a popular proposal, research is in its infancy. Experiments have been able to demonstrate and measure an MHD shock enhancement effect for a hypersonic double cone [34]. However significant challenges prevail in the numerical modelling, due to the sensitivity of feature formation and the thermochemistry of the weakly ionised plasma, as will be discussed in section 1.1.3.

Magnetic actuation technologies provide the motivating context for the extended studies in Chapter 6 of this thesis, where a non-simple geometry produces multiple shock-wave and boundary layer interactions. This particular flow configuration becomes a key focus of numerical simulation in this work due to the complex and coupled magneto-fluid dynamic effects which can be investigated.

Remote energy deposition - Joule heating methods

Given the practical limitations of generating strong magnetic fields on board flight vehicles, conductivity enhancement via remote energy deposition is an active area of research. Such concepts may extend the viability of magnetic flow control from the hypersonic to the supersonic flow regime. There are many different techniques currently being explored to generate and enhance the plasma, including: plasma arcs, laser pulse methods, microwave energy deposition, electron beams and electrical discharges, all of which can be classified as energy deposition methods. Many such methods have been investigated experimentally and numerically [38, 74], and are summarised in the extensive survey by Knight [75].

Russell et al. [74] conduct a comprehensive review of energy deposition methods which can be classed as Joule heating methods. The mechanism is analogous to a wire which becomes heated due to its resistivity when an electric current runs through it. Due to the resistivity of the air, the gas becomes almost instantaneously heated when electric, microwave or laser induced discharges are applied to the flow. In the case of laser energy deposition, active flow control is enacted either due to the blast wave generated at the source of energy deposition, or by the localised heating of the fluid. Zheltodov and Pimminov [37] note that such Joule heating methods can be utilised to achieve desirable properties including lift and drag control.

With rapid advancement currently under way in laser technology, it is expected in the near future that an efficient high-power and lightweight on-board laser system, such as a fiber laser system, will become available [76]. Therefore, over recent years, several experimental and numerical studies have examined whether laser energy deposition upstream of supersonic and hypersonic vehicles can serve to alter aerodynamic properties, and whether

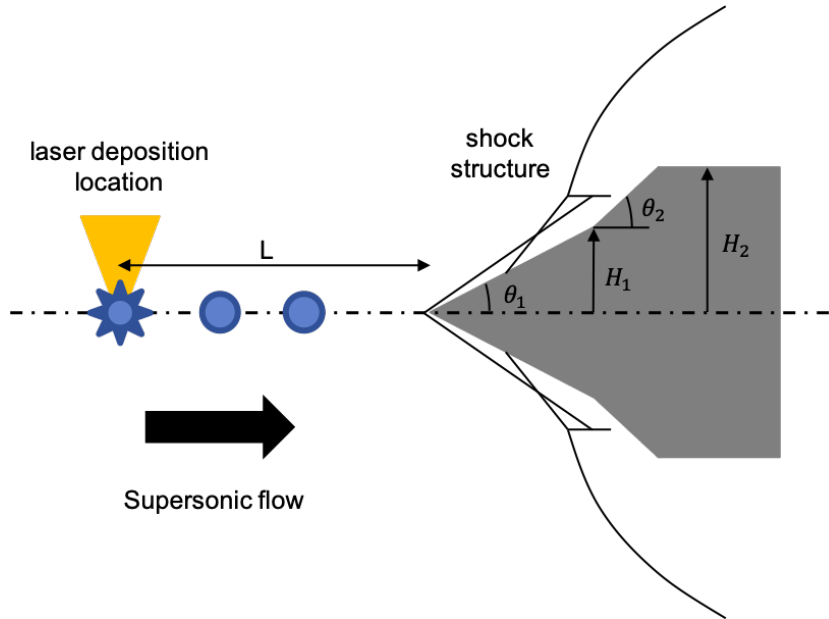


Fig. 1.4 Example configuration of remote laser energy deposition experiment (optical lens of laser located in vehicle nose - surprising as it may seem, the laser system is housed entirely on-board). Energy is deposited by the laser up-stream of the double cone geometry, with heated bounded volumes of gas then propagating over the vehicle.

this can be deliberately leveraged to achieve active flow control. An example of the proposed configuration is shown in Figure 1.4.

This is the motivating technology context for Chapter 7 of this thesis, which applies the developed numerical model to applications in remote energy deposition. A more extensive literature review on this application is contained therein.

1.1.3 Prevailing numerical modelling challenges

Whilst numerical modelling is foundational to the study of aerospace plasma technologies, many challenges remain in producing realistic and efficient numerical simulations. These prevailing challenges include:

Computationally tractable mathematical models

The governing MHD system equations are derived by combining the compressible Navier-Stokes equations for fluid dynamics, with Maxwell's equations for electromagnetism. Therefore, the full governing equations which describe the behaviour of magnetofluids are characterised by complex and coupled phenomena evolving on disparate spatial and temporal scales. This renders computation of the *complete* magneto fluid dynamics governing physics *intractable*, even for the most advanced computational infrastructures of today [77]. Therefore, any attempt in the computational modelling of magnetohydrodynamic systems necessitates some form of simplification and assumption-based reduction of the governing mathematical

model. The precise system reductions, and assessment of the extent of validity of such assumptions, is highly problem specific, and the subject of ongoing analysis in the literature [26]. There is a lack of general consensus of appropriate system reductions for various regimes, and there is an inevitable trade-off between the extent of physical phenomena accounted for and computational expediency.

Such analysis of the governing physics for the end-applications of interest is therefore the subject of Chapter 2 of this thesis. Certain model reductions can be assumed *a priori* and then assessed *a posteriori* for the various test problems under examination. Continual interrogation and analysis is necessary, and will be a theme of the dissertation.

Realistic thermochemistry for weakly ionised air plasma

The mathematical model must be closed with an equation of state (EoS). This EoS can be of the simple ideal gas form, or encompass a full thermochemistry model accounting for the dissociation and ionisation reactions under various governing equilibrium or non-equilibrium assumptions. The selection and development of EoS is cornerstone to realistic modelling of hypersonically generated air plasmas, including the computational of electric transport properties. However, very many different gas chemistry models are employed in hypersonics and MHD models, yielding large differences in the resultant computations and predictions. Again, there is a very strong reciprocation between exactitude and tractability.

This is the subject of extensive review in Chapter 3, leading to the adoption and extension of a new advanced 19-species equilibrium air-plasma model for this work.

Accurate resolution of electric properties

The prediction of key electromagnetic properties of the flow field: specifically electron number density (N_e) and electrical conductivity (σ) are tightly linked to the gas chemistry model, and remain problematic in the numerical modelling of aerospace plasmas. Niu et al. [2] demonstrate widely different predictions of electron number density even for very similar thermochemistry models, and Bisek [78] highlights how the semi-empirical electrical conductivity models commonly adopted in equilibrium plasma models remain problematic for MHD simulations.

Also covered in Chapter 3 of this thesis is the key extensions made to the EoS to ensure the direct and accurate calculation of key electrical properties: specifically N_e and σ . The prediction of N_e is the key parameter of interest for examining the communications blackout problem, and σ is critically important for accurately predicting flow alterations and shock augmentation due to imposed MHD effects. The expression for Lorentz forcing can be expanded to show the direct relationship to electrical conductivity:

$$\mathbf{Lorentz\ Force} = \mathbf{J} \times \mathbf{B} = \sigma(\mathbf{E} + \mathbf{u} \times \mathbf{B}) \times \mathbf{B} \quad (1.2)$$

By extension, the numerical integrations required to compute Lorentz forcing dynamics require careful consideration for numerical stability of Lorentz forcing dynamics and for property consistency.

Hypersonically robust numerical solvers

The simulation of hypersonic flows is known to test the limits of numerical solvers - especially in the cases of unsteady flow dynamics and for non-negligible viscous effects [79]. Even in the case of reduced governing physics to assume an inviscid flow, the interaction of strong shock with solid bodies in the hypersonic regime is known to induce transverse wave instabilities [80], requiring careful selection and adjustments to inviscid flux solvers.

Given that this thesis is primarily concerned with effective algorithm development for hypersonic flows (with MHD effects), careful attention is paid to the selection and development of a hypersonically stable flow solver, which is generalised and robust for a wide range of problems. This is a key component of the algorithm developments described in Chapter 4.

Complex geometries and meshing

Whilst the reentry applications of interest typically involve simple spherical nose-cones and blunt body geometries, an effective model should be able to handle arbitrarily complex geometries to be applied across various applications. Meshing methods and geometry implementation are interrelated in terms of the numerical model development. Effective meshing techniques, especially for complex geometries, remain to be a critical issue in hypersonic flow simulation [81]. Hypersonic flows over complex geometries are able to generate very strong vacuum and compression regions, even simultaneously in time at different locations along the vehicle surface. These extreme flow conditions test the sensitivity and robustness of the numerical solver. The effectiveness of the underlying mesh topology combined with the geometry construction fundamentally affect the accuracy of the flow solution - especially in the case of viscous flows which produce shock-wave boundary layer interaction.

Even in the case without imposed magnetic effects, the simulation of hypersonic flows over non-simple geometries with significant real gas effects remains a major validation challenge [82, 83].

The numerical approaches taken to develop effective geometry implementation for hypersonic viscous flows over arbitrarily complex geometries is addressed in the numerical methods of Chapter 4. The effectiveness of the proposed methodology to capture complex flows over non-simple geometries, with significant viscous and real gas effects is demonstrated in the validation tests of Chapter 5.

Efficient computation

It is one thing to compute realistic flow field solutions, it is another to achieve this within practicable computing time. The total computational cost has several dependencies and interdependencies, including: the extent of physics captured in the mathematical model, equation of state, underlying meshing framework, serial or parallel computing architectures, numerical methods and resulting temporal stability requirements, effective algorithmic implementation of selected methods, among other considerations.

The design of a holistically efficient numerical model is therefore a multifaceted undertaking and a constant consideration throughout this dissertation.

Quantitative prediction of MHD flow control - simple and complex flows

As described, the simulation of MHD effects in hypersonic flows is a complex problem with ongoing developments in numerical approaches. At present, qualitative agreement has been achieved between simulation and experiment in terms of: augmented shock structures due to Lorentz forcing (increase in shock stand-off distance), changes to surface properties and prediction of key electric properties through the shock layer [54, 26].

Where simple geometries can be considered to produce an elemental shock structure (e.g. a bow shock or an oblique shock), magnetically influenced shock layer enhancement leads to a *self-similar* shock structure. The MHD effect can typically be quantified through a singular variable (e.g. the increase in shock stand-off distance through the stagnation line, or, the change in angle of the leading oblique shock). Non-simple geometries which produce multiple shock interactions and complex shock structures cannot be analysed in such a simple way. Experiments on a hypersonic flows with multiple shock interactions and imposed MHD effects have presented a major challenge for quantitative replication via numerical simulation. This is primarily due to the sensitivity of feature formation and realistic thermochemistry modelling of the weakly ionised plasma (including electric property prediction) . This flow type is therefore selected as a key focus of this thesis in the MHD applications examined in Chapter 6.

The numerical methodology proposed in this thesis aims broadly to make improvements in quantitative predictions in regimes where identified governing assumptions can be verified.

Pilot studies into remote energy deposition and plasma enhancement

Emerging technologies in remote energy deposition and Joule heating methods for plasma-based flow control is an active area of research [74]. Several experiments are yet to be simulated or effectively replicated via numerical modelling, and the parameter space for new experiments and technologically viable configurations is largely undetermined. Therefore pilot studies into these emerging plasma-based aerospace technologies is of high research interest. Robust and realistic simulation is dependant upon effective implementation of the

instantaneously deposited energy, efficient and high resolution methods for dynamic feature tracking, and suitable equations of state for the air-plasma. Chapter 7 explores a number of contemporary applications for which the developed numerical model of this work is highly suitable, and can make practical predictions.

1.2 Thesis overview

1.2.1 Research objectives and novelty

This thesis reports on the development of an original numerical methodology suitable for the *realistic* and *efficient* simulation of weakly ionised plasmas formed from hypersonic flows, and their active manipulation via imposed MHD effects. The numerical methodology is implemented directly, and entirely from the ground-up within a state-of-the-art meshing framework: AMReX. The ‘from-scratch’ development has enabled complete control and flexibility of the algorithm design in order to combine established numerical methods and new extensions coupled with selected meshing and geometry approaches. This, in combination with a newly extended and advanced EoS presents what is collectively a novel approach to the numerical modelling of hypersonic plasmas in the equilibrium regime.

As alluded to from the described numerical modelling challenges, the notable aspects to highlight in the proposed formulation, numerical approach, and physics studies include:

- **Modularised derivation of problem-specific mathematical models:**

By adopting a modularised approach with clear governing assumptions and corresponding reductions, solution of the relevant system for different test problems yields important computational efficiency gains. The modularised mathematical modelling informs the numerical model design which can be specified to compute the full-model or any sub-model, combined with simple or advanced EoS. Sub-models and associated reductions are clearly identified and independently assessed.

- **Adoption and extension of a new advanced 19-species equilibrium air-plasma EoS:**

This work identifies the utility in adopting a new advanced 19-species air-plasma EoS to be applied for the first time to hypersonically generated air-plasmas. The EoS takes the form of tabulated database recently generated by Träuble in 2018 [84], based on theory developed by other authors [85–87]. This database has been extended in this work in order to be suitable for hypersonic flight regimes, and key improvements are made to the computation of electron number density and electrical conductivity. Improvements are also made to the efficiency of state access routines. While this EoS offers advancements in simulating equilibrium air-plasmas, naturally, it constrains

the model to the equilibrium regime, an assumption which must be assessed for each problem of interest.

- **Implementation within a high performance computing and meshing framework - AMReX:**

AMReX is adopted as the underlying meshing framework for this work. Clear designation of how the algorithms are developed within this framework is given in Chapter 4. The AMReX meshing framework offers block-structured parallelism (a highly efficient and scalable approach) and functionality for hierarchical adaptive mesh refinement, which is considered state-of-the-art in modern computational fluid dynamics [88]. The AMR offers significant advantages over standard meshing approaches, resulting in improved accuracy, especially for transient simulations where high effective resolution is maintained for critical flow features.

- **Arbitrarily complex geometries via an embedded rigid body Ghost Fluid Method:**

This work selectively implements an embedded boundary rigid body Ghost Fluid Method (GFM) in order to compute arbitrarily complex geometries within the block-structured Cartesian mesh of the AMReX framework. This method is determined to be suitable for hypersonic flows where very strong shocks interact with solid bodies. Validation demonstrates the ability of the implemented whole-cell rigid body GFM to capture viscous flows with complex shock wave boundary layer interaction over non-simple geometries within a block-structured Cartesian mesh - a distinct yet efficient approach compared with prevailing hypersonics simulations in the literature.

- **Hypersonically stable solver:**

An extension is made to the standard inviscid flow solver in order to ensure a generalised and robust inviscid flux computation, which ameliorates the instabilities known to manifest in numerical solvers for hypersonic flows over blunt bodies. The extension is specifically designed for a block-structured Cartesian AMR framework without the need for manual tuning parameters (which other implementations rely upon).

- **Unique combination of numerical methods:**

Whilst the majority of implemented algorithms are established and trusted numerical methods, the combination of methods and their extensions, implemented within the specified meshing framework, with advanced EoS, collectively presents a unique approach. The interdependent and unified development of which is not straightforward. Extensive validation is therefore important to demonstrate the efficacy of the new developed model.

- **High computational efficiency:**

The combination of: problem specific governing system reductions, equilibrium chemistry implemented with improved state-access routines, block-structured parallelism and efficient hierarchical AMR, fast-sweeping routines within the whole-cell GFM method for geometry, direct flux reconstruction within the hypersonically stable solver extension, conjointly results in an overall computational model which is designed for very high efficiency.

- **Quantitative accuracy for hypersonic flows with MHD effects:**

The proposed numerical methodology, implemented directly as a new numerical model, is quantitatively validated across a wide range of problems. Notably, the model demonstrates quantitative agreement with experiment for the prediction of MHD augmented shock position in a complex double cone flow. This is a step forward for flows of this type.

- **Numerical studies of the flow physics:**

The validated numerical model is applied to investigate the flow physics of a number of aerospace plasma problems of research interest. Numerical studies are conducted for hypersonic flows with complex shock interactions, and imposed MHD effects. Examination of simulation results reveals new insights into the detailed and coupled fluid and magneto dynamic behaviours at play. The studies seek to explore and explain the key mechanisms of action, and resultant effects. The model is also utilised to make meaningful predictions, relevant to hypersonic flight control technologies.

- **Model capabilities for future applications and studies:**

The high degree of generality of the developed (and modularised) numerical methodology, means it offers high suitability to new and emerging aerospace plasma research problems. A final study seeks to demonstrate model capabilities (specifically the utility of shock-tracking AMR in dynamic transient flows, where air-plasmas are generated and propagated), to showcase future applications of study.

Peer-reviewed publication

Contents of this dissertation have been published as a Chapter in the peer reviewed Springer-Nature Book: "Active Flow and Combustion Control 2021", which is part of the series: "Notes on Numerical Fluid Mechanics and Multidisciplinary Design (NNFMMD)". [89]

Publication details: "Numerical methodologies for magnetohydrodynamic flow control for hypersonic vehicles" - H.A. Muir¹, L. Michael, N. Nikiforakis

AFCC 2021, NNFM 152, Chapter 21 pp. 336–355, 2022,

DOI: https://doi.org/10.1007/978-3-030-90727-3_21

The scope of the paper covers the proposed numerical methodology pertaining to the *full system model*, including plasma equation of state, some primary validation test cases

from Chapter 5, and the result of the MHD double cone flow test (at experimental condition) of Chapter 6, section 6.2.

1.2.2 Thesis outline

An interesting facet of scientific dissertations is the clear distinction between the scientific object of development - in this case, a large numerical model comprising of approximately 10,755 directly written lines of code (excluding settings files) - and the deliverable of a written document. The written pages of this thesis are organised to best reflect and explain the development of those lines of code, and the many Gigabytes of data it produces at runtime. It is the arrangement, visualisation and analysis of that data which permits meaningful numerical investigations in aerospace plasma physics.

By now most of the dissertation contents have been introduced. This can all be drawn together into the hypothesis: *Advances in numerical modelling techniques, combined with an advanced EoS, permits the realistic and efficient simulation of hypersonically formed plasmas. Further, this enables new and useful predictions about the control of such flows by applied magnetic fields.*

To summarise the organisation of this document: the dissertation follows the logical process for numerical modelling development and application. This begins with the mathematical modelling of the problem-specific physics, explained and derived in Chapter 2. An important part of the theoretical problem formulation is the EoS. This is therefore a subject of its own in Chapter 3: covering aspects of both its formulation and embedded implementation. The foundational numerical methods implemented, extended, and combined within the AMReX framework is the subject of Chapter 4. Once the numerical model has been developed, extensive validation is essential, especially given the unique combination of numerics proposed in this work. Each of the derived sub-models is independently validated against benchmark results and experiments in Chapter 5. The model is then applied to the key applications of MHD flow control in Chapter 6. Simulations in this Chapter reveal improved predictive performance as compared with experiment, and the model is utilised for parameter studies to investigate a range of physical phenomena. A second class of applications is identified, for which the developed model offers high practical utility. Pilot studies into remote energy deposition is the subject of Chapter 7. In the final Chapter, notable avenues for future developments and applications are proposed, and the work undertaken over the course of this PhD is summarised.

Chapter 2

Mathematical modelling

Perhaps one of the greatest minds to contemplate problems of computer science, physics (including hydrodynamics), mathematics and logic, John Von Neumann had the following ponderings on the role of mathematical models in the sciences:

“The sciences do not try to explain, they hardly even try to interpret, they mainly make models. By a model, what is meant, is a mathematical construct, which, with the addition of certain verbal interpretations, describes observed phenomena. The justification of such a mathematical construct is solely and precisely that it is expected to work- that is, to correctly describe phenomena from a reasonably wide area.”

The musings “reasonably wide area” is particularly apt in the case of the fluid dynamics models. Naturally, the physical world is constituted of very many processes across discordant scales. Whilst the physics at the very smallest of scales inherently gives rise to all emergent physics at every broader scale, the emergent physics can be so dissimilar that entirely different governing mathematical models are required to (practically) describe the ensuing phenomena. This is cornerstone to the development of problem-specific physics models, and even more pivotal when considering the tractable computation of such mathematical models.

So called “direct numerical simulation” considers problems where the complete physics of a particular problem scale is described by the governing mathematical model, and solution with sufficient resolution to enclose this scale will explicitly produce all emergent phenomena. Within the limits of present computational resources, sufficient resolution across disparate scales often renders attempts at direct numerical simulation as impracticable or impossible. In such cases, physically justified assumptions and system reductions are not only useful, but essential.

Accounting for all of the physics which arises in a compressible, high temperature, high conductivity, magneto-fluid results in system equations of great complexity and of multi-scale phenomena, and which are ultimately computationally intractable. In this section we first develop a full mathematical model of the magnetohydrodynamic equations which govern an aerospace plasma. From this starting point we then consider important characterising

parameters and relative orders of magnitude in order to deduce reasonable system reductions. These system reductions are not only useful, but highly necessary in terms of tractable computation of governing MHD system equations for aerospace plasmas.

The reductions of this section therefore define a set of sub-models, and assumptions associated with each reduced model, constituting a modularised approach to the numerical modelling. A map of full and sub-models is developed to clearly delineate the underlying assumptions and resultant physics of each sub-model proposed for numerical solution.

2.1 Physics of fluids

With all matter fundamentally constituted of atoms and molecules, the most basic manner in which these particles interact with one another gives rise to the different fundamental states at the macroscopic scale: solids, liquids, gases and plasmas. From a “reasonably wide area” such that the field of view is much larger than the inter-atomic distances and, in the case of gases, mean free particle paths, then matter can be treated as continuously distributed in space. This work is interested in the mathematical treatment of gases and plasmas as a fluid in the so-called continuum regime.

2.1.1 Fundamental equations of fluid dynamics

The motion of viscous fluids is described in full by the system of Navier-Stokes equations. As per convenient reputation, these equations pose a number of challenges. Famously, a proof (or disproof) of existence and smoothness in three-dimensions, is to be rewarded with a US \$1 million prize as one of the seven Millennium Prize Problems [90]. This thesis does not set such a lucrative objective, however the spatio-temporal solution of the system in terms of primitive variables (velocity, density, pressure, internal energy) given initial and boundary conditions, is not trivial. Numerical solution, in practicable computing time, is especially difficult with consideration of viscous effects.

The system of non-linear partial differential equations reflect three basic principles of physics: the conservation of mass, momentum (Newton’s First Law), and energy (First Law of Thermodynamics). The compressible Navier-Stokes equations in conservative form are given by:

$$\frac{\partial}{\partial t} \rho + \nabla \cdot [\rho \mathbf{u}] = 0 \quad (2.1)$$

$$\frac{\partial}{\partial t} (\rho \mathbf{u}) + \nabla \cdot [\rho \mathbf{u} \otimes \mathbf{u} + p \mathbf{I}] = \nabla \cdot \boldsymbol{\tau} \quad (2.2)$$

$$\frac{\partial}{\partial t} E + \nabla \cdot [(E + p) \mathbf{u}] = \nabla \cdot (\boldsymbol{\tau} \mathbf{u}) + \nabla \cdot (\zeta (\nabla T)) \quad (2.3)$$

Compressible Navier-Stokes equations

where this form assumes that the Cauchy stress tensor τ is Galilean invariant, meaning it does not depend directly on the velocity field, only its gradient ($\nabla\mathbf{u}$), and further, this dependency is linear. The fluid is assumed to be isotropic, and consequently the stress tensor is symmetric and able to be represented by:

$$\tau = \mu(\nabla\mathbf{u} + \nabla\mathbf{u}^T) + \lambda(\nabla \cdot \mathbf{u})I \quad (2.4)$$

where μ is the fluid dynamic viscosity and λ is the so-called second viscosity coefficient, which is only required for compressible flows, and where here it is standard to adopt Stokes' hypothesis, setting $\lambda = -\frac{2}{3}\mu$. The flow is treated as laminar for the supersonic and hypersonic problems of interest in this work. ζ in the energy continuity equation 2.3 is the fluid's thermal conductivity.

The *conserved variables* of the system are naturally those of the basis conservation laws (per unit volume): mass (ρ), momentum ($\rho\mathbf{u}$), and energy (E) where E is defined as the sum of internal and kinetic energy:

$$E = \rho e + \frac{1}{2}\rho|\mathbf{u}|^2 \quad (2.5)$$

It is useful to consider the so-called primitive variables of the system: density (ρ), pressure (p), internal energy (e) and velocity (\mathbf{u}), which are a more rudimentary characterisation of the fluid state, and therefore useful as input arguments for transformations and operations on the fluid (see numerical methods section).

To mathematically close the system of equations, an equation of state is required which defines an explicit relationship between the primitive properties: $e = f(\rho, p)$. The choice of equation of state involves complex considerations, especially for the case of weakly ionised plasmas in hypersonic flows, and is the subject of Chapter 3.

In the most simple case for system closure, the ideal gas law is given by:

$$e = \frac{p}{\rho(\gamma - 1)} \quad (2.6)$$

where the adiabatic index γ is a fixed constant.

The development of the complex 19 species equilibrium air-plasma EoS - plasma19X - is detailed in Chapter 3.

2.1.2 Plasma- the fourth state of matter

First discovered in the 1920's by chemist Irving Langmuir, like a gas, plasma has no definite shape or volume. Unlike a gas, plasma is able to conduct electricity and is affected by magnetic fields. More than 90% of the observable matter in the Universe exists as a plasma state [91].

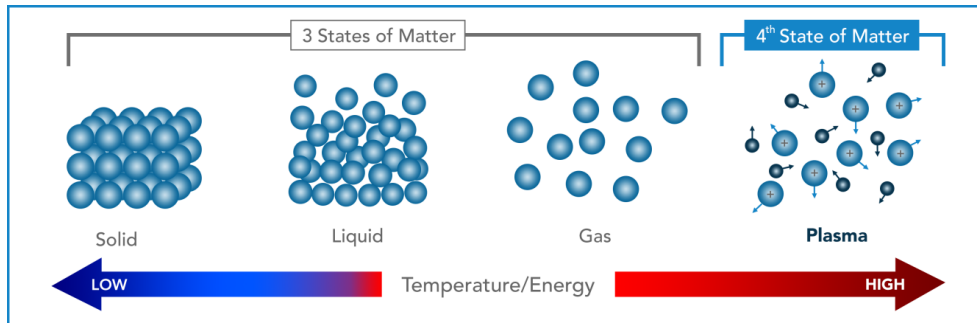


Fig. 2.1 Plasma: the fourth state of matter

In a very high energy state electrons dissociate from nuclei resulting in positively charged nuclei in a sea of negatively charge electrons, thus the medium is able to conduct electricity. Plasma, however, is an *electrically neutral medium* in the sense that the overall charge is zero (balanced).

There are two ways for a plasma to form from a gas: when a huge voltage difference is created between two points (as in lightning strikes), and when a gas is exposed to extreme temperatures (as in the shock layer of high enthalpy hypersonic vehicles). The medium can be categorised as either ‘partially ionised plasma’ when only some of the electrons have dissociated (Earth’s ionosphere and magnetosphere contains partially ionised plasma), or ‘fully ionised plasma’ when the gas had undergone complete dissociation. This constitutes a very high energy state under extreme energy conditions, as for example in the sun’s interior and other stars.

One of the key considerations in the study of plasma across different applications, is the handling of phenomena at different scales. The microscopic definition of plasma describes the motion of individual charged and neutral particles. The macroscopic view of plasma does not disregard the microscopic particle behaviours, but incorporates them in such a way as to establish and define collective behaviour [91]. The theory of plasma at the *macroscopic scale* is termed magnetohydrodynamics, and its much needed acronym: MHD.

Assuming the collision frequency within the plasma is sufficiently high, flow length scales are significantly larger than the Debye length, and time scales are larger than the reciprocal of the plasma resonant frequency, we may develop a continuum model such that the flow is characterised by a set of macroscopic quantities.

$$\lambda_D = \sqrt{\frac{\epsilon_0 k T}{N_e e^2}} \quad (2.7)$$

Debye length

$$\omega_P = \sqrt{\frac{N_e e^2}{M_e \epsilon_0}} \quad (2.8)$$

Plasma resonant frequency

On a scale where the spatial (λ_D) and temporal (ω_p^{-1}) criteria are satisfied, the MHD governing equations are derived by combining the Navier-Stokes equations for fluid dynamics, with Maxwell's equations for electromagnetism.

2.1.3 Maxwell's equations for electromagnetism

Inspired by Faraday's drawings of *Lines of Force*, a young James Clerk Maxwell set about conducting a series of "peculiar" experiments in the 1850s at the University of Cambridge physics laboratory, just a short stroll down the road. Though the experiments were described as "not well organised" and "confusing to scientists", ultimately they resulted in successfully unifying theories of light and electromagnetism, considered one of the *great unifications in Physics*. Now writing this thesis from The Maxwell Centre at the new Cavendish Laboratory, the set of Maxwell's equations can be neatly expressed as:

$$\nabla \times \mathbf{E} = -\frac{\partial \mathbf{B}}{\partial t} \quad (2.9)$$

Faraday's law of induction

$$\epsilon_0 c^2 \nabla \times \mathbf{B} = \mathbf{J} + \epsilon_0 \frac{\partial \mathbf{E}}{\partial t} \quad (2.10)$$

Ampere-Maxwell's law

$$\nabla \cdot \mathbf{E} = \frac{\rho_c}{\epsilon_0} \quad (2.11)$$

Gauss's law for electricity

$$\nabla \cdot \mathbf{B} = 0 \quad (2.12)$$

Gauss's law for magnetism

It can be shown that if equations 2.11 and 2.12 hold at an initial time, then they hold for all time. Consider that by re-arranging equation 2.10, and taking the divergence of both sides:

$$\nabla \cdot (\nabla \times \mathbf{B}) = \nabla \cdot \left(\frac{1}{\epsilon_0 c^2} \mathbf{J} + \frac{1}{c^2} \frac{\partial \mathbf{E}}{\partial t} \right) \quad (2.13)$$

where then the LHS becomes zero as $\nabla \cdot \nabla \times \mathbf{v} = 0$, $\forall \mathbf{v}$, and we have:

$$0 = \nabla \cdot \left(\mathbf{J} + \epsilon_0 \frac{\partial \mathbf{E}}{\partial t} \right) \quad (2.14)$$

Now substituting with the charge continuity equation: $\nabla \cdot \mathbf{J} = -\frac{\partial \rho_c}{\partial t}$, we arrive at:

$$\frac{\partial}{\partial t}(-\rho_c + \epsilon_0 \nabla \cdot \mathbf{E}) = 0 \quad (2.15)$$

and it can be seen that if equation 2.11 has an initial value of zero, then it remains zero for all subsequent time. Similarly applying the divergence operator to equation 2.9, under similar analysis we see that: $\frac{\partial}{\partial t}(\nabla \cdot \mathbf{B}) = 0$. These are important relationships to draw before combining Maxwell's equations with the Navier-Stokes equations to define the full set of MHD conservation equations.

2.1.4 MHD conservation equations

To represent the electric effects of charged particles on the continuum scale, we define the conservative variable: electric charge density ρ_c , by summing the electric charges per unit volume for each component, where Z_i is the charge of the individual component (ie. -1 for electrons, 0 for neutral species, +n for positive ions of charge n):

$$\rho_c = e \sum_{i=1}^n \frac{\rho_i}{m_i} Z_i \quad (2.16)$$

The flux of electric charge is given by the total electric current density \mathbf{J} . Importantly, \mathbf{J} is comprised of two components, the so-called *convection current* $\rho_c \mathbf{u}$, and *conduction current* \mathbf{J}_Q :

$$\mathbf{J} = \rho_c \mathbf{u} + \mathbf{J}_Q \quad (2.17)$$

and the conservation equation for electric charge is given by:

$$\frac{\partial \rho_c}{\partial t} + \nabla \cdot \mathbf{J} = 0 \quad (2.18)$$

Electric charge continuity

The conduction current \mathbf{J}_Q describes the flux of electric charge density due to diffusion, which, at a macroscopic level depends on the electromagnetic field via Lorentz force, and to a lesser extent, on pressure and temperature gradients via conduction or diffusion coefficient tensors: $\sigma_{e_j}^p$ for presso-electrical coefficient for gradients of partial pressures p_j , σ_e for electrical for Lorentz force and σ_e^T for thermo-electrical for temperature gradient [77].

$$\mathbf{J}_Q = \sigma_e \cdot (\mathbf{E} + \mathbf{u} \times \mathbf{B}) + \sigma_e^T \cdot \nabla T + \sum_{j=1}^n \sigma_{e_j}^p \cdot \nabla p_j \quad (2.19)$$

Ohm's Law for conduction current

Treating the fluid as a single, equilibrated (chemically and thermally) fluid, the total mass conservation equation for the system remains is as per the Navier-Stokes continuity equation 2.2.

The momentum balance is augmented via the Lorentz force. Here, the stress tensor $\bar{\tau}$ accounts for regular fluid viscosity as well as electromagnetic viscous effects. We then have:

$$\frac{\partial}{\partial t}(\rho \mathbf{u}) + \nabla \cdot [\rho \mathbf{u} \otimes \mathbf{u} + p \mathbf{I}] - \nabla \cdot \bar{\tau} = \rho_c \mathbf{E} + \mathbf{J} \times \mathbf{B} \quad (2.20)$$

Conservation of momentum

Similarly, the full energy equation must include a source term to describe the rate of conversion of electromagnetic energy into matter energy. The fluid medium also contains a diffusing flux current which is opposed by the convection of electromagnetically induced viscosity, and a radiative heating effect through S_R . In full the energy balance becomes:

$$\frac{\partial}{\partial t} E + \nabla \cdot [(E + p) \mathbf{u}] + \nabla \cdot (\mathbf{J}_U - \bar{\tau} \mathbf{u}) = \mathbf{J} \cdot \mathbf{E} + S_R \quad (2.21)$$

Conservation of energy

where E remains defined as per equation 2.5.

Therefore the full system consists of the conservation of mass equation 2.2, the four augmented conservation equations 2.17, 2.18, 2.20 and 2.21, alongside Maxwell's equations 2.9 and 2.10.

Complete form MHD system equations

$$\frac{\partial}{\partial t} \rho_c + \nabla \cdot \mathbf{J} = 0 \quad (2.22)$$

$$\frac{\partial}{\partial t} \rho + \nabla \cdot (\rho \mathbf{u}) = 0 \quad (2.23)$$

$$\frac{\partial}{\partial t}(\rho \mathbf{u}) + \nabla \cdot [\rho \mathbf{u} \otimes \mathbf{u} + p \mathbf{I}] = \rho_c \mathbf{E} + \mathbf{J} \times \mathbf{B} + \nabla \cdot \bar{\tau} \quad (2.24)$$

$$\frac{\partial}{\partial t} E + \nabla \cdot [(E + p) \mathbf{u}] = \mathbf{J} \cdot \mathbf{E} + \nabla \cdot (\bar{\tau} \mathbf{u}) + \nabla \cdot (\zeta (\nabla T)) \quad (2.25)$$

$$\frac{\partial \mathbf{B}}{\partial t} = -\nabla \times \mathbf{E} \quad (2.26)$$

$$\epsilon_0 c^2 \nabla \times \mathbf{B} = \mathbf{J} + \epsilon_0 \frac{\partial \mathbf{E}}{\partial t} \quad (2.27)$$

where the system is closed by the definitions of \mathbf{J} via Ohm's law, E as per equation 2.5, and primitive variables are related via an equation of state.

2.2 Modelling an aerospace plasma

2.2.1 Important dimensionless numbers

There are 4 dimensionless numbers which are highly useful for characterising the nature of a flow, and determining reasonable system reductions. The compressibility effects of a fluid at velocity are closely related to Mach number:

$$Ma = \frac{\text{Flow velocity}}{\text{Acoustic speed}} = \frac{V_0}{a} \quad (2.28)$$

The different compressibility regimes are classified in Figure 2.2.

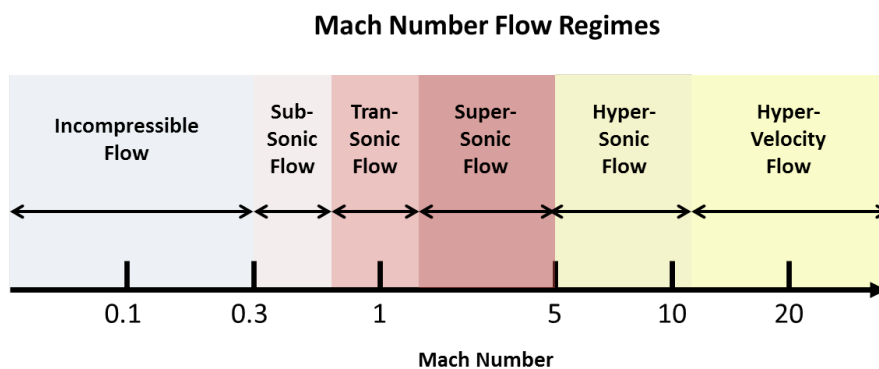


Fig. 2.2 Flow regimes as classified by Mach Number

While the most typical use of Mach number is to verify compressibility assumptions (and therefore the form of governing equations), in the very high Mach number bands of interest in this work, Mach number is a useful indicator of the extent of compressibility effects and the degree of post-shock thermal energy leading to gas dissociation and ionisation. In fact, one of the reasons hypersonic flight is classified as $Ma > 5$ is that this is typically the Mach regime (depending on geometry) where plasma forms.

Reynolds number (Re) indicates the ratio of inertial to viscous forces in a fluid flow and can be defined for this application based on a 2D void diameter (D_0):

$$Re = \frac{\text{Fluid inertial forces}}{\text{Fluid viscous forces}} = \frac{\rho_0 V_0 L_0}{\mu} \quad (2.29)$$

where ρ is the liquid density, V_0 its bulk velocity and μ the viscosity. This parameter is important for determining the ways in which viscous effects (and corresponding terms in the equations) should be accounted for.

The next dimensionless parameters pertain specifically to magnetofluids.

In a highly *conductive plasma*, the coupling between the electromagnetic field and the motion of charged particles is very strong. Magnetic flux is conserved and the motion of the conductive fluid produces an induced magnetic field, which dominates. In a highly *resistive*

plasma, the coupling is weak, such that the imposed magnetic field is only slightly perturbed through the fluid motion, and magnetic diffusion dominates. The strength of this coupling can be quantified through the magnetic Reynolds number.

Re_m is derived by considering the ratio of magnetic advection to diffusion effects within the Ampere-Maxwell equation (2.10):

$$\left| \frac{\sigma_e(\mathbf{u} \times \mathbf{B})}{\epsilon_0 c^2 \nabla \times \mathbf{B}} \right| = \mathcal{O}\left(\frac{\sigma_0 V_0 B_0 L_0}{\epsilon_0 c^2 B_0}\right) = \mathcal{O}\left(\frac{\sigma_0 V_0 L_0}{\epsilon_0 c^2}\right) \quad (2.30)$$

And therefore we define the magnetic Reynolds number.

$$Re_m = \frac{\text{Magnetic induction}}{\text{Magnetic diffusion}} = \frac{\sigma_0 V_0 L_0}{\epsilon_0 c^2} \quad (2.31)$$

Magnetic Reynolds number is a particularly important parameter for deriving problem-specific MHD equations. Where the Magnetic Reynolds number is very high (typically in a highly conductive plasma), then an ideal MHD formulation may be adopted, in which the velocities of charged particles in the plasma dynamically affect the magnetic field and so \mathbf{B} -field is evolved simultaneously within the equations. In many aerospace applications however Re_m is small, meaning the distortion of the magnetic field by the conductive flow can be neglected, and the magnetic evolution equation does not require solution, as will be explored in section 2.2.2.

A very useful parameter for quantifying the dynamic effect of MHD induced Lorentz forcing on the fluid flow, is the Magnetic interaction parameter (Q_{MHD}) which can be derived by considering the ratio of electromagnetic force to fluid inertial force:

$$\left| \frac{\sigma_e(\mathbf{u} \times \mathbf{B}) \times \mathbf{B}}{\nabla \cdot (\rho \mathbf{u} \otimes \mathbf{u})} \right| = \mathcal{O}\left(\frac{\sigma_0 V_0 B_0^2 L_0}{\rho V_0^2}\right) = \mathcal{O}\left(\frac{\sigma_0 B_0^2 L_0}{\rho V_0}\right) \quad (2.32)$$

And therefore defined as:

$$Q_{MHD} = \frac{\text{Lorentz force}}{\text{Fluid inertial force}} = \frac{\sigma_0 B_0^2 L_0}{\rho_0 V_0} \quad (2.33)$$

This parameter will become particularly useful in the analysis of imposed magnetic field applied to hypersonic vehicles in producing MHD flow control effects.

2.2.2 Order of magnitude analysis

Much of the difficulty in solving the complete form MHD system equations, is in the disparate scales of phenomena evolved. This becomes especially cumbersome in consideration of a numerical, time-stepped solution. Therefore, the modification of the equations via sensible magnitude-based approximations is paramount to amenable numerical solution. Here we conduct an order of magnitude analysis specific to weakly ionised plasmas generated around hypersonic vehicles, to therefore derive a reduced base model specific to this work.

To begin with, some baseline assumptions for aerospace plasmas include:

1. Maximum reentry velocity is much less than the speed of light ($V_0 \ll c$) and so relativistic effects can be neglected
2. Electrical conductivity is taken to be an isotropic (scalar) quantity
3. Magnetic viscosity is negligible so τ encapsulates purely the fluid viscosity
4. For an aerospace plasma, within Ohm's law for conduction current (equation 2.19), the thermo-electrical and presso-electro conductivity contributions are much smaller than the electrical conductivity contribution, and so are neglected.
5. Radiative heating: radiative heat transfer has classically been neglected (from equation 2.21) in the literature on the basis that maximum temperatures are not sufficiently high for radiative heating to be a significant heat transfer mode. Care should be taken here. In the case of real gases, the assumption of equilibrated gas chemistry is sensitive to radiative heat transfer and photo-ionisation reactions. For long duration real reentry flight, radiative heating may play an important role, however, on the time scale of short duration impulse facility experiments, or time scale considered for steady state simulations at a fixed freestream condition, it is more reasonable to neglect radiative heat transfer. As such, and for simplicity, radiation is not considered in this work.

We will later address the expansion with inclusion of the Hall current component, however for now we define a generalised Ohm's law as the sum of the convection current and conduction current (diffusion effect):

$$\mathbf{J} = \rho_c \mathbf{u} + \sigma_e \cdot (\mathbf{E} + \mathbf{u} \times \mathbf{B}) \quad (2.34)$$

Further to this, some physically reasonable bounds can be set on key dimensionless parameters for the analysis. The approach then taken in the analysis is to maintain generality by utilising dimensionless parameter Re_m and a *loading parameter* K , with known bounds, to determine reasonable system reductions.

For this analysis, "order" refers to base 10 order, i.e. $10^n = \mathcal{O}(n)$.

Assuming a typical degree of ionisation within a hypersonically generated plasma, we can confidently assert a range of conductivities between σ_0 (S/m) = $[\mathcal{O}(0) : \mathcal{O}(3)]$. For conductivity below 1 S/m MHD effects become unobservable, and energies required to produce plasma conductivities of greater than $\mathcal{O}(3)$ would become impossible in aerospace applications (as established later in the thesis, conductivities are almost always $\mathcal{O}(2)$) for problems of interest). Similarly, for any imposed magnetic field effects to be observable in the problems under study, \mathbf{B} -field strength can be defined as having a lower bound of $\mathcal{O}(-1)$ Tesla (T), and due to weight and size limitations in any wind tunnel testing or real flight, the upper bound has a practical limit of $\mathcal{O}(0)$ T. Hypersonic flight in air corresponding

to altitudes up to the upper atmosphere, can be defined as having a velocity range of V_0 (m/s) = $[\mathcal{O}(3) : \mathcal{O}(4)]$. And vehicle sizes studied in this work range from small test models in wind tunnels of the order of millimetres to a full scale reentry vehicle of the order of metres. Therefore we can quantify a range for length scale: $L_0 = [\mathcal{O}(-2) : \mathcal{O}(0)]$ with high confidence. We also note the following explicitly known orders of magnitude for the problem of interest: $c \approx 3 \times 10^8 = \mathcal{O}(8)$, $\epsilon_0 = 8.854 \times 10^{-12} = \mathcal{O}(-12)$.

Therefore we can define the known, problem-specific bounds on Re_m :

$$Re_m = \frac{\sigma_0 B_0^2 L_0}{\rho_0 V_0} = [\mathcal{O}(-5) : \mathcal{O}(3)] \quad (2.35)$$

It is important to keep in mind that the lower bound here is defined by the lowest possible combination of magnitudes, and highest possible combination for the higher bound. Broadly across the literature, hypersonic plasmas are considered to be in the low magnetic Reynolds number regime, where Re_m is of the order of unity or less [15, 3, 63]. Under this regime the imposed and induced magnetic fields are sufficiently decoupled such that the static imposed magnetic field is unaffected by the flow. However, based on the above defined possible bounds, it is important to still assess this assumption for each test problem.

The approach therefore taken in this analysis, is to maintain generality by retaining the dimensionless parameter Re_m . Similarly, we define another useful dimensionless parameter for the analysis, a *loading parameter* K . Since the respective contributions of \mathbf{E} and $\mathbf{u} \times \mathbf{B}$ in the diffusion current component of Ohm's law (equation 2.34) cannot be known at the outset of the analysis, an interdependence is instead related by defining:

$$K = \frac{V_0 B_0}{E_0} \quad (2.36)$$

Typically in plasmas generated thermally from aerospace applications, $\mathbf{u} \times \mathbf{B}$ is found to dominate over \mathbf{E} . Commonly in the governing equations, since $\mathbf{E} \ll \mathbf{u} \times \mathbf{B}$, the \mathbf{E} component is set to zero. Again to maintain generality of analysis, until this is verified for problem specific cases, we will simply assume a very conservative $K > 1$, meaning $\mathbf{u} \times \mathbf{B}$ is at least larger than \mathbf{E} .

Let's now consider the time and length scales of the problem, and resultant relative orders of magnitude for known quantities in the base equations. We note that spatial derivatives operate over a length scale: $|\nabla| \sim \frac{1}{L_0}$, and for temporal derivatives: $|\frac{\partial}{\partial t}| \sim \frac{1}{t_0}$ characteristic time for the dynamically evolving system is typically regarded as $t_0 = \frac{L_0}{V_0}$.

From rearrangement of Gauss's law (equation 2.11), we can estimate the size of electric charge:

$$\rho_c = \mathcal{O} \left(\frac{\epsilon_0 E_0}{L_0} \right) \quad (2.37)$$

Electric conductivity can be expressed in terms of Re_m via the rearrangement of equation 2.31:

$$\sigma_0 = \frac{Re_m \epsilon_0 c^2}{V_0 L_0} \quad (2.38)$$

Then the order of magnitude analysis for generalised Ohm's law can be expressed:

$$\mathbf{J} = \underbrace{\rho_c \mathbf{u}}_{\mathcal{O}\left(\frac{\epsilon_0 E_0 V_0}{L_0}\right)} + \underbrace{\sigma_e \mathbf{E}}_{\mathcal{O}\left(\frac{Re_m \epsilon_0 E_0 c^2}{V_0 L_0}\right)} + \underbrace{\sigma_e (\mathbf{u} \times \mathbf{B})}_{\mathcal{O}\left(\frac{K Re_m \epsilon_0 E_0 c^2}{V_0 L_0}\right)} \quad (2.39)$$

Considering then the ratio of convective current to diffusive current, we have:

$$\left| \frac{\rho_c \mathbf{u}}{\sigma_e \mathbf{E}} \right| = \mathcal{O}\left(\frac{V_0^2}{Re_m c^2}\right) \quad (2.40)$$

which conclusively shows for the defined bounds on Re_m that the diffusive current dominates and convective current can be neglected. Thus Ohm's law is further reduced to:

$$\mathbf{J} = \sigma_e (\mathbf{E} + \mathbf{u} \times \mathbf{B}) \quad (2.41)$$

Now we can similarly analyse charge continuity (equation 2.18), noting that $t_0 = \frac{L_0}{V_0}$:

$$\underbrace{\frac{\partial}{\partial t} \rho_c}_{\mathcal{O}\left(\frac{\epsilon_0 E_0 V_0}{L_0^2}\right)} + \underbrace{\nabla \cdot \mathbf{J}}_{\mathcal{O}\left(\frac{Re_m \epsilon_0 E_0 c^2}{V_0 L_0^2}\right)} = 0 \quad (2.42)$$

which means the relative magnitude of temporal charge density evolution to electric current divergence is $\mathcal{O}\left(\frac{V_0^2}{Re_m c^2}\right)$ meaning that the time derivative can be set to zero, and we obtain the elliptic equation for divergence free current density: $\nabla \cdot \mathbf{J} = 0$.

Moving our way down the complete form MHD system equations, the order of magnitude analysis for the RHS terms of the momentum equation(2.20) now expand to:

$$\rho_c \mathbf{E} + \mathbf{J} \times \mathbf{B} = \underbrace{\rho_c \mathbf{E}}_{\mathcal{O}\left(\frac{\epsilon_0 E_0^2}{L_0}\right)} + \underbrace{\sigma_e \mathbf{E} \times \mathbf{B}}_{\mathcal{O}\left(\frac{K Re_m \epsilon_0 E_0^2 c^2}{L_0 V_0^2}\right)} + \underbrace{\sigma_e (\mathbf{u} \times \mathbf{B}) \times \mathbf{B}}_{\mathcal{O}\left(\frac{K^2 Re_m \epsilon_0 E_0^2 c^2}{L_0 V_0^2}\right)} \quad (2.43)$$

and in considering therefore the relative magnitude of $\rho_c \mathbf{E}$ to $\sigma_e \mathbf{E} \times \mathbf{B}$ (the smaller of the expanded $\mathbf{J} \times \mathbf{B}$ terms):

$$\left| \frac{\rho_c \mathbf{E}}{\sigma_e \mathbf{E} \times \mathbf{B}} \right| = \mathcal{O} \left(\frac{V_0^2}{KR e_m c^2} \right) \quad (2.44)$$

meaning the $\rho_c \mathbf{E}$ component of magnetic forcing can be neglected and the RHS of the momentum equation is reduced to the $\mathbf{J} \times \mathbf{B}$ Lorentz forcing.

No further reductions of the energy balance of equation 2.25 are necessary given the existing simplification of Ohm's law. However, it is useful to rearrange the $\mathbf{J} \cdot \mathbf{E}$ term into a more intuitive form which defines the plasma resistivity term η as the reciprocal of electrical conductivity:

$$\mathbf{E} + \mathbf{u} \times \mathbf{B} = \left(\frac{1}{\sigma_e} \right) \mathbf{J} = \eta \mathbf{J} \quad (2.45)$$

then rearranging for \mathbf{E} and substituting into the RHS term of equation 2.25:

$$\mathbf{J} \cdot \mathbf{E} = \mathbf{J} \cdot (-\mathbf{u} \times \mathbf{B}) + \eta J^2 = \mathbf{u} \cdot (\mathbf{J} \times \mathbf{B}) + \eta J^2 \quad (2.46)$$

where we have drawn on the anticommutativity of the cross-product and the scalar triple product identity: $\mathbf{A} \cdot (\mathbf{B} \times \mathbf{C}) = -\mathbf{B} \cdot (\mathbf{A} \times \mathbf{C})$ in order to present a form of the equation which shows the role of Lorentz forcing energy conversion and Joule heating effect (ηJ^2).

Utilising the physical definition of the low magnetic Reynolds number, that the induced magnetic effects are negligible and \mathbf{B} is purely the static applied magnetic field, then the number of variables for solution is reduced and equations 2.26 and 2.27 are not required to be solved. Based on this analysis, we can therefore define a reduced base model which constitutes a resistive MHD system under low magnetic Reynolds number assumption:

Base MHD model

$$\frac{\partial}{\partial t} \rho + \nabla \cdot [\rho \mathbf{u}] = 0 \quad (2.47)$$

$$\frac{\partial}{\partial t} (\rho \mathbf{u}) + \nabla \cdot [\rho \mathbf{u} \otimes \mathbf{u} + p \mathbf{I}] = \mathbf{J} \times \mathbf{B} + \nabla \cdot \boldsymbol{\tau} \quad (2.48)$$

$$\begin{aligned} \frac{\partial}{\partial t} E + \nabla \cdot [(E + p) \mathbf{u}] &= \mathbf{u} \cdot (\mathbf{J} \times \mathbf{B}) + \eta J^2 \\ &+ \nabla \cdot (\boldsymbol{\tau} \mathbf{u}) + \nabla \cdot (\zeta (\nabla T)) \end{aligned} \quad (2.49)$$

$$\nabla \cdot \mathbf{J} = 0 \quad (2.50)$$

The total energy and current density are defined respectively as per equations 2.5 and 2.41.

In the reduced system which defines the base MHD model of this work, the fully static treatment of the imposed magnetic field means that Alfvén waves (charge oscillations which perturb the magnetic field in the transverse direction) and magnetoacoustic waves (driven by

an additional magnetic pressure term) are suppressed through this system reduction. The system equations taken in the limit of $Re_m \rightarrow 0$ treats these waves as fully omitted, when they may in fact be weak though physically present. However, the low Re_m nature of the system indicates the effect they have on perturbing the momentum equation of diffusing heat into the system is very small, and is therefore neglected.

2.2.3 Imposed magnetic field

Since all geometries of interest in the ensuing studies are either planar 2D or contain an axis of symmetry in 3D, all dimensional formulations are best expressed in the cylindrical coordinate system: $(\hat{r}, \hat{\theta}, \hat{z})$.

The magnetic field is static and imposed and takes the form of a dipole field with dimensional components $\mathbf{B} = (B_r, B_\theta, B_z)$, which can be defined analytically via:

$$\mathbf{B} = B_0 \left[\frac{3\mathbf{r}(\mathbf{r} \cdot \mathbf{m}) - r^2 \mathbf{m}}{r^5} \right] \quad (2.51)$$

Where \mathbf{r} is the radial vector from the dipole centre, and \mathbf{m} is an orientation vector aligned parallel to the dipole centreline. Within the axisymmetric governing system where \mathbf{r} and \mathbf{m} are defined in the r-z plane, the B_θ magnetic field component is zero.

2.2.4 Hall effect assessment

The analysis of section 2.2.2 assumed the electrical conductivity was an isotropic (scalar) variable. In the presence of a strong magnetic field, this is not strictly true, and an additional current forms and drives the generation of an electric field which has a complex interaction with the gas dynamics - termed *Hall effect*. The expansion of Ohm's law to account for Hall current is given by:

$$\mathbf{J} = \sigma_e(\mathbf{E} + \mathbf{u} \times \mathbf{B}) - C_H(\mathbf{J} \times \mathbf{B}) = \tilde{\sigma}_e(\mathbf{E} + \mathbf{u} \times \mathbf{B}) \quad (2.52)$$

The complex interaction in fact renders the electrical conductivity of the fluid anisotropic, which can be represented by a rank 3 tensor $\tilde{\sigma}_e$. The Hall coefficient of equation 2.52 is given by:

$$C_H = \frac{\sigma_0 B_0}{N_e e} \quad (2.53)$$

Given the definition of dipole B-field as comprising of (B_r, B_z) components, it can be noted that the $\mathbf{u} \times \mathbf{B}$ term drives a circumferential current, whereas the $C_H(\mathbf{J} \times \mathbf{B})$ Hall current generates r-z components. It is the circumferential current \mathbf{J}_θ which is the driving current for the shock enhancement phenomena, producing a Lorentz force in the r-z plane. The Hall current permits the possibility of electric field generation in the r-z plane, which

serves to drive a θ component of Lorentz force, resulting in a complex electrodynamic interaction. This interaction is complex and coupled since the θ Lorentz force induces moment in this direction, initialising a swirling flow. The resultant u_θ component acts to diminish the original \mathbf{J}_θ (which can be shown in the expansion of equation 2.60 of the electric field reduction of the next section) which ultimately diminishes the shock enhancement potential. This effect has been demonstrated numerically and experimentally by a number of authors [55, 9, 54, 56].

However - the mechanism by which the Hall current drives the electric field generation is dependant upon the surface treatment. In the case where the surface is treated as conductive, then the r-z current components interact with the vehicle surface (current is permitted to propagate into the surface), and electric potential builds, producing the Hall effect. This phenomena is sometimes phrased as the conductive surface "short-circuiting" the \mathbf{J}_θ current [9]. In the case of an insulated surface however, the current does not flow to the vehicle, and ultimately the \mathbf{J}_θ current is unaffected by the electric potential field. Therefore the Hall effect is found to have negligible effect, even if the Hall coefficient is very high, for the case where the vehicle surface is treated as insulative (via the electrodynamic boundary condition at the body) [9, 54].

Many studies on for MHD flow control regard the blunt body leading surface as an insulator and therefore justifiably neglect Hall effect [20, 92, 93], using the generalised Ohm's law for electric current as given in equation 2.41. As such, this work will also adopt the generalised Ohm's law form.

2.2.5 Electric field reduction

Noting the adoption of the generalised Ohm's law, and the defined axisymmetric system with electrically insulated boundary conditions on the geometry surface, an important reduction can be drawn regarding the computation of electric field.

The electric field \mathbf{E} is a conservative field where $\mathbf{E} = -\nabla\phi$ and ϕ is the electric potential. Therefore the governing system is comprised of three inhomogeneous hyperbolic PDE's coupled with an additional Poisson-type elliptic PDE maintaining divergence-free current density:

$$\nabla \cdot [\sigma(-\nabla\phi + \mathbf{u} \times \mathbf{B})] = 0 \quad (2.54)$$

The generalised problem geometry and electrodynamic boundary conditions on ϕ are shown in Figure 2.3.

For the left and lower boundaries the boundary conditions are then:

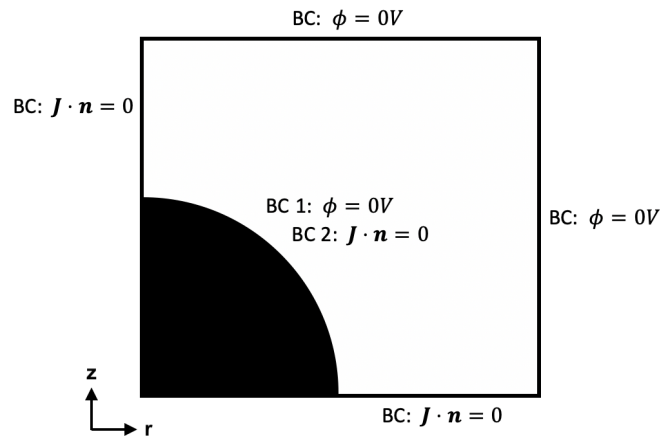


Fig. 2.3 2D profile for axisymmetric problem around z - quarter circle revolves to form half sphere

$$\text{Left: } \frac{\partial \phi}{\partial r} = -\mathbf{u} \times \mathbf{B}|_r = -(u_\theta B_z - u_z B_\theta) \hat{r} \quad (2.55)$$

$$\text{Lower: } \frac{\partial \phi}{\partial z} = -\mathbf{u} \times \mathbf{B}|_z = -(u_r B_\theta - u_\theta B_r) \hat{z} \quad (2.56)$$

It should be shown that for non-Hall Ohm's law, and where the electrodynamic boundary conditions are as defined, the ϕ field evaluates to zero, always.

Equation 2.54 is rearranged:

$$\nabla \cdot (\sigma \nabla \phi) = \nabla \cdot [\sigma (\mathbf{u} \times \mathbf{B})] \quad (2.57)$$

where σ is a non-constant scalar, the RHS of the equations expands to be:

$$\nabla \cdot [\sigma (\mathbf{u} \times \mathbf{B})] = \nabla \sigma \cdot (\mathbf{u} \times \mathbf{B}) + \sigma \nabla \cdot (\mathbf{u} \times \mathbf{B}) \quad (2.58)$$

$$= \left(\frac{\partial \sigma}{\partial r} \right) (u_\theta B_z - u_z B_\theta) + \left(\frac{\partial \sigma}{\partial z} \right) (u_r B_\theta - u_\theta B_r) \quad (2.59)$$

$$+ \sigma \cdot \left[\frac{\partial}{\partial r} (u_\theta B_z - u_z B_\theta) + \frac{\partial}{\partial z} (u_r B_\theta - u_\theta B_r) \right] \quad (2.60)$$

Since the imposed \mathbf{B} -field is defined with components $(B_r, 0, B_z)$, for the case where $u_\theta = 0$ (which is the initial condition on u_θ), the RHS equation 2.58 evaluates to zero. Similarly, the left and right boundary conditions given by (2.55, 2.56) become homogeneous Neumann on ϕ . Under these conditions the Poisson equation $\nabla \sigma \nabla \phi = 0$ has solution: $\phi = 0$ across the domain. N.B. this verifies the assumption in section 2.2.2 that the $\mathbf{u} \times \mathbf{B}$ terms dominates over \mathbf{E} , where loading parameter K was assumed to be > 1 . In fact, this case represents the limit where $K \rightarrow \infty$.

The current density is shown to have only a θ component resulting from the $\mathbf{u} \times \mathbf{B}$ term:

$$\mathbf{J} = -\sigma(u_r B_z - u_z B_r) \hat{\theta} = J_\theta \hat{\theta} \quad (2.61)$$

The Lorentz forcing components, which are the source terms of the momentum system equations 2.48, expand to show forcing only in the r-z plane:

$$\mathbf{J} \times \mathbf{B} = J_\theta B_z \hat{r} - 0 \hat{\theta} - J_\theta B_r \hat{z} \quad (2.62)$$

Therefore, since the θ -momentum source term is zero, u_θ remains unchanged from its initial value. The boundary conditions remain homogeneous Neumann and Dirichlet as determined, and for constant $\phi = 0$, we have shown the absence of electric field. This derivation allows for the analytical rather than numerical solution of the elliptic current density equation (2.50). Therefore the ensuing computation of the Lorentz forcing terms is vastly more expedient.

2.3 Model hierarchy

2.3.1 Full system model

From the base MHD model derived in section 2.2.2, combined with the electric field reduction of section 2.2.5, and the required transformation of a 2D axisymmetric coordinate system, the system model can be usefully expressed in the following vectorised form:

$$\frac{\partial \mathbf{U}}{\partial t} + \frac{\partial \mathbf{F}}{\partial r} + \frac{\partial \mathbf{G}}{\partial z} = \frac{\partial \mathbf{F}_v}{\partial r} + \frac{\partial \mathbf{G}_v}{\partial z} + \mathbf{S}^c + \mathbf{S}_v^c + \mathbf{S}_{MHD} \quad (2.63)$$

where \mathbf{U} , \mathbf{F} and \mathbf{G} denote the state vector, and r-z directional inviscid flux vectors respectively, and \mathbf{S}^c denotes the associated cylindrical source term vector. \mathbf{F}_v and \mathbf{G}_v are respectively the r-directional and z-directional viscous fluxes, \mathbf{S}_v^c are the viscous cylindrical source terms and \mathbf{S}_{MHD} is the vector of MHD source terms.

The divergence of a vector quantity \mathbf{A} in Cartesian coordinates is converted to a cylindrical system (revolved around the z-axis) as such:

$$\nabla \cdot \mathbf{A} = \frac{1}{r} \frac{\partial}{\partial r}(rA_r) + \frac{1}{r} \frac{\partial A_\theta}{\partial \theta} + \frac{\partial A_z}{\partial z} \quad (2.64)$$

For the 2D r-z system, we denote the velocity vector in the $(\hat{r}, \hat{z}, \hat{\theta})$ direction to have components (u, v, w) , and so the system state and inviscid flux vectors are defined as:

$$\frac{\partial \mathbf{U}}{\partial t} = \begin{pmatrix} \rho \\ \rho u \\ \rho w \\ \rho v \\ E \end{pmatrix}_t \quad \frac{\partial \mathbf{F}}{\partial r} = \begin{pmatrix} \rho u \\ \rho u^2 + p \\ \rho uw \\ \rho uv \\ u_r(E + p) \end{pmatrix}_r \quad \frac{\partial \mathbf{G}}{\partial z} = \begin{pmatrix} \rho w \\ \rho uv \\ \rho vw \\ \rho v^2 + p \\ v(E + p) \end{pmatrix}_z \quad \mathbf{S}^c = \begin{pmatrix} -\frac{1}{r}\rho u \\ -\frac{1}{r}\rho u^2 \\ -\frac{1}{r}\rho uw \\ -\frac{1}{r}\rho uv \\ -\frac{1}{r}u(E + p) \end{pmatrix} \quad (2.65)$$

where total energy E is given by: $E = \rho e + \frac{1}{2}\rho |\mathbf{u}|^2$.

For the 2D r-z system, we denote the velocity vector in the $(\hat{r}, \hat{z}, \hat{\theta})$ direction to have components (u, v, w) , and so the viscous flux vectors are defined as:

$$\mathbf{F}_v = \begin{pmatrix} 0 \\ \tau_{rr} \\ \tau_{rz} \\ \tau_{r\theta} \\ Q_r \end{pmatrix} = \begin{pmatrix} 0 \\ \mu\left(\frac{4}{3}u_r - \frac{2}{3}v_z - \frac{2}{3}\frac{u}{r}\right) \\ \mu(v_r + u_z) \\ \mu\left(w_r - \frac{w}{r}\right) \\ u\tau_{rr} + v\tau_{rz} + w\tau_{r\theta} + \zeta T_r \end{pmatrix} \quad (2.66)$$

$$\mathbf{G}_v = \begin{pmatrix} 0 \\ \tau_{zr} \\ \tau_{zz} \\ \tau_{z\theta} \\ Q_z \end{pmatrix} = \begin{pmatrix} 0 \\ \mu(u_z + v_r) \\ \mu\left(\frac{4}{3}v_z - \frac{2}{3}u_r - \frac{2}{3}\frac{u}{r}\right) \\ \mu w_z \\ u\tau_{zr} + v\tau_{zz} + w\tau_{z\theta} + \zeta T_z \end{pmatrix} \quad (2.67)$$

And the following source term vector is derived from the transformation to a cylindrical system with axi-symmetry around the z-axis.

$$\mathbf{S}_v^c = \frac{1}{r} \begin{pmatrix} 0 \\ \tau_{rr} - \tau_{\theta\theta} \\ \tau_{rz} \\ \tau_{r\theta} \\ Q_r \end{pmatrix} = \begin{pmatrix} 0 \\ \frac{2}{r}\mu\left(u_r - \frac{u}{r}\right) \\ \frac{1}{r}\mu(u_z + v_r) \\ \frac{2}{r}\mu\left(w_r - \frac{w}{r}\right) \\ \frac{1}{r}(u\tau_{rr} + v\tau_{rz} + w\tau_{r\theta} + \zeta T_r) \end{pmatrix} \quad (2.68)$$

It is worth noting that under the cylindrical transformation additional radial terms emerge in the viscous flux vectors in addition to the \mathbf{S}_v^c source term vector.

The dynamic viscosity and thermal conductivity are often given as constants in validation test cases. For realistic test cases and where the plasma19X equation of state is used, thermal conductivity is determined directly from the plasma19X database, and dynamic viscosity is computed as temperature dependant via Sutherland's law:

$$\mu = \frac{bT^{3/2}}{T + S} \quad (2.69)$$

where the constant $b = 1.458 \times 10^{-6} \text{ kg}/(\text{ms}\sqrt{\text{K}})^{-1}$ and Sutherland's temperature $S = 110.4 \text{ K}$ for air.

Finally, for the MHD source term vector, following the analysis in section 2.2.4 the Lorentz forcing terms can be defined directly, rendering the computation as vastly more expedient:

$$\mathbf{S}_{MHD} = \begin{pmatrix} 0 \\ (\mathbf{J} \times \mathbf{B})\hat{r} \\ (\mathbf{J} \times \mathbf{B})\hat{\theta} \\ (\mathbf{J} \times \mathbf{B})\hat{z} \\ \mathbf{u} \cdot (\mathbf{J} \times \mathbf{B}) + \sigma^{-1} J^2 \end{pmatrix} = \begin{pmatrix} 0 \\ -\sigma(u_r B_z^2 - u_z B_r B_z) \\ 0 \\ \sigma(u_r B_z B_r - u_z B_r^2) \\ u_r J_\theta B_z - u_z J_\theta B_r + \sigma^{-1} J^2 \end{pmatrix}$$

The full system model has two closure options in terms of equation of state: (1) the simple ideal gas law with a supplementary conductivity formulation (required since an ideal EoS does not inherently resolve conductivity), or (2) the advanced 19 species air plasma equation of state - plasma19X.

2.3.2 Magnetic field reduction

In the absence of an imposed magnetic field ($\mathbf{B} = 0$) the system automatically reduces to a base fluid dynamics model (flow induced magnetic induction effects are still determined to be negligible for the ionisation degree of the test problems of study). Therefore $\mathbf{S}_{MHD} = \mathbf{0}$, and the system is simply:

$$\frac{\partial \mathbf{U}}{\partial t} + \frac{\partial \mathbf{F}}{\partial r} + \frac{\partial \mathbf{G}}{\partial z} = \frac{\partial \mathbf{F}_v}{\partial r} + \frac{\partial \mathbf{G}_v}{\partial z} + \mathbf{S}^c + \mathbf{S}_v^c \quad (2.70)$$

Again for this base fluid dynamics model 2 EoS options can be adopted for closure. When closed with the plasma19X EoS, plasma properties of interest such as electron number density and electrical conductivity can still be resolved and studied. These properties would indicate the flow's susceptibility to MHD forcing effect were a \mathbf{B} -field to be subsequently imposed.

2.3.3 Transport property reductions

The most rudimentary reduction of the governing model is to neglect viscous and thermal transport properties, in which case the system reduces to the Euler equations - a hyperbolic system which describes the motion of an inviscid, adiabatic fluid.

$$\frac{\partial \mathbf{U}}{\partial t} + \frac{\partial \mathbf{F}}{\partial r} + \frac{\partial \mathbf{G}}{\partial z} = \mathbf{S}^c \quad (2.71)$$

The Reynolds number is useful for determining whether viscous effects should be accounted for - especially when applied to local regions of the flow, not just the free-stream

properties. Typically, hypersonic flows are characterised by an extremely thin viscous boundary layer, beyond which the flow can be treated as fully inviscid. However, certain geometric factors can undermine this assumption. Steps and angles in leading geometric surfaces can produce shock wave boundary layer interactions in supersonic and hypersonic flows, as will become apparent in several test cases in the applications chapters. Therefore, suitable reductions to the Navier-Stokes equations often require a more in-depth examination of a specific flow field.

From the top down - it is important to demonstrate that the full system model reduces to a valid base model, of a valid form for compressible flow problems. From the bottom up - in building the numerical models to solve each of these governing mathematical models, it is essential to begin with and extensively validate the base inviscid ideal gas model, since every built-up model draws on this solver as the foundation.

To convert between 2D planar simulations and axisymmetric, the source term \mathbf{S}^c can simply be dropped, and r-z space directly transposed to x-y.

2.3.4 Map of models

This thesis adopts a modularised approach to the system modelling - that is, a full system model and series of sub-models are defined. This provides flexibility, and improved efficiency, in applying a relevant model to a particular problem of study.

Different numerical methods must be applied to the solution of different constituent physics and terms in the governing models. The validation section will make frequent reference to the defined map of governing mathematical models and associated numerical models.

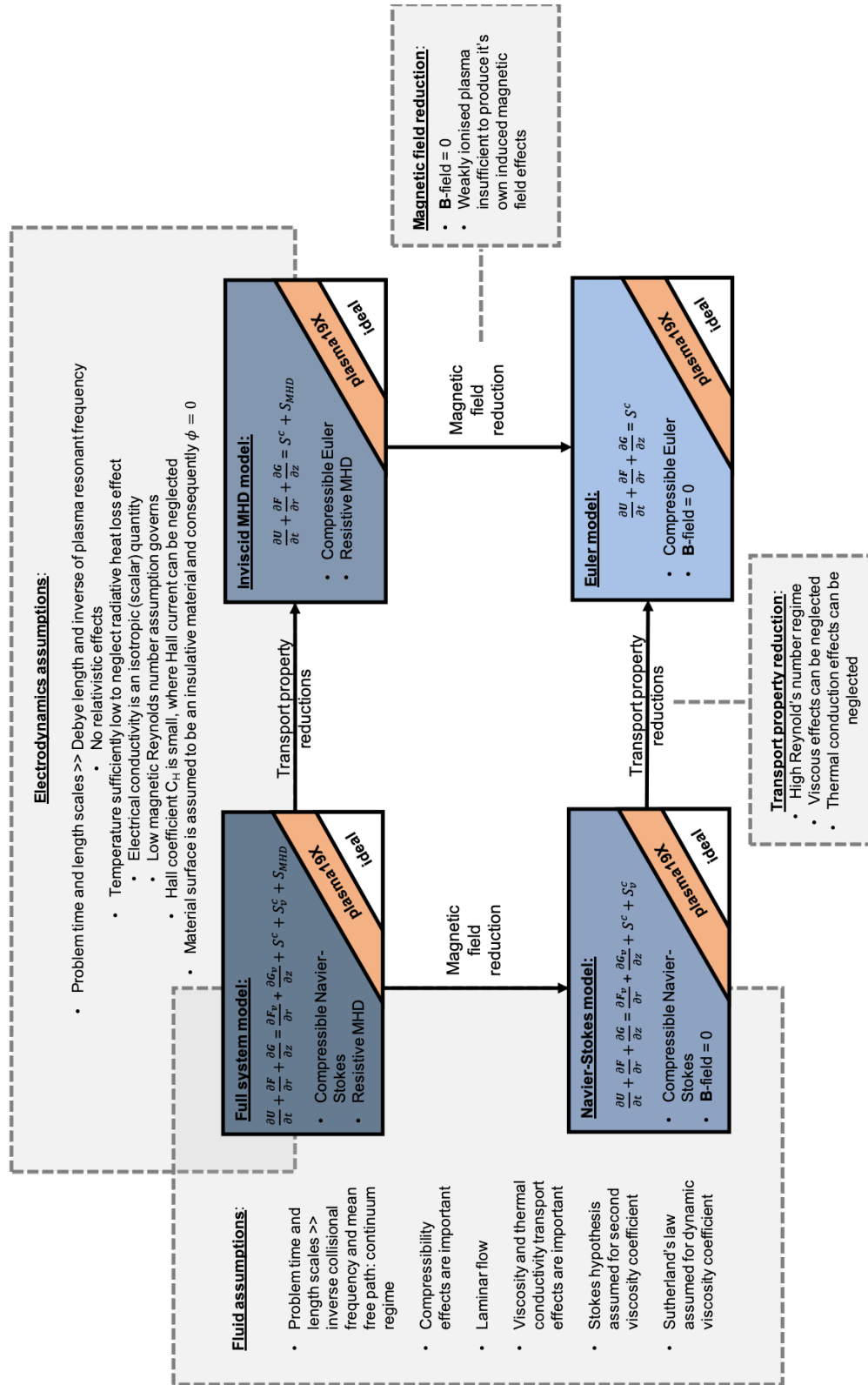


Fig. 2.4 Map of mathematical models and associated underlying assumptions, with defined conditions on system reductions.

Chapter 3

Equation of state for air-plasma

The incandescent glow of the heat shield of a reentry vehicle may be beautiful, but it signifies the extreme heat flux endured by the vehicle from the high temperature plasma environment. The macroscopic behaviour of air at moderate temperatures is described very well by the kinetic theory of gases [94]. However, at the very high temperatures reached in the shock layer of hypersonic flows, dissociation and ionisation reactions are known to occur. These chemical reactions alter the thermodynamic state. Accurately capturing the real gas effects is important for the prediction of the flow structure, heating effects and key properties of the fluid. Specifically, the ions and electrons produced by these reactions underpin the characterisation of the electromagnetic properties of the thermally generated plasma, critical to the study of MHD effects within or imposed upon such flows.

This chapter reviews the literature in regards to the treatment of the thermochemistry for simulations of weakly ionised plasmas formed from hypersonic flows. As identified in the previous chapters, the complexity of the hypersonic-magnetohydrodynamic governing physics means that a key aspect of advancement in the field in fact lies in the step of identifying useful system reductions, and regime-specific assumptions to support the tractability of the problem. Therefore, this chapter is not merely about determining which assumptions apply to which regimes, but about identifying which assumption-abiding regimes permit advancement in the modelling of certain classes of plasma-problems. As such, this informs the rationale for the focus on the equilibrium regime and opportunity for numerical modelling advances therein.

A new advanced 19-species equation of state for equilibrium air plasma, *plasma19*, was recently generated (Träuble et al., 2021 [95]) for application to lightning plasmas. However, its utility for advancements in the study of hypersonically formed plasmas has here been identified. The theory behind the generation of Träuble's tabulated EoS must be understood in order to develop physically consistent extensions such that the EoS can be applied to hypersonic flight regimes. This work develops and combines a physical extension of the property range, the implementation of a more accurate formulation for computing electron molar fraction, and improved state access routines for greater code efficiency and accuracy.

This results in an extended EoS - *plasma19X* - with improved capability for the simulation of equilibrium air plasmas formed from hypersonic flows. Advances specifically in the direct and accurate prediction of electrical properties are found to be very important for the study of MHD effects imposed upon such flows, as will be discussed.

3.1 Air plasmas formed in hypersonic flows

Depending on the flight conditions, the gas surrounding a hypersonic vehicle may be in equilibrium, non-equilibrium (chemical and/or thermal), or the flow may be considered chemically ‘frozen’ [96]. The state of the gas has complex interdependencies on free-stream density and pressure (therefore dependant upon altitude), as well as the vehicle size, geometry and Mach number. While different thermochemical models produce different results, it is often difficult to verify the thermochemical model validity due to the expense and challenge of obtaining flow chemistry data from flight tests and ground tests [97].

The validity and limits of thermochemical assumptions in hypersonic flight cases therefore remains an active area of research [1]. The assessment of various thermochemical models must be considered in unison with their numerical implementation, as their computational expediency differs widely. The following questions are therefore examined:

1. Which are the prevailing thermochemical models used for weakly ionised plasmas generated from hypersonic flows?
2. What are the limits of each model’s validity?
3. How does the tractability and efficiency of their computation compare?

Further, in the subsequent section the gas models’ inherent or supplementary computation of electrical conductivity is examined in order to assess the various gas models’ specific suitability for MHD applications. Based on this review, the justification for, and development of, the new extended *plasma19X* gas chemistry model used in this work is provided.

The simplest EoS still commonly used in the simulation of hypersonic flows, is the ideal gas law. A *perfect* or *ideal* gas is considered to be both thermally and calorically perfect. By thermally perfect, it is meant that it follows the ideal gas equation of state:

$$p = \rho RT \quad (3.1)$$

whereby internal energy and enthalpy depend only on temperature. By calorically perfect gas it is meant that the values of specific heat are held constant ie. $\gamma = c_p/c_v$ is constant for all temperatures. However for high temperature shock layers, the thermal energy causes diatomic molecules to become vibrationally excited and to dissociate and γ is no longer constant. Figure 3.1 shows the strong deviation in the maximum post-shock temperature predicted by an ideal gas model, as compared with chemically reacting gas in equilibrium

for a reentry vehicle scenario. It is observed that predicted temperature begins to deviate at about 500 K, and above approximately 2,000 K, perfect gas theory becomes very unrealistic.

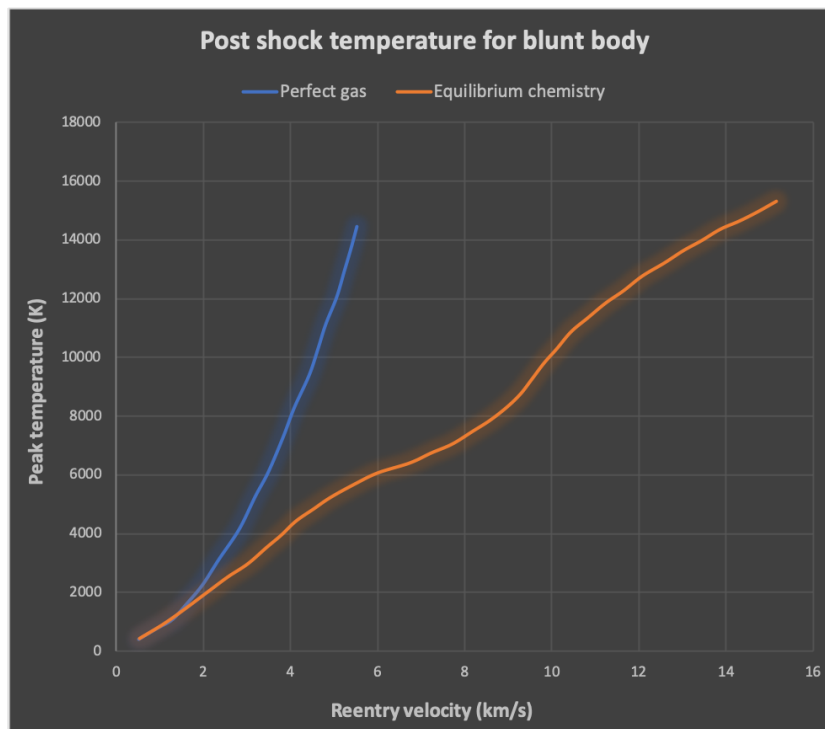


Fig. 3.1 Peak temperature in the stagnation region of the shock layer for a blunt body reentry vehicle at 52 km altitude. Plot adapted from sketch by Fletcher [1]

From a computing standpoint however, the ideal gas law provides the most efficient way of closing the system equations, since all primitive variables can be computed directly from analytic relations. For this reason, the ideal gas law is still used widely in hypersonics codes.

There was a very real danger during one of the Shuttle reentries when a manual override was required to adjust pitching angle due to a miscalculation based on a perfect gas approximation [1]. Several studies have since sought to determine the differences predicted by ideal gas models and equilibrium chemistry models for hypersonic and reentry applications.

Maus et al. (1984) [98] simulated the Space Shuttle Orbiter geometry at both Mach 8 and Mach 23 finding that the summation of the pressure field along the vehicle body results in differences in predicted pitching moment between the two chemistry models, with a greater difference in the Mach 23 case. The prediction of the equilibrium chemistry model was found to be in good agreement with experimental measurement for the Orbiter reentry flight.

Numerous other studies compare predictions between ideal gas and equilibrium gas models for highly hypersonic regimes. Chalot and Hughes (1994) [99] simulate hypersonic flows over blunt body geometries at Mach 19, and Wood and Thomson (1993) [100] simulate sphere-cone configurations at Mach 25 between 22 km and 60 km altitude. Consistent findings across studies include a significant over-prediction of peak temperatures and shock stand-off distances by ideal gas models, and the generally high suitability of equilibrium

models for the tested reentry and hypersonic flight regime as compared with experiment. Hu et. al (2017) [101] also highlight that viscous effects do not influence the gas properties and flow predictions for blunt body vehicles in these regimes. Importantly, authors of such studies highlight that the most efficient implementations of equilibrium chemistry models achieve a computational run time only 20% slower than the ideal gas model [99].

Ekici et al. [102] alternatively proposes air in the weakly ionised plasma regime be modelled with an effective adiabatic index of $\gamma = 1.16$. Sawada and Dendau [103] recommend weakly ionised plasmas formed from ballistic trajectories use $\gamma = 1.21$.

Since ideal gas with augmented γ can provide reasonable results in terms of shock structure and qualitative pressure profile for hypersonic flows, it is commonly employed as a computationally efficient method to study isolated or relative effects within the flow. For this reason, many numerical MHD flow control studies employ an ideal gas model: [15, 9, 58, 54] to investigate specific MHD effects, such as shock stand-off distance increase at different magnetic field strengths [20]. It is important to note that since the ideal gas model does not inherently capture electrical conductivity of the fluid, a supplementary conductivity approximation must be adopted. This is explored further in the next section on conductivity modelling.

It is also clear that a perfect gas model is insufficient for resolving any kind of species composition for the air. Therefore any studies which wish to obtain electron number density directly (a key parameter for communications studies), must adopt a real gas chemistry model.

Plooster [104] proposed an improved surrogate method for capturing the real gas effects of air plasma. The study examined the behaviour of atmospheric air raised to high temperatures from cylindrical shock waves emanating from an instantaneous energy release. The model considers the dissociation and ionisation reactions of O_2 and N_2 and the weighted average properties based on molecular weight of the dissociated and ionised product species. This method approximates the thermodynamic properties of real air to reasonable accuracy above temperatures of 10,000 K, however there is significant error in the range of 3,000 - 9,000 K. This is due to the different dissociation energies of O_2 and N_2 as well as the neglected contribution of NO .

Villa et al. [12] improve upon this by considering 11 different air species, each as ideal gases with respective equations of states. The 11 species are combined via generalised ideal gas mixture rules with linear combinations of individual species' specific heats and formation heats. It is difficult to validate the thermodynamic properties across the full range of conditions due to a lack of experimental data. Therefore it is benchmarked by comparison to more advanced models which account for many more species reactions and additional physics. By this benchmark, key differences in computed properties emerge (especially species mass fractions and conductivity) and properties lack sufficient agreement and smoothness, particularly in the low (<5,000 K) and high (>10,000 K) temperature limits

[84]. Specifically the prediction of electrical conductivity is scattered and anomalous over the low temperature range. The issue of insufficient smoothness poses numerical challenges for algorithms which leverage those properties in gradient based computations. To improve upon these simplified multi-species equations, a full equilibrium chemistry model is required.

An equilibrium chemistry model computes thermodynamic properties based on the real chemical reactions (ionisation and dissociation) occurring between species, typically through a minimization-of-free-energy approach [105]. The method assumes that the chemical reactions have time to complete (i.e. reaching chemical equilibrium), and that all component species have time to reach a single temperature (i.e. thermal equilibrium). More precisely, if the particles' energies in a local neighbourhood obey Maxwell-Boltzmann distributions, such that a single local temperature and pressure can be defined, then the gas is considered to be in local thermodynamic equilibrium (LTE). The governing system of equations can then be formulated as a 'single fluid' at a single temperature.

An equilibrium chemistry model is implemented as a 'look-up table' whereby two independent properties (typically pressure and temperature) are sufficient as inputs to determine the thermodynamic state. Interpolation (or extrapolation) routines are utilised to determine the precise state within the table of precomputed data. While not as direct as a perfect gas model, the efficiency can be comparable (run-times of the same order) with effective implementation of the interpolation routines.

Over the last 60 years, several computer programs have been developed to compute the data representing the equilibrium state of air over a defined property range [106, 105, 107, 108, 85]. One of the historical challenges of these algorithms was attaining convergence (within practical computing time) of the computationally complex system of equations representing the chemical reactions. With ongoing advances in computing hardware, and improved methods for selecting initial conditions to accelerate convergence, this issue has largely been overcome. The prevailing - both theoretical and computational - challenge of equilibrium chemistry algorithms today is choosing an optimum basis of species and reactions for the chemical system. The optimal basis varies across the wide pressure-temperature range desired for data generation (subject of theoretical analysis), and this variation presents coefficients of matrices used in the linear solution algorithms which vary by many orders of magnitude. This leads to large numerical errors and unphysical solutions [107]. This was also identified as a major issue for the chemical equilibrium solver developed by NASA for atmospheric reentry and propulsion applications [109].

Since the 1960's, NASA has been making incremental advances to their program: *CEA: Chemical Equilibrium with Applications* (available as open source for internet download [110]). Since the first version of the program was developed in 1959 by Gordon et al. continuous advances have been made by Svehla (1962), McBride (1973) and Zeleznik and Gordon (1988), with the most current version as developed in 1994 [105] which has been widely accepted for use by compressible CFD codes around the world.

The current CEA program for air considers 11 chemical species, 32 reactions, and takes pairs of inputs in various combinations (temperature, pressure) or (enthalpy, pressure). The 11 species considered are:

$$N, O, N_2, O_2, NO, N^+, O^+, N_2^+, O_2^+, NO^+ \text{ and } e^-$$

The thermodynamic state is solved based on minimisation of Gibbs free energy theory and computed via a Newton-Raphson iteration procedure. While NASA's CEA reliably computes thermodynamic properties such as: temperature, enthalpy, internal energy, density and thermal conductivity, CEA does not include capability for generalized calculation of electrical transport properties. This is essential for any MHD applications. Extensions to NASA's CEA for use in MHD studies is discussed in section 3.1.1.

A non-equilibrium chemistry model requires a mass conservation equation for every species considered in the model. The set of inhomogeneous species conservation equations includes a \dot{w}_i RHS source term to account for the net production of each chemical species i considered in the model:

$$\frac{\partial \rho_i}{\partial t} + \nabla \cdot (\mathbf{u} \rho_i) = \dot{w}_i \quad (3.2)$$

$$\rho = \sum_{i=0}^s \rho_i \quad (3.3)$$

The species production source term is dependent upon the forwards and backwards reactions accounted for, and the rates of those reactions. Therefore, solution of the non-equilibrium gas model requires the solution of an additional set of s species continuity PDEs which adds significant complexity [97]. Where rates of reaction may vary broadly across the flowfield, time-stepping to meet the stability criteria of the ODE of fastest chemical reaction renders the simulation as numerically stiff.

In terms of air-plasmas for hypersonic reentry simulations, the most commonly implemented 5-species non-equilibrium model is that of Park (1990) [29], various 7-species models are used, and the most advanced 11-species non-equilibrium models are that of Dunn and Kang (1973) [111], Gupta (1990) [28], Park (1993) [112] and most recently Ozawa (2008) [30]. A recent (2018) study by Niu et al. [2] compared the results produced by the prevailing 11-species models of Gupta, Park and Ozawa. The test case was a blunt body sphere-cone geometry at high altitudes (61-71 km) and high Mach numbers (23.9-25.9). The comparative study showed that while the pressure profiles and translational temperature profiles had very good agreement, there were small differences observed in the computed molar fractions of species. Even small differences in the chemical dissociations and ionisations can lead to large differences in resultant electron number density. The differences between the three most commonly used 11-species models are shown in Figure 3.2.

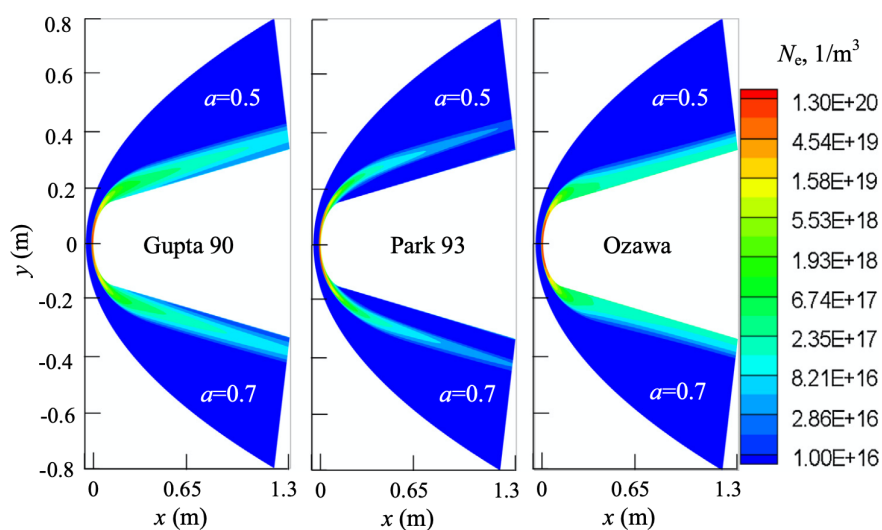


Fig. 3.2 Computed electron number density from three different 11-species non-equilibrium chemistry models for the RAM-C II geometry at 61 km travelling at Mach 23.9. Figure from Niu et al. [2]. a is a selected weighting factor of the forward vs backward ($b = 1 - a$) reaction rates (values $a=0.5-0.7$ debated in the literature).

This finding is consistent with the study of Hao (2016) [113] who also compared the results from the Gupta and Park non-equilibrium chemistry models. For the extreme Mach 38 FIRE II reentry capsule test case, the Park model predicts a higher peak electron number density (in the stagnation region) by a factor of 2, and the shock stand-off distance is approximately 5% greater with the Gupta model.

In the literature on MHD flow control, Fujino *et. al.* [3, 55, 19] and Li *et. al.* [56, 45, 57] conduct feasibility studies of the OREX (Japan's Orbital Reentry Experiment [114]) trajectory at the high altitude range of its reentry trajectory via an 11-species, two-temperature thermochemical non-equilibrium gas chemistry model. The gas chemistry modelling is essential to the prediction of N_e and electrical conductivity to drive the Lorentz forcing effects in assessing MHD flow control efficacy. As highlighted, the vast differences in prediction of N_e therefore raise uncertainty about resultant MHD studies which rely directly on this property prediction. The gas chemistry and Lorentz forcing fluid dynamics are thus inextricably linked through the electrical conductivity model - which we will now turn our attention to.

3.1.1 Electrical conductivity models

Accurate modelling of any magnetogasdynamic effects is underpinned by the accuracy of the computed electrical conductivity. Obtaining an accurate electrical conductivity model remains a primary challenge in MHD research. This section explores the current state of conductivity modelling across the literature.

Supplementary conductivity approximations for ideal gas models

The standard supplementary conductivity approximation for ideal gas MHD studies, takes the form of an analytic power function of temperature:

$$\sigma = \sigma_0 \left(\frac{T}{T_0} \right)^n \quad (3.4)$$

where σ_0 is a reference conductivity value, and T_0 is typically taken to be the peak temperature in the shock layer. Poggie & Gaitonde [20] examined the effect of varying the exponent n in the range of 0-4, concluding the conductivity approximation has a significant effect on observed MHD control efficacy. Therefore, realistic MHD models, require a realistic estimate of electrical conductivity, and cannot rely on analytic approximation.

MHD extension to chemical equilibrium codes

As Bisek [78] clearly highlights, accurate conductivity modeling in the LTE regime typically involves semi-empirical approximations and remains problematic.

Chemical equilibrium programs consider either 2,5,7,11 or in the model of this work 19 species in their calculation. Models considering 7 or more species are able to resolve electron molar or mass fractions explicitly, though the accuracy varies across programs [107]. For plasma studies which are interested in determining the electron number density through the shock layer, 7-species must be the minimum basis. The accuracy of the electron number density computation can also be important in resolving electrical conductivity.

The electrical conductivity of a plasma can be related to the electron number density (n_e) as follows:

$$\sigma = \frac{n_e e^2}{m_e \nu_{coll}} = \frac{n_e e^2}{m_e u_e (Q_{en} n_n + Q_{ei} n_i)} \quad (3.5)$$

where n_e is the electron number density, e is the electron charge, m_e is the electron mass, and ν_{coll} is the effective electron-neutral and electron-ion collision frequency. ν_{coll} is given by the product of u_e the average thermal velocity of electrons and $Q \cdot n$ the collision cross sections by number density of electrons and neutrals ($Q_{en} n_n$) and electrons and ions ($Q_{ei} n_i$).

Alternatively, several other formulations for ν_{coll} (where the gas is assumed to follow the Maxwell Boltzmann distribution) are commonly considered [115]. These are typically in the form of analytic functions of pressure and or temperature, where constants vary depending on the empirically identified regime [78].

Another option for an equilibrium gas composition is to compute conductivity via a Boltzmann solver. Boltzmann solvers are a function of EoS computed pressure, temperature and species mole fractions of each considered species and involve the complex direct solution of a large set of coupled ODEs which renders the method as computationally expensive. The solver computes collision frequencies (used in the expression for σ) by convolving the

electron energy distribution functions derived by solving Boltzmann's equation with the mole-fraction weighted momentum transfer cross-sections for each species [11]. A set of n coupled ODE's are then solved numerically by dividing the electron energy spectrum into n energy bins.

At present, 11-species models, such as NASA's CEA, are the most advanced equilibrium models being applied to hypersonics and reentry studies. Turner et al. [116] (2009) developed for NASA a Multi-Grid Magnetohydrodynamics (MGMHD) program which is primarily used for MHD augmented propulsion. The gas chemistry model for the program is NASA's CEA. Therefore, the MGMHD program does not have the inherent capability for calculating electrical transport properties in partially ionized gases [116]. The thermoelectric chemistry module therefore comprises two sub-models: the thermochemical sub-model (CEA) and an electrical conductivity sub-model (a separate Fortran program *thermhd.f*). This electrical conductivity sub-model computes σ based on the method of Devoto [117] which derives the similar equation:

$$\sigma = \frac{e^2 n}{\rho k T} \sum_{j=1}^{\zeta} n_j m_j Z_j D_{1j} \quad (3.6)$$

where e is the electron charge, n is the total number density, ρ is the total mass density, k is the Boltzmann constant, n_j and Z_j are the number density and internal partition function of the j -th species, D_{1j} is the first order diffusion coefficient, and counter j from 1 through ζ accounts for electrons and each ionic species. Therefore the species composition of all charged particles are used to calculate electrical conductivity at a given time.

Electrical conductivity in non-equilibrium chemistry models

These models compute electrical conductivity (σ) as a function of electron number density (n_e):

$$\sigma = \frac{n_e e^2}{m_e \sum_{i \neq e} \nu_{e,s}^m} \quad (3.7)$$

where e , m_e , and $\nu_{e,s}^m$ are respectively electron charge, electron mass and effective momentum transfer collision frequency of electrons with the other chemical species. The effective momentum transfer collision frequency is given by the expression:

$$\nu_{e,s}^m = \begin{cases} 6\pi \left(\frac{e^2}{12\pi\epsilon_0 k_b T_{ve}} \right)^2 \ln \left[12\pi \left(\frac{\epsilon_0 k_b}{e^2} \right)^{3/2} \sqrt{\frac{T_{ve}^3}{n_e}} \right] n_s \sqrt{\frac{8k_b T_{ve}}{\pi m_e}} & \text{if } s \text{ is ion species} \\ \frac{4}{3} \sigma_{e,s}^m n_s \sqrt{\frac{8k_b T_{ve}}{\pi m_e}} & \text{otherwise} \end{cases} \quad (3.8)$$

Accurately resolving electron number density remains challenging, given the difficulty in tracking electron species density which is many orders of magnitude smaller than the positive ion and neutral species.

The macroscopic fluid electrical conductivity can only be computed above the critical temperature where the ionisation reactions produce free electrons, as accounted for in the 20 reaction (Li *et. al.*) or 32 reaction (Fujino *et. al.*) chemistry model employed.

Fujino *et al.* [19] assess MHD flow control efficacy across the altitude range of 72 km – 48 km. For this reentry trajectory, the weakly ionised shock layer does not reach chemical equilibrium until the 55 km altitude mark, at which point the maximum post shock temperature is approximately 5,000 K and electrical conductivity approaches zero based on the $\sigma = f(n_e)$ formulation with the set of species reactions accounted for. Therefore MHD flow control simulation is ineffective below this altitude regardless of imposed magnetic field strength (Lorentz force cannot be produced in the non-conductive gas). However air ionisation and electrical conductivity (and therefore the possibility for MHD flow control) is known to persist far below this temperature-altitude range. Therefore, in general, the limits of MHD prediction are limited by the non-equilibrium air chemistry modelling.

Rationale for LTE-MHD studies

The development and extension of an equilibrium air-plasma model with direct and highly accurate prediction of electrical properties presents opportunity for advancement of MHD flow control studies. Where previously the semi-empirical approximations, or excessively cumbersome numerical stiffness of non-equilibrium codes applied in the LTE regime rendered these types of studies unrealistic or intractable. The major advantage - computationally - in employing an equilibrium model, is that the global time step is not restricted by the rate of chemical reaction, rendering the computation vastly more expedient.

It should be highlighted that the modularised approach for the models of this work (described in the previous chapter) offers flexibility of EoS and governing physics for different test problems. It is therefore important to clarify the bounds of equilibrium assumption, and considerations when assessing its validity, such that test problems can be identified as suitable for the LTE-MHD model. Let's consider the works of those who have grappled with this same question.

3.1.2 Extent of LTE validity

The validity of assuming thermodynamic equilibrium is primarily determined by the rate of chemical reaction compared to the rate at which particles traverse the shock layer (i.e. the post-shock velocity). If the chemical reactions occur very fast, such that the associated molecules traverse a short distance before completing, then the flow can be considered in equilibrium. If the chemical reactions are still completing as the molecules pass dynamically

through the shock layer, then chemical compositions and thermodynamic state will become inaccurate unless computed based on finite-rate chemistry. It is useful to characterise this in terms of the Damköhler number:

$$Da = \frac{\tau_f}{\tau_c} \quad (3.9)$$

where τ_f is the characteristic flow time (time for a particle to pass through the flow domain of interest), and τ_c is the characteristic chemical reaction time. Therefore a large Da indicates chemical equilibrium is suitable, and small Da indicates a non-equilibrium chemistry model is required.

Given that equilibrium/non-equilibrium state therefore depends on the complex interplay of free-stream conditions and vehicle size and geometry, the assessment of equilibrium is highly problem specific. This is the subject of a great number of studies, with ongoing investigation.

In terms of geometry, larger vehicles with blunt leading surfaces (producing large stagnation regions) tend more towards equilibrium. A comprehensive "Perspective on Hypersonic Nonequilibrium Flow" was written by Cheng and Emanuel in 1995 [118]. The authors highlight that in a study of the FIRE II reentry capsule, which is a highly blunted body configuration (see Figure 3.3), that equilibrium chemistry provided very good agreement with non-equilibrium chemistry through both the boundary layer and inviscid shock layer, except for altitudes above 80 km.

In comparing LTE to non-equilibrium (NEQ) models for the sphere-cone geometry, broadly in the literature equilibrium chemistry is considered valid in the altitude range of 15 km - 45 km [119] for up to extremely high Mach number flows.

von Karman Institute similarly find very good agreement between LTE and NEQ versions of their COOLFluid code for high Mach number (12-14) flows within this altitude in terms of density and pressure through the shock layer [120].

A 2019 study by Candler [121] closely examined non-equilibrium considerations in hypersonic flows. A streamline around a sphere-cone blunt body geometry at 5 km/s was assessed for finite rate chemistry effects at 40 km, 60 km and 80 km altitude. In good agreement with the aggregate findings of the literature, it is found that at 40 km altitude the streamline is in thermochemical equilibrium as it passes around the spherical nose portion,

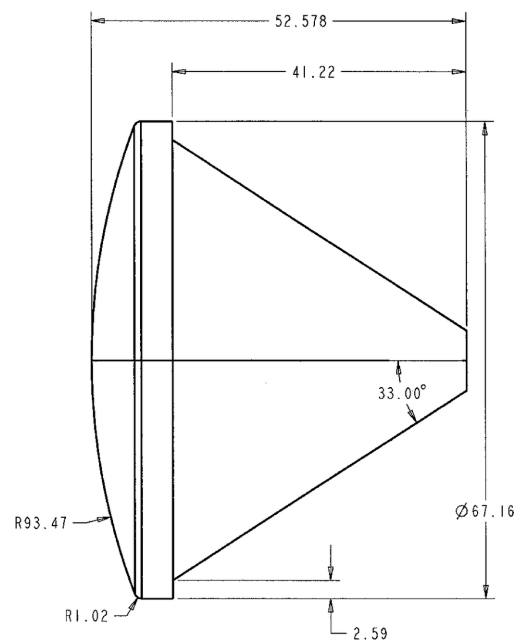


Fig. 3.3 FIRE II reentry capsule geometry diagram

but non-equilibrium effects become more important as the streamline is traced up to the trailing corner. The 60 km altitude case is again close to equilibrium in the stagnation region and the forward region of the sphere. At 80 km altitude the streamline around the vehicle is not in equilibrium.

In terms of specific MHD problems where a magnetic field is present, Damevin & Hoffmann [122] compared solutions for equilibrium and non-equilibrium MHD models at varying altitudes and Mach number over a half sphere. They found equilibrium chemistry provides very good similarity with the finite rate chemistry model up to an altitude of approximately 50 km with a velocity of 6,000 m/s (Mach 18). Above this altitude-Mach number pairing, the key difference is a short region of elevated temperature immediately downstream of the shock.

Development of reentry thermochemistry map

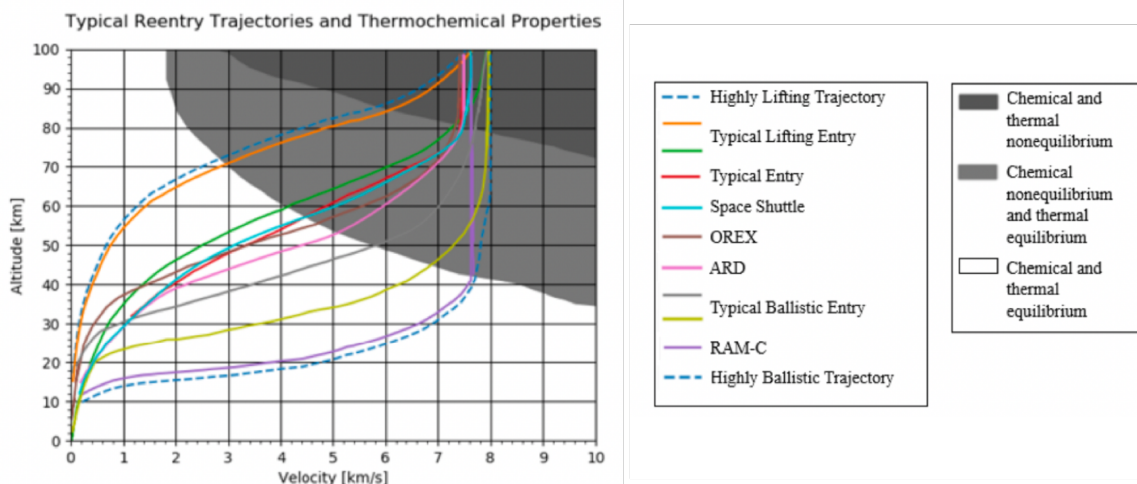


Fig. 3.4 Plot demonstrating regions of valid thermochemical assumptions, with overlaid reentry trajectories given by velocity-altitude coordinates. The zones of equilibrium states are as classified by Fujino *et. al.* [3], and the set of reentry trajectories is modelled from reference trajectory data [4] [5].

Figure 3.4 has been developed as a tool for this work to show clearly the portion of various reentry trajectories where distinct thermochemical assumptions are valid for the case of a spherical body with characteristic length $O(1m)$. The figure was constructed by aggregating altitude-velocity trajectory data from sources [4] [5], with equilibrium zones classified by [3] based on corresponding free-stream conditions. It is recognised that for a large portion of reentry trajectories the gas chemistry is in - or very close to - local thermochemical equilibrium (LTE) [120]. Figure 3.4 shows that the more ballistic the reentry trajectory, the greater the portion of flight occurs under chemical and thermal equilibrium. A number of other MHD flow control applications also fall within this identified LTE valid regime.

3.2 Plasma19

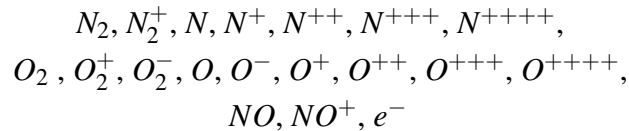
The shortfalls of 11-species non-equilibrium and equilibrium models relate to difficulties in accurately capturing electron molar fraction and consequently electrical conductivity in the low altitude, low temperature band of reentry. This has impeded the realistic study of MHD effects in this regime. The advanced 19 species EoS recently developed by Träuble makes important improvements in the accuracy of computed species composition and electrical conductivity for low temperature equilibrium air-plasmas. However, this EoS was developed for application to lightning strikes, and therefore the tabulated property range is not sufficient for applications in hypersonically formed plasmas. The theory behind the original development of plasma19 is briefly outlined, in order to inform key extensions developed in this work. With such extensions, it is possible - for the first time - to apply a 19 species equilibrium air-plasma EoS to hypersonic MHD studies. This section also details improvements to the property search and interpolation algorithms.

3.2.1 Theory and development

Dry air is constituted by:

78.084% nitrogen, 20.9465% oxygen, 0.9345% argon, 0.036% carbon dioxide

along with negligible traces of noble gas elements. Over different pressures, temperatures and reaction timescales, air can comprise very many different species resulting from the dissociation and ionisation reactions. The 19-species considered in the air-plasma model of this work are:



The threshold for inclusion is that the species makes up more than 1%, or leads to the production of a species exceeding 1% of the total composition. Thus why Argon and CO_2 are omitted.

The development of an accurate theoretical model to describe the thermodynamic and transport properties of equilibrated air constituted by the above 19 species, has been the subject of studies over many years by Capitelli [123], Colonna [108, 86] and D'Angola [85, 124]. This theory has formed the basis for the development of the specific 19-species equilibrium air-plasma EoS (plasma19) by Träuble in 2018 [84], with application to lightning plasma published in 2021 [95].

LTE is more precisely defined to be a state where: the particles' energies in a local neighbourhood obey Maxwell-Boltzmann distributions, such that a local temperature and pressure can be defined. For a gas in LTE, the intensive properties of temperature and pressure

correspond to a unique chemical composition, and resultant macroscopic thermodynamic properties.

The theory developed for the 19 species model considers a large number of basis chemical reactions, which are listed in the original work [84]. Given the very high temperature of 60,000 K, for which plasma19 was originally developed, the double, triple and quadruple ionisation reactions incorporated as basis reactions do not play a role in the temperature band of this work. Photo-ionisation reactions are not incorporated into the chemistry model, since radiative heating effects are presently neglected. Nonetheless, the other dissociation and single ionisation basis reactions accounted for give rise to computed equilibrated state in the temperature band of interest for this work. Every such reaction is governed by a law of mass action corresponding to dynamic equilibrium, given by:

$$K_r^P(T) = \prod_{s=1}^{N_s} P_s^{v_{r,s}}, \quad r = 1, 2, \dots, N_R \quad (3.10)$$

where $K_r^P(T)$ is the temperature dependant equilibrium constant of the r^{th} reaction, P_s is the partial pressure of the s^{th} species, $v_{r,s}$ represents the stoichiometric coefficients of the s^{th} species in the r^{th} reaction. N_s is the total number of species considered (19) and N_R is the number of different reactions.

The total pressure of the gas mixture is then given by Dalton's Law:

$$P = \sum_{s=1}^{N_s} P_s + P_{DH}, \quad P_s = n_s k_B T \quad (3.11)$$

where k_B is the Boltzmann constant, n_s the particle number density of the s^{th} species, T the equilibrated mixture temperature, and P_{DH} is a pressure correction derived from Debye-Hückel theory, and accounts for additional effects for ionised gas mixtures.

A further constraint on the system is, naturally, the conservation of the predetermined total mass across species. Therefore, for a specified intensive property pair (pressure, temperature) a large, determined, system of non-linear equations governs the precise species composition. However, the equilibrium constants in such a system vary by many orders of magnitude, making the numerical solution of such a system extremely costly and difficult. An accurate hierarchical algorithm for computation of chemical composition at equilibrium of a given reactive mixture has been developed by D'Angola [85]. Once the chemical composition is determined, the thermodynamic properties and potentials (Gibbs free energy, total free energy, total internal energy and enthalpy) can be ascertained from the relevant partition functions. And heat capacities can then be ascertained via:

$$C_P = \left(\frac{\partial H}{\partial T} \right)_P, \quad C_V = \left(\frac{\partial U}{\partial T} \right)_V \quad (3.12)$$

D'Angola has then developed detailed numerical fits for the computed properties. For transport properties of the system (such as thermal and electrical conductivity), the equations are based on Chapman-Enskog theory, a detailed derivation of which can be found in Capitelli et al. [123]. For the remainder of the specifics of the developed theory for plasma19, please refer to the detailed description in [84].

The state properties computed by Plasma19 have been extensively validated against empirical measurements. When used as the EoS within a larger hydrodynamic code to produce simulations of plasma arc generation, the full model could be validated against experimental results [95], demonstrating the accuracy of plasma19 in this regime.

3.2.2 Data structure of tabulated EoS

Whilst the numerical basis functions developed by D'Angola take pressure and temperature as arguments, the implementation by Treüble converts to density and pressure as the intensive property pairing, and structuring of the tabulated database. Properties are computed over a density range of $0.001\text{-}10.0\text{ kg/m}^3$ and pressure range of $1013.25\text{-}18238500\text{ Pa}$ ($0.01\text{-}180$ atmospheres), with 500 data values logarithmically scaled over each of these ranges. The property data then consists of size 500×500 matrices for the property spaces, as listed and depicted in Figure 3.5.

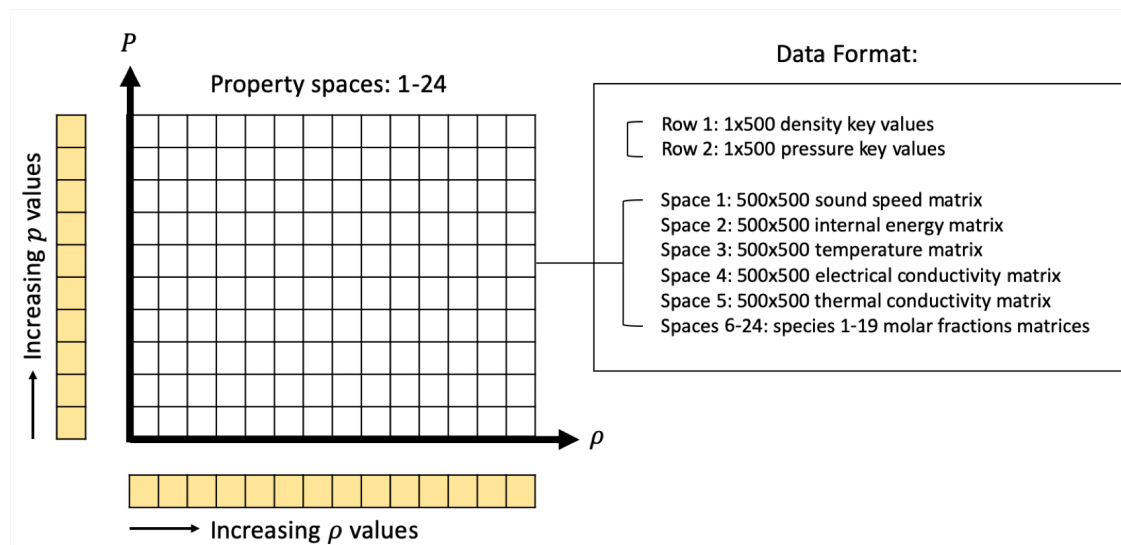


Fig. 3.5 Tabulated equation of state data structure depiction, with ordered list of computed property spaces.

3.2.3 Property extensions

The remarkable story of British Aeronauts James Glaisher and Henry Coxwell was of a coal-gas filled hot air-balloon journeying up into the atmosphere in 1862 which set a new record by reaching 9-11km altitude, and in doing so confirmed the existence of layers in the

atmosphere, discovering the troposphere and the stratosphere. Reports suggest the aeronauts were unprepared for the dramatic drop in air density and temperature at this altitude, leading to life threatening hypothermia and hypoxia (Glaisher even fell unconscious) on their mission to further the cause of science.

From the comfort of a warm home office, the test problems under study in this work require knowledge of free-stream atmospheric properties up to approximately 70km altitude (since much of this work is motivated by the context of atmospheric reentry). The notoriously very low density and pressure of the upper atmosphere mean that free-stream conditions of high altitude test cases extend below the lower bounds of the original plasma19 database. Additionally, for hypersonic flows cases, a near-vacuum region of low density and pressure forms over the ‘shoulder’ of many geometries, which also often exceeds look-up table limits for certain test cases of interest. The current lowest (density, pressure) pairing is ($1.0 \times 10^{-3} \text{ kg/m}^3$, 1013.25 Pa), whereas the atmospheric density and pressure at, for example, 61 km altitude (where data was obtained for the RAMC test flight) is ($2.414 \times 10^{-4} \text{ kg/m}^3$, 17.66 Pa).

It was stated in the original development work that it is reasonable to exceed the current bounds of the tabulated EoS [84] (i.e. the same basis theory holds over extended property ranges), however, the detailed chemical composition and resultant numerical basis functions for data fitting have not currently been computed beyond the current property domain. Furthermore, the hierarchical algorithm for solving the large set of non-linear chemical reaction equations may be particularly cumbersome for the reaction coefficients of the very low pressure range, making it difficult or impossible to generate new data at very low pressures and densities. Were the selection of basis species and reactions to be adapted for the lower temperature band only, the set of reactions coefficients may permit a more practicable direct solution. However, with the selected 19-species which cover a wide temperature band, an alternate method of extension is required.

Previously a ‘switching’ technique had been recommended, where the ideal gas law ($\gamma = 1.4$) can be ‘switched on’ beyond the bounds of the look-up table. However, by investigating this technique, it is found that ‘switching’ is only suitable for a narrow temperature band: 10 K - 1,000 K where a smooth transition to ideal gas properties can be obtained. Elsewhere a problematic ‘jump’ is observed over the property boundaries. This can be seen in the temperature and conductivity plots of Figure 3.6. The property discontinuities are problematic because any non-smooth property fields in the EoS lead to numerical instabilities when embedded in a larger hydrodynamic code.

Additionally, the ideal gas law has no means of resolving electrical and thermal conductivity, or species mass fractions to be able to extend the property domain. The right side plot of Figure 3.6 applies the analytic conductivity approximation of equation 3.4 as recommended by Poggie & Gaitonde [20], with $\sigma_0 = 200 \text{ S/m}$ and mid-range $T_0 = 25,000 \text{ K}$ as subsequently used in the studies by Otsu [58] [9]. Though this can be fit more specifically

to each test problem, very clear discontinuities emerge regardless of fixed n , σ_0 and T_0 pairings.

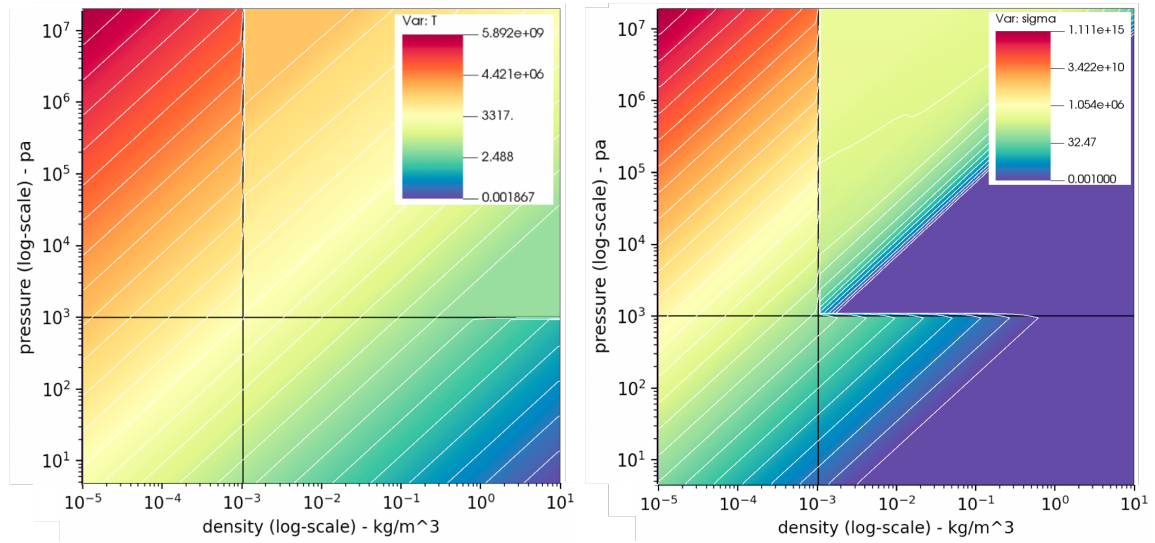


Fig. 3.6 Temperature and electrical conductivity computed within existing plasma19 database over region: $[\rho = 10^{-3} - 10 \text{ kg/m}^3] \times [p = 1.013 \times 10^3 - 1.823 \times 10^7 \text{ Pa}]$ with 'switching' applied to ideal gas ($\gamma = 1.4$) over low density $[\rho = 10^{-5} - 10^{-3} \text{ kg/m}^3]$ and low pressure $[p = 7.55187 - 1.013 \times 10^3 \text{ Pa}]$ regions. Original plasma19 property borders shown in black. Supplementary conductivity model adopted for ideal EoS switching is as per equation 3.4 with exponent of $n=2$.

This work proposes instead an isotherm-based property extension. Via analysis of a transform of the computed properties, and from the theory underlying the computation of chemical composition, a temperature-dependant effective adiabatic index assumption can be applied. This is found to permit physically realistic property extensions.

The physical basis of the proposed property extension considers the following: chemical composition is a unique product of temperature and pressure pairing (as identified from the theory: the chemical reaction equations depend upon intensive properties p and T), once chemical composition is determined, bulk thermodynamic properties have a basis in the sums of mixtures which locally follow an ideal gas law form: $P_s = n_s k_b T$ as per equation 3.11. Globally, the ideal gas law breaks down because the adiabatic index γ is variable depending on species composition. We can however compute the effective adiabatic at local indices across the original plasma19 property space and analyse its partial derivatives with respect to p and T .

In order to compare the variation of effective γ with respect to p and T , the following variational parameter is defined:

$$V = \frac{\left(\frac{\partial \gamma(p,T)}{\partial p/p}\right)_T}{\left(\frac{\partial \gamma(p,T)}{\partial T/T}\right)_p} \quad (3.13)$$

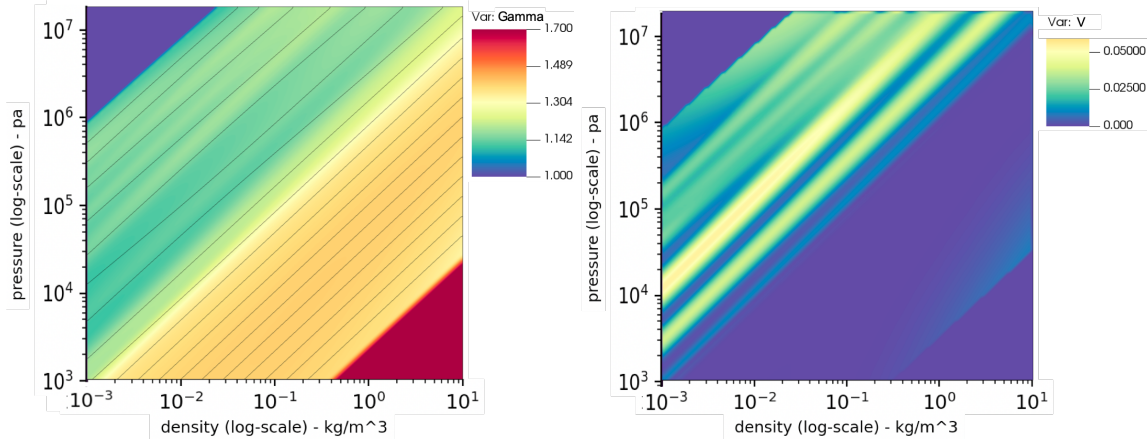


Fig. 3.7 Left) colour plot of adiabatic index computed using the internal energy as a basis: $\gamma = 1 + \frac{p}{\rho \cdot e}$ with temperature contours overlaid in black. Right) Variational parameter of equation 3.13 computed through finite difference routines over the plasma19 property space, showing the relative ratio of partial derivative of γ with respect to pressure, scaled by partial derivative with respect to temperature.

As shown in the left-side plot of Figure 3.7, the gradient of computed adiabatic index space is aligned almost exactly with temperature gradient. The partial derivative terms of equation 3.13 are computed over the property space through numerical finite different routines and shown in the right-side plot of Figure 3.7. This shows $V \approx 0$ over much of the property space, with a peak value of 0.055 reached in a very narrow temperature band, and 97% of the property space is computed to have $V < 0.03$. This analysis supports the assumption that treating γ as temperature dependant is a good approximation (far superior to the ‘switching method’ with constant γ), which can therefore be used as a physically reasonable basis for property extrapolation.

The following effective forms of the ideal gas law are therefore proposed for the thermodynamic properties: a , e and T , where the effects of γ are contained within the respective $\alpha(T)$ coefficients:

$$a = \sqrt{\left(\frac{\gamma p}{\rho}\right)} \rightarrow a = \alpha_a(T) \sqrt{\left(\frac{p}{\rho}\right)} \quad (3.14)$$

$$e = \frac{p}{\rho(\gamma - 1)} \rightarrow e = \alpha_e(T) \left(\frac{p}{\rho}\right) \quad (3.15)$$

$$T = \frac{p}{\rho \cdot C_p \left(\frac{\gamma - 1}{\gamma}\right)} \rightarrow T = \alpha_T(T) \left(\frac{p}{\rho}\right) \quad (3.16)$$

and similarly a power function of (p/ρ) is assumed for electrical and thermal conductivities:

$$\sigma = \alpha_{\sigma}(T) \left(\frac{p}{\rho} \right)^n, \quad \sigma_T = \alpha_{\sigma,T}(T) \left(\frac{p}{\rho} \right)^n \quad (3.17)$$

Noting that locally $T \propto \left(\frac{p}{\rho} \right)$, the method for property extension is as follows:

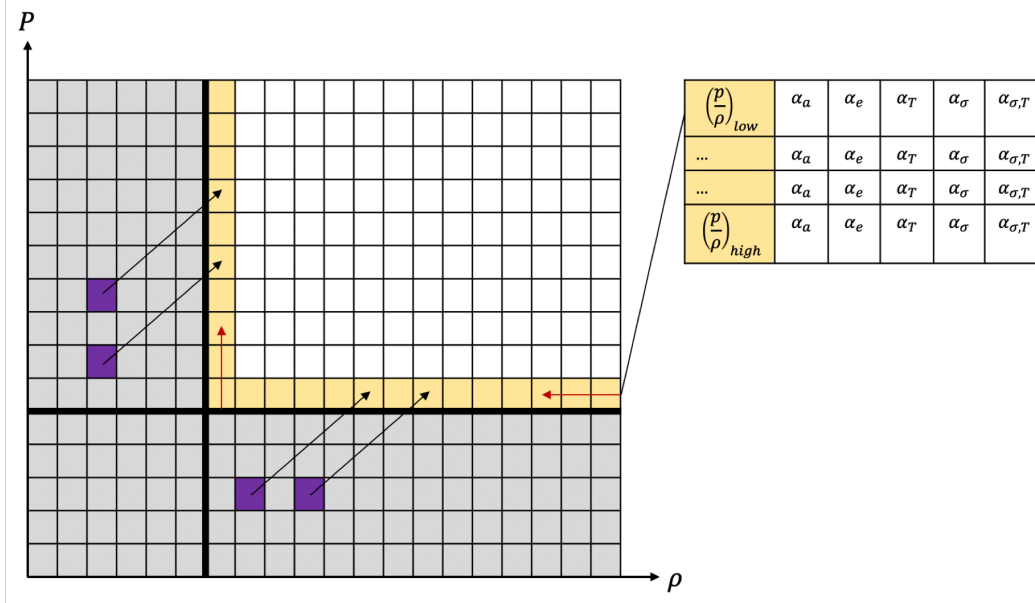


Fig. 3.8 Depiction of extension process: Boundary cells identified with indexing (p/ρ) stored, along with computed α coefficients for each corresponding property. Properties in cells of extension region are computed from the α variables identified from a projection along isotherms.

1. Construct a matrix with rows corresponding to (p/ρ) of the border cells, and column corresponding $\alpha_a, \alpha_e, \alpha_T, \alpha_{\sigma,T}, \alpha_{\sigma}$ computed in the boundary cells
2. For every new data point in the extended property region, use the (p/ρ) to identify the corresponding boundary element (effectively projecting along the isotherm) determining the values of the α coefficients corresponding to that cell
3. Compute the thermodynamic property according to equations 3.15-3.17 from the identified α coefficients

Analysis of the best fit exponent (n) in the σ and σ_T functions of 3.17, found an exponent of very close to 1.0 was in fact the best fit.

The resultant extended property spaces are shown:

Having expanded the thermodynamic properties over the defined wider range - from here, the extended version of plasma19 will be referred to as *plasma19X*. This encompasses the original plasma19 database, as well as the extended region. The electron molar fraction extension in the next section overwrites the original plasma19 data (with a more accurate computation) as well as extending over the widened plasma19X property region.

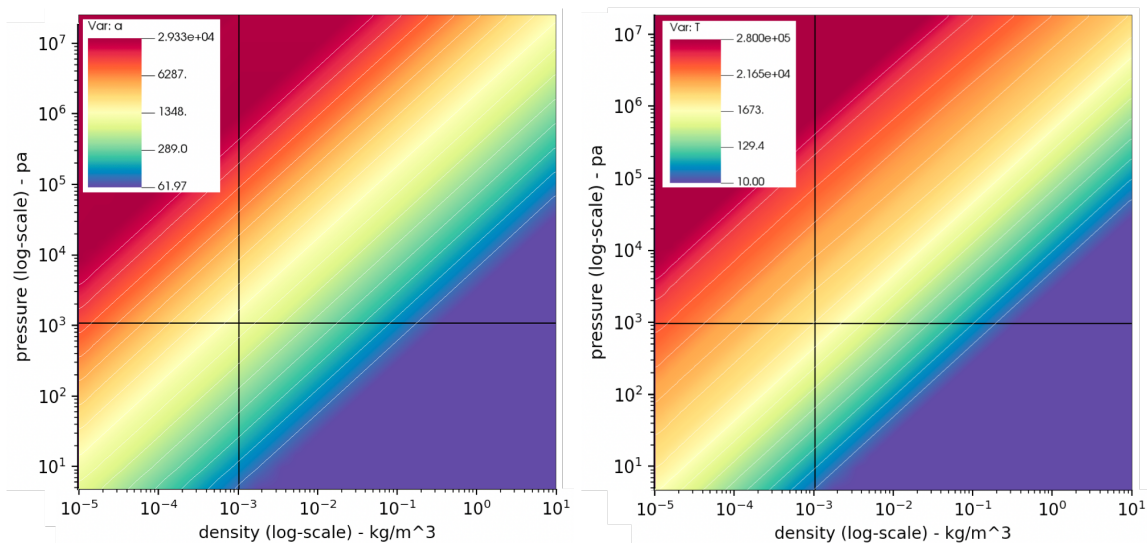


Fig. 3.9 Left) computed sound speed, and right) computed temperature, over extended property space.

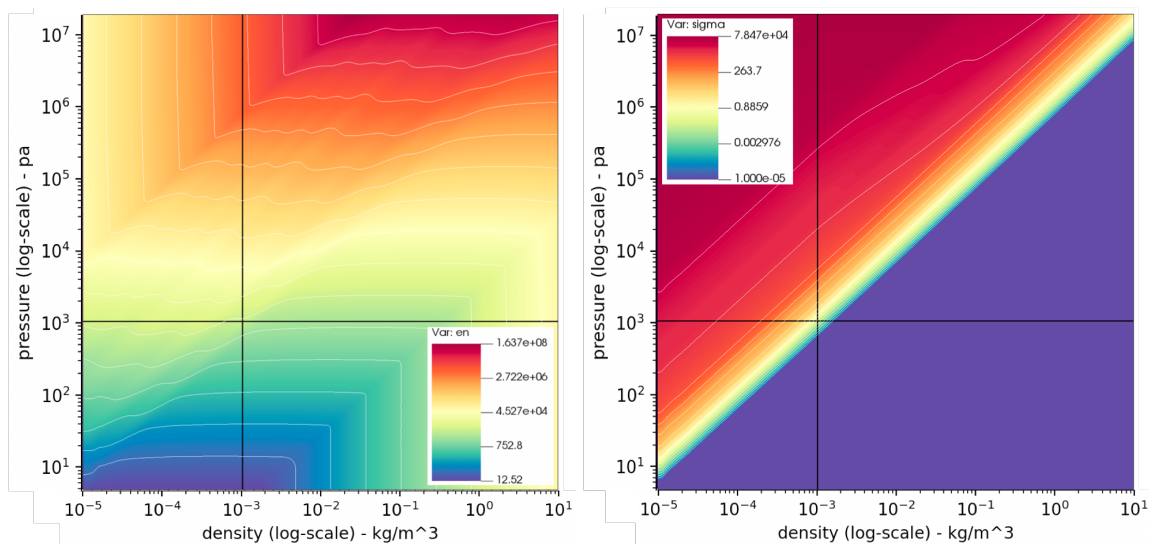


Fig. 3.10 Left) computed total energy, and right) computed electrical conductivity, over extended property space.

3.2.4 Computing electron molar fraction and number density

An important extension is made to resolve the electron number density accurately across the full, extended, property range. The electron species molar fractions previously computed in the plasma19 database is found to be accurate for temperatures greater than 15,000 K, however abruptly truncates to zero below this temperature. This is problematic since the specific temperature band of interest for reentry plasmas is sub 15,000 K.

Therefore the previous work of Träuble is now extended to additionally compute and store property data for electron molar fraction (χ_e) and electron number density (N_e), replacing the data within the existing (ρ, p) tabulated data set and computing new values across

extended plasma19X (ρ, p) range. Unlike the previous property extensions, an isotherm based extrapolation technique is not suitable for 2 reasons: (1) the current values are incomplete or unreliable within the existing property space, and (2) the $\left(\frac{\partial \gamma}{\partial p/p}\right)_T$ term does not approach zero in the domain, since the electron number fraction has a non-negligible, independent pressure dependence.

The extended implementation is therefore based on theory developed by D'Angola *et. al.* in [124] designed to achieve high accuracy over the temperature range of 50 K - 20,000 K. Following this theory, the electron molar fraction is computed as a set of basis functions of pressure and temperature as defined by equation 3.18:

$$\chi_e(p, T) = (1 - \sigma_0(T)) \exp \left[\sum_{i=0}^6 \delta_i(p) T^i \right] + a_1 \sigma_0(T) \times \sigma_1(T) \sigma_m(T) + \sigma_0(T) [a_2 \sigma_2(T) + a_3 \sigma_3(T) - a_4 \gamma_4(T)] \quad (3.18)$$

where

$$\delta_i(p) = \sum_{k=0}^6 \beta_{k,i} [\log(p)]^k \quad (3.19)$$

and where σ and γ expand to be sigmoid and Gaussian functions respectively, given by:

$$\sigma(T; c, \Delta) = \frac{e^q}{e^q + e^{-q}}, q = \frac{T - c}{\Delta} \quad (3.20)$$

$$\sigma_i(T) = \sigma(T; c_i, \Delta_i) \quad (3.21)$$

and

$$\gamma(T; c, \Delta) = e^{-q^2}, q = \frac{T - c}{\Delta} \quad (3.22)$$

$$\gamma_i(T) = \gamma(T; c_i, \Delta_i) \quad (3.23)$$

Further, the parameters $a_i, \beta_i, c_i, \Delta_i$ all take on the general form:

$$C(p) = \sum_{j=0}^n \alpha_j [\log(p)]^j \quad (3.24)$$

where C represents either $a_i, \beta_i, c_i, \Delta_i$ or its natural logarithm, as defined in the table of Appendix A, which also contains the coefficients $\alpha_{i,j}$ associated with each polynomial expansion.

For implementation within the plasma19X look-up table which takes density and pressure as the input intensive property pair, temperature is first internally computed internally as $T(\rho, p)$, then electron molar fraction is computed as $\chi_e(T, p)$ and stored by extending the database. Electron number density (N_e) can then be computed as a function of χ_e and ρ .

Where electron mass fraction is:

$$M_e = \frac{\chi_e MW_e}{MW_{air}} \quad (3.25)$$

with molecular weights of electrons and air respectively: $MW_e = 5.485799 \times 10^{-4}$ g/mol and $MW_{air} = 28.9628$ g/mol. Then the total density of electrons in the fluid is simply $\rho_e = M_e \times \rho$, and therefore electron number density is given by:

$$N_e = \frac{\chi_e MW_e \cdot \rho}{MW_{air} \cdot m_e} \quad (3.26)$$

where $m_e = 9.10938356 \times 10^{-31}$ kg is the mass of a single electron.

The computed results of this model are compared with D'Angola's result in Figure 3.11 to verify the correct implementation of the theoretical model and resultant computed properties.

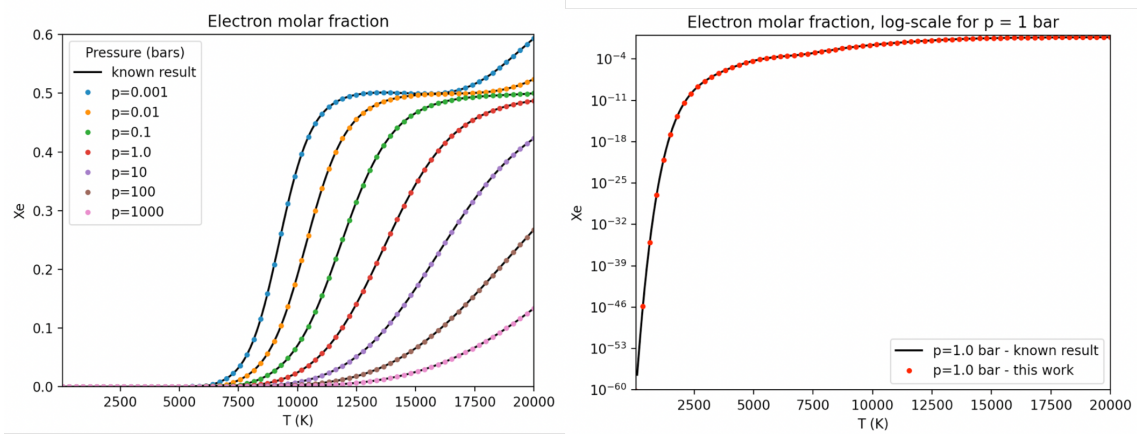


Fig. 3.11 Implementation of electron molar fraction for accurate computation over 50 K - 20,000 K (this work: coloured data points), validated against the results of D'Angola (solid black lines), for pressure values: 0.001 bar - 1000 bar. Linearly-scaled molar fraction shown for various pressures on left, and log-scaled molar fraction for $p=1.0$ bar shown on right.

As shown from the log-scaled plot of Figure 3.11, a small but smooth electron molar fraction can be computed down to a very low temperature range, demonstrating the ability of the new EoS to resolve even very minute concentrations of electrons in a low temperature air-plasma.

A comparison of the original property space for electron number density and the new extended implementation result is shown in figure 3.12.

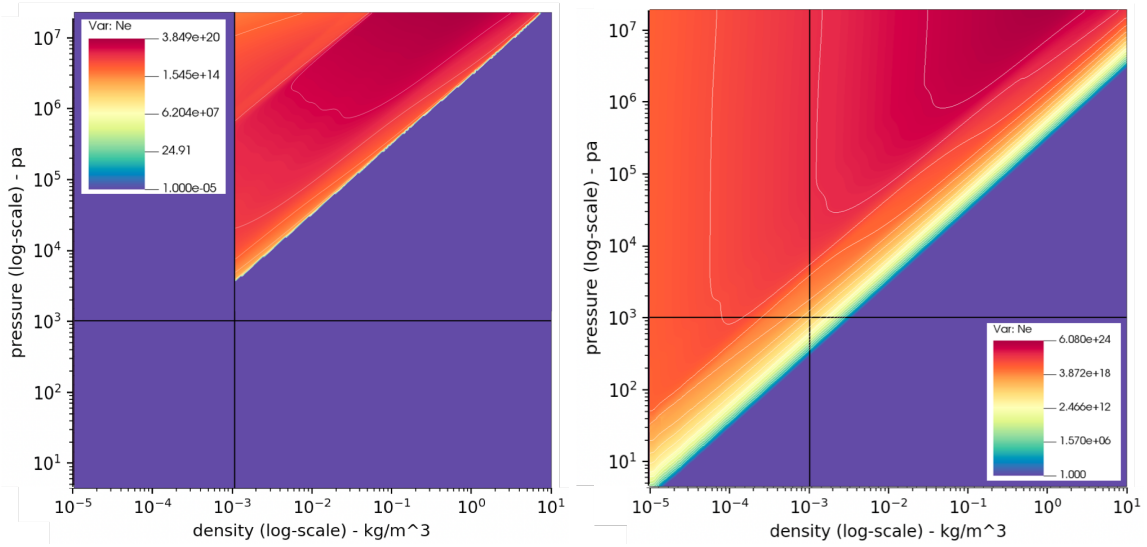


Fig. 3.12 Left) Original plasma19 electron number density property space, Right) new generated plasma19X N_e property space after implementing the extended formulation for computing electron number density.

3.3 Computing electrical conductivity

It is important to highlight the ability of the new EoS to accurately compute electrical conductivity directly and accurately across the relevant temperature range for hypersonically generated air-plasmas.

Various methods for computing σ were discussed in section 3.1.1, which highly simplified analytic power laws, and empty empirical function for v_{coll} in equation 3.5. The electrical conductivity given by plasma19X, however, was computed by the detailed theory of perturbative Chapman-Enskog method, which derives a full set of collision integrals from the species compositions, and a third order approximated diffusion coefficient ($D_{ee}(3)$), which then computes electrical conductivity as:

$$\sigma = e^2 \frac{N_e m_e n}{\rho k_B T} D_{ee}(3) \quad (3.27)$$

where n is the total number density and k_B is the Boltzmann constant. The detailed derivation can be found in Capitelli et al. [87].

The accuracy of plasma19X can be attributed to the detailed method of derivation of σ in equation 3.27 including the additional species dissociations and ionisations captured at relatively low air-plasma temperatures in the 19 vs 11 species approach. With relevance to the application of this work, the double and triple ionised species captured by plasma19X are only present at higher temperatures (>20,000 K), and largely do not effect the state in the temperature band of interest (approximately 2,000 K - 10,000 K). The negatively charged O^- , O_2^- and N_2^- species however, are not captured by an 11-species model but are computed to be present in small concentrations in the low air-plasma temperature range.

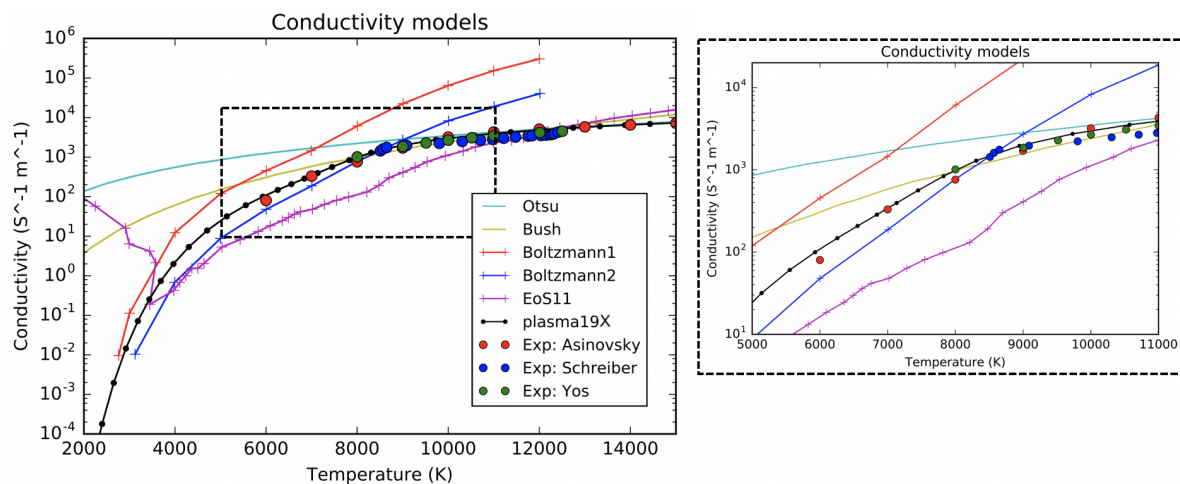


Fig. 3.13 Electrical conductivity across low air-plasma temperature range at pressure = 1 atm. Comparison of σ computed by plasma19X with other models currently used in the literature and to experimental measurements. Three sets of experimental measurements have been obtained from the works of Asinovsky et al. (1973) [6], Schreiber et al. (1971) [7] and Yos (1963) [8] where a low-temperature equilibrium plasma was generated via a stabilised DC arc applied to a column of air maintained at atmospheric pressure. Otsu [9] and Bush [10] use the simple analytic power law approximation defined in equation 3.4 with exponents 2 and 4 respectively. Solution to the Boltzmann equation is as per the solver developed by Weng and Kushner [11] for two different levels of resolution. EoS11 is an 11-species equilibrium model as implemented by Villa et al. [12].

Comparison of the computed electrical conductivity by plasma19X shows very high accuracy as compared with experiment- critically, in the low temperature range relevant to hypersonic flight in the LTE regime. As can be seen in Figure 3.13, the non-physical species molar fractions over the low temperature range, and resultant anomalous electrical conductivity, render EoS11 as problematic for LTE MHD studies. The anomalous conductivity values at low temperatures are not only physically unrealistic, but sharp jumps in properties lead to numerical instability when integrating the MHD source terms. It is also clear that the analytic approximations used by Otsu and Bush produce reasonable estimations at temperatures above approximately 9,000 K, but fail to accurately represent σ as temperature decreases. The conductivity computed by plasma19X obtains a smooth profile down to very low air-plasma temperatures. Additionally, the pre-computed σ values can be accessed directly without the need for a supplementary conductivity model, rendering the model as highly efficient.

The smooth and accurate conductivity values computed by plasma19X over the low temperature range enables the direct and realistic simulation of LTE MHD flow control for this regime.

3.4 Implementation advances

The algorithms for the solution of the gas dynamic system detailed in the next chapter involve the conversion from conserved variables to primitive variables and back again for every cell for every global time-step. Additionally, every additional property computed and stored as cell data will call on the EoS. In equilibrium chemistry codes where a look-up table of pre-computed values is accessed, and state properties are computed via interpolation routines, the efficiency of the interpolation routine is critical for overall run-time efficiency.

Given the established (ρ, p) keys of the tabulated data structure, the $[\rho_i, \rho_{i+1}]$ and $[p_i, p_{i+1}]$ pairs which collectively bound the (ρ, p) input, must be identified, and the return property can be interpolated therein.

The most basic option for the property search method is an ascending search which converges in $O(N)$ operations for each key-property vector of size N . Implementing the faster binary search method (as recommended in a previous implementation of plasma19 [84]), which converges in $O(\log_2(N))$ operations, significantly improves the performance of the overall code. Pseudocode is shown to describe the two search methods:

Algorithm 1 Pseudocode for ascending search method

Ensure: Values in *property_vector* are positive and ascending

Ensure: $property_vector[0] \leq prop \leq property_vector[N]$

▷ Ensure statements apply to all 3 algorithms

```

index = 0
while (prop > property_vector[index]) do
    index+ = 1
end while
indexL = index
indexR = index + 1

```

Algorithm 2 Pseudocode for binary search method

```

indexL = 0
indexR = N
while (indexR - indexL > 1) do
    indexM = floor((indexL + indexR)/2)
    if (prop >= property_vector[indexM]) then
        indexL = indexM
    else
        indexR = indexM
    end if
end while

```

This work instead proposes a direct search method which is able to directly identify the contiguous bounding indices:

Algorithm 3 Pseudocode for direct search method

$$\begin{aligned} \delta_n &= (\log_{10}(prop) - \log_{10}(prop_{min})) / (\log_{10}(prop_{max}) - \log_{10}(prop_{min})) \\ indexL &= \text{int}(\delta_n * N) \\ indexR &= indexL + 1 \end{aligned}$$

Ensure: $property_vector[indexL] \leq prop \leq property_vector[indexR]$

This method critically requires the key density and pressure property vectors being perfectly logarithmically spaced. This spacing therefore governs the range of the additional data points for the extended property range. Based on the existing 125 points per factor 10 scaling of the tabulated data structure, selecting a new lower density bound of $1 \times 10^{-5} \text{ kg/m}^3$ necessitates 250 new data points added for extension. The new lower pressure bound stated earlier (7.55187 Pa) was not merely plucked from the (upper atmospheric) air, but is the logarithmically extrapolated pressure value at an additional 250 data points below the previous p_{min} .

Once the 4 bounding property indices have been found, a more precise return property can be ascertained from interpolation. Standard implementations of a tabulated EoS utilise a bilinear interpolation. However, this work proposes a more accurate approach.

Consider the input key pair (p, ρ) and the 4 identified bounding data points for internal energy e in linearly scaled space, as shown in Figure 3.14. The bilinearly interpolated value based on the black linearly determined contours will be very slightly off-set from the true contours of internal energy, which have been identified to approximately follow the form: $e = \alpha_e(\frac{p}{\rho})$. This may seem like splitting hairs, since the slightly rounded e-contours are very-near tangential to the linearly determined contours in the very small bounded areas of $[e_{11}, e_{12}, e_{21}, e_{22}]$ of the tabulated data-set. However, consider that in every fluid update step in the hydrodynamic code, a conversion from $e \rightarrow p$ and then $p \rightarrow e$ occurs (with operations on both p and e between conversion steps). If the bilinearly interpolated value very slightly overestimates e , therefore very slightly overestimating p when converting back then this results in ‘property creep’ over a large number of evolutions. Similarly, very slight over or under estimation of a effects the wave-speed estimates used in the flux computations and property evolutions. Given that we are interested in computing steady state flow field solutions, which converge over a potentially very large number of fluid dynamic time steps, minimisation of interpolation error is essential to the true steadiness of a steady-state.

Implementing the standard bilinear interpolation routine resulted in the frustrated programmer watching the freestream properties very slowly creep during the iterative convergence toward steady state. The programmer is left with two choices: disregard the property creep as an acceptably small margin of error, or, determinedly combat the creep. From the analysis of section 3.2.3, the following combat-approach is developed:

1. Once the bounding $[e_{11}, e_{12}, e_{21}, e_{22}]$ properties are identified, convert these points to α_e coefficients according to equation 3.16.

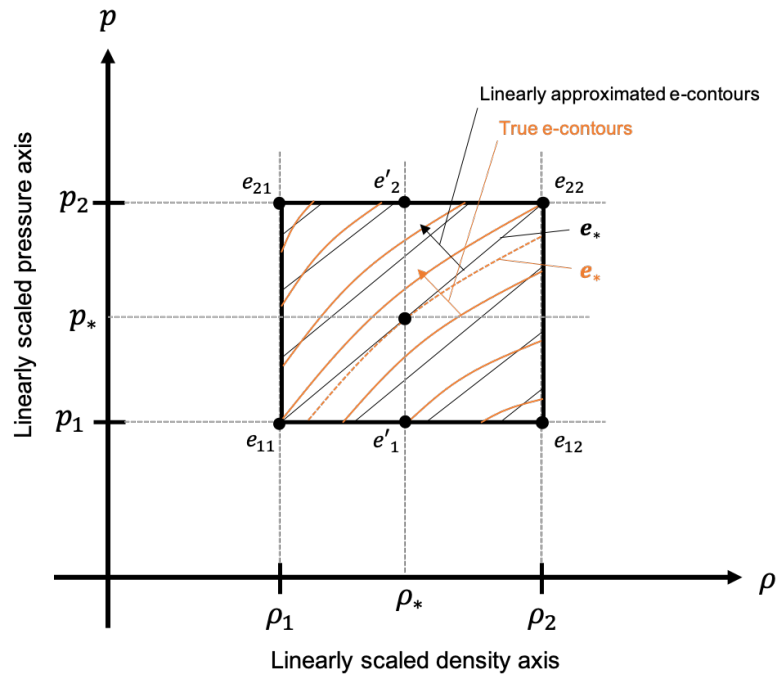


Fig. 3.14 Difference between bilinearly interpolated internal energy value (black e_*) and exact value (orange e_*) corresponding to input intensive properties (p, ρ) .

2. Rather than interpolate on e values, interpolate on the α_e coefficients, following a logarithmic interpolation function. i.e. whereas previously, the bilinear interpolation is given by:

$$\Delta\rho = \frac{\rho_* - \rho_1}{\rho_2 - \rho_1} \quad (3.28)$$

$$\Delta p = \frac{p_* - p_1}{p_2 - p_1} \quad (3.29)$$

$$e'_1 = e_{11} + \Delta\rho \cdot (e_{12} - e_{11}) \quad (3.30)$$

$$e'_2 = e_{21} + \Delta\rho \cdot (e_{22} - e_{21}) \quad (3.31)$$

$$e_* = e'_1 + \Delta p \cdot (e'_2 - e'_1) \quad (3.32)$$

This is replaced by:

$$\Delta\rho = \frac{\log_{10}(\rho_*) - \log_{10}(\rho_1)}{\log_{10}(\rho_2) - \log_{10}(\rho_1)} \quad (3.33)$$

$$\Delta p = \frac{\log_{10}(p_*) - \log_{10}(p_1)}{\log_{10}(p_2) - \log_{10}(p_1)} \quad (3.34)$$

$$\alpha'_1 = \alpha_{11} + \Delta\rho \cdot (\alpha_{12} - \alpha_{11}) \quad (3.35)$$

$$\alpha'_2 = \alpha_{21} + \Delta\rho \cdot (\alpha_{22} - \alpha_{21}) \quad (3.36)$$

$$\alpha_* = \alpha'_1 + \Delta p \cdot (\alpha'_2 - \alpha'_1) \quad (3.37)$$

3. Then resultant e_* can be computed by converting back to: $e = \alpha_*(\frac{p_*}{\rho_*})$. The same improved interpolation method is used for all thermodynamic properties, not just e .

For the extension to the property region $[\rho = 10^{-5} - 10^{-3} \text{ kg/m}^3]$, $[p = 7.55187 - 1.01325 \times 10^3 \text{ Pa}]$, this new interpolation method eliminates creep completely, since the interpolation follows exactly the method for property generation.

It is difficult to quantify the creep in a generalised way since, as shown by the V-parameter of Figure 3.7, the accuracy of approximation utilised in the interpolation method varies across the plasma19X property space. To offer some indication, creep in the original plasma19 data region is tested by running a hypersonic flow test case over a sphere at free stream conditions equivalent to 30 km altitude ($\rho = 0.01841 \text{ kg/m}^3$, $p = 1197 \text{ Pa}$). Property creep is observed for the recommended bilinear interpolation method, causing free stream pressure to increase progressively over the full simulation, with a total increase of 10.94% by the final 1000th time step. Creep however is almost entirely eliminated with the α based interpolation technique, with free stream pressure dropping by only 1.16% gradually in the first 120 time-steps, and then stabilizing to a converged fixed constant value up to the end 1000th step run for the test simulation.

3.5 EoS comments

It is worth highlighting the exact role played by the extended plasma19X property region. Without extension, we would exit the bounds of the original plasma19 tabulated database when free stream properties were equivalent to exceeding an altitude of about 32 km ($p < 1013.25 \text{ Pa}$). This is not particularly useful for hypersonic flight regimes. Naturally, however, post-shock pressures produced from supersonic or hypersonic flows are well above the order of 1 kPa falling into the $p - \rho$ region defined by the original plasma19 database. The key is in obtaining a smooth property transition from the free stream to the post-shock region. Without such smooth transition, rapid and significant instabilities manifest when embedded in the full hydrodynamic code. The original recommendation of a ‘switching method’ is highly problematic for this reason.

The smooth property profiles obtained from the isotherm based property extension are essential to the stability of test problems of interest, however, where the focus of the subsequent MHD studies are on the properties in the post-shock layer, the extended region therefore plays somewhat of a supporting role. The extended implementation of electron molar fraction (and therefore electron number density) however is essential in all test cases pertaining to the ionised shock layer properties.

In terms of implementation, it is interesting to consider the way in which interpolation routines and minimisation of property creep are interrelated, and, both related to the database size N . An obvious way to minimise creep is to increase generated data density such that the discretised data space more closely approximates the true curvature of the property

profiles. However, in the standard search methods for property look-up, computing time is proportional to N . So there is a trade-off between property creep and data-density (leading to N). The new proposed direct search method liberates the implementation from this forced trade-off. Following the defined method of exact logarithmic spacing and corresponding direct search algorithm, the computational time to compute a new property is independent of the database size. This is a major advantage when embedded within the larger hydrodynamic model. In theory, one could therefore adopt a very large tabulated EoS of this form without compromising on simulation run-time. However, for the current database, increasing the data point density is redundant without generating new data from the original plasma19 generation algorithms, since otherwise the new data points are merely a product of further interpolation.

On the contrary, given the improved accuracy of the new recommended α -based interpolation method, one might consider actually reducing the data density. When paired with the proposed direct search method, this will not impact computational time, however, perhaps one encounters a scenario where storage is a constraint or file read time is desired to be minimised. The fact that the analysis of section 3.2.3 reveals useful physical approximations of the property field, which can be leveraged in formulas for interpolation, greater accuracy of interpolation could theoretically be achieved with reduced generated data density. Note however, that this is not equally valid for all properties. N_e for example will not follow the α form for interpolation (though it is still a better approximation than bilinear interpolation).

In other thoughts on EoS implementation, AMR, and creep: one should consider that the sub-cycling of time steps which occurs in the hierarchical AMR method described in the subsequent numerical methods chapter means that higher resolution (via additional AMR levels) results in more total time-steps, and therefore more total property conversions in the hydrodynamic code, leading to creep. If creep is significant this has the potential to even result in small property divergences at the borders of fine cell (high resolution) blocks and coarse cell (low resolution) blocks. This adds credence to the effective minimisation of creep through the improved interpolation technique within an AMR framework.

While it is possible to clearly identify the occurrence of property creep in the free stream state in a simulation (known fixed free-stream properties do not hide themselves well when they change over time steps), it is much more difficult to determine the degree of creep in post shock properties which are yet to converge to a steady state (or near impossible in a transient simulation with properties in perpetual flux). Therefore, determining from the free stream that properties are held fixed, gives high confidence to the post shock or transient regions. Consider as well that not all properties are created equal. It should be noted that some properties: p , ρ , e , a , u are the primitive and interdependent basis to the inviscid fluid evolution. For the simple Euler model identified in Chapter 2, other properties, for example T and σ are computed strictly as resultant (secondary) properties. Therefore inaccuracies in calculating $T(\rho, p)$ or $\sigma(\rho, p)$ does not directly influence the underlying fluid dynamics.

Another seemingly esoteric, yet important, consideration is the data precision and format for the tabulated EoS. When dealing with properties varying by many orders of magnitude, data format and computing precision is no longer trivial. For the key look-up values of ρ in the extended property range, up to 8 decimal places are required for sufficient accuracy of the float output-to-file format, in order to retain the lowest ρ values. In general, great care must be taken with significant figures and decimal vs scientific output form, to avoid truncation error in generating an accurate tabulated EoS - especially one paired with the direct search method.

One can look forward to the validation results for the extended plasma19X EoS to come in Chapter 5.

Chapter 4

Numerical methods and algorithm development

At the heart of computational science lies the problem: *how does one model a continuous world view as a discrete set of data?*

Continuous properties defined in space which evolve in time, governed by the partial differential equations described in Chapter 2, are of a mathematical form where pen-to-paper analytic solution is simply unattainable.

The mathematical bridge, built in 1749 and which crosses the River Cam within Queen's College, was celebrated for having the appearance of a smooth arc despite being composed of a finite number of straight timbers. Much like the tangent-based planks which form the smooth radial profile of the mathematical bridge, conversion of the continuous problem to a discrete property space and the application of first principles approximations in differential calculus combined with iterative solution procedures, offers a means of generating realistic approximations to true continuous solutions.

Iterative numerical approaches were once conducted by hand, with papers passed down lines of "human computers" to produce iteration-based solutions. Today, with the advancements of modern computing, sophisticated numerical algorithms are solved in practicable times by passing electrons through transistors rather than papers down tables. It is important to therefore consider the interplay between numerical algorithm development and computing architecture when formulating large computational models.



Fig. 4.1 Mathematical Bridge, as seen from the river bank at Queens' College, Cambridge. C.G. Harper, 1892 [13].

This chapter describes the numerical methods directly implemented for the development of the full computational model of this work. The focus is on the algorithm development, however high performance computing considerations are intrinsically linked. The specific contributions are made clear in the Development designation of section 4.1.

In developing algorithms and numerical methods to best approximate a physical system, there are a number of core concepts of importance: stability and robustness, convergence (order of convergence and convergence to the correct physical solution), and computational cost. This chapter outlines the numerical methods implemented based on these key principals. A new extension to the Euler base-model numerical solver has been developed in order to ensure stability up to the hypersonic regime. Special consideration and adaptations were required to be made for the numerical methods applied to solving the extended Navier-Stokes model when paired with the selected meshing and geometry methods. A two-step method which conserves internal energy is implemented for the MHD source term integration. High performance computing aspects are also considered in tandem. The combination of numerical methods adopted, extended, and merged within a high efficiency framework, results in a computational model with substantial advantages over prevailing technologies, as will be described.

4.1 Development designation

To clearly signpost the direct contributions in regard to model development: this work has adopted as a base code structure, the AMReX framework, which handles block-structured mesh generation (with hierarchical AMR) and parallelism routines, and was developed by AMReX framework Developed by A. Almgren, J. Bell and team at the Lawrence Berkeley National Laboratory [35]. This could be imagined as a “book case” skeleton code, configured to house numerical methods written directly by the Author. A description of AMR and block-structured parallelism is given in section 4.2. It is highlighted here that the efficiency, scalability, and configurability offered by this choice of underlying meshing topology and framework is considered state-of-the-art in modern computational fluid dynamics [125]. Though there are various example codes for application-specific physics available as open-source AMReX codes, in order to build a fully configurable model for the specific objectives of this work, the chosen and developed numerical methods required direct implementation in this newly adopted framework. As such, all system solution algorithms have been implemented from scratch as c++ code, drawing only on in-built AMReX functionality for: pre-defined grid-based data structures, MPI-configurable iterators, and simple geometry declarations.

Whilst the majority of the implemented algorithms are established and trusted numerical methods, the Author’s combination of: a hypersonically stable gas dynamics solver with non-simple EoS, Navier-Stokes extensions, MHD forcing dynamics, paired with embedded

boundary Ghost Fluid Method for complex geometries, within a hierarchical AMR meshing framework, is collectively a novel approach. The harmonious numerical implementation of which is highly non-trivial.

4.2 Mesh topology and the AMReX framework

The discretisation of space fundamentally underlies the fluid dynamics solver, which operates upon the space-associated state data. Meshing types can broadly be classified as unstructured, body-fitted structured or structured Cartesian. Structured meshes have the advantage that the ordered data storage directly implies cell connectivity, which reduces memory requirements (no additional connectivity information required), and is programmatically beneficial when defining operations across contiguously stored neighbouring cells. For low level code (such as the c++ code in which this model is developed), compiler optimisations can provide large efficiency improvements for operations on data ordered in such a way. The trouble for body-fitted meshes is that complex geometric shapes can cause skewing (see Figure 4.2) and non-orthogonality of cells which leads to unphysical solutions due to the transformation of the governing equations across skewed cells [126]. Structured meshes often also result in an unnecessarily large number of computational cells where high resolution is desired in a particular region but cell size must not transition rapidly [127]. Therefore, unstructured meshes are often adopted for complex geometries, and to reduce the number of cells while achieving desired effective resolution. The downsides of unstructured meshes include: additional connectivity data must be stored and the data access routines are less efficient. More importantly, the fluid solver algorithms are required to be more complex, in consideration of fluxes across irregular and varying edge angles. Finally, triangular cells of unstructured meshes tend to be ineffective in resolving wall boundary layers due to difficulties in computing diffusive fluxes across thin triangular cells adjacent to a wall boundary [126].

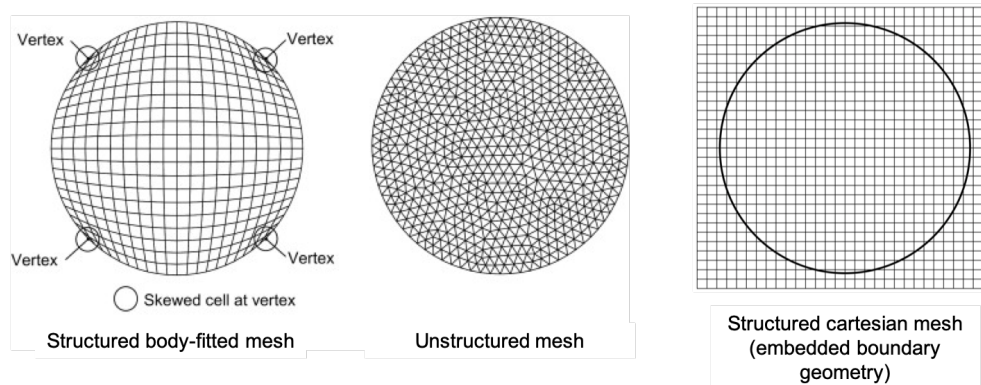


Fig. 4.2 Three different mesh topologies demonstrated for a hypothetical bounded circular domain region

A means of resolving these complementary complications, is the proposal of structured Cartesian meshes, with embedded boundary geometries (right side Figure 4.2). One of the key advantages of a full-domain structured Cartesian meshing topology, is that it is directly amenable to hierarchical adaptive mesh refinement (AMR) and block-structured parallelism.

4.2.1 Hierarchical adaptive mesh refinement

Fluid dynamics simulations tend to involve regions of low fluid complexity (small to no property gradients) and regions of high complexity (large and dynamic property gradients), whereby computational resources are best optimised by locally refining regions of high property complexity and retaining low resolution elsewhere in order to achieve high *effective resolution*. Mesh refinement can be instrumented with varying degrees of sophistication. Hierarchical adaptive mesh refinement, originally proposed by Berger et al. in 1984 [40], is a particularly effective technique whereby the dynamically evolved solution automatically informs the active and progressive refinement.

The AMReX framework considers quadrilateral (2D rectangular) and hexahedral (3D cuboid) domains which are fully discretised with a Cartesian base mesh. The base mesh is then refined by symmetrically splitting cells through division by R^D where R is the integer refinement factor and D is the spatial dimensionality. Since Cartesian meshes can straightforwardly be subdivided into blocks or *patches*, progressive refinement of identified patches constructs a hierarchy of refinement levels. This concept is depicted in Figure 4.3.

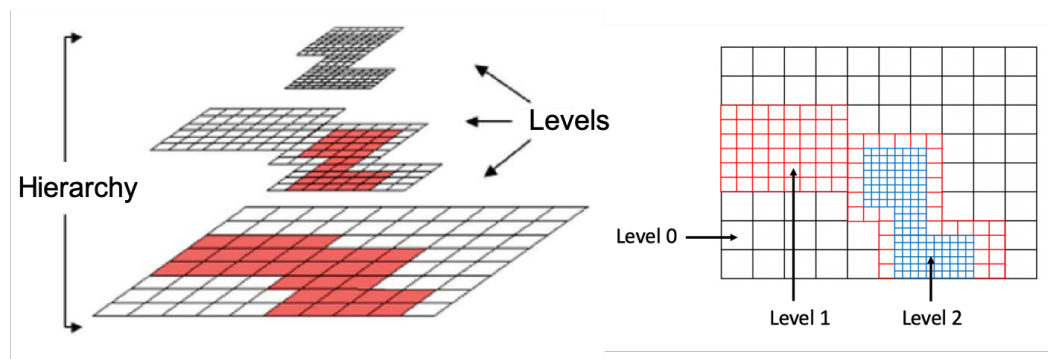


Fig. 4.3 Block-structured AMR grid containing a hierarchy of nested refinement levels. Figure adapted from the image by [14].

Fundamental to the efficacy of hierarchical AMR, is that the refinement is enacted temporally as well as spatially through efficient time-step sub-cycling routines. As derived in section 4.3.1, time stepping is subjected to stability requirements which have a direct dependency of cell size and maximum wave speed. In standard single-level refinement techniques, the time-step remains to be globally restricted based on the smallest contained computational cell. Hierarchical AMR subverts this restriction via synchronised sub-cycling in time, depicted in Figure 4.4. This results in substantial efficiency improvements due to both temporal and spatial discretisation optimisations.

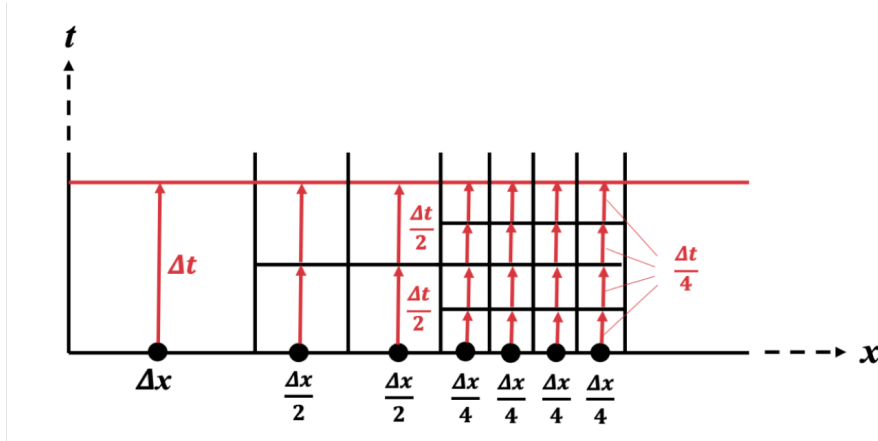


Fig. 4.4 1D space-time diagram: cells are refined spatially by a refinement factor $R^D = 2^1$, and corresponding temporal refinement factor $R = 2$ maintains global time equivalence with the base level after synchronised sub-cycled smaller time steps.

Synchronisation refers to the fact that time steps of higher levels are precise integer subdivisions of the lowest level, such that time is still synchronised between a single coarse cell (lowest level) time step and R^D refined level time steps. Additionally, coarse-cell (lowest level) data is interpolated for use at coarse-fine cell boundaries, for use in sub-cycled flux computations.

4.2.2 Refinement conditions

The process of adaptive refinement within AMReX is simple: cells are *tagged* if a certain refinement criterion is met, then whole patches which contain tagged cells are hierarchically refined. The number of levels for refinement, the refinement factor R and the refinement criteria can all be selectively defined.

Given that this work deals with compressible fluid flows whereby strong shocks form, as well as rarefaction and contact waves, the natural choice for a refinement property is density gradient (effective for detection of all 3 wave types - whereas pressure and velocity are constant across a contact wave). However this work proposes a novel approach to the level-by-level refinement condition. Since this work deals with very strong shocks, corresponding to very high density gradients relative to other wave features, field-relative and logarithmic scaling are found to be important conditions for effective refinement routines. This work therefore proposes a specific, logical, refinement condition based on thresholds of global maximum density gradient, permitted to vary between levels.

The algorithm simply computes a global maximum (relative, logarithmic) density gradient, then tags cells which exceed the threshold fraction (typically set between 0.5-0.7) of the global maximum gradient. The global maximum gradient is reset level by level, such that refinement occurs for desired total number of N levels. This procedure is described by the pseudo-code of algorithm 4.

Algorithm 4 Adaptive refinement condition algorithm**Define:** $Max_Level = N$ $List_of_Fractions = [frac_0, frac_1 \dots frac_N]$ **for** $n \leftarrow 0$ to N **do** $max_gradient = 0$ **for** each cell in domain **do** \rightarrow compute($cell_gradient = \log(\frac{\nabla \rho}{|\rho|} + 1)$)**if** ($cell_gradient > max_gradient$) **then** $max_gradient = cell_gradient$ **end if****end for****for** each cell in domain **do****if** ($cell_gradient > (List_of_Fractions[n] \times max_gradient)$) **then** \rightarrow tag cell()**end if****end for****end for**

User-defined definition of threshold fractions for level-by-level refinement, offers a high degree of control over *sharpness* of refinement: i.e. whether to only tightly refine around peak gradients (high threshold fraction) or to loosely refine over flow gradients (low threshold fraction).

4.2.3 Parallelism and scalability

Since hyperbolic and parabolic partial differential equations propagate information in a wave-like nature with finite signalling velocities, the numerical methods applied to solving them have a discrete and finite domain of dependance. The expanse of the domain of dependance is intrinsic to the selected numerical methods (typically related to order of accuracy), however, by virtue of the bounded expanse of dependant cells, explicit numerical update formulas are highly amenable to parallelisation.

In order to evolve cells in the computational domain, a number of ghost cells (n_G) are required to bound the border of the domain, where n_G is the one-sided extent of cells in the numerical update stencil which encloses the domain of dependance. Serial computations iterate over every cell in the computational domain in an ordered way to execute a global time step. However, by subdividing the domain into blocks, it can be recognised that information from defined patch plus n_G border cells of the adjacent patches, at the present time step (for time-explicit numerical update schemes), is all that is required to evolve that specific patch in time. Therefore all such defined patches can evolve in time in a parallel manner. The same concept pertains to blocks on higher levels of refinement, which draw on boundary ghost cells of the lower level.

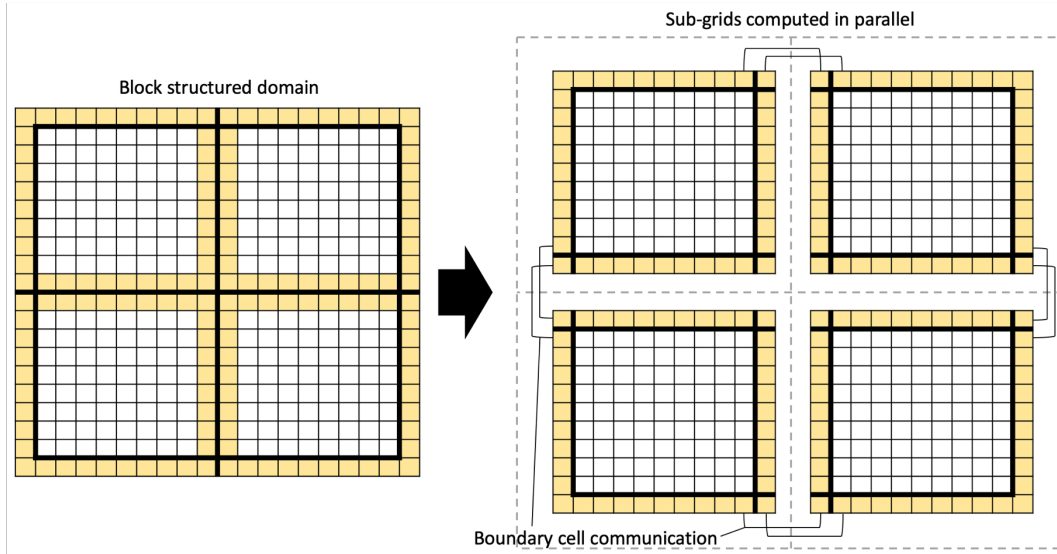


Fig. 4.5 Block structured domain subdivided into sub-grids which retain ghost cells ($nG = 1$) populated via boundary cell communication, such that the sub-grids can be computed in parallel across nodes.

Since the domain can be subdivided into very many blocks, this renders the approach highly scalable, whereby the system can be parallelised across as many computing nodes as are available. Parallel computation is handled via Message Passing Interface (MPI). Speed-up is not directly proportional to the number of subdivided blocks, since some overhead is associated with the message passing between blocks.

Additionally, geometry boundary cells are always tagged for refinement to ensure maximum resolution along the body surfaces.

4.3 Numerical methods for inviscid compressible flows

Now that the AMReX framework is described as the “book shelf” structure to house the core numerical methods, the central theory of selected flux solvers is detailed. Explanations of the base theory are important for informing the extensions made to standard solvers, and the new tailoring required for the combination of numerical methods and meshing framework.

4.3.1 Riemann solvers and finite volume methods

While the differential form of the equations hold over smooth solutions, flow features such as shock and contact waves present as property discontinuities. In order to capture these discontinuities in the solution, the integral form of the conservation equations must be considered. The integral form is applied locally over each discrete cell, given in 1-dimension as $v = [x_{i-1/2}, x_{i+1/2}] \times [t^n, t^{n+1}]$ which has equivalent area: $\Delta x \times \Delta t$. This defines a finite volume method.

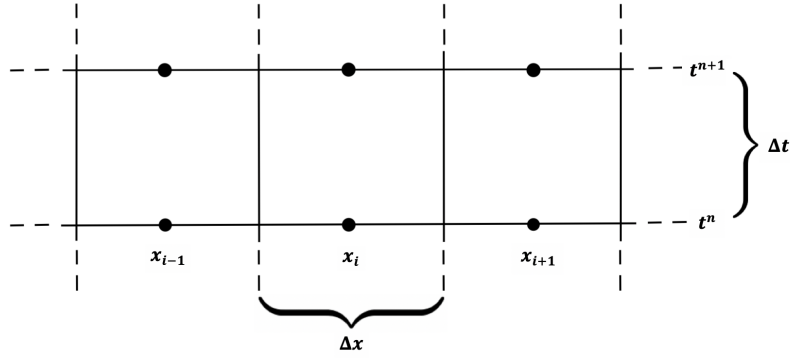


Fig. 4.6 Finite volume discretisation with one spatial dimensional and one temporal axis.

The construction of a finite volume method can be considered naturally as defining a set of Riemann problems. A Riemann problem is defined by (1) an initial value problem described by piecewise constant data with a single discontinuity at the cell boundary, and (2) conservation equations are applied across the cell boundary. In this way, every cell boundary in the domain defines a local Riemann problem between the cell-centred piecewise discontinuous state data.

Where the governing system of Euler conservation equations can be written for the one dimensional case as:

$$\mathbf{U}_t + \mathbf{F}(\mathbf{U})_x = \mathbf{0} \quad (4.1)$$

The integral form of equations applied over the defined finite volume can be equated to a surface integral via Green's theorem:

$$\int_v \frac{\partial \mathbf{U}}{\partial t} + \frac{\partial \mathbf{F}}{\partial x} dx dt = \oint_S \mathbf{U} dx - \mathbf{F} dt = 0 \quad (4.2)$$

Applied to the boundary of the finite volume, we obtain:

$$\int_{x_{i-1/2}}^{x_{i+1/2}} \mathbf{U}(t^{n+1}, x) dx - \int_{x_{i-1/2}}^{x_{i+1/2}} \mathbf{U}(t^n, x) dx = \int_{t^n}^{t^{n+1}} \mathbf{F}(t, x_{i-1/2}) dt - \int_{t^n}^{t^{n+1}} \mathbf{F}(t, x_{i+1/2}) dt \quad (4.3)$$

For the conserved variables of \mathbf{U} , in one dimensional space, the integral average quantity is defined as:

$$\mathbf{U}_i^n = \frac{1}{\Delta x} \int_{x_{i-1/2}}^{x_{i+1/2}} \mathbf{U}(x, t^n) dx \quad (4.4)$$

Similarly the flux vectors $\mathbf{F}_{i\pm 1/2}$ are defined as the integral average of the flux over one time-step:

$$\mathbf{F}_{i\pm 1/2} = \frac{1}{\Delta t} \int_{t^n}^{t^{n+1}} \mathbf{F}(\mathbf{U}(x_{i\pm 1/2}, t)) dt \quad (4.5)$$

With these integral average definitions we arrive at the conservative numerical update formula:

$$\mathbf{U}_i^{n+1} = \mathbf{U}_i^n + \frac{\Delta t}{\Delta x} (\mathbf{F}_{i-1/2} - \mathbf{F}_{i+1/2}) \quad (4.6)$$

Godunov's method considers the integral average flux in terms of a forward Euler method step where the flux's are calculated at every cell spatial boundary from the properties at time step n :

$$\int_{t^n}^{t^{n+1}} \mathbf{F}(t, x_{i-1/2}) dt \approx \Delta t \mathbf{F}(U_{i-1}^n, U_i^n) \quad (4.7)$$

The Godunov flux therefore requires the exact or approximate solution of the local Riemann problem, capturing the physical behaviour of the system by resolving the discontinuity at the interface as a superposition of waves.

It is clear from this time-explicit numerical update formula how all subsequent time solutions evolve from given initial data (\mathbf{U}^0). However, the solution will evolve to become numerically *unstable* unless certain criteria are met. The Courant-Friedrichs-Lewy (CFL) condition must hold (necessary, but not always sufficient) for the simulation to evolve in a stable manner. For the simplest 1D Euler system, this is derived as:

$$\Delta t = \frac{CFL \cdot \Delta x}{S_{max}} \quad (4.8)$$

The CFL condition places a restriction on the time-step Δt such that waves emanating from neighbouring interfaces do not interact within the local computational cell. The maximum global time-step is therefore limited based on the minimum Δt as a function of the distance between adjacent cells (Δx) and the propagation speed of the fastest wave (S_{max}).

4.3.2 HLL and HLLC approximate Riemann solvers

All mathematical models defined in Chapter 2 have, as a basis, the Euler equations. Therefore, the solution of inviscid fluxes which comprise the hyperbolic system dynamics is the foundation to all of the numerical models. Here numerical methods are defined to solve the 1D Euler equations (which can be straightforwardly extended to 2D).

While there is no exact closed-form solution to the Riemann problem for the Euler equations, it is possible to formulate iterative schemes which converge to within a desired tolerance. Such schemes are nonetheless termed *exact solvers*. An exact solver could certainly be implemented for this problem, however, the requirement for reasonable initial guesses, and iterative procedures operating upon the guessed state, adds considerable computational

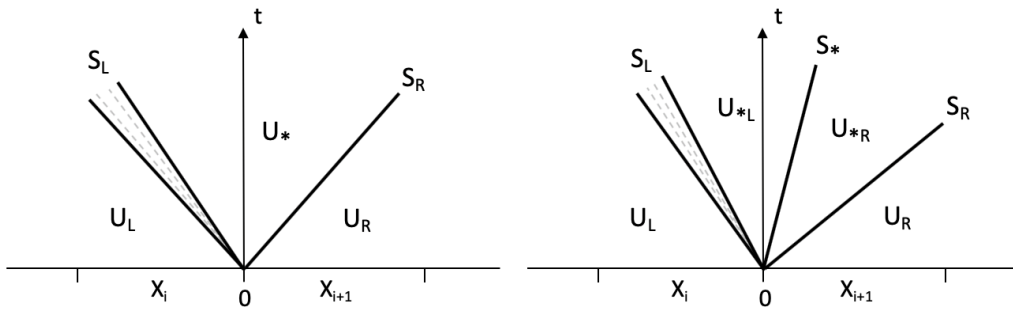


Fig. 4.7 Assumed two-wave and three-wave configuration for HLL and HLLC methods respectively. Constant states are separated in x - t space by computed wave speeds S_L , S_R , and S_* . The left and right waves may be a shock wave or a rarefaction wave, whereas the centre HLLC wave is always a contact wave.

cost, especially for large hydrodynamic codes where solution of the local Riemann problem is called for every cell at every time step, making it the single most demanding operation of the numerical method.

Therefore a more efficient alternative is the use of approximate-state Riemann solvers. The approximate approach over the exact approach has been selected for this work due to the efficiency gain. Some popular choices include the Roe Solver (which assumes a linearisation of the Jacobian, which is then solved exactly), and the HLLE solver (assumes largest and smallest signal velocities at the interface). This work implements the HLLC solver due to the desirable properties: robustness (including in the cases of strong shocks and rarefactions), high efficiency, and complete-wave capturing.

The central idea of the family of HLL approximate Riemann solvers is to assume a wave configuration, whereby the wave speeds are given by estimates, and then numerical inter-cell fluxes are computed directly as closed formed expressions from the conservation laws. The HLL solver first proposed by Harten Lax and van Leer [128] assumes a two-wave configuration - the minimum and maximum speed waves. The HLLC solver (proposed by Toro [16]) is an extension of the HLL solver in that it additionally captures the intermediate contact wave in the solution. The assumed wave configurations are depicted in Figure 4.7.

In generating the solution, we are evolving the conserved variables in \mathbf{U} using the explicit conservative update formula of equation (4.6), where $\mathbf{F}_{i+1/2} = \mathbf{F}(\mathbf{U}_{i+1/2}(0))$ is the Godunov intercell numerical flux, for which an approximation is obtained directly.

The wave speeds S_L and S_R are computed as the minimum and maximum cases ie. $S_L = \min\{u_L - a_L, u_R - a_R\}$ and $S_R = \max\{u_L + a_L, u_R + a_R\}$. The *star region* (as represented in Figure 4.7), consists of a single intermediate state for the HLL solver. The intercell numerical flux at $x_{i+1/2}$ is computed as:

$$\mathbf{F}_{i+1/2}^{HLL} = \begin{cases} \mathbf{F}_L, & \text{if } 0 \leq S_L \\ \mathbf{F}_*^{HLL}, & \text{if } S_L < 0 \leq S_R \\ \mathbf{F}_R, & \text{if } S_R < 0 \end{cases} \quad (4.9)$$

where the star state flux is given by:

$$\mathbf{F}_*^{HLL} = \frac{S_R \mathbf{F}_L - S_L \mathbf{F}_R + S_L S_R (\mathbf{U}_R - \mathbf{U}_L)}{S_R - S_L} \quad (4.10)$$

The HLLC method extends the construction to a three wave model (2 shock or rarefaction waves with intermediate contact wave) separating 4 constant states, where pressure and velocity are constant across the contact wave separating the left and right star states. Figure 4.7 illustrates the 3-wave solution fan.

The equation for the contact wave speed S_* is derived under the constant pressure (across contact) assumption and given by:

$$S_* = \frac{p_R - p_L + \rho_L u_L (S_L - u_L) - \rho_R u_R (S_R - u_R)}{\rho_L (S_L - u_L) - \rho_R (S_R - u_R)} \quad (4.11)$$

Having computed the 3 wave velocities S_L , S_R and S_* , star states U_{*L} , U_{*R} and star state fluxes F_{*L} , F_{*R} are computed via algebraic manipulations of the Rankine-Hugoniot conditions. Where the subscript K denotes left or right evaluations, the star states are given by:

$$\mathbf{U}_{*K} = \left(\frac{S_K - u_K}{S_K - S_*} \right) \begin{bmatrix} \rho_K \\ \rho_K S_* \\ E_K + \rho_K (S_* - u_K) \left[S_* + \frac{p_K}{\rho_K (S_K - u_K)} \right] \end{bmatrix} \quad (4.12)$$

Then the star state fluxes are:

$$\mathbf{F}_{*K} = \mathbf{F}_K + S_K (\mathbf{U}_{*K} - \mathbf{U}_K) \quad (4.13)$$

Based on the sound speeds computed in the local Riemann problem solution fan, the approximate inter-cell flux is computed such that:

$$\mathbf{F}_{i+1/2}^{HLLC} = \begin{cases} \mathbf{F}_L, & \text{if } 0 \leq S_L \\ \mathbf{F}_{*L}, & \text{if } S_L < 0 \leq S_* \\ \mathbf{F}_{*R}, & \text{if } S_* < 0 \leq S_R \\ \mathbf{F}_R, & \text{if } S_R < 0 \end{cases} \quad (4.14)$$

For the full derivations please, refer to Toro [16].

4.3.3 High resolution extension

High resolution methods aim to satisfy the contradictory requirements: second (or higher) order accuracy, and the absence of spurious oscillations in the vicinity of large gradients. A high resolution method should also render discontinuities sharply (over very few cells), and exhibit non-linear stability whereby convergence is achieved as the grid is refined.

The true solution of the system of Euler-based equations in conservative form is total variation diminishing (TVD), and so it is also desirable that the numerical method produce a solution which also exhibits the TVD property. A TVD method prevents unbounded growth of oscillations, a potential form of instability associated with higher order methods (though mild spurious oscillations may still be present).

The first order Godunov-type HLLC solver can be extended to second order by implementing a flux or slope limiter form of extension satisfying the TVD property. Whilst there are many possible choices for the high-resolution extension, a slope-limited MUSCL-Hancock scheme was selected.

The MUSCL (Monotone Upstream-centred Scheme for Conservation Laws) is a development of Van Leer's proposal to generate higher order methods by linearly reconstructing the piecewise constant data of the solution.

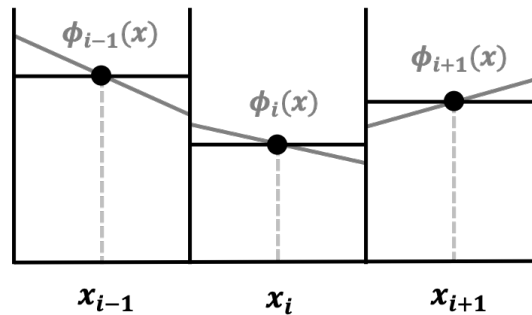


Fig. 4.8 The linear reconstruction is performed by replacing constant state variables ϕ_n^i by piecewise linear functions $\phi_i^n(x)$.

The MUSCL-Hancock extension involves three key steps in order to construct a fully discrete, second order accurate (in time and in space) scheme:

1. Data reconstruction:

$$\mathbf{U}_i^L = \mathbf{U}_i^n - \frac{1}{2}\Delta i, \quad \mathbf{U}_i^R = \mathbf{U}_i^n + \frac{1}{2}\Delta i$$

where:

$$\Delta i = \frac{1}{2}(1 + \omega)(\mathbf{U}_i^n - \mathbf{U}_{i-1}^n) + \frac{1}{2}(1 - \omega)(\mathbf{U}_{i+1}^n - \mathbf{U}_i^n)$$

$$\omega \in [-1, 1]$$

2. Evolution of \mathbf{U}_L and \mathbf{U}_R by a half time step:

$$\begin{aligned}\bar{\mathbf{U}}_L^{n+1} &= \mathbf{U}_i^L + \frac{1}{2} \frac{\Delta t}{\Delta x} (\mathbf{F}(\mathbf{U}_i^L) - \mathbf{F}(\mathbf{U}_i^R)) \\ \bar{\mathbf{U}}_R^{n+1} &= \mathbf{U}_i^R + \frac{1}{2} \frac{\Delta t}{\Delta x} (\mathbf{F}(\mathbf{U}_i^L) - \mathbf{F}(\mathbf{U}_i^R))\end{aligned}$$

3. Solution of the piecewise stepped Riemann problem with $\bar{\mathbf{U}}_L$ and $\bar{\mathbf{U}}_R$ using the HLLC solver.

To eliminate spurious oscillations in the new second order construction, and to achieve the TVD solution property, the slopes Δi are replaced by limited slopes, with a choice of slope limiting scheme $\xi_i(r)$:

$$\bar{\Delta}_i = \xi_i(r) \Delta_i \quad (4.15)$$

where r is the ratio of adjacent property slopes. There are a number of potential slope limiter schemes ($\xi_i(r)$) to choose from, including ‘‘Super-bee’’, ‘‘Min-bee’’, ‘‘van-Leer’’ and ‘‘Ultra-bee’’. Min-bee and van-Leer are more diffusive in the region of solution discontinuities, however Super-bee and Ultra-bee may retain some mild spurious oscillations.

Higher order methods (3^{rd} or 4^{th} order) could also be selected, however there is again an accuracy-efficiency trade-off to be made. 2^{nd} order in combination with the efficient high resolution meshing method offered by the AMReX framework, is considered to achieve a good balance between accuracy and efficiency.

4.3.4 Numerical solution strategy

The numerical solution strategy for the 2D cylindrical-coordinate form of the Euler base model described in section 2.3.4 is via a dimensionally-split and operator-split approach.

In two-dimensions the full system is replaced by a coupled pair of one-dimensional IVP’s:

$$\text{PDE 1: } \frac{\partial \mathbf{U}}{\partial t} + \frac{\partial \mathbf{F}}{\partial r} = 0, \text{ IC: } \mathbf{U}^n \quad (4.16)$$

$$\text{PDE 2: } \frac{\partial \mathbf{U}}{\partial t} + \frac{\partial \mathbf{G}}{\partial z} = 0, \text{ IC: } \mathbf{U}^{n+1/2} \quad (4.17)$$

Which is solved in terms of this pair of conservative numerical updates:

$$\mathbf{U}^{n+1/2} = \mathbf{U}^n + \frac{\Delta t}{\Delta r} (\mathbf{F}_{i+1/2} - \mathbf{F}_{i-1/2}) \quad (4.18)$$

$$\mathbf{U}^{n+1} = \mathbf{U}^{n+1/2} + \frac{\Delta t}{\Delta z} (\mathbf{G}_{i+1/2} - \mathbf{G}_{i-1/2}) \quad (4.19)$$

where the state $\mathbf{U}^{n+1/2}$ has been used as initial conditions to compute the \mathbf{G} flux terms in the second dimensional sweep. We denote this pair of hyperbolic flux update by the operator: $H_{\Delta t}(\mathbf{U}^n)$

The solution preserves second order accuracy in space and time, and is stable in two-dimensions with a $CFL \leq 1$.

In order to implement the cylindrical source term integration in a way which also preserves second order accuracy, a three-step Strang splitting approach is adopted. Whereby the hyperbolic update of the previous step is denoted $H_{\Delta t}$, the total conservative variable update is performed via the three step update:

$$\mathbf{U}^{n+1} = S_{\Delta t/2}^c H_{\Delta t} S_{\Delta t/2}^c \mathbf{U}^n \quad (4.20)$$

where $S_{\Delta t/2}^c$ denotes the cylindrical source term integration via a simple Euler half time step:

$$S_{\Delta t/2}^c(\mathbf{U}^n) = \mathbf{U}^n + \frac{\Delta t}{2} \mathbf{S}^c \quad (4.21)$$

The numerical methods described thus far, are sufficient for solving supersonic, inviscid fluid test cases, embedded within the the AMReX framework, which adaptively refines over property gradients. A selection of test cases to validate this base solver implementation is presented in section 5.1.

To move from simple fluid-only test cases, to useful tests which contain vehicle bodies, a geometry implementation is required.

4.4 Embedded boundaries and the Ghost Fluid Method

In relation to standard CFD codes, geometry is commonly employed via structured body-fitted meshes [129], whereby the computational grid aligns with the edge of the defined geometry, and wall boundary conditions are simply applied at the row of cells along the body. In terms of the atmospheric reentry literature, almost all studies apply a body fitted mesh, such as those shown in Figure 4.9. While this works well for very simple geometries (e.g. smooth spheres and curves), geometry which becomes more complex results in skewing and distortion of the body-fitted mesh. For many geometries - for example, those which consist of sharp corners and edges - a body fitted mesh becomes too distorted, leading to untenable numerical error.

As per the discussion in section 4.2, adoption of a structured Cartesian mesh offers many advantages. Since the structured mesh discretises the full rectangular domain, the geometry must therefore be embedded. Immersed or embedded boundary (EB) methods provide an efficient and effective way of simulating flow over arbitrary shaped bodies.

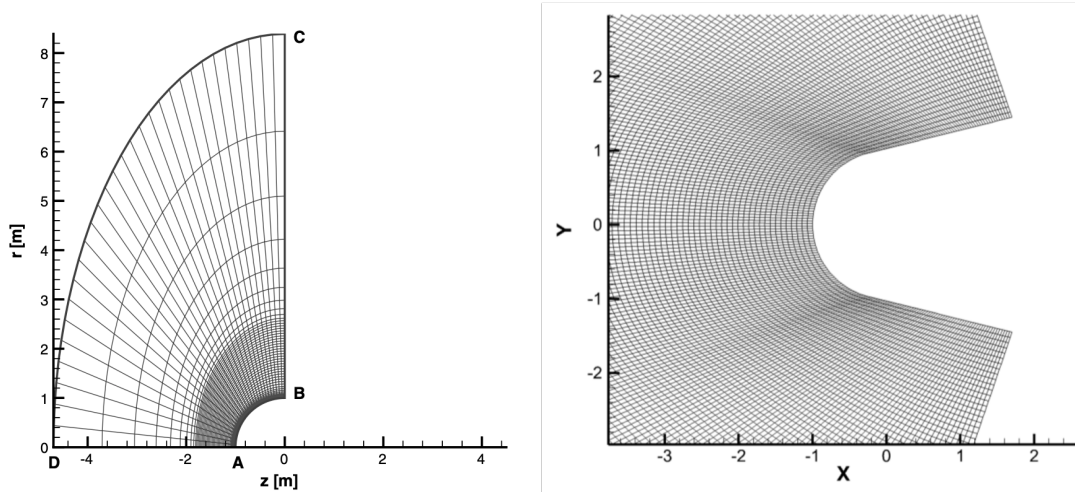


Fig. 4.9 Body-fitted computational meshes used in the spherical body re-entry simulations: left) Otsu & Abe [9], and right) Dias & Xisto [15]

In recent years there has been an increased prevalence of EB-based flow solvers due to the ease of grid generation and efficacy in simulating problems involving complex geometries [130]. Such methods are suitable for simulating both a fluid-fluid or fluid-solid interface. An EB based method also has the advantage of retaining a sharp interface representation, as compared with the diffused boundary of a Volume of Fluid (VOF) method (references for VOF method). A sharp interface representation is a pragmatic choice for any fluid-solid interface which does not significantly deform over the duration of simulation.

Treatment of a sharp interface solid-fluid boundary can be considered in terms of whole cells or cut-cells. Early developments on cut-cell boundary methods within a regular Cartesian mesh were made by Colella *et. al.* [131] and Hu *et. al.* [132]. Their work has been more recently extended to dimensionally split methods with moving boundaries by Bennett *et. al.* [133] with substantial advances in cut-cell methods for complex geometries with inviscid and viscous flows made by Gokhale *et. al.* [41, 134] in 2018. Both whole-cell and cut-cell methods for Cartesian methods are able to be implemented with adaptive hierarchical AMR, facilitating a high degree of efficiency and parallelism, as demonstrated by the recent works of Sverdrup *et. al.* [88] and Yamashita *et. al.* [135].

In terms of the application of EB based methods to high speed compressible flows, the earliest foundational work which treated boundary cells as whole cells, within a regular cartesian grid, was by Forrer and Jeltsch [136] which considered an immersed stationary cylinder and airfoil. The major difficulty posed by whole-cell EB based methods is the treatment of the boundary-intersected cell in imposing the solid-body boundary conditions. Brahmachary *et. al.* [130] and de Tullio *et. al.* [137] both consider high-speed compressible flow problems and apply an inverse distance weighting function to create a fluid reconstruction within the immersed boundary cell.

A whole cell approach has advantages in its simplicity and efficiency, provided that accuracy can be ensured by: sufficient resolution at the boundary (this can be aided by multiple AMR levels at the boundary), in combination with a sufficiently advanced boundary treatment. This work therefore combines a whole cell embedded boundary construction, with a rigid body Ghost Fluid Method (GFM).

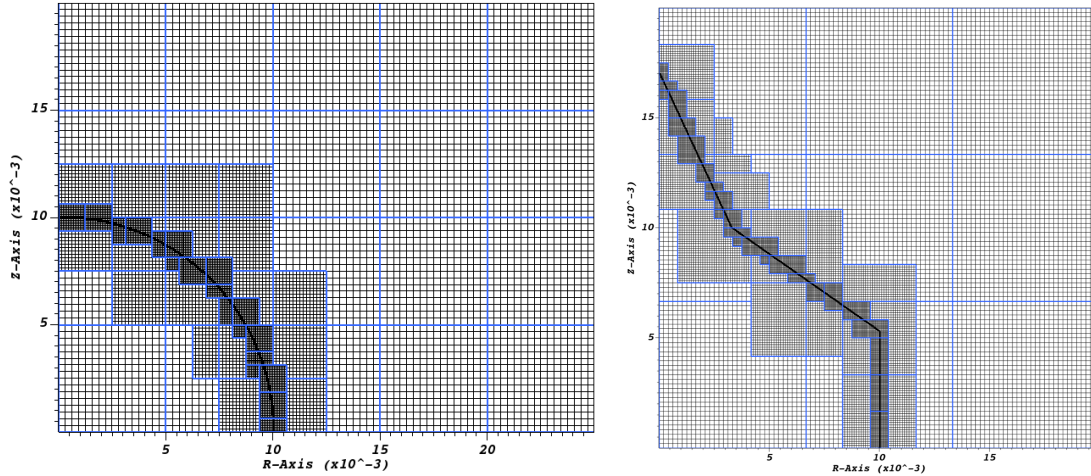


Fig. 4.10 Cartesian mesh configuration with two levels of hierarchical AMR. Blue borders show subdivision of the domain into ‘blocks’ which can be computed in parallel.

The very high velocity impact and interaction of the fluid with an embedded boundary - especially in reentry simulations - presents challenges for all compressible embedded boundary methods. Sambasivan and UdayKumar [18] reviewed the performance of GFM based approaches (first proposed by Fedkiw et al. [138]). They found that reflective boundary conditions used in conjunction with a Riemann Solver at the boundary was stable, accurate and robust for a wide range of problems involving strong shocks interacting with embedded solid objects. As such, for this work, a rigid body GFM method is employed, suitable for the simulation of supersonic flows over arbitrarily complex geometries, for implementation on an adaptive Cartesian mesh.

Example embedded geometries defined in the Cartesian AMR meshes of this work are shown in Figure 4.10.

4.4.1 Formulation

The implementation of the rigid body GFM is somewhat simpler than the original fluid-fluid GFM. Since the ghost cells of the rigid body can be treated as an extension of a single fluid type (governed by a singular EoS - be that ideal or plasma19X), the entropy preserving extrapolation to calculate ghost fluid ρ trivially reduces to a direct extrapolation of ρ from the fluid region. The core aspect of a 2D rigid body GFM is an accurate and efficient boundary condition extrapolation and construction. The specific implementation adopted for this work can be summarised as follows:

1. Construct a two-dimensional level set function throughout the domain where $\phi(x, y)$ is the signed shortest distance to the embedded interface:

$$\phi(x, y) = \begin{cases} = 0, & \text{at interface} \\ < 0, & \text{within the interface} \\ > 0, & \text{outside of the interface} \end{cases} \quad (4.22)$$

2. Compute the normal vectors relative to the geometry surface throughout the domain. Where the normals can be computed from the gradient of the level set function:

$$\hat{\mathbf{n}} = (\hat{n}_x, \hat{n}_y) = \frac{\nabla\phi}{|\nabla\phi|} \quad (4.23)$$

3. Boundary cell identification:

- 3a) Using the analytic definition of the embedded boundary location (as tracked through the level set function values in each cell), identify all cells ‘cut’ by the EB
- 3b) Conducting an x-sweep and a y-sweep, identify pairs of neighbouring cells where the cell centre can be identified as a solid ($\phi \leq 0$) and a fluid ($\phi > 0$)

4. Corresponding boundary state construction:

- 4a) In the identified solid interior boundary cells, compute the primitive variable properties using a ‘probe method’. The probe method identifies a sample point, a short distance (taken to be 1-2 times the cell hypotenuse, such that the probe reaches the fluid region) along the normal direction from the body, into the fluid. A mixture property value is computed using bilinear interpolation of the 4 cell centres enclosing the precise sample point. This mixture value is copied into its associated boundary cell. This concept is represented by the diagram of Figure 4.11.
- 4b) From each boundary cell, stepping along the x-axis and y-axis corresponding to the sign of the normal: $\mathbf{sign}(\hat{n}_x, \hat{n}_y)$, to identify the first-most neighbouring fluid cell. In the case of x-only or y-only neighbours, translate the properties. In the case of x – y neighbours, compute the bilinearly weighted mixture value based on distances from boundary cell centre to fluid cell centres.

5. In the identified boundary cells, reflect the velocities where the normal velocity is reversed and the *slip condition* is applied such that the tangential velocity is retained. The velocity transformation can be computed in Cartesian coordinates via:

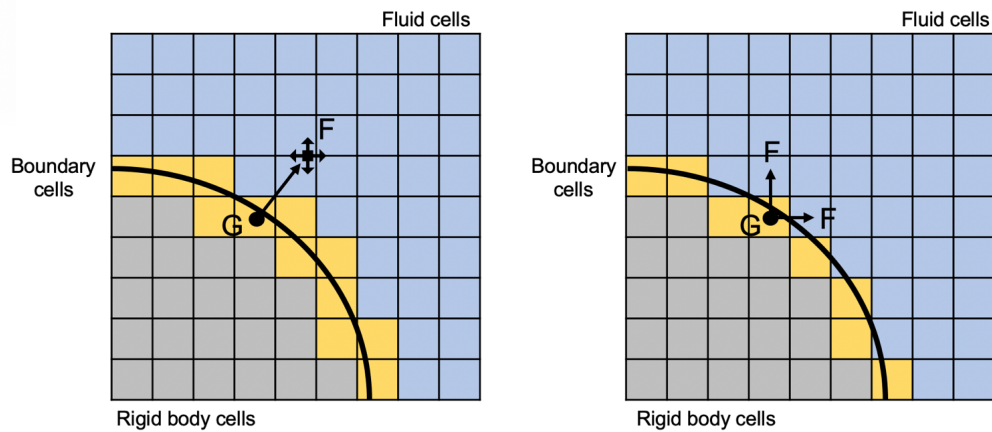


Fig. 4.11 Two methods of fluid, boundary and rigid body cell identification. Left) The fluid sample point, denoted F , is determined from a projection from the cell normal, where bilinear interpolation of surrounding cells determines the mixture value, and is copied into boundary cell G . Right) left and right bordering fluid cells are identified, and bilinearly interpolated mixture value again copied to G .

$$\tilde{\mathbf{v}}_i = \mathbf{v}_i - 2(\hat{\mathbf{n}}_i \cdot \mathbf{v}_i)\hat{\mathbf{n}}_i \quad (4.24)$$

- An extension to the described rigid body GFM (as proposed in [18]) is to reconstruct the interface by populating boundary ghost cells with the star state ($*$) of the Riemann solver, then computing fluxes using the star state as the boundary fluid state. This extension is important for ameliorating the known numerical artefact of wall heating (corresponding to density reduction near a shock-impacted surface).

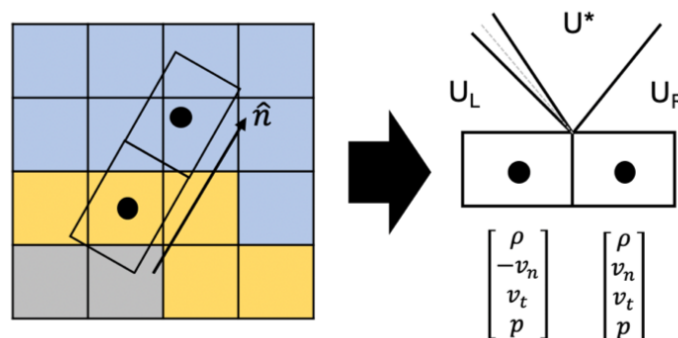


Fig. 4.12 Riemann based GFM: 1D problem constructed along the normal direction of the local problem geometry, with U^* subsequently substituted (transformed back to x - y coordinates) into the boundary cell. Effective slip-boundary condition property state vectors are shown for the normal-tangential coordinate system in which the Riemann problem is solved.

By reconstructing the Riemann problem in the local normal-tangential coordinate system at the embedded boundary, a 1D Riemann problem can be solved, then the 1D HLL \mathbf{U}^* state is computed, transformed back to the global Cartesian coordinate system, and substituted as the boundary cell state.

7. The solid interior region is populated via a two-dimensional linear extrapolation. This is a first order finite difference solution of the PDE:

$$H(\phi)\hat{\mathbf{n}} \cdot \nabla q = 0 \quad (4.25)$$

where q is any primitive variable, and $H(\phi)$ is a unit Heaviside function, defined:

$$H(\phi) = \begin{cases} 1, & \phi \leq 0 \\ 0, & \phi > 0 \end{cases} \quad (4.26)$$

The first order stencil is therefore given by:

$$\tilde{q}_{i,j} = \frac{n_{i,j}^x q_{i,j}^x / \Delta x + n_{i,j}^y q_{i,j}^y / \Delta y}{n_{i,j}^x / \Delta x + n_{i,j}^y / \Delta y} \quad (4.27)$$

where $q_{i,j}^x$ and $q_{i,j}^y$ are ‘upwinded’ as determined by the level set normals:

$$q_{i,j}^x = \begin{cases} q_{i-1,j}^x, & \text{if } n_{i,j}^x \geq 0 \\ q_{i+1,j}^x, & \text{if } n_{i,j}^x \leq 0 \end{cases} \quad (4.28)$$

$$q_{i,j}^y = \begin{cases} q_{i,j-1}^y, & \text{if } n_{i,j}^y \geq 0 \\ q_{i,j+1}^y, & \text{if } n_{i,j}^y \leq 0 \end{cases} \quad (4.29)$$

Complete linear extrapolation requires 4 directional sweeps applying the equation 4.27 stencil.

In a first order solver, only the first band of internal rigid body ghost fluid cells will contribute to the flow solution, and similarly for an n-order method, n internal cells ghost cells are necessary. For generality and since it is not overly costly, the entire rigid body region is populated as ghost cells.

This formulation is amenable to be paired with any fluid dynamics solver and any consistent equation of state (same EoS applied to the fluid as the ghost cells). The rigid body GFM is constructed at the start of every global fluid dynamic time step, such that fluxes are computed based on present-state fluid properties and GFM constructed boundary cell states.

The part (b) steps of the above construction (3b and 4b) were not the default implementation as per Sambasivan [18], but were introduced as more effective ways to handle complex geometries with acute angles. Part (a) would sometimes fail if the user defined probe length did not exceed the boundary cell region, or projected back into the interior of the defined geometry (occurring in cases of sharp leading edges or concave boundaries). Problem-specific adjustment of probe length can resolve the error, however this introduces a undesirable degree of empiricism and manual involvement. The proposed part (b) alternative is found to be more robust and general since it guarantees the identification of a neighbouring fluid cell for boundary reconstruction, without any problem-specific settings.

The Riemann GFM extension to the solver is particularly important for the hypervelocity test cases of interest in this work, which otherwise produce significant wall-heating errors without such reconstruction.

4.5 Hypersonically stable solver

4.5.1 In the literature

Extreme hypersonic flows, and their interactions with solid bodies, are known to test the limits of numerical compressible flow solvers. Complete wave Riemann solvers, such as the HLLC (and additionally HLLEM, HLLE+ and HLLEMS) are popular for their ability to capture the contact and shear waves of the Euler system. However, complete wave Riemann solvers are susceptible to various instability manifestations.

Under the umbrella of “Carbuncle phenomena”, there exists: the moving shock instability, the standing shock instability (including odd-even decoupling) and the kinked Mach stem. Quirk [139] and Liou [140] who have conducted analysis on the origins of the instability highlight that in all cases, the instability is related to a perturbation transfer in the transverse direction of a strong shock. Interestingly, although the oscillation does not occur in real fluid flows, it may not be *theoretically unphysical*.

Studies [141] suggest that the instability is not of purely numerical genealogy, but rather, may rightfully resolve an internal instability mechanism of the Euler equations. That is, under the assumption of zero viscosity within the Euler equations, it is theorised that an unstable oscillatory mode can be activated for high Mach number normal shocks. For this reason, even the exact Riemann solver is not immune to emergence of instabilities.

Several methods have been investigated to suppress the instability, with varying degrees of success. Perfect mitigation (without solution degradation) remains illusive, with Van Leer stating that the carbuncle phenomenon is considered “the greatest unresolved problem of classical finite-volume schemes” [142].

Quirk’s work concludes that a method based upon a single complete-wave Riemann solver is inescapably fallible when it comes to shock instability. Incomplete-wave type solvers

(HLL, HLLE, HLLS) however, do not succumb to shock instability owing to the more diffuse resolution of the centre contact. Quirk therefore recommended hybrid or combination solvers. The aim of the game is to allow the more numerically diffuse contact resolution of the incomplete-wave solver to cure the instability in regions very close to the strong shock, without compromising on the complete and sharp resolution of flow behaviour elsewhere. One might consider this to be a special case where numerical diffusivity in fact aligns the approximated solution *more closely* with the physical: in this case numerical diffusivity acts in the same way as physical viscosity, suppressing the shock aligned instability.

Investigative numerical studies demonstrate that the instability is highly sensitive to:

- Mach number
- spatial resolution
- cell aspect ratio
- normal shock alignment relative to the grid
- numerical solver type
- order of accuracy and extension type (ie. slope or flux limiter)

These instabilities are known to manifest both for transient flow problems and those which approach a steady state.

Combination solvers have been developed by Kim *et. al* [80] and Shen *et al* [143] where pressure based or flux based shock detection sensors are utilised to switch between two solvers in a binary manner. That is, in any given region either the diffusive or contact preserving scheme is ‘switched on’. The switching conditions are defined internally based on a fixed tolerance.

It is noted in Tramel’s study [144] that binary switching between schemes causes too abrupt of a transition between fluxes, resulting in other numerical errors. Tramel instead proposes the HLLE++ method which introduces a more progressive switching function which blends the computed eigenvalues of the HLLE solver, and the more dissipative Roe solver. However the switching function involves a user defined tuning parameter (*ALPHA*) which is varied from 1-10 depending on the problem. Similarly, Sangeeth & Mandal [145] proposed a method termed ‘Selective Wave Modification’ whereby the HLLC flux star state is deconstructed into a base component, a diffusing term and an anti-diffusive term. Using a form of grid aligned based shock-sensing, the diffusing term is amplified in shock-detected regions, thereby not switching in a binary matter, and retaining a construction of a contact wave via so called ‘anti-diffusion control’. This method however is still heavily reliant on a tuning parameter α which weights the degree of amplification of the diffusive component. The value of α is important in determining the success and suitability of the method. The value is problem specific and a suggested heuristic is offered based on free

stream Mach number for a given test case (not necessarily straightforward for more complex and interacting wave structures). Therefore, like HLLC++, this method faces challenges in its generalisation and requires a degree of manual parameter setting and judgement, which influences its efficacy.

In this work simple alterations to the previous methods are proposed. The approach taken is based on the construction of a local and continuous linear combination of the complete-wave HLLC and incomplete-wave HLL intermediate star states (ie. retains improved contact wave construction as compared to binary switching method), with an alternative grid-aligned shock strength detection method. The grid aligned shock strength detection is incorporated into a new internal weighting function for the flux combination such that the method is liberated from tuning parameters and exhibits high accuracy and generalised performance as demonstrated across several test problems of varying Mach number and geometry. The flux reconstructions are applied only for the transverse wave solutions with respect to the strong normal shock direction, therefore also retaining flux solution given by the complete wave solver across the span of shock waves. The new detection and weighting methods are specifically designed with AMR in mind, such that ‘Carbuncle susceptibility’ is controlled for inherently and globally with consideration of varying cell size through the domain. The method constructed for this work is denoted HLLC-HS (**h**ypersonic **s**tabilisation).

4.5.2 Proposed formulation

The proposed HLLC-HS solver uses a weighted combination of HLLC and HLL intermediate state fluxes in a way which retains full resolution of physical contact waves through the domain, and which controls for shock instability automatically and with consideration of varying cell sizes within an AMR framework.

Sangeeth & Mandel’s HLLC-SWM method requires a tuning parameter α which amplifies diffusivity and is required to be set manually to a higher value for a test problem with higher free stream Mach number. In the HLLC-HS approach the tuning parameter is bypassed by defining the weighting parameter ω to internally account for the interacting effects of local Mach number *and* shock proximity, which are both known to effect instability susceptibility. While both methods use a shock detection method to amplify/diminish transverse contact wave diffusion based on shock proximity, the formulation of ω aims to improve the method by having a *local* and *automatic* tuning parameter, rather than a *global* and *manually* applied α .

The HLLC fluxes for the left and right star states are as defined in the earlier section 4.3.2 and denoted here as \mathbf{F}_*^{HLLC} , \mathbf{F}_*^{HLLC} . The single star state flux for the HLL solver is defined as \mathbf{F}_*^{HLL} .

The HLLC-HS flux is defined simply as:

$$\mathbf{F}^{HLLC-HS} = \begin{cases} \mathbf{FL}, & \text{if } 0 \leq S_L \\ (1 - \omega)\mathbf{FL}_*^{HLLC} + \omega\mathbf{F}_*^{HLL}, & \text{if } S_L < 0 \leq S^* \\ (1 - \omega)\mathbf{FR}_*^{HLLC} + \omega\mathbf{F}_*^{HLL}, & \text{if } S^* < 0 \leq S_R \\ \mathbf{FR}, & \text{if } S_R < 0 \end{cases} \quad (4.30)$$

The weighting parameter ω is defined as follows:

$$\omega_{i,j} = \frac{\frac{\varepsilon_{i,j}}{a_{i,j}}}{1 + \frac{\varepsilon_{i,j}}{a_{i,j}}} \cdot \kappa_{i,j} \quad (4.31)$$

where $\varepsilon_{i,j}$ at the cell located at (i, j) is the maximum normal velocity increment across neighbouring cell boundaries in the direction transverse to the shock alignment. $\kappa_{i,j}$ is an alignment factor computed as the normalised projection of the detected shock along the given grid direction (defined in full below). Therefore the term $\frac{\varepsilon_{i,j}}{a_{i,j}}$ is effectively the increment in local Mach number at cell (i, j) . That is, the velocity increment is computed in the cell-neighbourhood of the shock detection stencils shown in Figure 4.13 and converted to a local change in Mach number based on the acoustic speed of the centre cell state.

Carbuncle effects and instabilities emerge only in two and three spatial dimensions, given the mechanism is associated with *transverse* flux computation. Therefore the remaining work considers the two-dimensional case.

The definition of ε is based on the flux stencil originally proposed by Pandolfi [146]. However, where Pandolfi computes the maximum change in total *wave speed* across cell boundaries in the stencil, here the maximum change in transverse *velocity* is instead computed.

$$\varepsilon_{i,j} = \max(\varepsilon_1, \varepsilon_2, \varepsilon_3, \varepsilon_4) \quad (4.32)$$

and the velocity increments:

$$\varepsilon_k = |\Delta u_{n,k}| \quad (4.33)$$

It is known that the instability worsens for normal shock alignment with grid direction and with cell aspect ratio.

To stabilise the \mathbf{F} flux, we therefore wish to detect strong, grid-aligned shocks with a horizontal alignment (where \mathbf{F} is therefore the transverse direction flux). The horizontally aligned cell interfaces $k=1-4$ are labelled in the **F-stencil** of Figure 4.13. The normal velocity increments $\Delta u_{n,k}$ are computed over these interfaces to determine the local maximum: $\varepsilon_{i,j}^F$.

In order to determine the grid-alignment of the shock, we can similarly calculate $\varepsilon_{i,j}^G$ to detect the vertically aligned shock strength, then the alignment factor κ can be computed as the shock's horizontal projection:

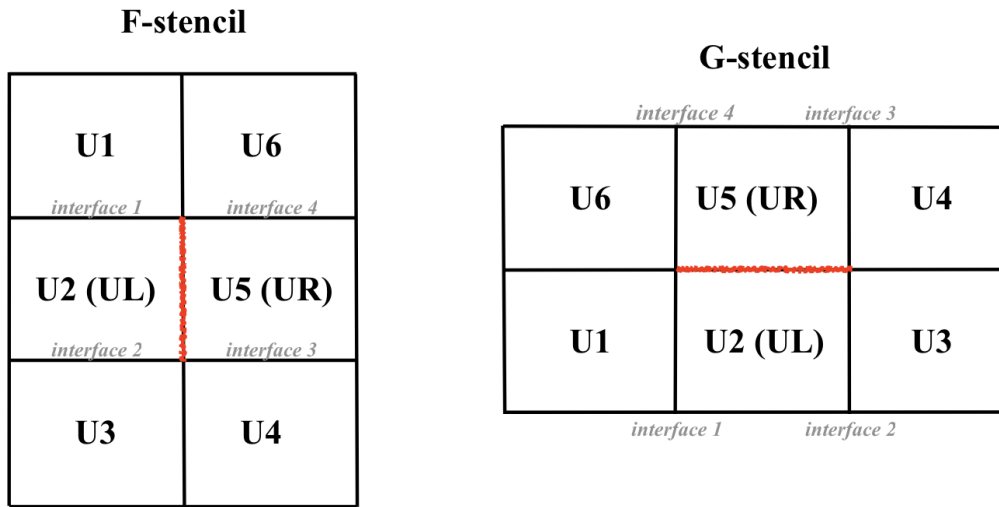


Fig. 4.13 Cell stencil for computed normal velocity increments

$$\kappa_{i,j} = \cos(\theta_{alignment}) = \left| \frac{\epsilon_{i,j}^F}{\sqrt{(\epsilon_{i,j}^F)^2 + (\epsilon_{i,j}^G)^2}} \right| \quad (4.34)$$

This therefore inherently captures the effect of grid aspect ratio since the shock is always captured over an integer number of cells whereas the transverse velocity gradient varies smoothly over space. Importantly, this method works well in an AMR context since all parameters are computed in a local cell neighbourhood, and not ‘switched’ relative to global parameter magnitudes acting across regions of varying cell sizes.

4.5.3 Solver performance

The proposed formulation demonstrates very good generalised performance across a number of key tests known to produce significant instabilities in the hypersonic regime. These results are presented in Chapter 5.

The key points to highlight based on the outlined formulation, is that the construction is liberated from any manual tuning parameters, whilst demonstrating high efficacy on a wide range of tests. Naturally, the solver extension comes at some additional computational cost. This is found to be small - approximately only 0.8-2.0 % slower than the base HLLC solver, however, this is affected by geometry implementation (and the portion of the domain covered by the embedded geometry) as well as the degree to which strong shocks are detected in the domain. On a fluid-only test case (which does not experience Carbuncle instability in the first place) the HLLC-HS solver runs approximately 13% slower than the HLLC solver.

4.6 Numerical methods for compressible Navier-Stokes equations

Collectively, the combination of a compressible Navier-Stokes solver paired with a whole-cell rigid body GFM, implemented within the AMReX framework, presents a new modelling approach.

4.6.1 Computing viscous fluxes

Special care needs to be taken in computing the velocity partial derivatives at the cell interfaces before the flux updates. For cell (i, j) we define the partial derivatives at the $(i - 1/2, j)$ and $(i, j - 1/2)$ interfaces as follows:

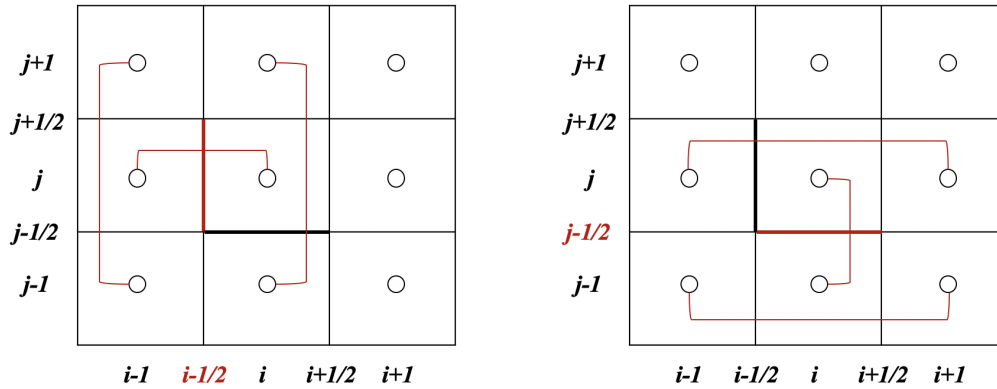


Fig. 4.14 Finite difference stencils for computing the partial derivatives in the viscous flux vectors at cell boundaries.

For the partial derivatives contained in the \mathbf{F}_v viscous flux vector, and evaluated at the $(i - 1/2, j)$ interface, the direct r-directional derivative for a variable ω is simply:

$$\omega_r = \frac{\omega_{i,j} - \omega_{i-1,j}}{\Delta r} \quad (4.35)$$

which is second order accurate and applies to the terms: u_r , v_r , w_r , T_r . Second order accuracy can be achieved in the transverse derivative direction by applying the stencil:

$$\omega_z = \frac{1}{2} \left(\frac{\omega_{i-1,j+1} - \omega_{i-1,j-1}}{2\Delta z} + \frac{\omega_{i,j+1} - \omega_{i,j-1}}{2\Delta z} \right) \quad (4.36)$$

which applies for the terms: u_z , v_z .

Similarly for the $(i, j - 1/2)$ interface, the direct z-directional second order accurate finite difference stencil is given by:

$$\omega_z = \frac{\omega_{i,j} - \omega_{i,j-1}}{\Delta z} \quad (4.37)$$

and used to compute the \mathbf{G}_v flux vector terms: u_z, v_z, w_z . While the transverse direction stencil for the $j - 1/2$ interface becomes:

$$\omega_r = \frac{1}{2} \left(\frac{\omega_{i+1,j} - \omega_{i-1,j}}{2\Delta r} + \frac{\omega_{i+1,j-1} - \omega_{i-1,j-1}}{2\Delta r} \right) \quad (4.38)$$

for: u_r and v_r .

With the inclusion of viscosity comes the physical consideration of the wall-fluid interaction. In a real viscous fluid the molecules closest to the surface are considered ‘stuck’ to the surface. Therefore by asserting a ‘no-slip’ boundary condition, the fluid cells adjacent to the material will have zero velocity relative to the boundary cells. For a ‘no-slip’ boundary condition we assert the following condition:

$$\mathbf{u}_{G,\hat{n}} = -\mathbf{u}_{F,\hat{n}}, \quad \mathbf{u}_{G,\hat{t}} = -\mathbf{u}_{F,\hat{t}} \quad (4.39)$$

where the subscripts G and F denote the ghost cell and fluid cell respectively at the boundary. For \mathbf{u} in Cartesian coordinates, and where \hat{n} and \hat{t} are the normal and tangential directions, this is given by:

$$\mathbf{u}_G = -\mathbf{u}_{F,\hat{n}} \cdot \hat{n} + -\mathbf{u}_{F,\hat{t}} \cdot \hat{t} \quad (4.40)$$

$$u_G = -(un_x + vn_y)n_x + (-un_y + vn_x)n_y \quad (4.41)$$

$$v_G = -(un_x + vn_y)n_y - (-un_y + vn_x)n_x \quad (4.42)$$

As per the prescribed Ghost Fluid Method, the fluid cells (whose properties are transformed into the ghost cell) are taken from a projection along the normals of the level set into the fluid region. The remaining primitive variables are directly copied as per the original GFM.

In the case of viscous fluids, we can consider two different thermal BC assumptions: (1) an adiabatic wall where $\frac{\partial T}{\partial \hat{n}} = 0$ at the wall, or (2) a fixed wall temperature T_w is imposed. The adiabatic wall condition arises naturally through the GFM construction from the direct extrapolation of density and pressure values in the normal direction. The fixed wall temperature boundary condition can be applied by simply setting $T = T_w$ in the internal ghost cells of the GFM. Note that this is applied *only* in the operator split step of computing viscous fluxes. Application to the inviscid flux update would lead to conservation errors and unphysical solutions.

4.6.2 Numerical solution strategy

The divergence of the viscous fluxes is evaluated through a conservative finite volume update, much like the hyperbolic flux update. It is therefore important that the terms of the viscous

flux vector are evaluated at the cell interfaces, leading to the dimensionally split update scheme:

$$\mathbf{U}^{n+1/2} = \mathbf{U}^n + \frac{\Delta t}{\Delta r} (\mathbf{F}v_{i+1/2} - \mathbf{F}v_{i-1/2}) \quad (4.43)$$

$$\mathbf{U}^{n+1} = \mathbf{U}^{n+1/2} + \frac{\Delta t}{\Delta z} (\mathbf{G}v_{i+1/2} - \mathbf{G}v_{i-1/2}) \quad (4.44)$$

where the state $\mathbf{U}^{n+1/2}$ has been used as initial conditions to compute the $\mathbf{G}v$ viscous flux terms before the second dimensional sweep. We denote this diffusive flux update by the operator: $D_{\Delta t}(\mathbf{U}^n)$

The sequence of update steps are therefore split as: hyperbolic flux update ($H_{\Delta t}$), cylindrical hyperbolic source term update ($S_{\Delta t}^c$), diffusive flux update ($D_{\Delta t}$), cylindrical diffusive source term update ($Sv_{\Delta t}^c$). The chain of operator split updates can therefore be written:

$$\mathbf{U}^{n+1} = Sv_{\Delta t}^c(\mathbf{U}^{n+3/4})D_{\Delta t}(\mathbf{U}^{n+2/4})S_{\Delta t}^c(\mathbf{U}^{n+1/4})H_{\Delta t}(\mathbf{U}^n) \quad (4.45)$$

where the operators act right to left on \mathbf{U}^n , with intermediate step states defined as nominal fractions of the total number of operations.

Importantly, by adopting an operator split approach for the hyperbolic and diffusive fluxes, combined with application of the GFM for the geometry, special surface treatment must be considered. Applying no-slip BCs in the GFM before the hyperbolic flux update result in non-physical boundary treatment - inviscid flux computation on no-slip BCs are physically inconsistent conditions. Similarly, the density augmentation to apply thermal BCs is unphysical for the inviscid flux calculation at the boundary.

The operator split approach is a useful way of ensuring physically consistent conditions at the boundary. However, an intermediate GFM step must be introduced for viscous simulations. The sequence of boundary operations is therefore given by:

- ⇒ Apply slip condition GFM (constant density extrapolation)
- ⇒ Compute hyperbolic flux update
- ⇒ Integrate cylindrical hyperbolic source terms
- ⇒ Apply no-slip condition GFM (including thermal BCs if application)
- ⇒ Compute diffusive flux update
- ⇒ Integrate cylindrical diffusive source terms

Notably, due to the operator split strategy, the hyperbolic flux step is still susceptible to Carbuncle instability in cases where the problem is strongly pre-disposed. Therefore,

even for the extended Navier-Stokes model, it is still recommended to adopt the proposed HLLC-HS solver for computation of inviscid fluxes (for high Mach number, blunt body tests).

4.6.3 Time step with AMR considerations

The operator split approach permits us to maintain the stability limit $CFL \leq 1.0$ (typically taken to be $CFL = 0.9$) for the split hyperbolic flux step. However, for the simulation to evolve with a stable Δt within the chain of operator split updates, Δt becomes restricted as the minimum of the hyperbolic and diffusive stable time steps, given by:

$$\Delta t = \min[\Delta t_{hyp}, \Delta t_{diff}] \quad (4.46)$$

$$\Delta t_{hyp} = \min\left[\frac{CFL \cdot \Delta x_{d,i}}{S_{max,i}}\right] \quad (4.47)$$

$$\Delta t_{diff} = \min\left[\frac{(\Delta x_{d,i})^2}{2 \cdot \max\left[\frac{\mu_i}{\rho_i}, \frac{\zeta_i}{(\rho c_p)_i}\right]}\right] \quad (4.48)$$

where $x_{d,i}$ represents the step size in every dimension d for each cell i . Δt_{diff} is based on the formulation recommended by Gokhale [21].

Special care must be taken to ensure stability of the system within the AMR framework. The stability limited time-step is computed for both Δt_{hyp} and Δt_{diff} on the base (unrefined) mesh level. Whilst the hyperbolically restricted time step scales linearly with resolution ($\Delta t_{hyp} \propto \Delta x$), the diffusive time step restriction scales parabolically ($\Delta t_{diff} \propto (\Delta x)^2$). Therefore, it is important that the computed time-step restriction be calculated based on $\Delta x_{d,i}$ at the highest level of mesh refinement. Figure 4.15 illustrates the relative time step restrictions, demonstrating the level of refinement at which the diffusive flux restricts Δt .

The conditional statement at the 0^{th} level, where Δt is computed in the AMR sequence of the code, assuming factor of 2 hierarchical refinement and where N_MAX is the highest AMR level, is given as:

$$\Delta t = \begin{cases} \Delta t_{diff}, & \text{if } (\Delta t_{diff} \cdot (\frac{1}{2})^{2 \cdot N_MAX}) < (\Delta t_{hyp} \cdot (\frac{1}{2})^{N_MAX}) \\ \Delta t_{hyp}, & \text{otherwise} \end{cases}$$

which therefore defines the AMR-specific stability requirement.

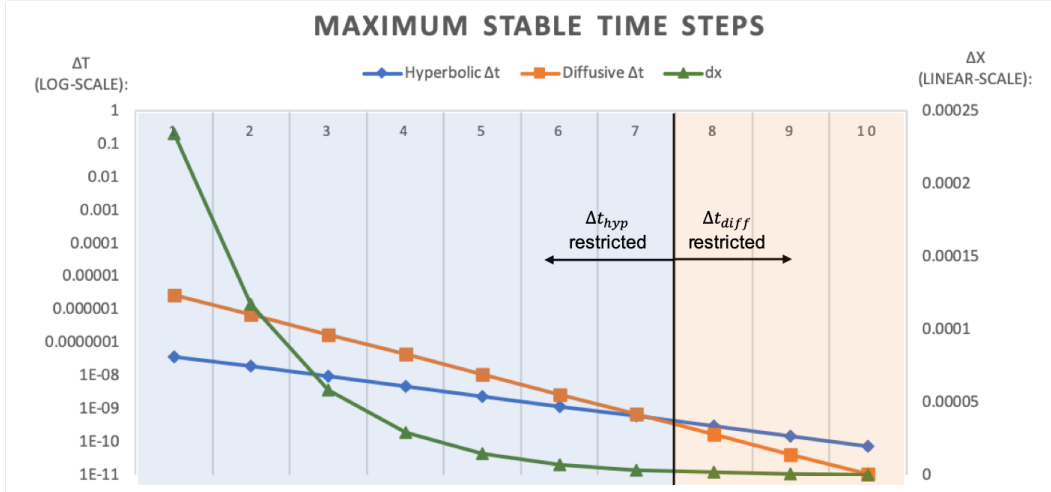


Fig. 4.15 Using the example of the flow conditions given in the supersonic wedge test of subsequent section 5.4.2, this plot shows the computed stable Δt (log-scaled) on the hyperbolic and diffusive fluxes for increasing AMR levels. As can be seen, up to the 7th AMR level the global time step is still hyperbolically restricted, however, by the 8th AMR level, the diffusive flux becomes restrictive. The corresponding cell size is also shown (exponential decrease with increasing AMR levels).

4.7 Full system solution

The last remaining set of numerics for the solution of the full system model, is the handling of the MHD associated source terms. Some careful consideration is necessary for this final system component.

4.7.1 MHD forcing terms

With reference to the system reduction of section 2.3.1, the Lorentz forcing ODEs of the MHD models, can be expressed in the condensed form:

$$\frac{\partial}{\partial t} \begin{pmatrix} \rho \mathbf{u} \\ E \end{pmatrix} = \begin{pmatrix} \mathbf{J} \times \mathbf{B} \\ \mathbf{u} \cdot (\mathbf{J} \times \mathbf{B}) + \eta J^2 \end{pmatrix} \quad (4.49)$$

An explicit Euler integration approach is adopted, where an additional momentum half-step is carefully utilised:

$$(\rho \mathbf{u})^{n+\frac{1}{2}} = (\rho \mathbf{u})^n + \frac{\Delta t}{2} \cdot (\mathbf{J}^n \times \mathbf{B}) \quad (4.50)$$

$$(\rho \mathbf{u})^{n+1} = (\rho \mathbf{u})^{n+\frac{1}{2}} + \frac{\Delta t}{2} \cdot (\mathbf{J}^n \times \mathbf{B}) \quad (4.51)$$

$$E^{n+1} = E^n + \Delta t \cdot \left(\mathbf{u}^{n+\frac{1}{2}} \cdot (\mathbf{J}^n \times \mathbf{B}) + \eta^n (J^2)^n \right) \quad (4.52)$$

The momentum half-step, and resultant $\mathbf{u}^{n+\frac{1}{2}}$ is not an arbitrary choice. While it does not increase the order of accuracy of the momentum integration (\mathbf{J}^n is not evolved to an intermediate $\mathbf{J}(\mathbf{u}^{n+\frac{1}{2}})$), it is important for the energy integration step.

The arrangement of the energy source terms make distinct the kinetic energy contribution ($\mathbf{u} \cdot (\mathbf{J} \times \mathbf{B})$) and the Joule heating contribution (ηJ^2). The integration is conducted using the conservative variables. However, total energy comprises both kinetic and internal energy components. The kinetic energy component of the MHD energy source term must convert directly to the kinetic energy component of the total energy, otherwise inconsistencies arise when converting between conservative and primitive variables in the various fluid solver steps.

Since ρ is unaffected by the conversion between conservative and primitive variables, and unaffected by the Lorentz forcing integration over the time step of this specific operation, then: $\rho^{n+1} = \rho^n$. And we can simply treat: $(\rho \mathbf{u})^n = (\rho \mathbf{u}^n)$.

Reducing the total energy ODE to deal directly with the kinetic energy component, we wish to preserve internal energy such that: $e^{n+1} = e^n$. Therefore rearranging the total energy equation (2.5), we wish to prove the numerical method can ensure:

$$e^{n+1} = \frac{E^{n+1}}{\rho} - \frac{1}{2}(\mathbf{u}^{n+1})^2 = \frac{E^n}{\rho} - \frac{1}{2}(\mathbf{u}^n)^2 = e^n \quad (4.53)$$

and therefore:

$$E^{n+1} = E^n + \rho \left(\frac{1}{2}(\mathbf{u}^{n+1})^2 - \frac{1}{2}(\mathbf{u}^n)^2 \right) \quad (4.54)$$

Let's examine the expansion of $\frac{1}{2}(\mathbf{u}^{n+1})^2$ considering the numerical integration of the momentum ODE (4.50)-(4.51):

$$\frac{1}{2}(\mathbf{u}^{n+1})^2 = \frac{1}{2} \left(\mathbf{u}^n + \frac{\Delta t}{\rho} (\mathbf{J}^n \times \mathbf{B}) \right)^2 \quad (4.55)$$

$$= \frac{1}{2}(\mathbf{u}^n)^2 + \frac{\Delta t \mathbf{u}^n}{\rho} (\mathbf{J}^n \times \mathbf{B}) + \frac{1}{2} \frac{\Delta t^2}{\rho^2} (\mathbf{J}^n \times \mathbf{B})^2 \quad (4.56)$$

$$= \frac{1}{2}(\mathbf{u}^n)^2 + \frac{\Delta t}{\rho^2} (\mathbf{J}^n \times \mathbf{B}) \left(\rho \mathbf{u}^n + \frac{\Delta t}{2} (\mathbf{J}^n \times \mathbf{B}) \right) \quad (4.57)$$

where the final term can be replaced by the defined half momentum step of equation 4.50, then:

$$\frac{1}{2}(\mathbf{u}^{n+1})^2 = \frac{1}{2}(\mathbf{u}^n)^2 + \frac{\Delta t}{\rho} \mathbf{u}^{n+\frac{1}{2}} \cdot (\mathbf{J}^n \times \mathbf{B}) \quad (4.58)$$

Which therefore substituting this result into equation 4.54, we can prove:

$$E^{n+1} = E^n + \Delta t \cdot \mathbf{u}^{n+\frac{1}{2}} \cdot (\mathbf{J}^n \times \mathbf{B}) \quad (4.59)$$

preserves internal energy.

This was the basis for the derivation of the half time stepped $\mathbf{u}^{n+\frac{1}{2}}$ utilised in the energy ODE of equation 4.52.

The Δt used in this source term integration is assumed to be calculated from the restriction $\min(\Delta t_{diff}, \Delta t_{hyp})$ as per section 4.6.3. However, it is important to ensure this Δt is sufficiently small for a stable source term integration.

The stability of a simple Euler integration method can be determined via growth factor analysis. For an ODE of the general form:

$$u' = \lambda u \quad (4.60)$$

the discretised numerical Euler integration takes the form:

$$u^{n+1} = u^n + h\lambda u^n \quad (4.61)$$

$$u^{n+1} = (1 + h\lambda)u^n \quad (4.62)$$

where h represents some dimensional (temporal or spatial) discrete step size depending on the specific ODE. The ODE becomes unbounded if the growth factor $|(1 + h\lambda)| > 1$. Therefore we assess stability on the basis of deriving a bounded growth factor for the MHD source term Euler integration at hand.

Substituting $\mathbf{J} = \sigma \cdot (\mathbf{u} \times \mathbf{B})$ into the momentum integration equation 4.51 we can write:

$$\mathbf{u}^{n+1} = \mathbf{u}^n + \Delta t \cdot \left(\frac{\sigma}{\rho} (\mathbf{u}^n \times \mathbf{B}) \times \mathbf{B} \right) \quad (4.63)$$

We can arrange the numerical integration as a growth factor multiplying \mathbf{u}^n :

$$|\mathbf{u}^{n+1}| = (1 - |\Delta t \frac{\sigma B^2}{\rho}|) |\mathbf{u}^n| \quad (4.64)$$

noting that for positive (u, v) velocities and positive (B_r, B_z) magnetic field components, results in a $-J_\theta$ term, thus the negatively signed second term.

Therefore the stability requirement is that Δt ensure:

$$|(1 - |\Delta t \frac{\sigma B^2}{\rho}|)| \leq 1 \quad (4.65)$$

$$\Delta t \leq \left| \frac{2\rho}{\sigma B^2} \right| \quad (4.66)$$

Whilst inevitably problem dependant, considering the orders of magnitudes discussed in the previous sections, generally test cases will result in:

$$\left| \frac{CFL \cdot \Delta x}{S_{max}} \right| \ll \left| \min \left(\frac{2\rho}{\sigma B^2} \right) \right| \quad (4.67)$$

and so the time-step for the operator split Lorentz forcing ODE need not be restricted below the existing Δt to maintain stability.

4.7.2 Numerical solution strategy

Finally, the full chain of operator split explicit numerical updates can be written:

$$\mathbf{U}^{n+1} = S_{\Delta t}^{MHD}(\mathbf{U}^{n+4/5}) S_{V_{\Delta t}}^c(\mathbf{U}^{n+3/5}) D_{\Delta t}(\mathbf{U}^{n+2/5}) S_{\Delta t}^c(\mathbf{U}^{n+1/5}) H_{\Delta t}(\mathbf{U}^n) \quad (4.68)$$

where the $S_{\Delta t}^{MHD}$ operator is the ODE integration method described above. The cylindrical source terms are each Strang split to maintain second order accuracy, whereas the MHD source terms are integrated simply through a single forward Euler step (since their magnitude is much smaller than the other system fluxes). The MHD forcing dynamics are unaffected by the geometry boundary treatment since \mathbf{J} and \mathbf{B} are defined to be zero in the geometry interior. The operator split strategy lends itself very well to the problem modularisation described in the theory section of Chapter 2, where the map of models was defined. The operations can easily be removed or incorporated depending on the relevant mathematical model for the system.

Chapter 5

Validation of models

Validation is an essential process in the development of numerical models. There are two levels of correspondence when it comes to model validation as compared with experiment:

Level 1) do the numerical algorithms sufficiently reproduce the mathematical model?

Level 0) does the mathematical model sufficiently reproduce the underlying physics?

In evaluating level 1 it can be useful to benchmark against other simulations, and against theoretical solutions wherever possible. Given the second level of correspondence required when comparing simulation results directly to physical experiment, comparison of simulation to experiment is both more arduous and more authoritative. Successful experimental validation implies efficacy of both the mathematical modelling and numerical modelling, whereas unsuccessful experimental validation could be undermined by either component.

Since this work presents an original numerical methodology (unique combination of methods, with extensions and adaptations) in combination with an advanced equation of state newly applied in the hypersonic regime, extensive validation is paramount.

Validation of each of the mathematical sub-models defined in Chapter 2, is presented, in order to progressively validate each constituent component of the full-system model. Performance of the new hypersonic stabilisation extension to the base inviscid flow solver is also assessed. Careful attention is paid to the results produced by the combined Navier-Stokes, Rigid body GFM with advanced EoS model for non-simple geometry against available experimental data. MHD forcing dynamics are validated against a standardised theoretical test from the literature.

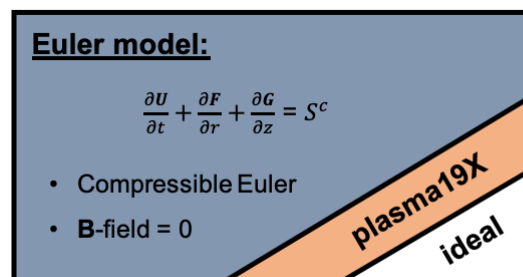
Whilst experimental data is the foremost authority, obtaining sufficient high-quality data from high enthalpy facilities remains a challenge [147]. Generally, impulse facilities, involving shock tubes with free piston drivers, or expansion tubes are needed to generate sufficient energy in the freestream flow. Adverse consequences are that test times are short (a few milliseconds for free piston shock tubes and about 300 microseconds for expansion tubes). Significant non-uniformities can arise across the free-stream flow, which, for free piston shock tunnels, might also contain some dissociated species. Because this

contamination is avoided with expansion tubes and ballistic ranges, most of the experimental data used in this Chapter are from these facilities. Compromises have to be made between the model size and the non-dimensional flow parameters. In terms of the electric properties of interest, specific data on post-shock species composition and electron number density is difficult to obtain.

Where possible, experimental data is used for validation. For a number of tests, experimental Schlieren images from high enthalpy test facilities are used to validate flow field shock-structure and pressure traces along model surfaces. A real reentry flight test which used Langmuir probes to measure electron number density is used to validate the computation of N_e by the extended plasma19X EoS.

Experiments on magnetic flow control typically use Argon as the test gas due to its much lower ionisation potential than air [54]. Without a real gas chemistry model for Argon, conductivity cannot be realistically computed and MHD effect cannot be directly validated from such experiments. Therefore studies of MHD control is specifically the subject of the next Chapter.

5.1 Ideal Euler model



The inviscid gas dynamics solver is the base component of all of the defined models. Therefore validation of this model underlies the validation of all other models. We first validate fluid only test cases, examining the AMR configuration before presenting the combined fluid-rigid body tests for transient shock-body interaction problems.

5.1.1 2D Circular Sod Test

The Sod shock tube problem is a classic validation test for Riemann solvers. Whilst typically conducted in 1D with a left and right Riemann problem state, the test can also be conducted with a circular initialisation to produce 2-dimensional effects, with known solution. All units are non-dimensional, the initial conditions are given as interior state W_i and exterior state W_o in primitive variables, with an initial radius bounding the interior state $r_i = 0.4$, the system is closed with ideal gas law with $\gamma = 1.4$, and test run time is $t_f = 0.25$. The test is first

conducted with only the base single level mesh (no additional AMR levels), with resolution 208×208 cells over the 2×2 domain. All tests are run with the default HLLC solver with SuperBee slope limiter.

$$W_i = \begin{pmatrix} \rho = 1.0 \\ u = 0.0 \\ v = 0.0 \\ p = 1.0 \end{pmatrix}, \quad W_o = \begin{pmatrix} \rho = 0.125 \\ u = 0.0 \\ v = 0.0 \\ p = 0.1 \end{pmatrix} \quad (5.1)$$

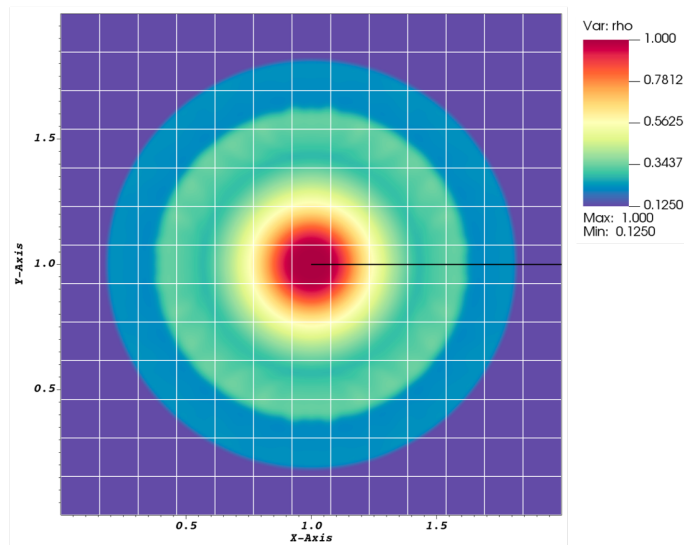


Fig. 5.1 2D Circular Sod test at final time $t_f = 0.25$: plot of density with base level mesh patches shown, radial line for property trace shown in black

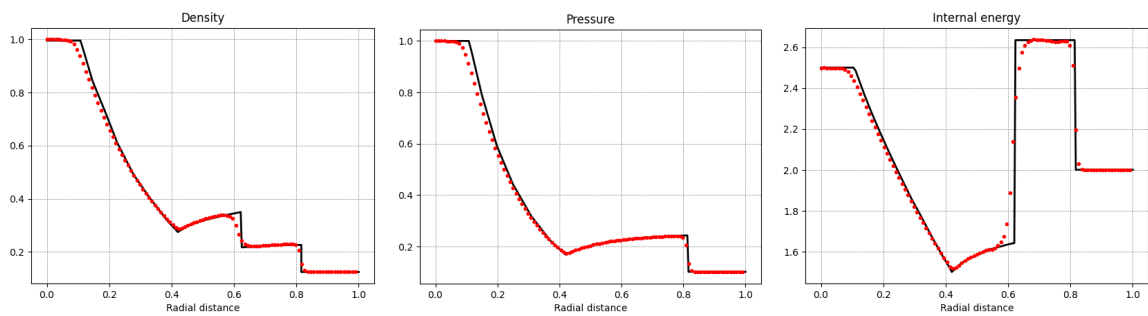


Fig. 5.2 Primitive variable property traces along centre radial line, at $t_f = 0.25$: known exact solution in black [16], and computed result in red, discrete markers representing each cell along the radial line.

5.1.2 AMR configuration

We now initialise 2 additional AMR levels, with tagging condition as per section 4.2.2. Tagging threshold fractions of 0.5 are set for each AMR level. With 2 levels of factor 2

hierarchical AMR an effective resolution of 4 times the base resolution is achieved in the refined regions with only a total of 1.93 times as many cells: 50.1% of the domain is factor 2 refined, and 14.3% is factor 4 refined.

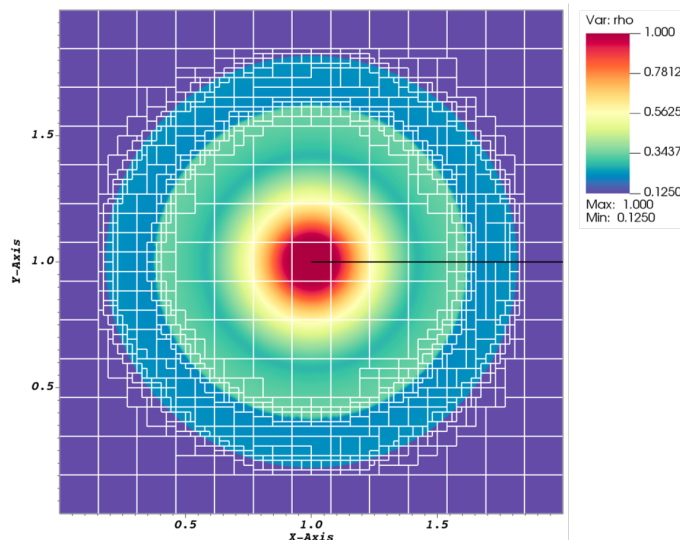


Fig. 5.3 2D Circular Sod test at final time $t_f = 0.25$: plot of density with patches shown to mark the borders of the 2 AMR levels (radial line for property trace shown in black)

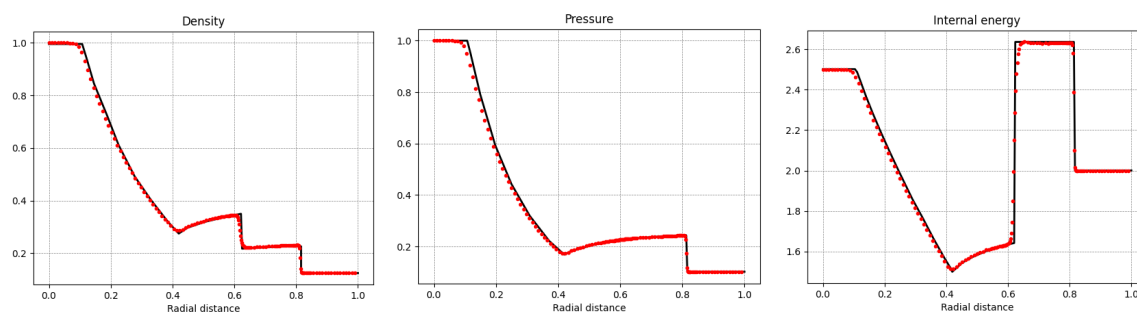


Fig. 5.4 Primitive variable property traces along centre radial line, at $t_f = 0.25$: known exact solution in black [16], and computed result in red, note that the discrete markers are clustered represented the refined regions.

The efficacy of the AMR is shown in the property traces of Figure 5.4. Higher refinement thresholds can be specified to obtain tighter refinement around shocks and contact waves.

5.1.3 Supersonic rigid body GFM tests

We now validate the full 2D compressible rigid body GFM code against experimental results for shocks passing over non-simple geometries and producing complex wave structures.

Supersonic wedge test

The first test follows the experimental set-up from Sivier *et. al.* [17] where a Mach 1.3 shock wave passes over a 27.4° wedge inside a tube with reflective top and bottom boundaries. The computational mesh at time 0 is shown in Figure 5.5. The simulation is configured with a base resolution of 448×128 cells, and 2 levels of hierarchical mesh refinement.

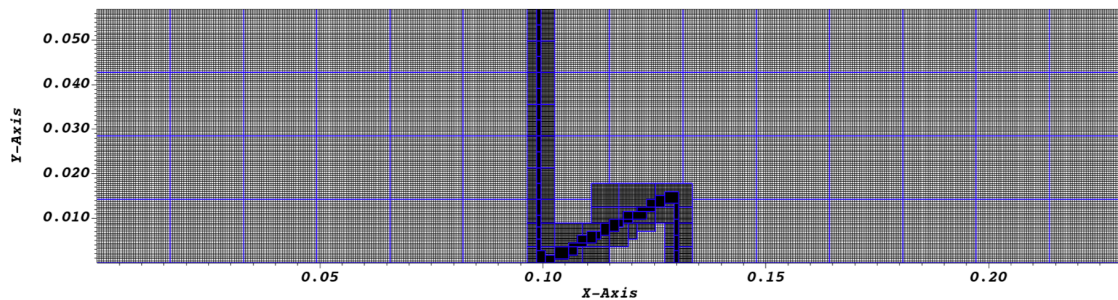


Fig. 5.5 2D supersonic wedge test- initial Cartesian mesh shown with 2 additional levels of refinement shown around the triangular geometry and the incident normal shock wave, initialised at position $x=0.099$ m. AMR ‘blocks’ defined for parallel computation are shown with blue boundaries.

A numerical Schlieren plot (log-scaled density gradient) is produced for comparative time-steps to the experimental Schlieren images produced by Sivier [17]. The final time-step image of Figure 5.8 is a comparative plot to the numerical solution of the rigid body GFM model of Sambasivan [18], who also validated with the earlier time-frames of Sivier.

As can be seen from the final time mesh of Figure 5.9, the AMR+tagging implementation is very effective to capture the temporal evolution of the property field.

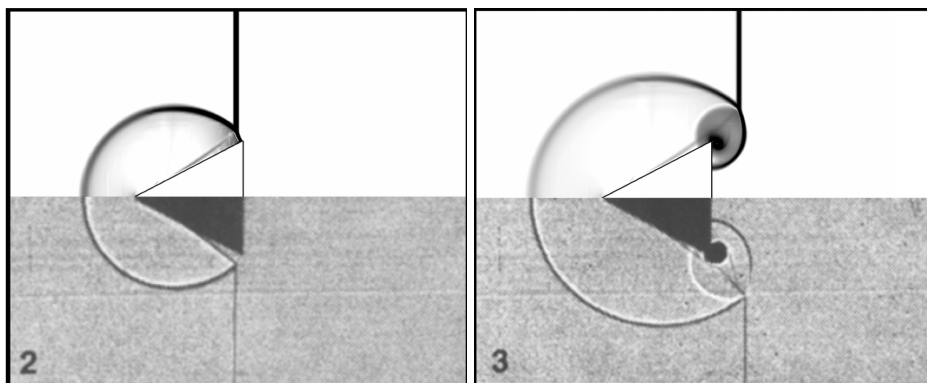


Fig. 5.6 Upper) numerical Schlieren result of this work, and lower) experimental image obtained from Sivier [17]. Matching time frames 2 and 3.

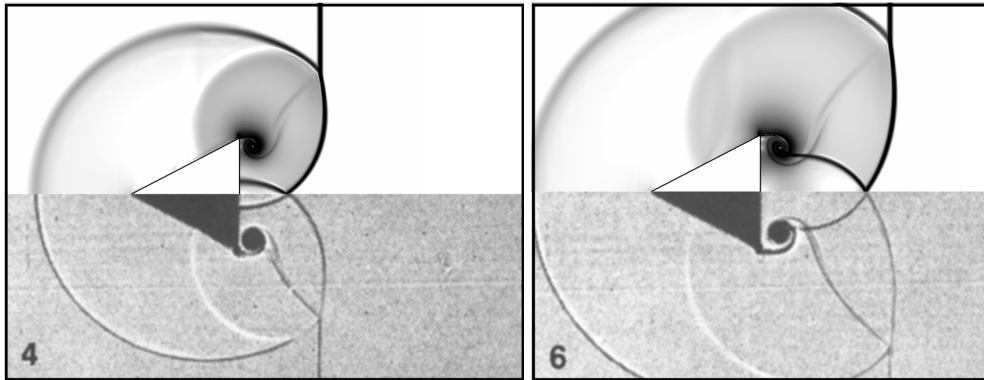


Fig. 5.7 Upper) numerical Schlieren result of this work, and lower) experimental image obtained from Sivier [17]. Matching time frames 4 and 6.

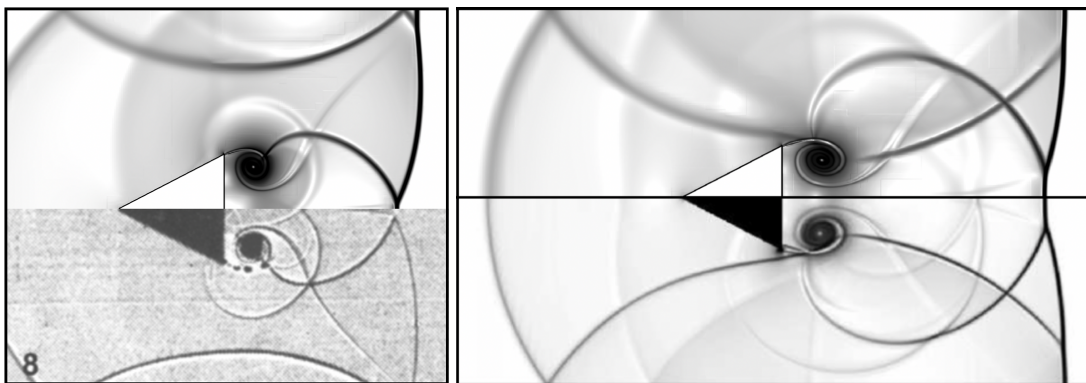


Fig. 5.8 Left) comparison of numerical Schlieren of this work to Sivier [17], and right) comparison of final time frame to numerical result of Sambasivan et al. [18].

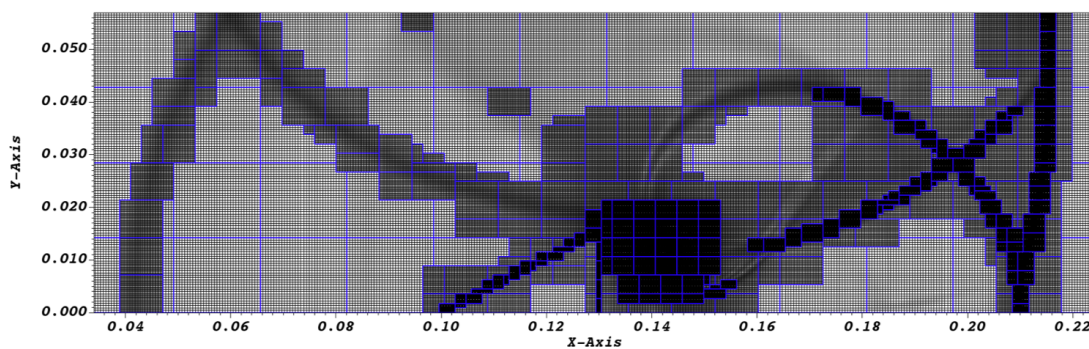


Fig. 5.9 Final time mesh shown with mesh levels adaptively refined based on density gradient and geometry boundary.

Mach 3 flow over group of cylinders

This test case aims to capture the complex and interacting wave structure produced by a Mach 3 normal shock wave propagating left to right over a group of cylinders. The domain is $1 \text{ m} \times 1 \text{ m}$, each cylinder has a radius of 0.1 m and the three centre locations are (0.3 m,

0.3 m), (0.35 m, 0.7 m), (0.6 m, 0.5 m). The upstream conditions are ambient: $\rho = 1.225 \text{ kg/m}^3$ and $p = 1 \text{ atm}$.

Each time frame shown is compared with the equivalent time frame from the simulation of Sambasivan [18], which has also been validated on simpler geometries against Sivier [17].

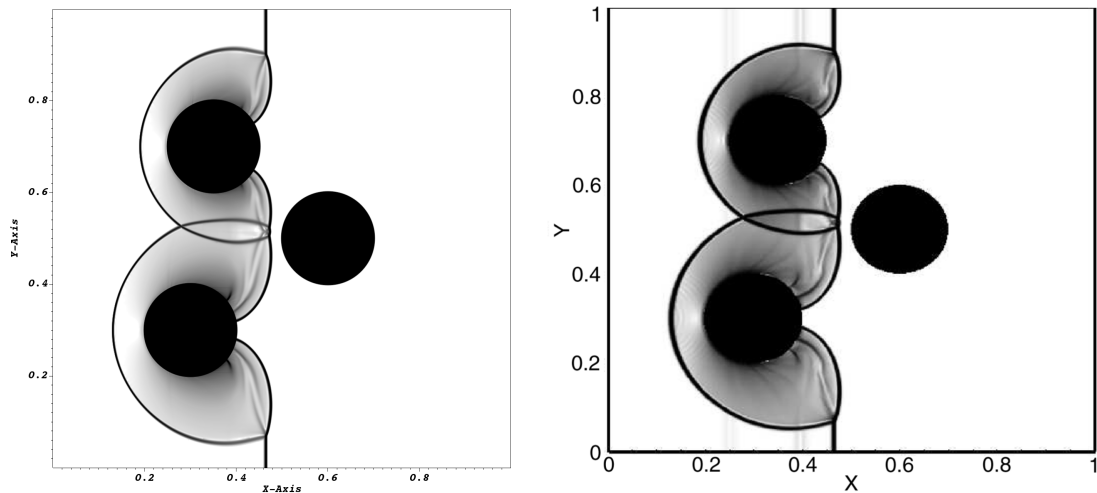


Fig. 5.10 Left) solution of this work, right) solution by Sambasivan et al. [18]

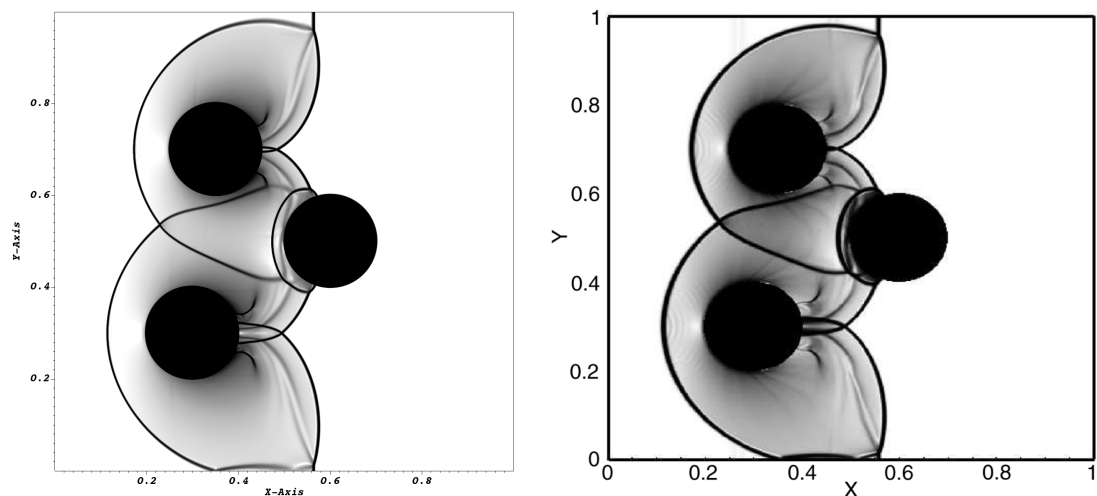


Fig. 5.11 Left) solution of this work, right) solution by Sambasivan et al. [18]

This test demonstrates the major advantages offered by the embedded boundary GFM implementation. The same problem would be near impossible to capture with a body-fitted mesh, without significant distortion and skewing. We also note that the immediate solution field immediately around the body is less “crinkled” in the implementation of this work compared to Sambasivan. This could be due to the different base fluid solver used (Sambasivan implement a convex ENO scheme with 3rd order RK integrations), or the slight alterations to the GFM proposed in 4.4.1. In any case, the results of this work produce consistent, sharp results, with smooth resolution around the body surfaces.

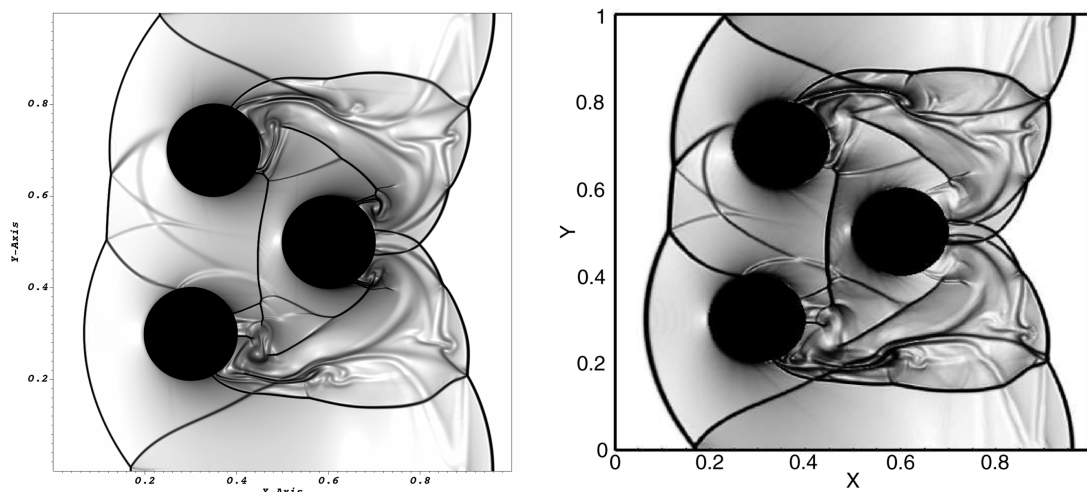


Fig. 5.12 Left) solution of this work, right) solution by Sambasivan et al. [18]

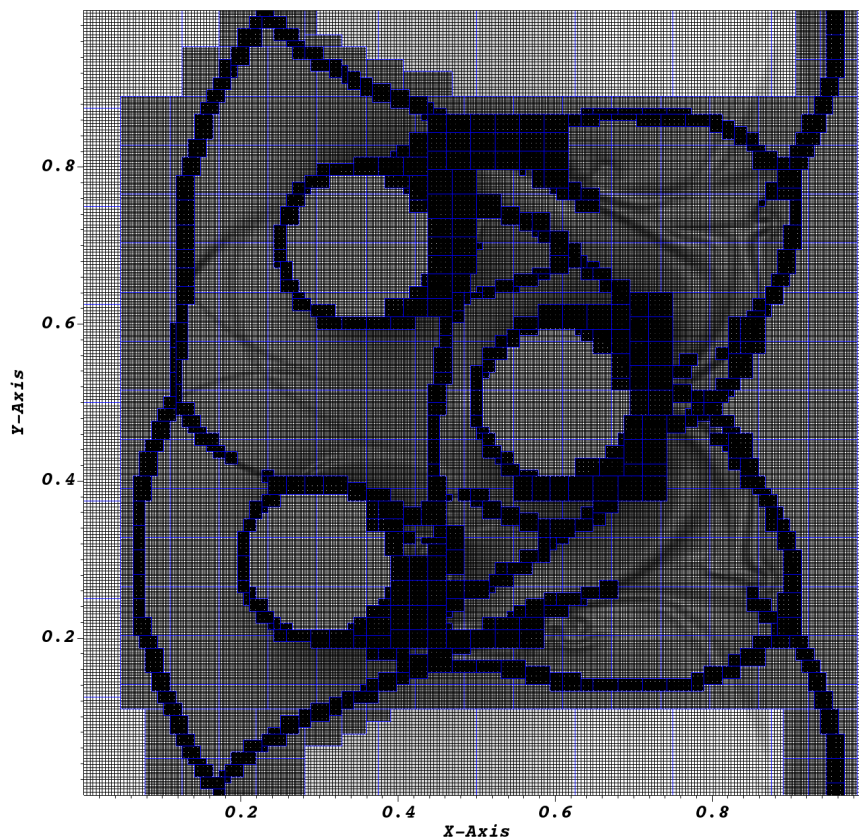


Fig. 5.13 Adaptively refined mesh with two levels, as at the final time frame.

5.2 Hypersonically stable solver

The HLLC-HS solver is tested across standardised tests from the literature on Carbuncle instabilities. The tests are configured such that base level resolution is comparable to the literature. The increased resolution in high gradient regions resulting from the AMR increases susceptibility to Carbuncle-type phenomena. All tests are computed in this work as

second order (MUSCL) with UltraBee slope limiter. UltraBee is chosen as the least diffusive limiter and therefore most instability-prone.

5.2.1 Standardised tests

Hypersonic flow over a blunt body

A routine test for Carbuncle phenomena is an extreme hypervelocity flow over a blunt body. We test a Mach 20 flow over a cylinder. The entire domain is initialised to ambient density and pressure ($1.225\text{kg}/\text{m}^3$ and 101.325kPa) with a Mach 20 (6805.88 m/s) velocity, over a half cylinder which has a radius of 0.5 m.

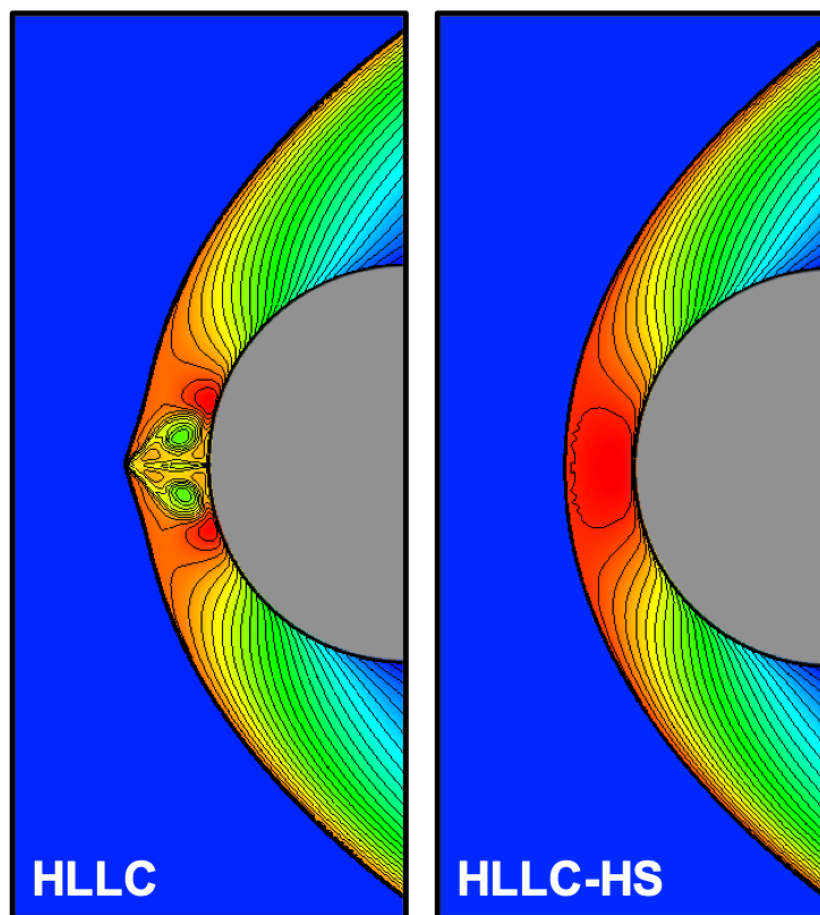


Fig. 5.14 Plot of density with contours: left) HLLC solution, right) HLLC-HS steady-state solution

In the HLLC solver, what begins as a transverse oscillation behind the shock near the stagnation region, grows to become a significant unphysical flow feature, forming a vortex pair, and ultimately creating a protrusion in the centre of the bow shock. The HLLC solution does not reach a steady state, but continues to evolve the strange Carbuncle feature. The HLLC-HS solution is shown to be free of such an emergent instability, and reaches a convergent steady-state.

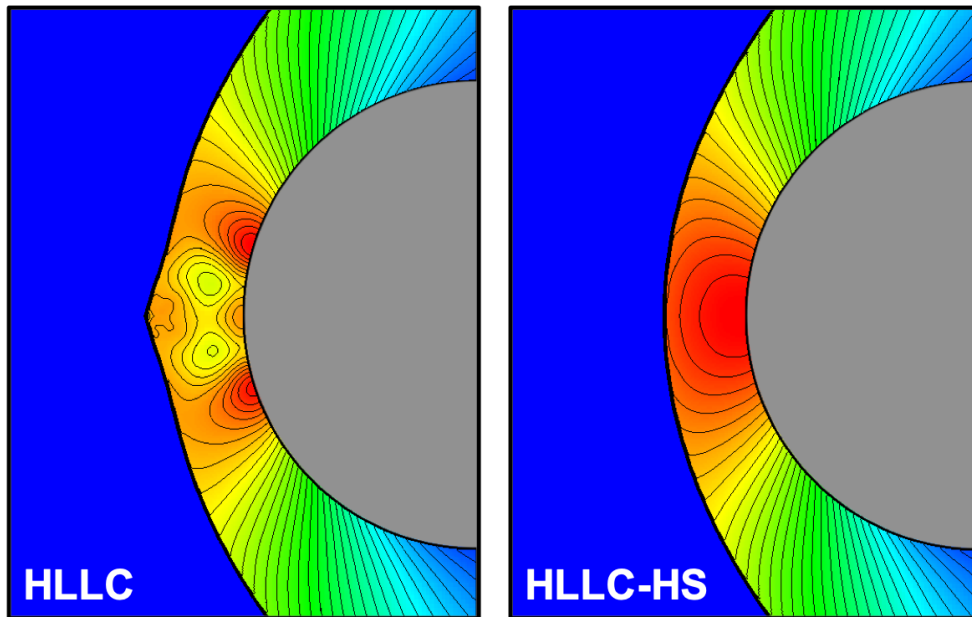


Fig. 5.15 Plot of pressure with contours: left) HLLC, right) HLLC-HS

Supersonic flow over a forward facing step

In this problem, a Mach 3 flow passes over a small step (0.2m high, 0.6m from inlet boundary). The domain is $3\text{m} \times 1\text{m}$ and is entirely initialised to ambient conditions with a rightward moving velocity of 1020.88m/s. As well as the solid step, the top and bottom wall of the domain are reflective boundaries. The base level resolution is quite low at 120×40 cells, however two levels of refinement (factor 2) are permitted within the hierarchical AMR, therefore resolving key features more finely.

Once the bow shock forms around the leading edge of the forward facing step it contacts the upper boundary, causing a reflection which eventually forms into a triple point separated from the upper surface. The reflected oblique shock contacts the step, causing a second reflection and double compressions. The results shown in Figure 5.16 highlight key regions to better examine notably unphysical features.

Key erroneous features are highlighted in the solutions of Figure 5.16. The HLLC solution exhibits odd-even decoupling in the vicinity of the upper vertical leading shock (*1) and in the centre of the bow shock formed ahead of the step (*2). Significantly, the HLLC solver erroneously forms a ‘bubble’ in the middle of the step surface, which grows to eventually split the reflected shock, affecting much of the downstream solution (*3). The HLL solution ameliorates these three anomalies, however, looking at the density contours in the central upper region one observes the loss of resolution of HLL solution as compared to the HLLC: the contours significantly diffuse downstream of the triple-point in the HLL solution (*1). We can see how the HLLC-HS solution corrects the Carbuncle anomalies whilst fully retaining resolution in the intermediate regions.

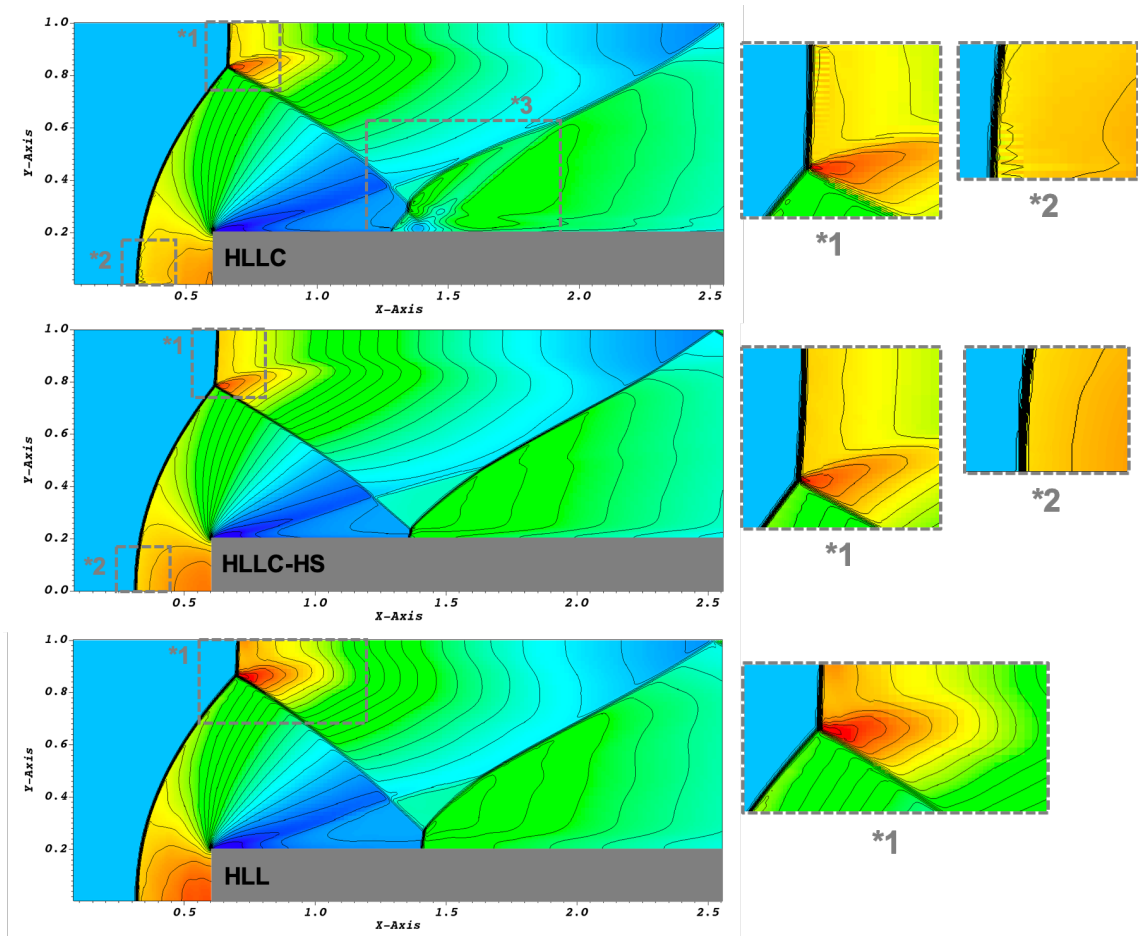


Fig. 5.16 Plot of density with contours: top) HLLC, middle) HLLC-HS, bottom) HLL

Figure 5.17 shows the value of ω applied to the transverse sweeps relative to the shock detection alignment. The plot also includes the hierarchical AMR refinement patches which influence shock resolution and therefore computed ω .

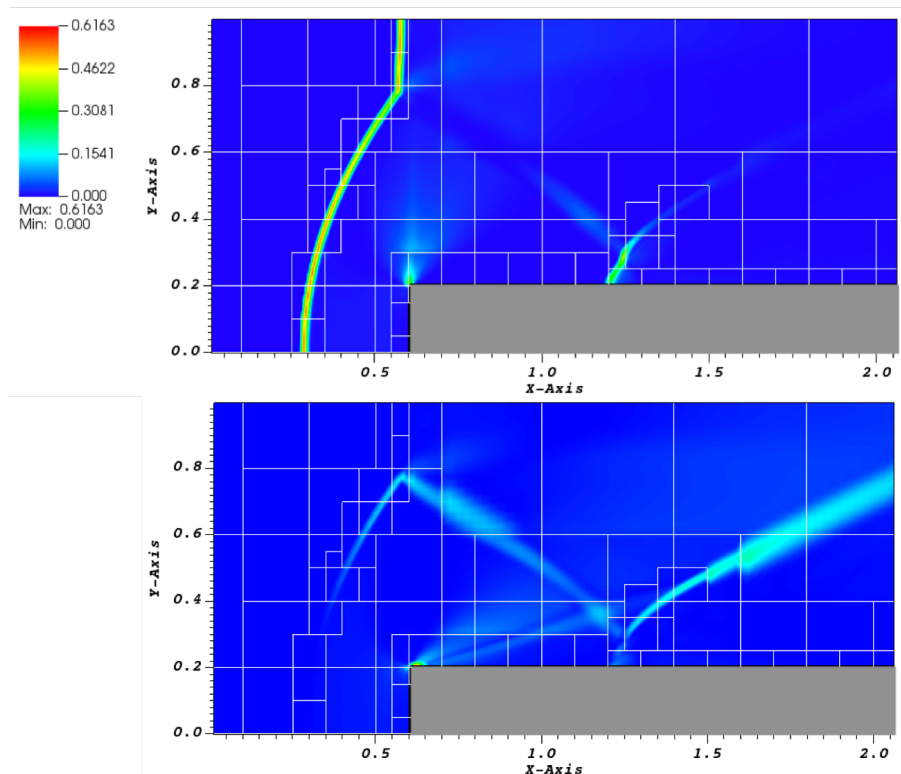


Fig. 5.17 Plot of internally computed ω values for: upper) **G**-flux sweep to detect strong vertically aligned shocks, and lower) **F**-flux sweep to detect strength of horizontally aligned shocks. Shown with AMR level boxes.

Diffraction of a moving normal shock over a 90° corner

Quirk [139] showed through a test of a Mach 5.09 normal shock moving adjacent to a solid block, that as the shock diffracts around the corner, Carbuncle-type anomalies are observed. While the literature results show a significant instability behind the leading normal shock which propagates horizontally along the upper boundary, the unadjusted HLLC solver in this work does not exhibit such an initial instability. It is suspected that the solver of other works is dimensionally unsplit (with a cited CFL of 0.4) whereas the dimensional splitting (with CFL=0.9) employed in the current solver may already stabilise the instabilities. A high resolution simulation of base level of 240×240 cells with 2 AMR levels for the HLLC and HLLC-HS solvers are compared.

The result is still presented, since it is one of the standardised Carbuncle tests, and demonstrates that no resolution or accuracy is compromised in the HLLC-HS result.

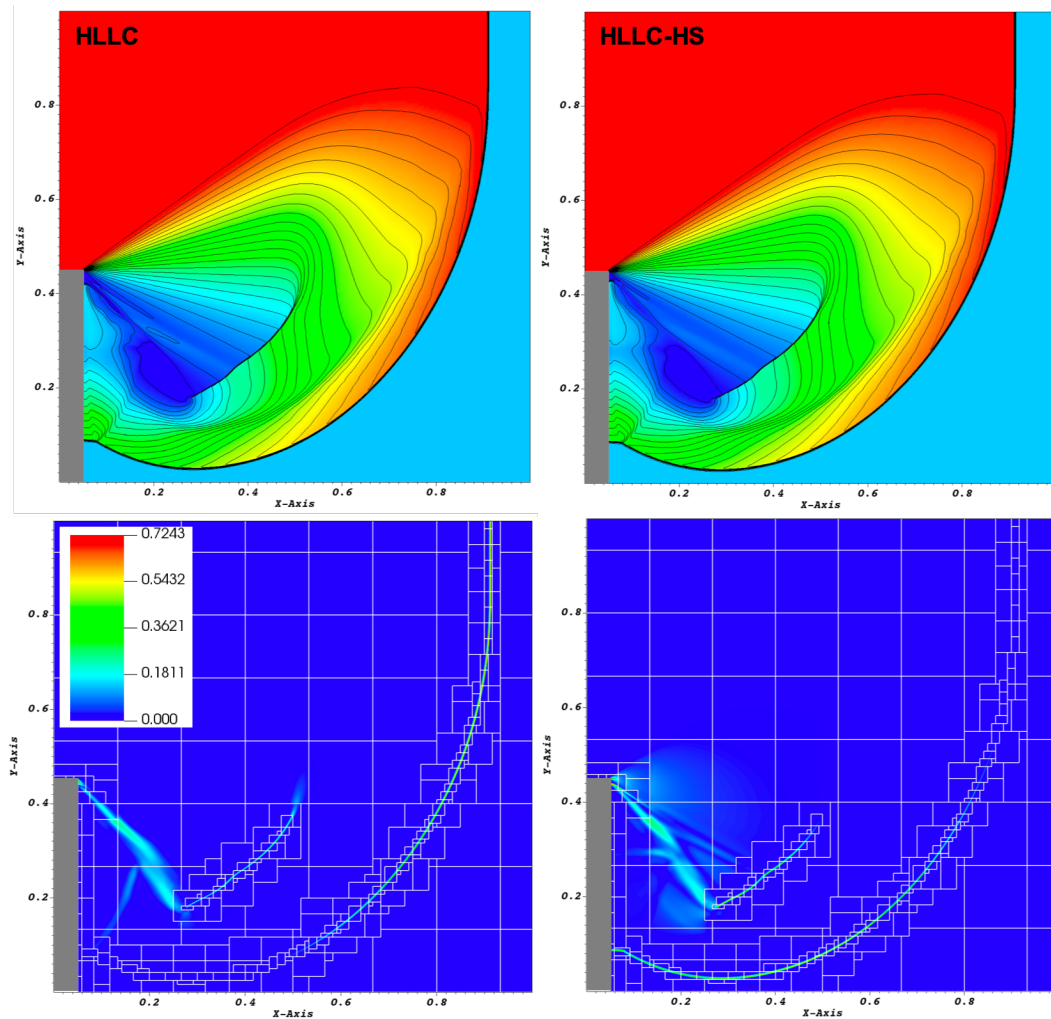


Fig. 5.18 Plot of density with contours: upper left) HLLC, upper right) HLLC-HS. With HLLC-HS computed: lower left) G-flux ω , and lower right) F-flux ω

Double Mach reflection problem

The double Mach reflection was a problem proposed by Woodward & Colella [148] and now reproduced widely as a key test of the robustness of numerical solvers for strong shocks. A Mach 10 flow is initialised at $x=0.16667m$ into the domain and impacts an inclined plane at an angle of 60° relative to the normal shock. The problem can be translated to the equivalent problem of angled flow impacting a partially reflective bottom boundary (as shown here). The resolution of this problem is a key parameter, as the vortex seen near the Mach stem, only forms under sufficiently high resolution. The base resolution set for this problem is 200×64 cells for the $3m \times 1m$ region shown. The free stream region is initialised to zero velocity and ambient air conditions ($1.225kg/m^3$ and $101.325kPa$), and Mach 10 post normal shock conditions computed at the 60° angled velocity.

This test is included in studies of Carbuncle phenomena as it tends to produce a kinked Mach stem (along the shock wave in contact with the lower reflective boundary), whereas that transmitted normal shock should remain straight. Again, we observe that the unadjusted

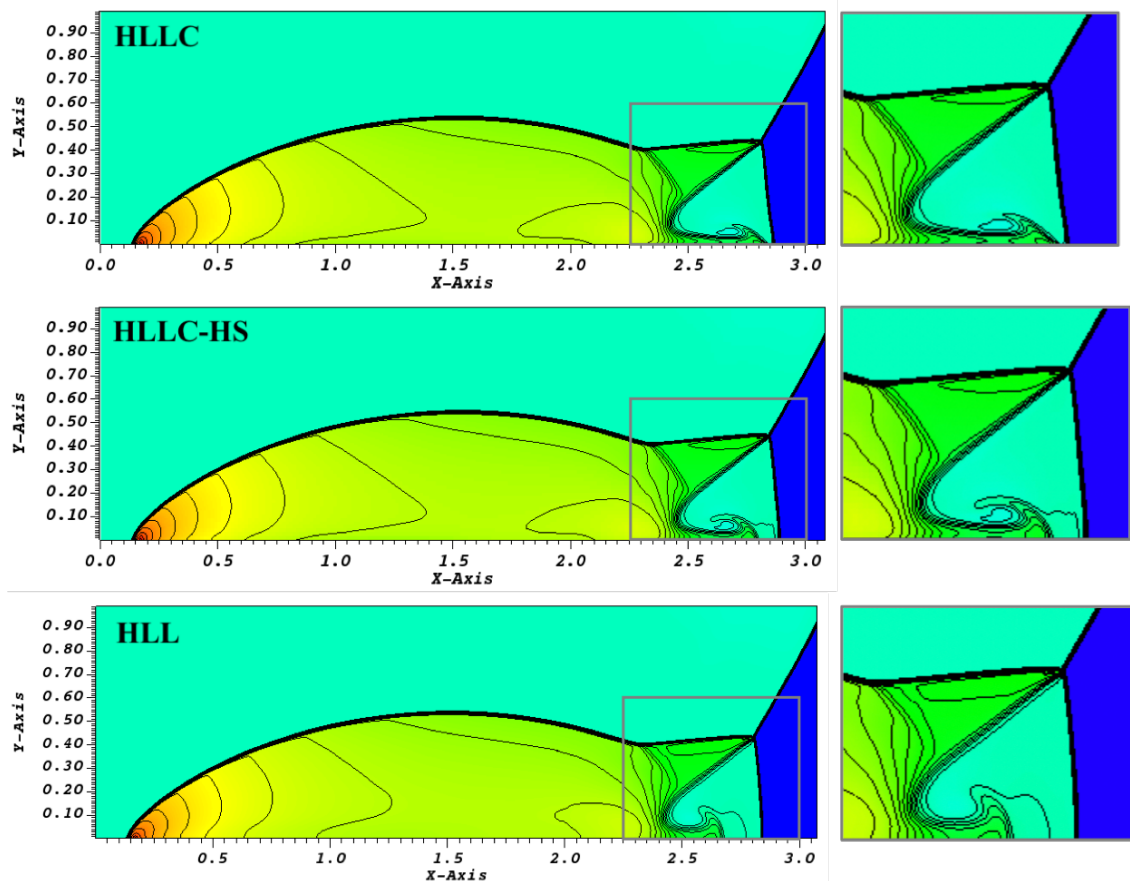


Fig. 5.19 Plot of density with contours as computed by the different numerical solvers

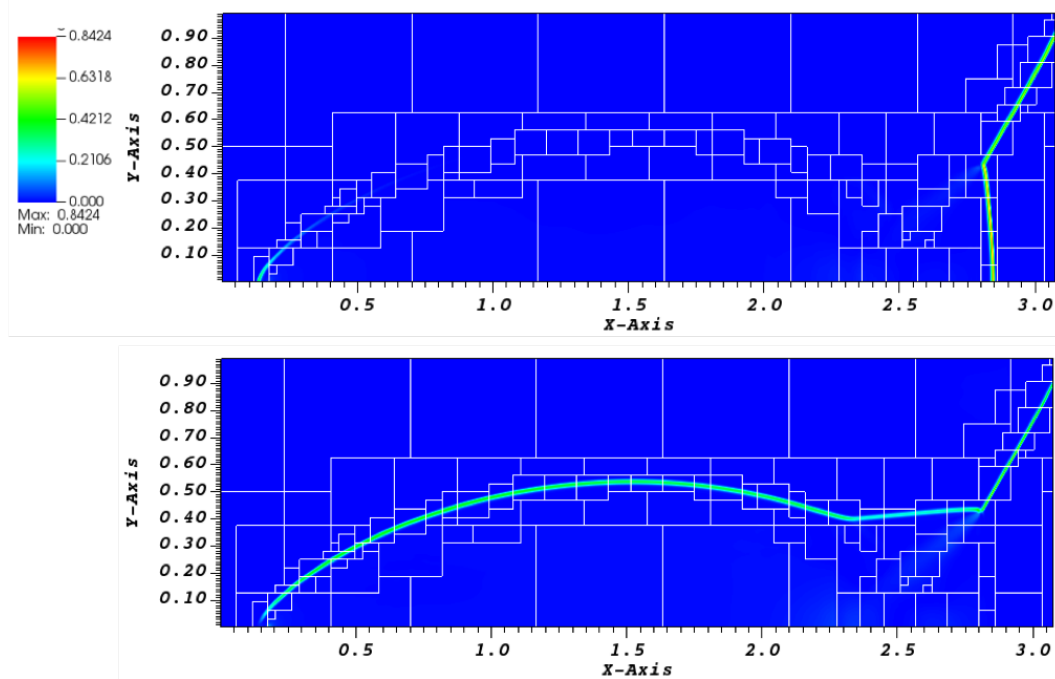


Fig. 5.20 Plot of internally computed ω values for: left) G-flux sweep and right) F-flux sweep. Shown with AMR level boxes.

HLLC solver of this work does not suffer badly from this expected effect, though close inspection does determine a minute convex ‘kink’ in the HLLC shock, a minutely concave bend in the HLL wave, and a near-exactly straight shock for the HLLC-HS. It is the proximity of the vortex base, to the forward shock which contributes to the kink. Its position is closest in the HLLC solver, farthest in the HLL, and we notice that under the same grid resolution, the vortex is most developed in the HLLC-HS solution. There are much more observable differences in the vortex formation of the 3 solvers. What is interesting from inspection of the plots of ω , is that the internal solver modification is not activated in the region where the vortex is developing, however, the correction and stabilisation achieved along the Mach stem, leads to the more complete resolution of this adjacent flow feature in the HLLC-HS solution.

5.2.2 Performance assessment

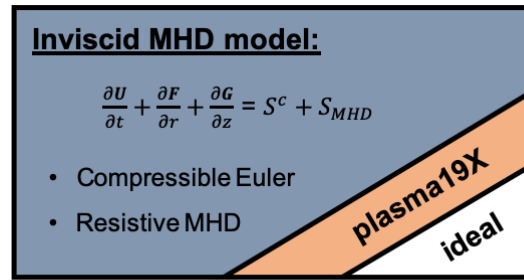
Analysis of the HLLC-HS solver across the standard set of validation tests shows very effective correction of Carbuncle instabilities and associated features. Although the base, dimensionally split, HLLC solver does not suffer badly in a number of standardised hypersonic tests, other tests such as the Mach 20 flow over a cylinder and Mach 3 flow over forward facing step produce significant unphysical features, which are completely ameliorated in the HLLC-HS solution. Importantly, the tests vary widely in Mach number (Mach 3 - Mach 20) and in geometry, and the HLLC-HS demonstrates generalised efficacy across all tests without the use of any manual tuning parameters. Similar binary switching or eigenvalue adjustment methods in the literature require manual tuning parameters which depend upon Mach number and resolution. The fact the HLLC-HS solver is liberated from manual tuning, and is effective within an AMR framework with varying cell-size, is a major advantage.

It is important to note that the operator split strategy where: Inviscid fluxes are computed (and dimensionally split) and the system is evolved, then viscous fluxes are subsequently computed and the system is evolved, means that the Navier-Stokes model (validated later in this chapter) is not immune from Carbuncle instabilities in the most extreme cases where their instabilities arise. The Mach 20 cylinder test was computed by the viscous Navier-Stokes model and revealed small oscillations emerging near the bow shock. Therefore, even for the NS model, the HLLC-HS solver is still recommended to compute the operator split inviscid flux component for blunt body hypersonic test cases.

The additional calculations involved in the HLLC-HS solver of course come at some computational cost. For the standardised test cases presented in this section, the HLLC-HS solver runs approximately 6.04% - 11.12% slower than the base HLLC solver.

The developed solver is shown to be robust up to highly hypersonic test cases known to push the limits of high order, complete wave, Riemann solvers. This is crucial for many of the applications of interest.

5.3 Inviscid MHD model



The inviscid MHD model is validated against a standardised theoretical test used in the literature to validate the Lorentz forcing dynamics of a low Re_m resistive MHD system.

5.3.1 Resistive MHD system under ideal gas law

For the purpose of validating the underlying resistive MHD model, an ideal gas equation of state is first employed to close the system (as consistent with the literature test cases). The most prevalent validation test is the case originally studied by Poggie & Gaitonde [20], and replicated subsequently by Damevin & Hoffmann [122] and most recently by Fujino et. al [19].

The set-up for this problem is a Mach 5 flow over a 10 mm radius sphere. Other conditions are $Re=80,000$ and free stream temperature of 100 K. This free stream temperature makes the test physically unrealistic (air, even in the very upper atmosphere, never drops below 200 K, and especially not at the density and pressure which satisfies the Mach and Reynolds numbers), and it is therefore used purely for validation purposes. The calculated free stream conditions are consequently:

Free stream test conditions:

$$M_\infty = 5.0, \rho_\infty = 0.0798 \text{ kg/m}^3, p_\infty = 2290.85 \text{ Pa}, V_\infty = 1002.25 \text{ m/s}, \gamma = 1.4$$

The MHD effect is shown to increase shock stand-off distance with increased ‘magnetic interaction parameter’ (Q_{MHD}) defined as:

$$Q_{MHD} = \frac{\text{Lorentz force}}{\text{Fluid inertial force}} = \frac{\sigma_0 B_0^2 R_0}{\rho_\infty V_\infty} \quad (5.2)$$

The gas model is taken to be ideal gas with finite conductivity. However, the exact model assumed for conductivity is somewhat precarious. Because the gas conductivity is not captured by the ideal gas EoS, a supplementary analytic equation for conductivity is defined. Models from various studies assume an approximate conductivity model of the following form:

$$\sigma = \sigma_0 \left(\frac{T}{T_{ref}} \right)^n \quad (5.3)$$

where T_{ref} is taken to be the maximum temperature in the stagnation region.

Poggie & Gaitonde investigate different valued exponents ($n=0-4$), and conclude that the exponent, and conductivity model more generally, has a notable impact on the MHD control effects. For this initial set of validation tests they assume a constant conductivity of $\sigma_0 = 300 (\Omega m)^{-1}$, ie. $n=0$, in the post-shock region. Magnetic field strength is varied in order to produce integer values from $Q_{MHD} = 0$ to $Q_{MHD} = 6$. The resultant pressure profiles are shown for Fujino et. al along with the computed shock stand-off distance comparison for this work vs both literature cases for $Q_{MHD} = 0 - 6$.

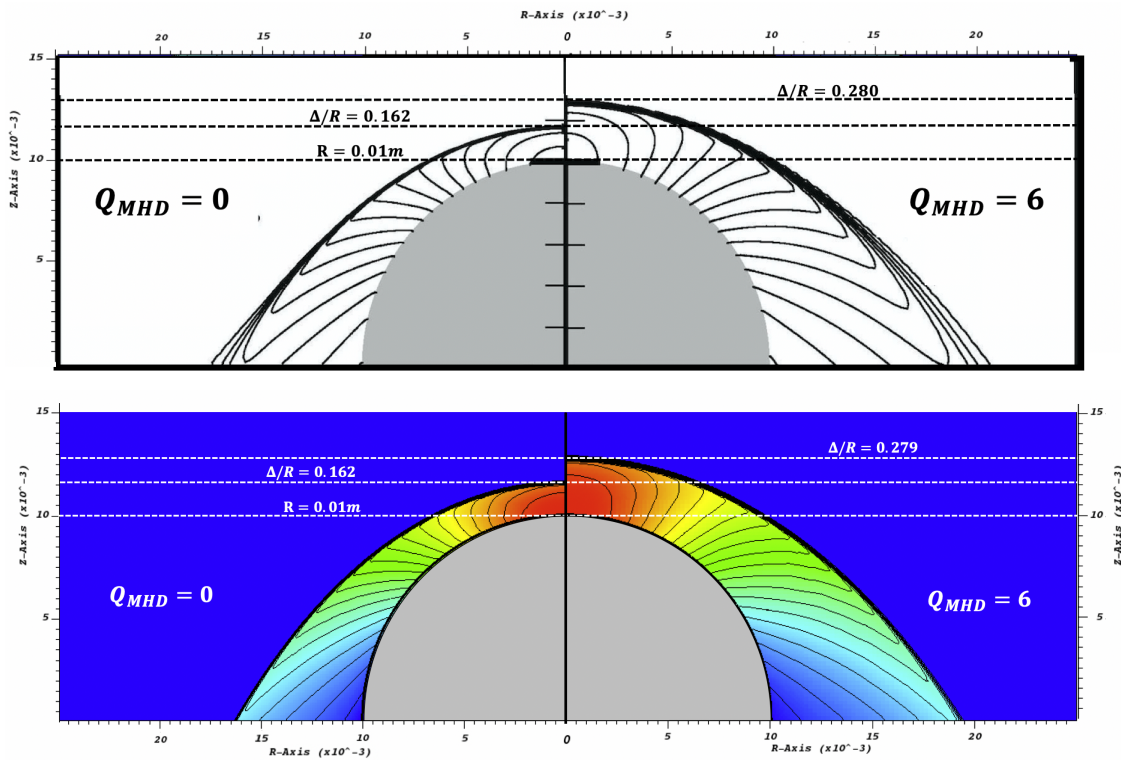


Fig. 5.21 Upper: Figure adapted from results of [19], pressure contours computed by Fujino et. al, validated in that study against Poggie & Gaitonde [20]. Lower: Pressure profiles with contours as computed in this work for $Q_{MHD} = 0$ and $Q_{MHD} = 6$.

Figure 5.22 shows that the shock stand-off distances computed under different Magnetic field strengths (corresponding to $Q_{MHD} = 0 - 6$) exhibit excellent agreement with literature results, and with the single theoretical value for the $\mathbf{B} = 0$ case where an analytic equation for shock stand-off is known as a function of Mach number and vehicle radius.

Examining also the full shock structure for the $\mathbf{B} = 0$ and $\mathbf{B} = B_{max}$ cases, Figure 5.21 shows the pressure profiles computed by Fujino et. al as compared with this work. This shows the full shock structure is in very good agreement with the literature.

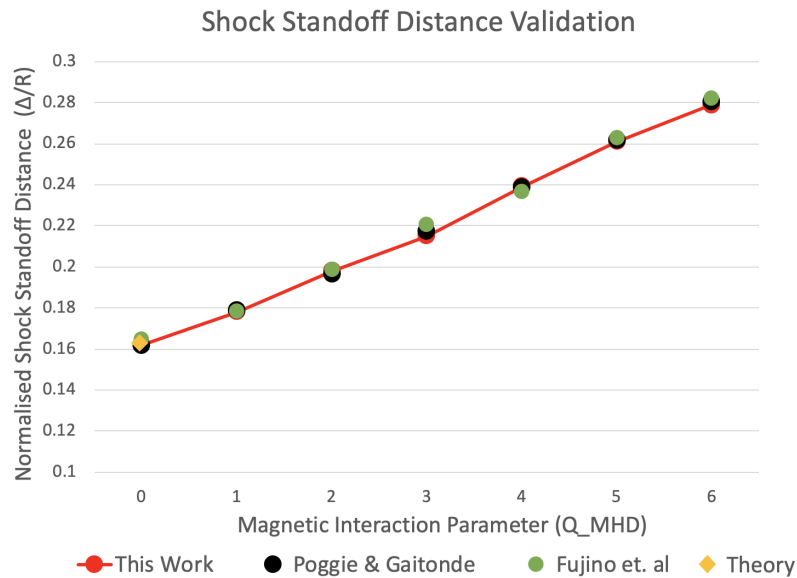


Fig. 5.22 Quantitative comparison of shock stand-off distance for this work vs previous studies for $Q_{MHD} = 0 - 6$.

5.4 Navier-Stokes fluid model

Navier-Stokes model:

$$\frac{\partial u}{\partial t} + \frac{\partial F}{\partial r} + \frac{\partial G}{\partial z} = \frac{\partial F_v}{\partial r} + \frac{\partial G_v}{\partial z} + S^c + S_v^c$$

- Compressible Navier-Stokes
- **B-field = 0**

plasma19X

ideal

Extensive validation of the Navier-Stokes model is particularly important to demonstrate that the whole-cell rigid body GFM paired with a central difference method for viscous flux calculation is able to correctly resolve viscous boundary layers and ensuring effects and interactions. A very complete set of validation test cases are conducted, where various features of the results can be compared to known solutions.

5.4.1 Subsonic flows

Subsonic boundary layer formation

The first test ensures the correct formation of a viscous boundary layer by examining the velocity profile which forms along a flat plate. Where the plate length is considerably larger than the width of the boundary layer formed from the surface, the plate can be considered

‘infinite’ and the analytic Blasius solution applies. The non-dimensional Blasius parameter is given by:

$$\eta = y \sqrt{\frac{\mathbf{u}_\infty}{\nu x}} \quad (5.4)$$

where y is the perpendicular distance away from the boundary, \mathbf{u}_∞ is the inflow velocity flowing parallel to the plate, ν is the kinematic viscosity and x is the distance along the flat plate.

As indicated through the expression for the Blasius parameter, the thickness of the boundary layer increases with the square root of distance along the flat plate.

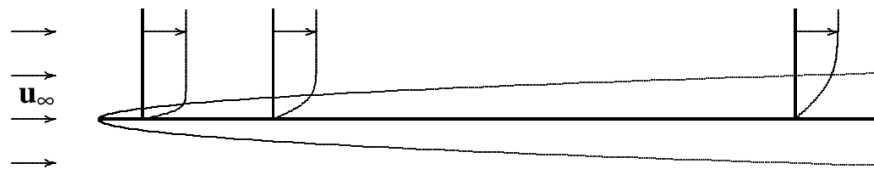


Fig. 5.23 Velocity profile through the boundary layer at varying distances along a flat plate. The boundary layer thickness doubles for every quadrupling of distance from the plate edge.

A subsonic test case is constructed which corresponds to $Ma = 0.2$ and $Re = 30,000$ for the inflow fluid. The problem set-up is for a plate of length 10 mm in a rectangular domain of size 10×1 mm with base resolution 192×192 cells and 2 levels of AMR. The fluid flow is left to right with the left side of the domain maintaining subsonic inflow conditions and right side outflow, with fluid initial conditions then given by:

Subsonic flow over flat plate:

$$\mu = 1.7886 \times 10^{-5} \text{ kg/(ms)}, u_\infty = 43.8 \text{ m/s}, \rho_\infty = 1.225 \text{ kg/m}^3, p = 41965.9 \text{ Pa}$$

Taking the velocity profile at an arbitrary point along the plate, the velocity profile of this work is compared to the known Blasius solution:

The very small discrepancy observed is likely due to an accumulation of truncation error since the compressible flow solver must run *off design* for a subsonic (incompressible) test case, requiring an extremely large number of iterations (3810 for this case, with an additional two levels of AMR time-step sub-cycling) before the boundary layer converges to a steady state along the length of the plate.

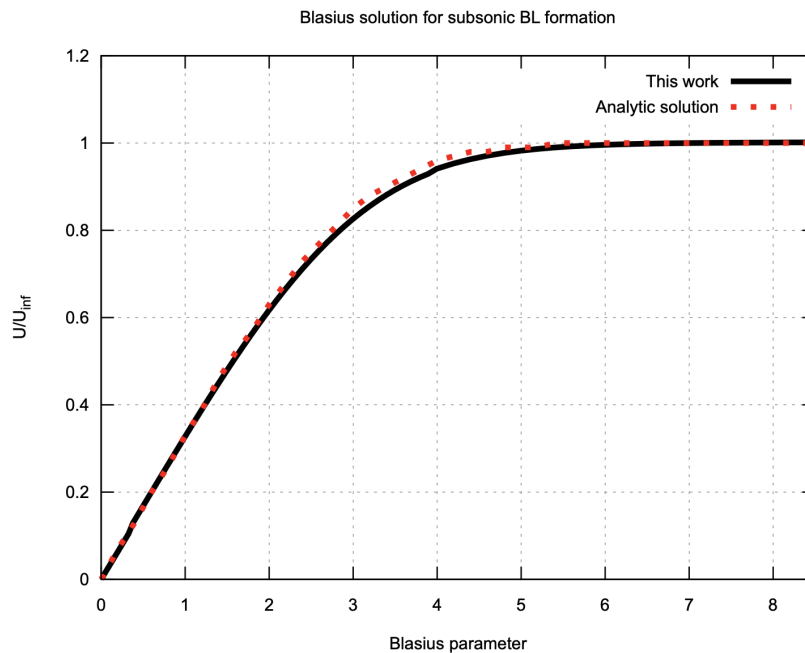


Fig. 5.24 Comparison of velocity profile vs Blasius parameter for subsonic flat plate simulation vs known solution.

Viscous flow over a cylinder - Re 100

This problem considers the subsonic 2D (Cartesian) flow over a cylinder at a Reynolds number of 100. For a viscous air flow, vortices form behind the cylinder and become detached in a process known as vortex shedding. The drag coefficient of the cylinder and the vorticity of the flow wake can be compared to experiment and to results in the literature. The frequency of vortex shedding can be quantified through the Strouhal number, which can be defined as:

$$St = \frac{fD}{U_\infty} \quad (5.5)$$

where f is the frequency of vortex shedding which can be computed from the oscillation of y -directional velocity at the point in the wake 1.5 diameters downstream of the cylinder.

The problem geometry is shown in Figure 5.25 and the initial conditions are given by:

Subsonic flow over cylinder:

$$Re = 100, M_\infty = 0.25, \mu = 1.7886 \times 10^{-5} \text{ kg/(ms)}, u_\infty = 85.07 \text{ m/s}, \rho_\infty = 1.225 \text{ kg/m}^3, \\ p = 101325 \text{ Pa}$$

The cylinder diameter is therefore calculated as:

$$D_{cyl} = \frac{Re\mu}{\rho_\infty u_\infty} = 1.7163 \times 10^{-5} \text{ m} \quad (5.6)$$

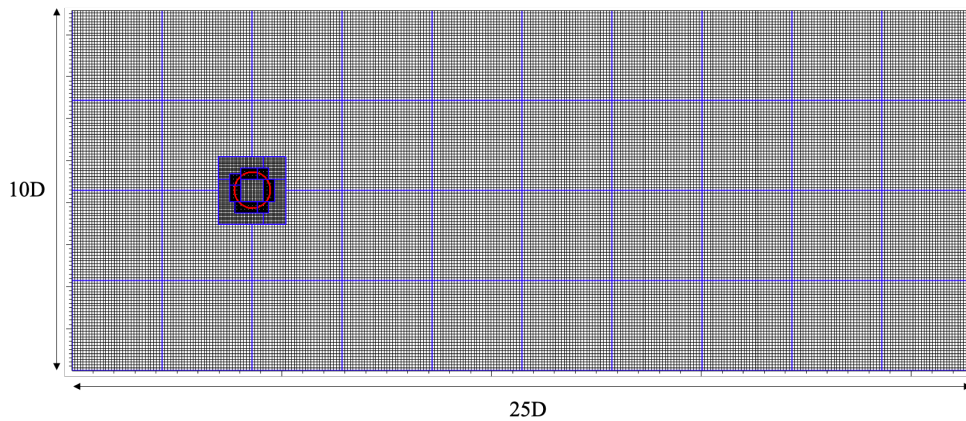


Fig. 5.25 Domain configuration for the viscous cylinder test case. Base resolution of 192×96 with two levels of AMR, refined around boundary of embedded cylinder at T_0 .

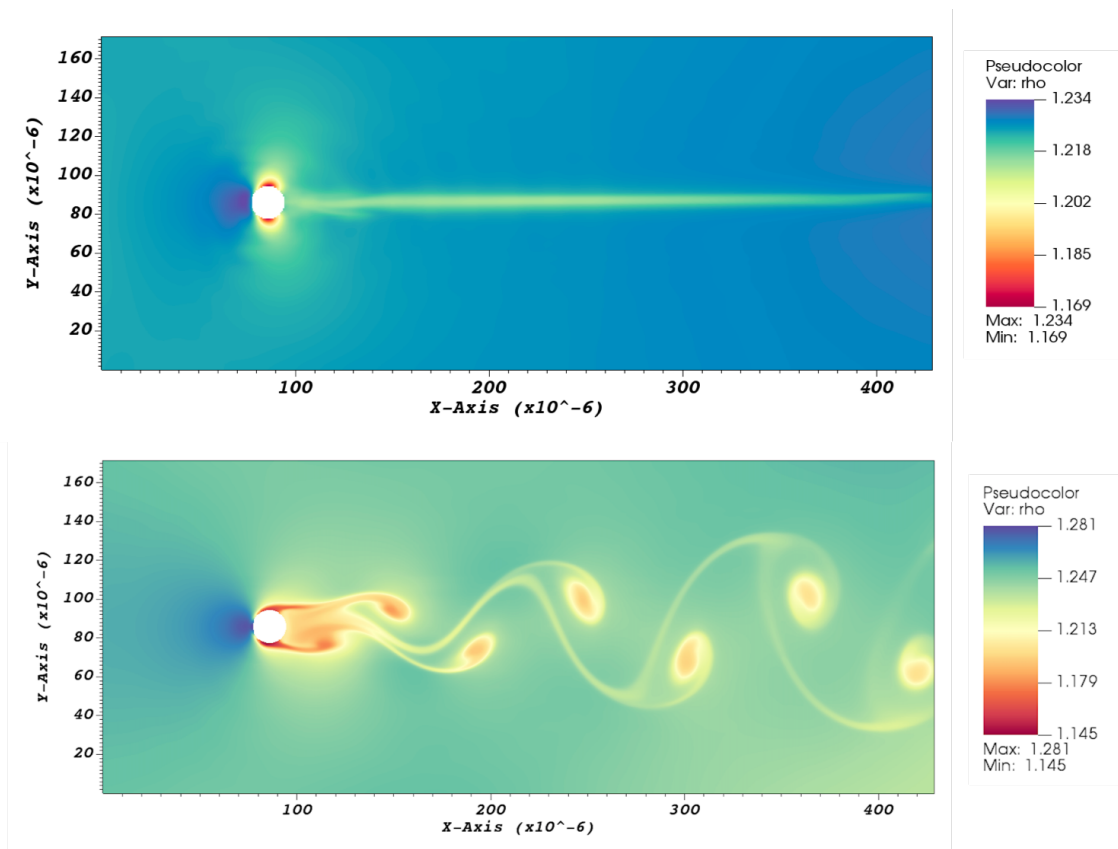


Fig. 5.26 Top) Density plot for inviscid simulation, bottom) density plot for viscous simulation

The difference between the inviscid and viscous solution is shown in Figure 5.26. As can be seen, the Von Karman vortex shedding which occurs in the wake of the cylinder in the viscous case does not form at all in the wake of the inviscid simulation.

The simulation must be of a sufficiently high resolution before the frequency of vortex shedding converges to a solution. The effective resolution is measured by the number

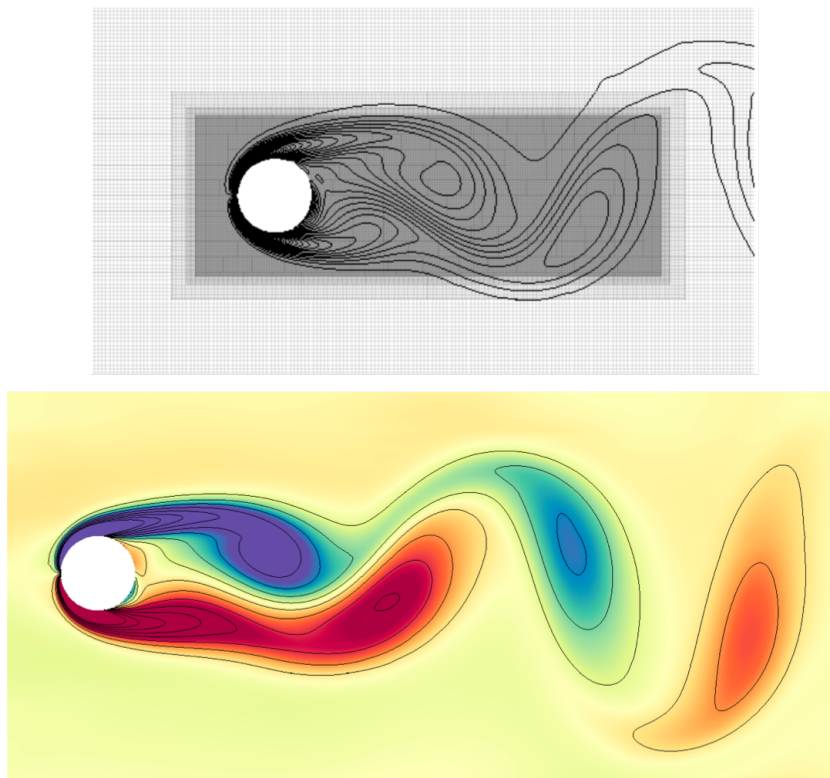


Fig. 5.27 Comparison of plots of vorticity ($\nabla \times \mathbf{u}$) with contours during steady vortex shedding formation: upper result by Gokhale [21], and lower result is this work. The results show good structural similarity.

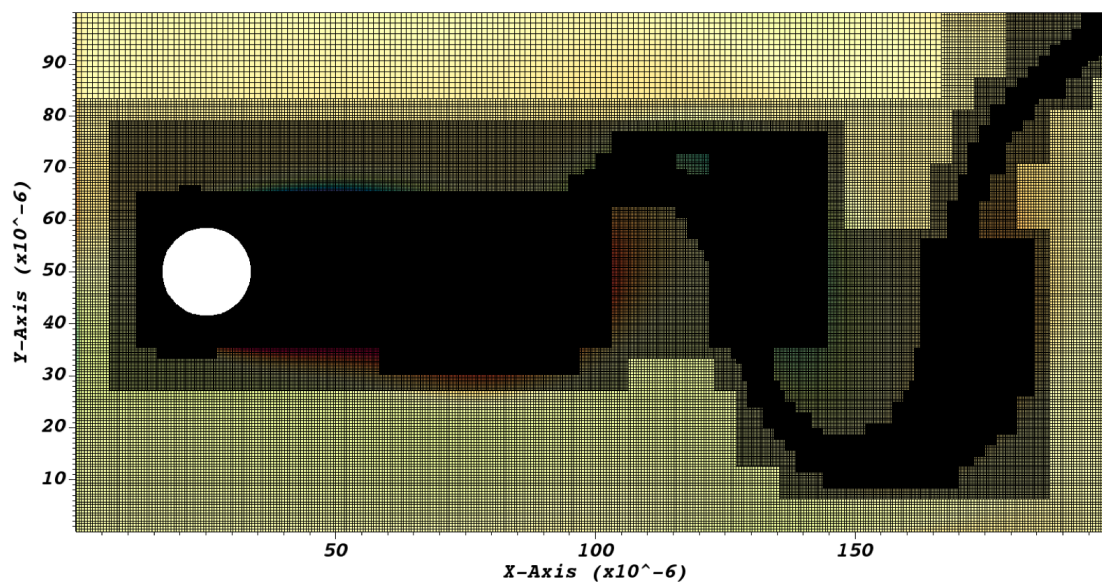


Fig. 5.28 High resolution mesh with 4 AMR levels, producing effective resolution $\frac{D}{\Delta x} = 132$.

of discrete cells within one cylinder diameter at the highest AMR refinement level ($\frac{D}{\Delta x}$). The reference simulation has effective resolution $\frac{D}{\Delta x} = 160$. A high resolution test case is simulated on a smaller domain size and with $\frac{D}{\Delta x} = 132$. A plot of the vertical velocity

Comparative works	Strouhal Number (S_f)
This work	0.166
Gokhale (2018)	0.165
Al-Marouf and Samtaney (2017)	0.164 - 0.166
Berger and Wille (1972) - experiment	0.160 - 0.170

Table 5.1 Comparison of the result of this work to two recent numerical results by Gokhale [21] and Al-Marouf and Samtaney [39], as well as an established experimental result by Berger and Wille [40].

component is shown in Figure 5.29 and its value at the point 1.5D downstream of the cylinder over time is used to compute the frequency of oscillation in the Strouhal number definition. The unsteady simulation is run for a sufficiently long time that the frequency and amplitude of oscillating v both converge to constant values.

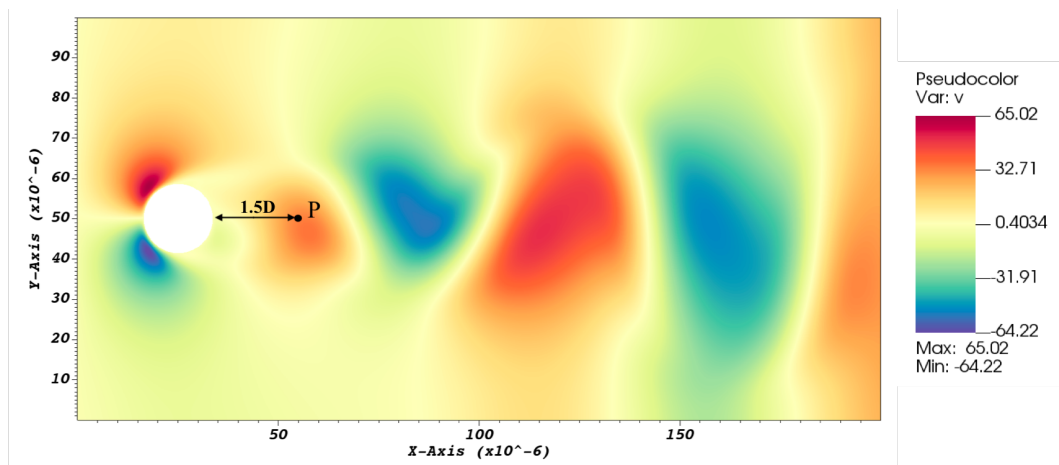


Fig. 5.29 Plot of vertical component of velocity v taken at a time interval when vortices have fully formed in the wake. A time trace of the vertical velocity at point P is taken to determine the vortex shedding frequency.

The Strouhal number is calculated to be 0.166, which is in very good agreement for the reference results in the literature presented in Table 5.1.

5.4.2 Supersonic flow tests

Supersonic flat plate

A more detailed interrogation of properties along a flat plate and through the boundary layer is conducted for a test in the compressible flow regime. The test follows the very detailed configuration details of Anderson's test problem [22]. The test problem is at a scale which ensures physically laminar flow and where viscous fluxes are of comparable magnitude to the hyperbolic flux, and so viscous stability criteria play an important role.

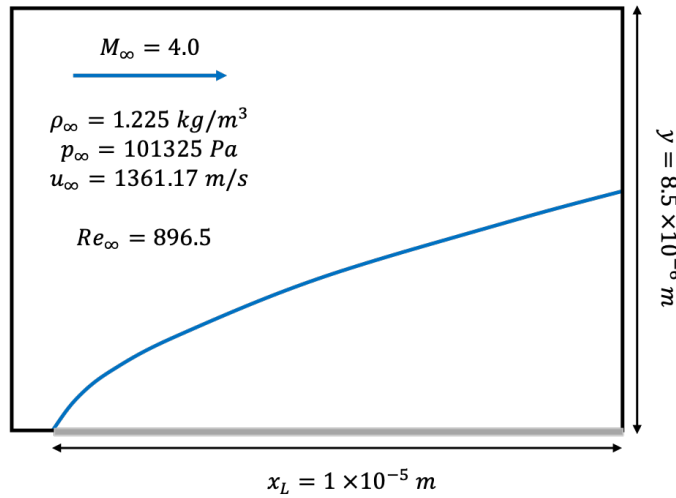


Fig. 5.30 Supersonic flat plate test configuration matching that of Anderson [22].

The height of the domain as shown in Figure 5.30 is set specifically to $5 \times \delta$ where δ is given by:

$$\delta = \frac{5 \times x_L}{\sqrt{Re_\infty}} \quad (5.7)$$

The resolution of Anderson's test case is 70×70 cells. Since the AMReX construction requires a domain cell count as a multiple of 8, the domain is configured with 80 cells across the extended length $1.1 \times 10^{-5} \text{ m}$ with excess distance ahead of plate leading edge, to match approximately the resolution along the plate surface.

Anderson's numerical method is second order accurate in space and first order in time. This work therefore employs second order MUSCL (Ultrabee) extension. Anderson cites that the simulation is stable with a CFL of 0.5-0.8. The CFL is set to 0.8 for this work.

The system is closed via the ideal gas law with $\gamma = 1.4$ and $R = 287 \text{ J/(kg} \cdot \text{K)}$, dynamic viscosity is computed through Sutherland's law, and thermal conductivity is computed assuming constant Prandtl number of 0.71:

$$k = \frac{C_p \mu}{Pr} = \frac{\gamma R \mu}{(\gamma - 1) Pr} \quad (5.8)$$

Two different wall conditions are considered for this test case: 1) the adiabatic wall condition, and 2) a fixed wall temperature condition at the ambient initial free stream temperature of 288.2 K.

The code in this work is a cell-centred data structure, therefore the plate-fluid interface occurs at the face between the first domain ghost cell and interface cell, and solutions have been plotted as shifted 1/2 cell accordingly such that $y=0$ represents the plate interface.

Both algorithms are time-marched to convergence after approximately 10^3 time steps. Property profiles are taken at the plate trailing edge at the right border of the domain, over the full height of the domain. As depicted, the leading bow shock intersects the boundary at this distance, and so the effect of this shock wave is captured in the property traces. The properties p, u and T are non-dimensionalised by their free stream values, and distance through the boundary layer is non-dimensionalised by:

$$\bar{y} = y \cdot \frac{\sqrt{Re_\infty}}{x_L} \quad (5.9)$$

Additionally the pressure along the surface of the plate is plotted.

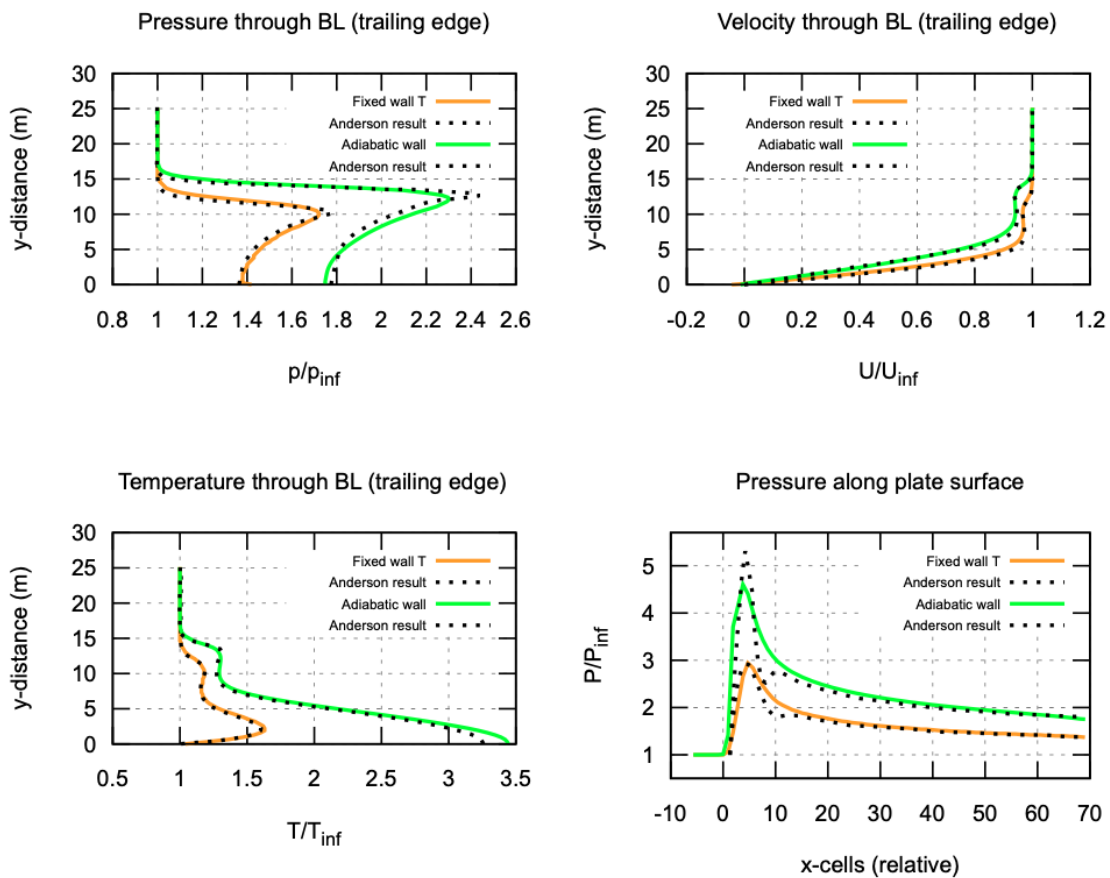


Fig. 5.31 Pressure trace taking at the plate trailing edge ($x_L = 1 \times 10^{-5}$ m) through the boundary layer. Results of this work compared to Anderson [22] for both wall conditions: Fixed wall $T = 288.2$ K and an adiabatic wall.

As can be seen in Figure 5.31, the calculations of this work are in very good agreement with the prescribed results by Anderson. The slight overshoots and undershoots of Anderson's result should be attributed to the simple finite difference scheme implemented. The slope-limited 2nd order finite volume method implemented in this work is verified to be TVD and avoid solution overshoots and oscillations. The smooth decline in pressure after the initial peak (in the trace along the plate surface) is known to follow the smooth profile of this work, without the additional undershoot of the Anderson solution.

This validation test is useful for ensuring the correct effect of implementing an isothermal wall condition versus the default adiabatic condition, with notable property differences observed in the property traces.

Supersonic flow over wedge

In section 5.1.3 of the rigid body validation, the results of the inviscid Euler model were compared to experiments and other simulations of shock-wave rigid body interactions. Looking carefully at Figure 5.8 one can notice the emergence of viscous features in the experimental Schlieren which are absent in the inviscid simulation result. This test case is therefore revisited, this time applying a full Navier-Stokes model.

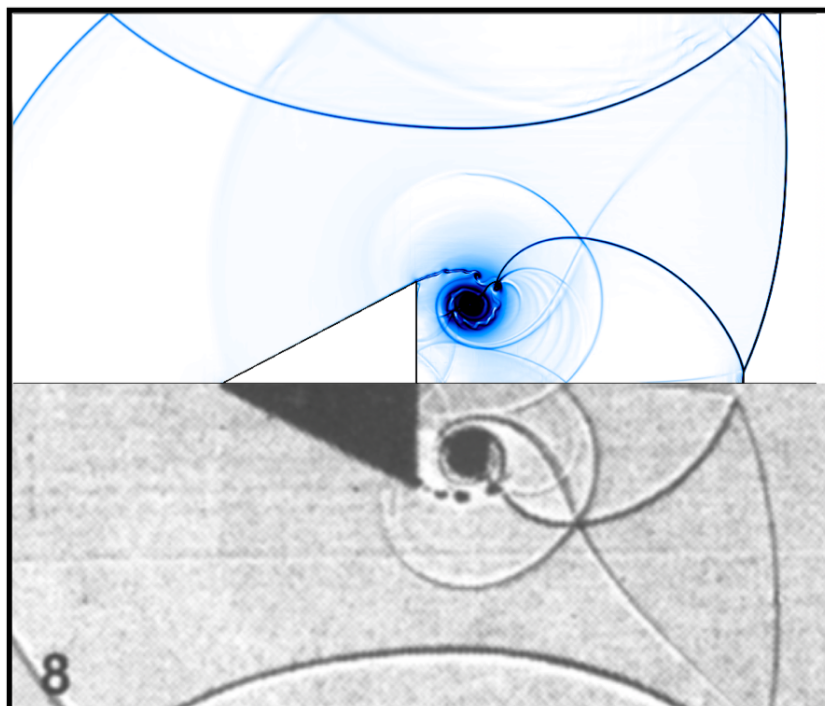


Fig. 5.32 Comparison of Navier-Stokes model numerical Schlieren (top) to the experimental Schlieren image (bottom).

Standard viscous assumptions for air are adopted: Sutherland's law for dynamic viscosity as given by equation 2.69 with standard constants for air. Thermal conductivity is set to a constant $k = 0.024$. Otherwise the problem configuration is replicated as per section 5.1.3,

but at higher resolution. The full Navier-Stokes model is run at 2.5 times greater effective resolution, with: 280×72 cells, with 4 levels of AMR. in order to sufficiently capture viscous effects which produce coherent structures on a very small spatio-temporal scale.

Figure 5.32 shows the small vortical cascade off the shoulder of the embedded wedge. Exact numerical replication of such features is notoriously challenging. Features of the numerical Schlieren show good topological agreement: the phenomenology of feature emergence, the size and the form of the coherent vortical structures show reasonable similarity. The AMR functionality of the code is highly beneficial in this simulation, where the temporal evolution of small-scale features is efficiently tracked via local mesh refinement.

Oblique shock wave boundary layer interaction

The next test consists of a supersonic flow with an oblique shock wave incident on a flat plate which reflects a shock wave whilst forming a separation region at the incident location on the flat plate. This particular test is constructed to match the NASA experiment by Hakkinen et al. in 1959 [149], where the pressure profile along the surface of the plate was measured. This test therefore serves as a very good means of experimentally validating the pressure profile produced by the extended Navier-Stokes model, which is a key parameter used when comparing the model to future experimental results, including MHD flow tests. It is particularly important to validate the model's ability to effectively capture separation and reattachment points arising from shock wave boundary layer interaction - a key feature of the flows studied in the applications of interest for this research.

In this test, a Mach 2 oblique shock impinges on the boundary layer of a flat plate causing an adverse pressure gradient leading to a separation region where a small region of flow recirculation occurs and a steady state shock structure is obtained.

The original experiment has been replicated a number of times including by Degrez et al. in 1987 [23] where they produced the Schlieren image shown in Figure 5.33, the key features of which are depicted and described in Figure 5.34.

The key test case parameters are given as:

Oblique shock wave BL interaction:

$$Re = 2.96 \times 10^5, M_\infty = 2.0, T_\infty = 160 \text{ K}, T_{0\infty} = 288 \text{ K}, \theta_s = 32.6^\circ$$

The remaining free-stream and post shock conditions are therefore computed as depicted in Figure 5.35.

The dynamic viscosity is computed using Sutherland's law and an adiabatic wall condition is assumed along the surface of the flat plate.

Since the physical boundary layer is only a few mm thick, a reduced-domain high resolution test is simulated to more accurately resolve and validate key property profiles through the boundary layer and between the plate leading edge and the impingement zone.

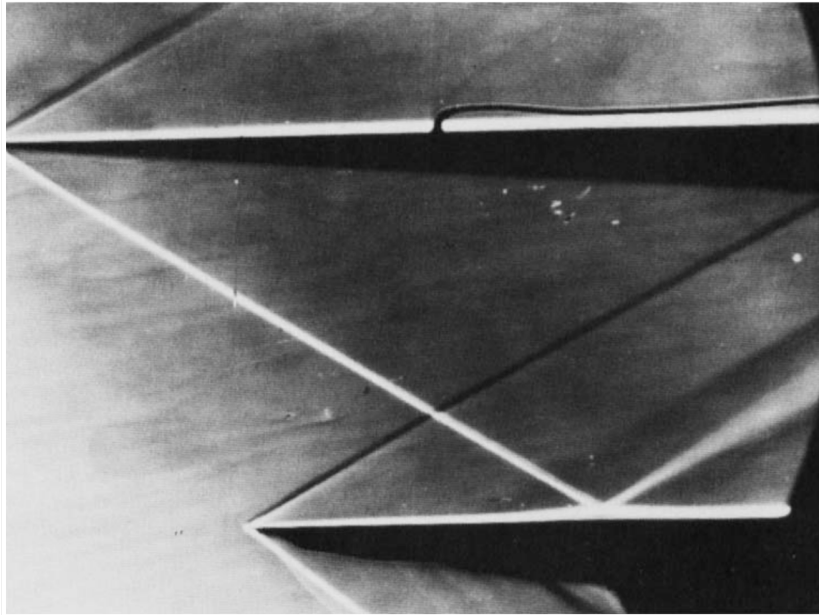


Fig. 5.33 Schlieren image captured in the experiments of Degrez et al. [23], showing steady state shock wave formation from a Mach 2.0 flow over a 3.09° angled wedge at the top of the test section which produces a 32.6° oblique shock wave impinging on the boundary layer of the lower flat plate at a distance of 0.05m from the leading edge where a secondary oblique shock has formed at an angle of 30° .

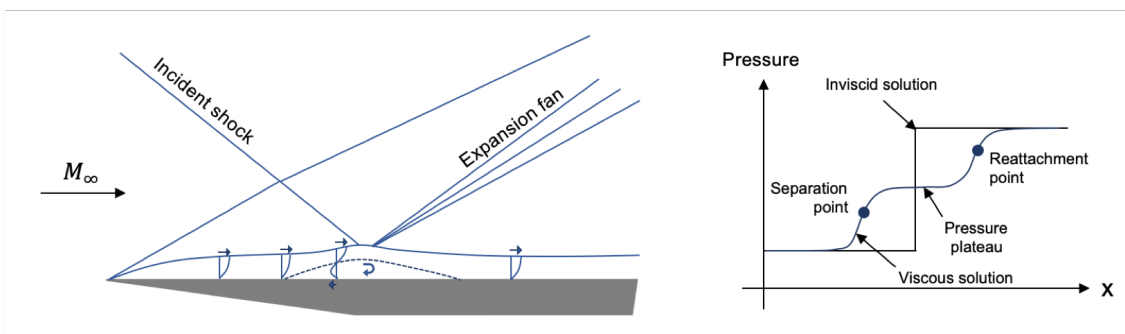


Fig. 5.34 The interaction of the impinging shock wave with the viscous boundary layer produces a separation region where there is a small amount of flow recirculation. The boundary layer (exaggerated in the diagram) becomes thickened along the plate surface downstream of the impingement point. The velocity profiles are depicted, with the impingement point resulting in a small recirculation region near the body surface. The reflected shock wave is split into two shock features separated by an expansion fan. The pressure along the surface of the plate exhibits a plateau beneath the separation region, whereas the inviscid solution only resolves a shock discontinuity at the surface.

The domain subset depicted in the middle density plot of Figure 5.36 is simulated with effective resolutions of 23.9 cells per mm in the x -direction, and 46.5 cells per mm in the y -direction.

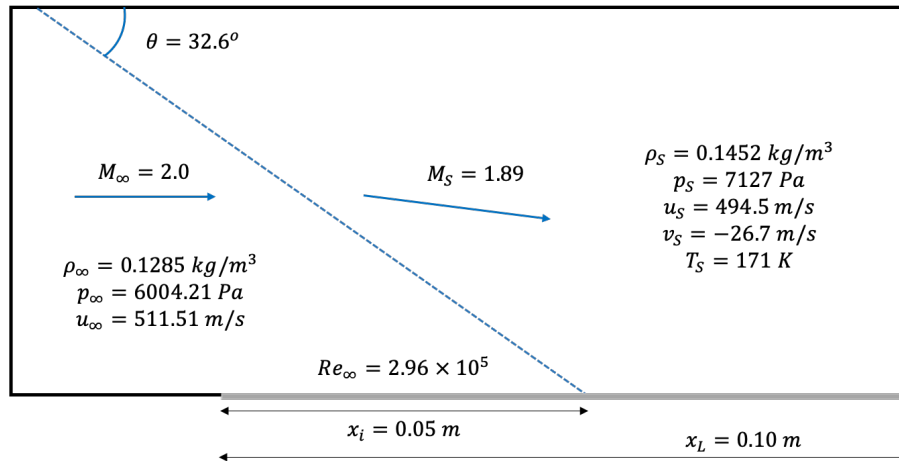


Fig. 5.35 Problem configuration and initial conditions for Oblique Shock BL interaction test. The flat plate depicted at the lower surface is configured with a no-slip boundary condition, where x_L is the plate length and x_i is the length from the leading edge to the shock impingement location. Free stream conditions denoted ∞ and post shock conditions labelled s .

A pressure trace is taken along the surface of the plate and compared with the experimental measurements of Hakkinen [149] and the numerical result of MacCormack [150]. Additionally, a trace of x -direction velocity u is taken through the boundary layer, perpendicular to the flat point, at the centre of the separation region, and compared to the result of MacCormack.

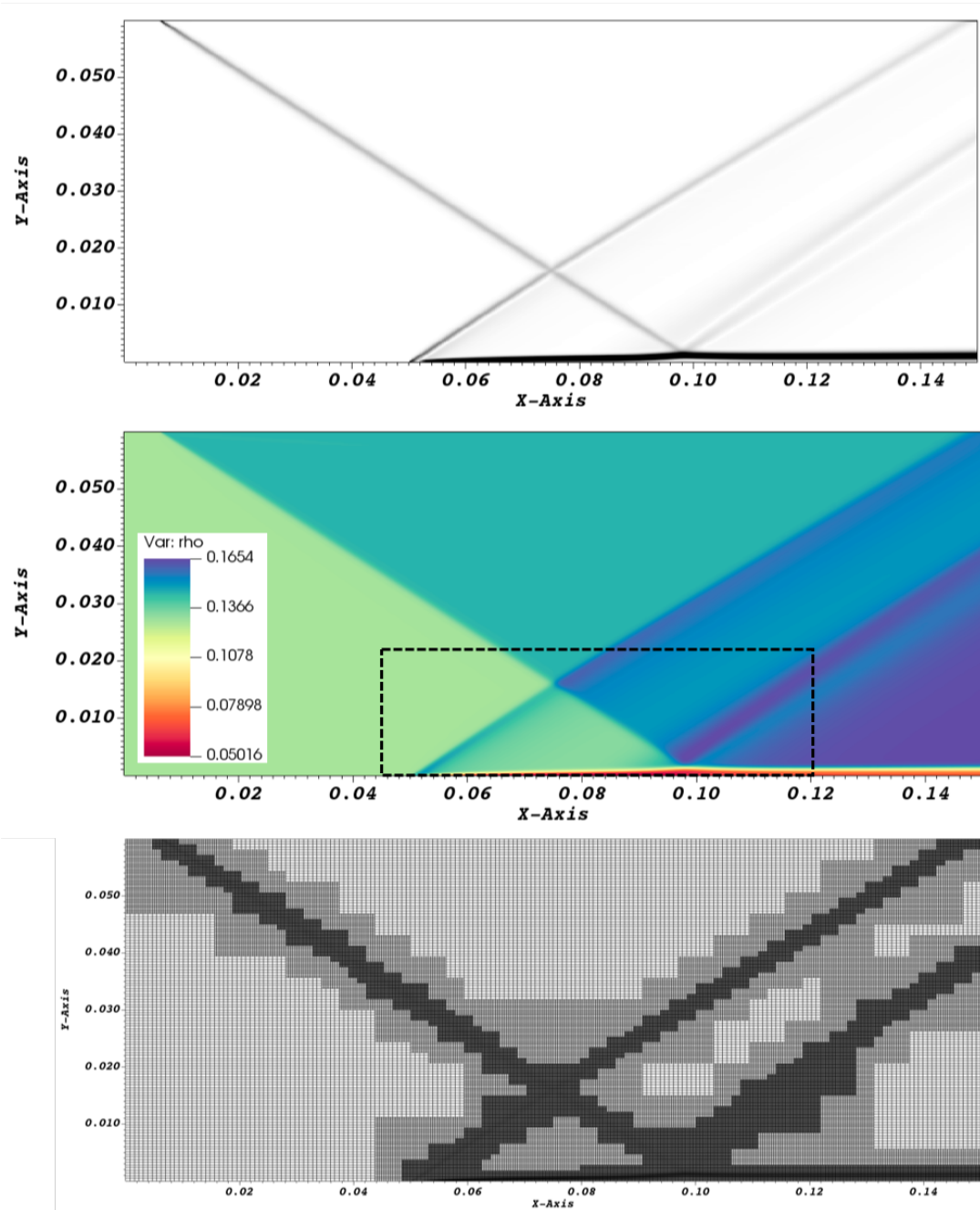


Fig. 5.36 Top) numerical Schlieren of computed result, middle) density plot showing reduced-region for subsequent high resolution test, bottom) computational mesh with base resolution: x -direction - 1.28 cells per mm, y -direction - 2.13 cells per mm, and 2 levels of hierarchical AMR, giving effective resolutions of 5.12 cells per x -mm and 8.52 cells per y -mm

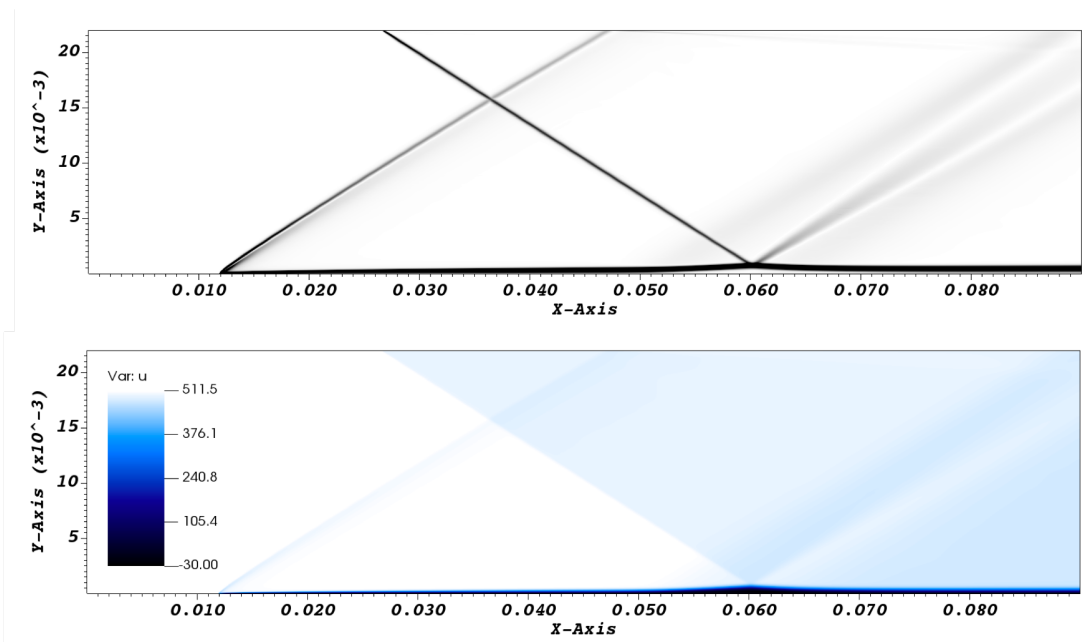


Fig. 5.37 Top) numerical Schlieren of domain sub-section, bottom) x-component of velocity showing a negative minimum velocity which occurs inside the separation region where the flow recirculates

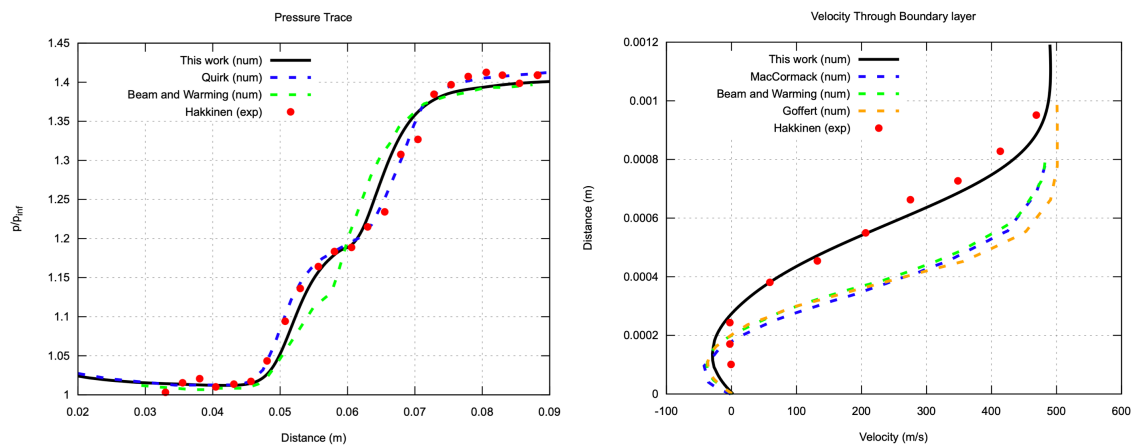


Fig. 5.38 Comparison of computed property profiles to other numerical studies (num) and to the recorded experimental values (exp). Left) trace of pressure along surface of plate, distance from leading edge, right) x-direction velocity u through boundary layer, perpendicular to flat plate at shock impingement point $x=0.061$ m. The negative velocities through the boundary layer could not be measured experimentally, thus the flat series of red dots, however is known to occur phenomenologically.

The salient features of the property traces are the kink in the centre of the pressure discontinuity (not captured at all in the inviscid case), and the initial zone of negative u -velocity away from the surface of the plate. Although the pressure plateau is evidently not as broad as the experimental measurement, the existence and location of the kink demonstrate the general features captured by the extended Navier-Stokes model. The u -profile demonstrates very good quantitative agreement with the experimental measurements, even more accurate than the other numerical models in the literature.

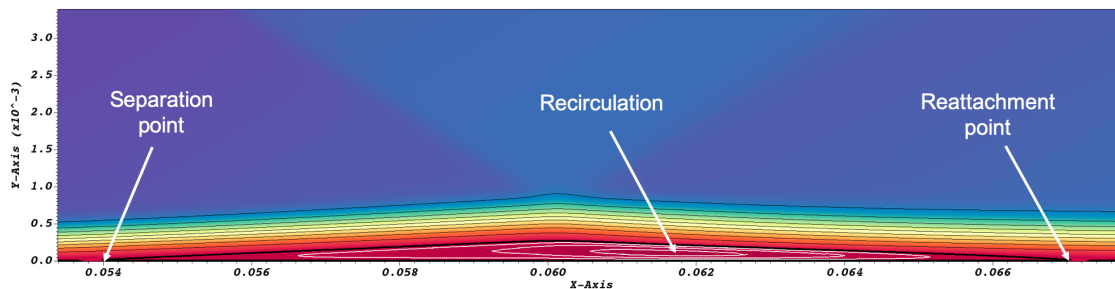


Fig. 5.39 Velocity profile through boundary layer showing separation and reattachment where the solid contour line traces $u = 0$. The white interior contours show a region of recirculation with negative u -velocity, and outer black contours are of positive velocity through the boundary layer.

In Figure 5.39 a close look is taken at the recirculation region which emerges at the shock impingement location along the bottom surface. The challenge in capturing these features within a time-explicit numerical code, is that the velocities of the recirculation are highly subsonic ($u_{min} \approx -26\text{m/s}$ at the centre of the recirculation, whereas the global fluid evolution is still restricted by the supersonic inflow conditions. The simulation must be run for a sufficiently long time to allow the subsonic recirculation to fully converge to its steady state value. This is achieved as per the quantitative comparison of profiles in Figure 5.38.

Shock reflection from a wedge

The following test considers a Mach 7.1 normal shock wave propagating left to right over a 49° inclined wedge. This test is conducted by Graves et al. [24] and has been reproduced in the literature to demonstrate the boundary shock wave interaction which forms in a viscous flow solution as compared with a known experimental result. The initial conditions of the problem are depicted in Figure 5.40.

The ratio of the length of the Mach stem offset from the wall compared with the length the Mach stem has travelled up the wedge incline is compared to experiment and other literature test cases. With reference to the problem configuration diagram of Figure 5.40, this is calculated as:

$$R_M = \frac{L_M}{L_R} \quad (5.10)$$

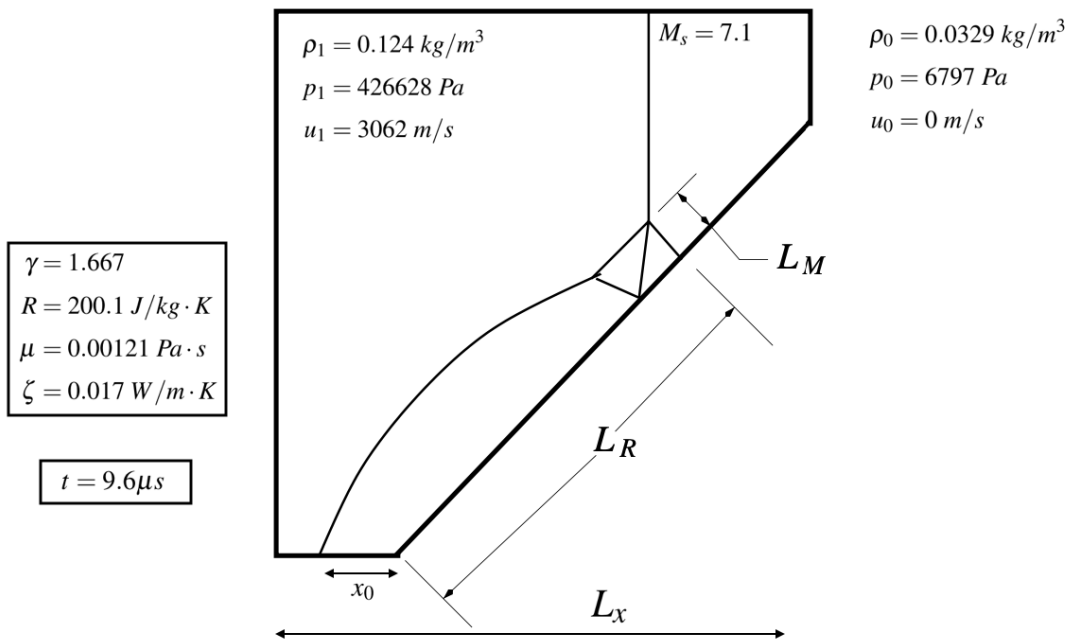


Fig. 5.40 Problem configuration including initial conditions for upstream gas (state 0) and post-shock gas (state 1). Gas constants for the problem are given on the left, and the Mach stem is depicted for the desired time evolution of $9.6 \mu s$. The length x_0 is the initial distance between the wedge and the normal shock at time = 0, and L_x is the 2D domain length. Both the 49° inclined wedge and the lower wall are viscous no-slip boundaries. Remaining domain boundaries are transmissive.

The inclusion of viscosity causes shock separation at the wedge leading edge and a vortex feature forming ahead of the wedge, it also causes the ratio R_M to become significantly reduced. The inviscid result and resultant mesh is shown first for comparison in Figure 5.41.

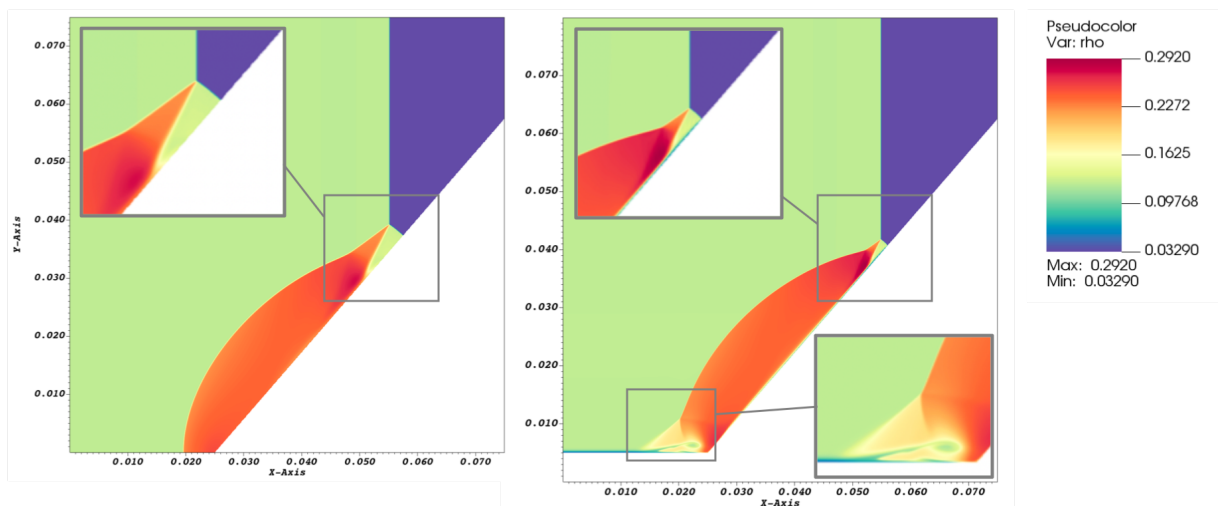


Fig. 5.41 Left) inviscid solution, right) viscous solution, at time = $9.6 \mu s$.

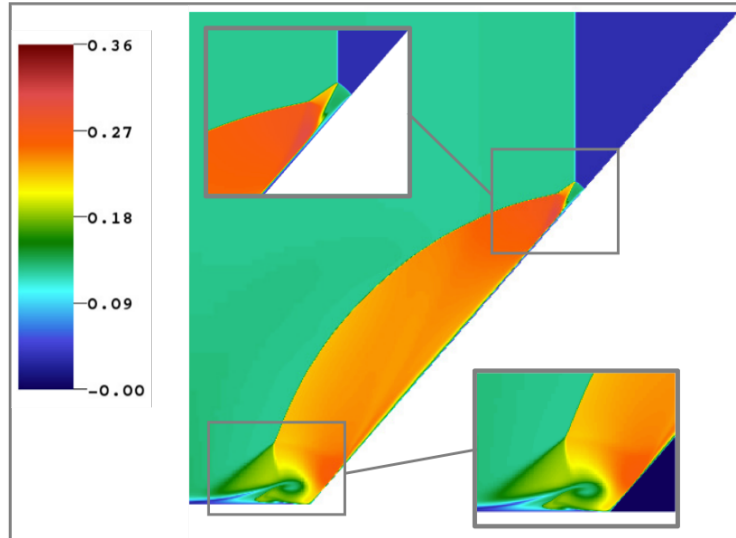


Fig. 5.42 Numerical solution from Graves et al. [24] for the viscous case, at time = 9.6 μs .

Comparison of the computed viscous solution of this work shows excellent agreement with the solution published by Graves et al. [24] including the reduced size of the Mach stem, and the vortex formation ahead of the wedge.

It is important that the test be of sufficient resolution to accurately capture the boundary layer, vortex formation and Mach stem lengths. Therefore the base resolution of the defined problem is set to 160×160 with 4 levels of AMR implemented around the geometry boundaries and high density gradients - shown in Figure 5.43. It is found the Mach stem ratio R_m converges to a consistent value by the resolution, and remains constant for higher resolution runs - therefore demonstrating the grid-independence of the numerical solution.

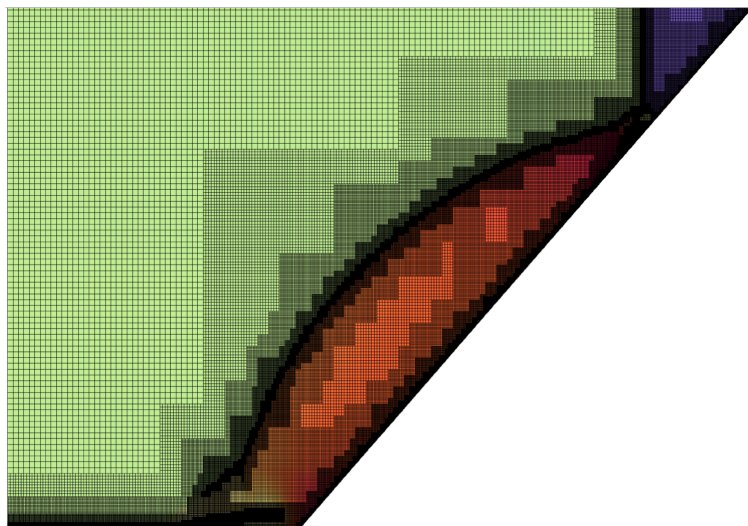


Fig. 5.43 Adaptively refined mesh for the viscous solution at time = 9.6 μs .

Comparative works	Strouhal Number (S_f)
This work	0.0298
Gokhale (2018)	0.0293
Al-Marouf and Samtaney (2017)	0.0270
Graves et al. (2013)	0.0300

Table 5.2 Comparison of R_M ratio between this work and reference sources: Gokhale [41], Al-Marouf and Samtaney [39], and Graves et al. [24].

Quantitative measurement of the the Mach stem ratio is conducted with results presented in the table of Figure 5.2. The result of this work falls nicely within the range of reported values in the literature.

5.5 plasma19X real-flight EoS validation

The extended property spaces of plasma19X were presented in Chapter 3, as well as the improved search and interpolation routines. Here we validate the plasma19X EoS as embedded within the full hydrodynamic model. We can assess the resultant flow solutions for flight tests where real gas chemistry effects are important.

5.5.1 Equilibrium validity for reentry regime

Damevin & Hoffmann [122] employ a 5-species non-equilibrium chemistry model for various Mach numbers and altitudes, and compare results to a 5-species equilibrium chemistry model for the highest Mach number case. We use this test case of a Mach 18 flow at 30 km altitude to validate the property profiles along the stagnation line for their equilibrium and non-equilibrium chemistry models (denoted DH in the figures) to the results of both the new plasma19X and ideal gas models of this work.

The geometric configuration of this test is a 0.12 m radius cylinder (Cartesian coordinate system). Real atmospheric properties are used for ambient free stream conditions in accordance with the US Standard Atmosphere [151].

Free stream test conditions:

$$M_\infty = 18.0, \rho_\infty = 0.01841 \text{ kg/m}^3, p_\infty = 1197.0 \text{ Pa}, V_\infty = 5430.27 \text{ m/s}$$

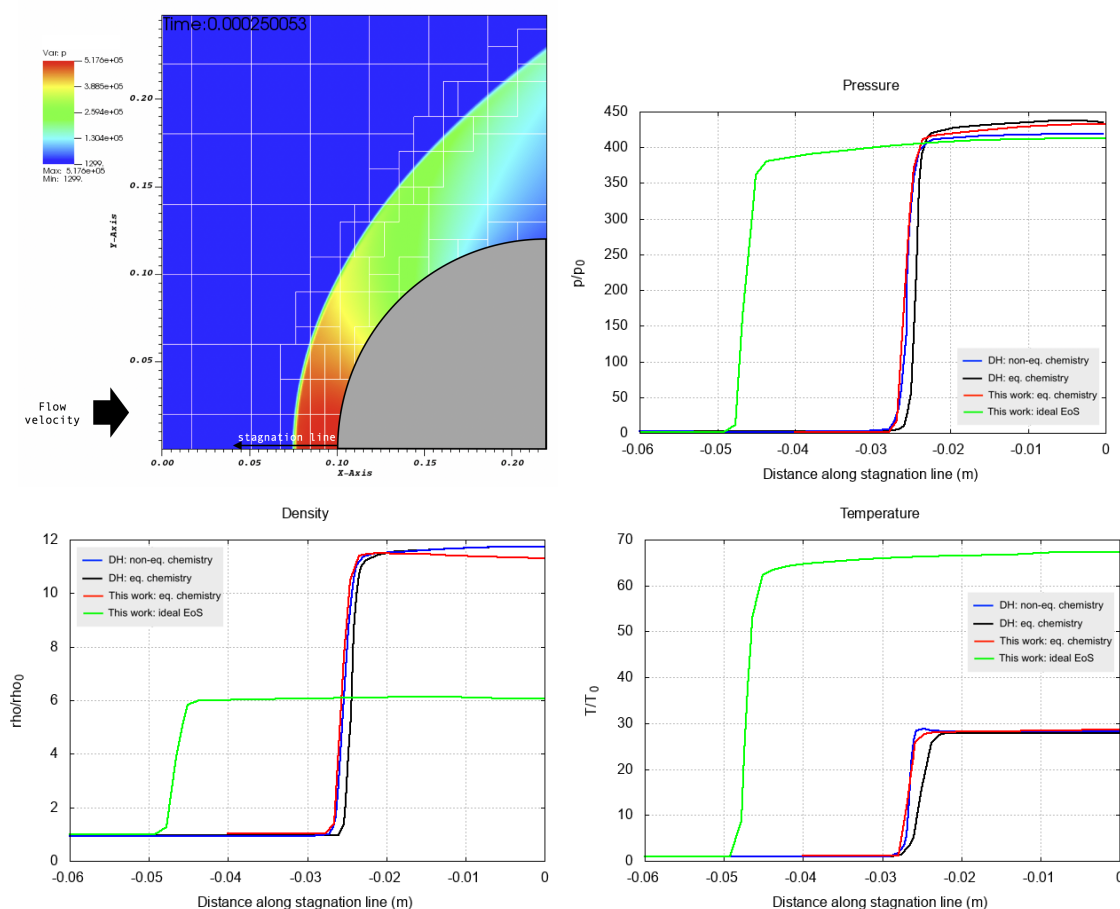


Fig. 5.44 2D plot of pressure, and property profiles along the stagnation line, comparing the models of Damevin & Hoffmann (DH) to the chemistry model of this work for the 30km altitude Mach 18 test case.

Damevin & Hoffmann concluded in their work that the equilibrium model exhibits excellent agreement with the non-equilibrium model for up to very high Mach numbers, in the lower altitude range (30km-50km). The key difference for higher altitudes at lower atmospheric pressure being the very short spike in temperature post shock where chemical reactions have not yet relaxed to equilibrium. Capturing this very small non-equilibrium chemistry portion limits full system computation to the time scale of chemical reactions, adding significant computational cost.

As shown in Figure 5.44, the results of this work are in very good agreement with the Damevin & Hoffmann studies. The stagnation line property trace is in closer alignment in fact with the non-equilibrium, than equilibrium model, though all three have high similarity. The shock stand-off distance and peak temperatures computed under the ideal gas law clearly demonstrate that this EoS is inadequate for capturing the real gas behaviour within the tested regime.

Therefore, it is concluded that the equilibrium model of this work provides an accurate and efficient gas chemistry model for bulk thermodynamic properties in the high Mach number regime at free stream properties corresponding to a sub 50 km altitude range.

5.5.2 Reentry flight electron number density measurement

Obtaining any experimental data for shock properties during real reentry vehicle flight is, understandably, precarious. However, in 1973 - and to the jubilation of CFD developers ever since - NASA launched a rocket from the test facility on Wallops Island Virginia, aimed at testing radio-blackout during reentry. The so-called **R**adio-Frequency **A**ttenuation **M**easurement **C**apsule (RAM-C) vehicle has since been seminal for the validation of codes aimed at simulating plasma formed around reentry vehicles, since measurements of electron number density were recorded along various points on the vehicle body. Electron number density is a key parameter in studying the communications attenuation problem experienced during re-entry.

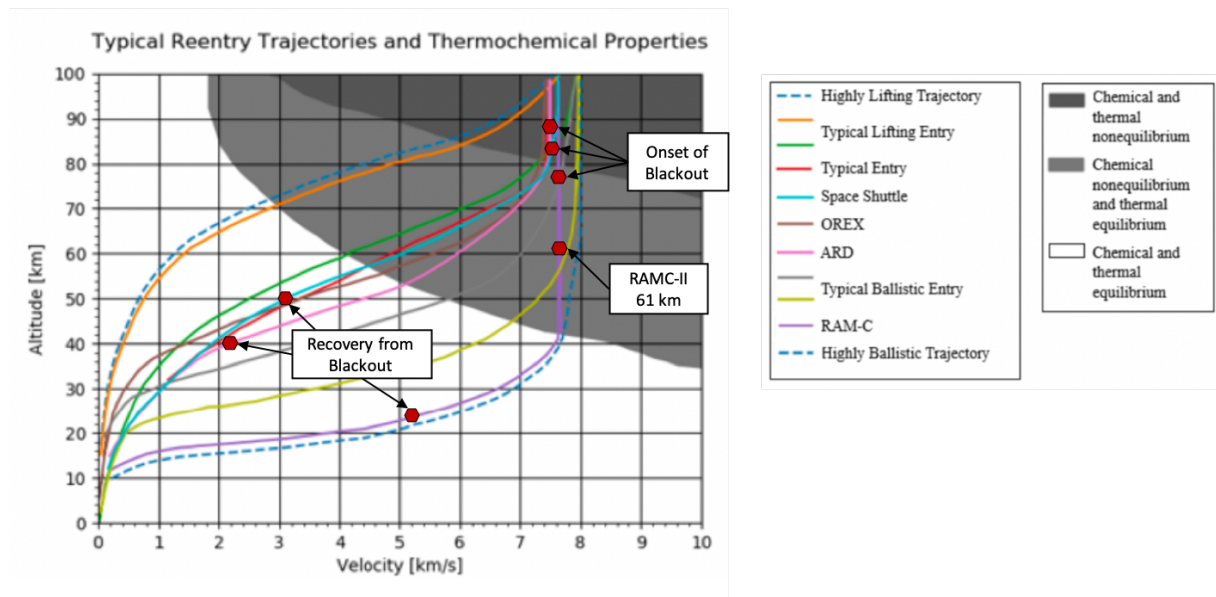


Fig. 5.45 Reentry trajectory and thermochemical assumptions map with known markers of blackout onset and recovery as reported by Savino et al. [25]. RAMC-II test point of this analysis also marked.

The RAM-C II reentry trajectory was known to produce a weakly ionised plasma sheath down to an altitude of 15km, with the peak plasma density occurring at 27 km altitude [152]. Radio-blackout persisted as low as 24 km altitude. The RAM-C II vehicle geometry is depicted in the diagram of Figure 5.46. The probe locations are depicted whereby the electron number density was measured as the peak value outward (in the normal direction) from the vehicle surface at various points along the body.

Studies tend to adopt a 5-species: [49, 59] 7-species: [153–156] or 11-species: [112, 155, 61] non-equilibrium chemistry model, though 11 species equilibrium chemistry models

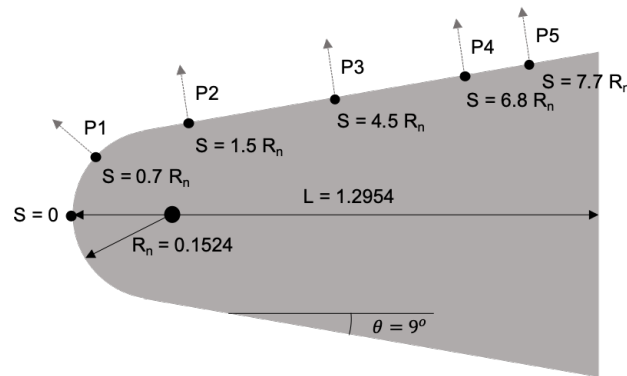


Fig. 5.46 RAMC-II geometry with marked probe positions along vehicle surface

have also been adopted [26]. By cross-comparison across all of these studies however, again significant discrepancies between computed electron number density arise. Figure 5.47 compiles the computed peak electron number density at various altitudes with the corresponding flight condition of the RAM-C experiment, as generated by the different models. Results are shown to vary by up to almost 2 orders of magnitude across the different altitude conditions. Results for peak N_e cannot be compared to the experiment because peak N_e occurs in the stagnation region of the vehicle where there is no probe located (shown in Figure 5.46). Whilst we show from the velocity altitude map (Figure 5.45) that the shock layer cannot be treated in general as being in equilibrium for altitudes of approximately 42 km and above, the stagnation region specifically where peak electron number density occurs is very likely to be equilibrated, so comparison of peak N_e is not fraught, though some caution should still be taken. Simulations could not be run at > 71 km however, since free-stream pressure falls below the limit of the plasma19X table ($p_{min} = 7.55187$ Pa).

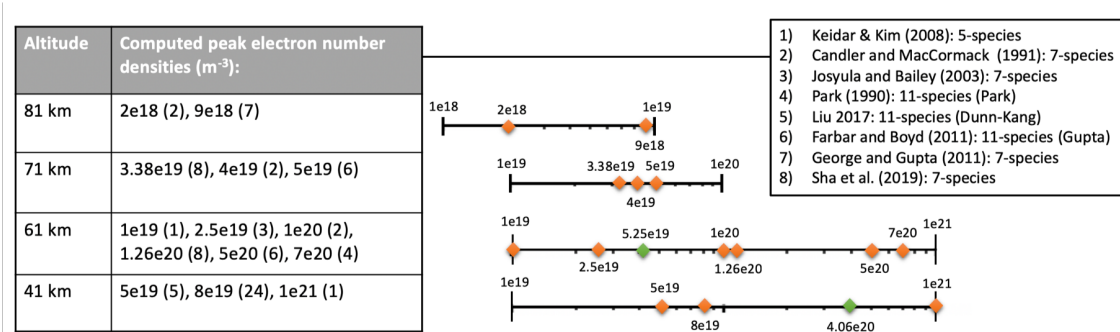


Fig. 5.47 Compiled results for peak N_e from different model in the literature, as listed. Literature results presented along log-scaled number lines in orange, with the computed results of this work for 41 km and 61 km altitude shown in green.

While radio blackout was found to persist down to an altitude of about 24 km, incomplete data was obtained for the lower altitude range. Complete data is obtained for the 71 km and 61 km altitude marks. Whilst the 61km altitude is identified to be beyond the limits of the equilibrium validity range, equilibrium solvers are still found to perform surprisingly

well in calculating peak N_e values along the vehicle surface, as examined by Shang [26]. Given the absence of real-flight experimental data below this altitude, we use the 61km case, with the caution that complete accuracy is not expected in this regime, as compared with approximately the < 50 km altitude range where equilibrium would be expected.

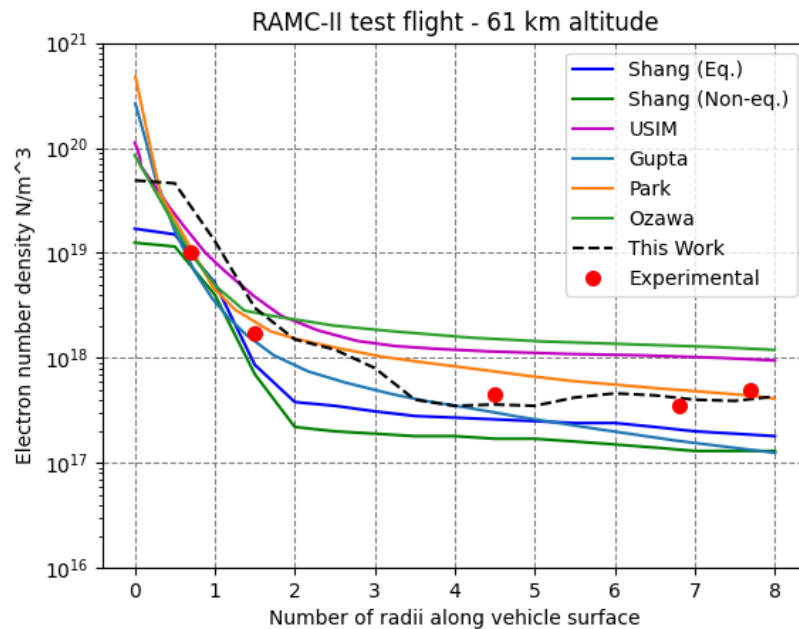


Fig. 5.48 RAMC-II electron number density comparison of a collection of literature results: Equilibrium and non-equilibrium solution compared by Shang [26], a 7-species non-equilibrium result (USIM) computed by Kundrapu [27], the various 11-species equilibrium results of Gupta [28], Park [29] and Ozawa [30], compared with the plasma19X result of this work.

The simulations of this work are run as full Navier-Stokes fluid model, with adiabatic wall condition and plasma19X as the gas chemistry model. As shown in Figure 5.48 the equilibrium result computed in this work falls within the reasonable range of computed values from the various non-equilibrium and equilibrium chemistry results in the literature. The full computed temperature and N_e profiles are shown in the composite plot of Figure 5.49. This plot highlights the temperature-dependency of the chemical reactions leading to ionisation and production of free electrons.

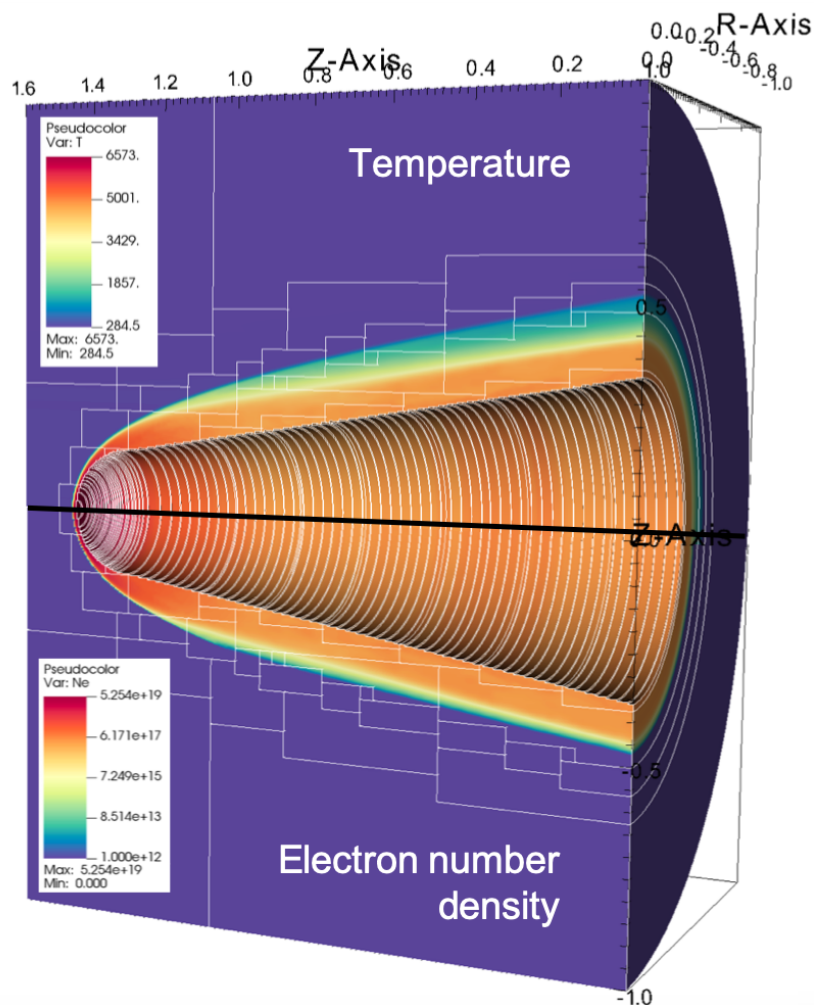


Fig. 5.49 RAMC-II plot of computed steady state temperature and electron number density profiles for 61 km flight conditions.

5.6 Hypersonic double cone tests

These tests are particularly important for validating the model of this work, since one of the key test problems of interest in the subsequent chapter is a hypersonic flow over a double cone model with imposed magnetic effects. Performance of the Navier-Stokes model of this work (without magnetic effects) with plasma19X EoS provides the base physics before such a complex test (additional of mHD effects) can be attempted.

The hypersonic double cone tests are famously used for the validation of Navier-Stokes codes to model non-simple geometries and capture boundary layer shock wave interactions. Experimental data has been obtained from a large number of tests in the CUBRC LENS facilities [157] producing a high enthalpy, hypersonic, laminar flow with shock wave boundary layer interactions.

Accurate simulation of this flow, capturing all flow features, requires the full Navier-Stokes system with capacity for solving highly hypersonic flows to a steady state with a

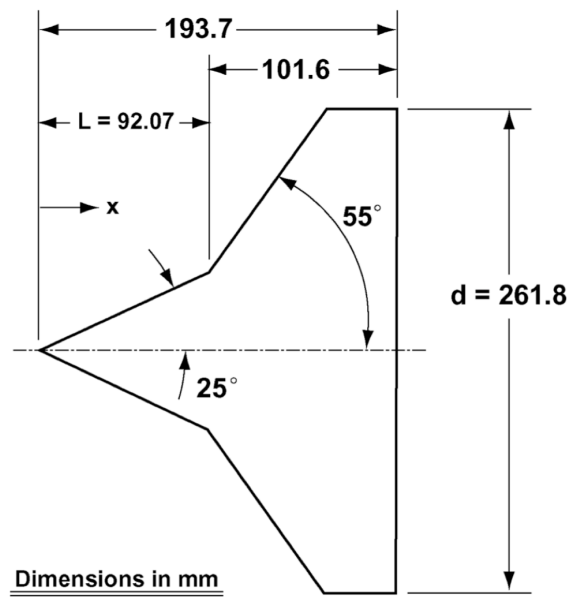


Fig. 5.50 Geometry specifications of the CUBRC 25/55° double cone model

complex geometry. The schematic of Figure 5.51 shows a numerical Schlieren result from the model of this work for a typical CUBRC test condition (test run 1 is chosen as it is a clear and average representation of the features formed across *all* CUBRC test cases). This demonstrates the ability of the Navier-Stokes rigid body GFM model to capture the complete feature formation known to be produced for all test cases at steady state.

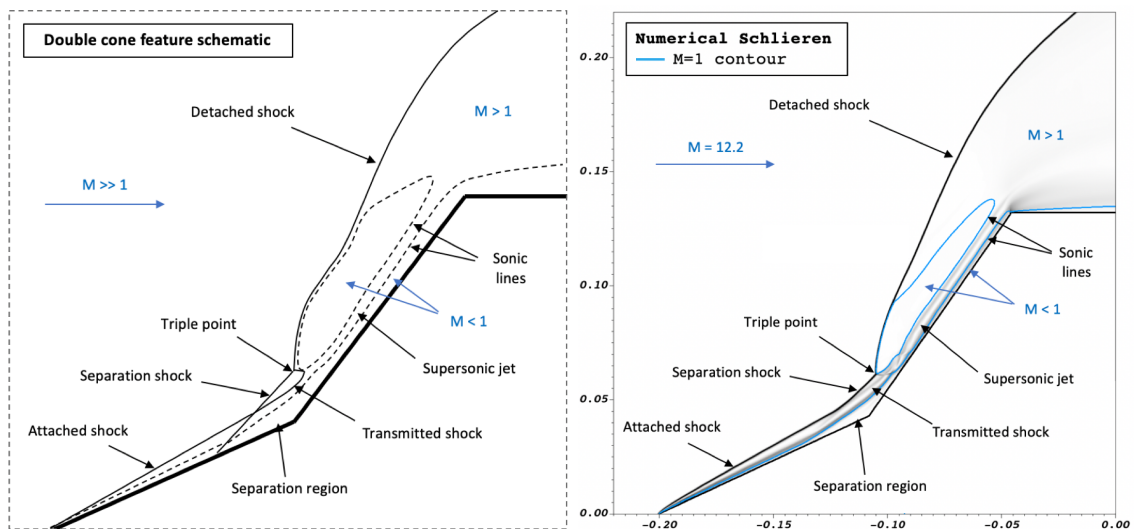


Fig. 5.51 Top) schematic of features formed in hypersonic double cone flow, bottom) numerical Schlieren result of this work from test conditions of the CUBRC run 1 flow. Comparison shows complete feature formation captured by the full Navier-Stokes rigid body GFM model of this work for a hypersonic flow over a non-simple geometry.

The full 3D depiction of the flow is given by the revolved plot of Figure 5.52.

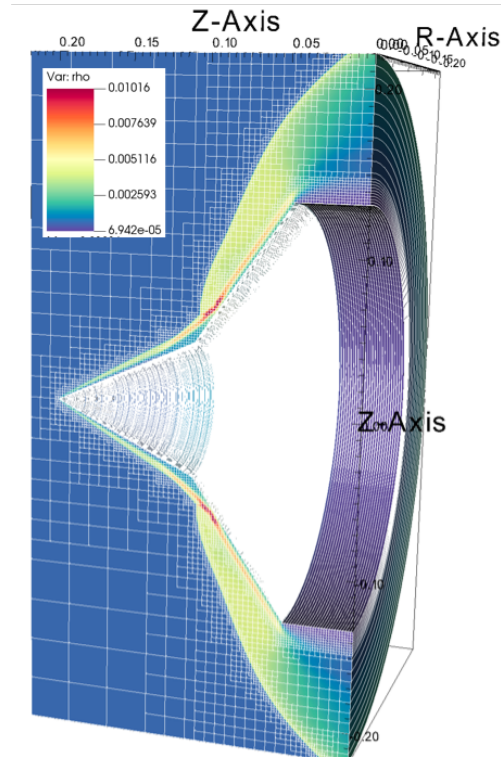


Fig. 5.52 3D rendered visualisation of the double cone flow for CUBRC run 1 conditions. Plot of density is shown with AMR block borders indicating regions of adaptive refinement.

5.6.1 Non-reactive Nitrogen test

To validate the system quantitatively a pressure trace is taken along the surface of the vehicle and compared with the results of the experiments and other simulations. The first case considers the test run 7 conditions for non-reactive nitrogen (N_2) gas, where experimental data could be obtained for the pressure trace along the model surface. With comparative result shown in Figure 5.53.

CUBRC run 7 conditions:

$$M = 15.6, V_\infty = 2073 \text{ m/s}, T_\infty = 42.6 \text{ K}, T_w = 300 \text{ K}, \\ \rho_\infty = 1.57 \times 10^{-4} \text{ kg/m}^3, p_\infty = 2.23 \text{ Pa}, \text{ Gas} = N_2$$

Good agreement has known to be able to be attained in the literature for this case where the Nitrogen test gas is effectively un-reactive, and solutions employ ideal gas models to simulate non-reactive nitrogen with $\gamma = 1.4$, $R = 297.0$ and Sutherland's law for viscosity adopts the coefficients for Nitrogen: $b = 1.663 \times 10^{-5} \text{ kg}/(\text{ms}\sqrt{K})^{-1}$, and Sutherland's temperature $S = 107.0 \text{ K}$.

The numerical result of this work shows very good agreement with the calculations by other Authors, and with the experimental pressure values. All numerical models tend to under-predict the length of the separation region, and we observe a small additional pressure dip along the second surface in the numerical results of Nagata and Moss which is absent in

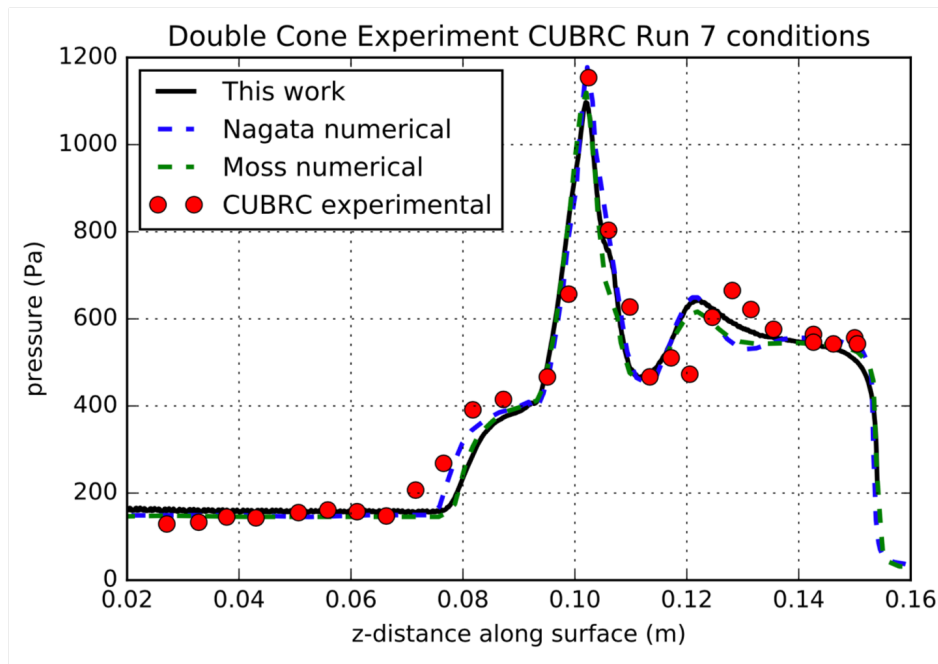


Fig. 5.53 Pressure trace along surface of double cone: CUBRC run 7 result of this work compared with experimental result and simulations of Nagata et al. [31] and Moss et al. [32].

the calculation of this work and also unclear in the experimental result. Given the complexity of the double cone flow dynamics, this result can be considered to effectively capture the key feature of the surface pressure.

5.6.2 Reactive air test

For other cases including air test runs, where real reactive gas effects are at play, good quantitative agreement between experiment and simulation remains illusive and has been the subject of many studies: [83, 158, 157] among others. Though all models struggle to exactly match experiments in terms of heat flux and pressure distribution, generally good agreement is found between numerical models themselves. Zuo recently (2021) [159] showed that for runs with air as the test gas, similar results are obtained between thermochemical equilibrium and non-equilibrium models in terms of qualitative flow structure and key surface properties. Another recent (2020) study by Holloway [33] showed that equilibrium and non-equilibrium models demonstrated reasonably good agreement in terms of overall shock structure and property fields for the air-gas composition test case.

The air test case of CUBRC run 43 is studied by Holloway [33] and compares results for 11 species equilibrium and 11 species non-equilibrium (two-temperature) models. The quantitative results of these models are compared to the result of this work and the experimental data, as shown in Figure 5.54.

CUBRC run 43 conditions:

$$M = 8.87, V_\infty = 4267 \text{ m/s}, T_\infty = 576 \text{ K}, T_w = 296.2 \text{ K},$$

$$\rho_\infty = 2.134 \times 10^{-3} \text{ kg/m}^3, p_\infty = 352.77 \text{ Pa}, \text{ Gas} = \text{Air}$$

The simulation of this work is conducted with the plasma19X equilibrium EoS, with μ calculated from Sutherland's law with standard air constants, and thermal conductivity calculated directly as a stored transport property of the EoS. An isothermal wall condition is applied with $T_w = 296.2 \text{ K}$ to replicate the condition over the short time span of the experiment.

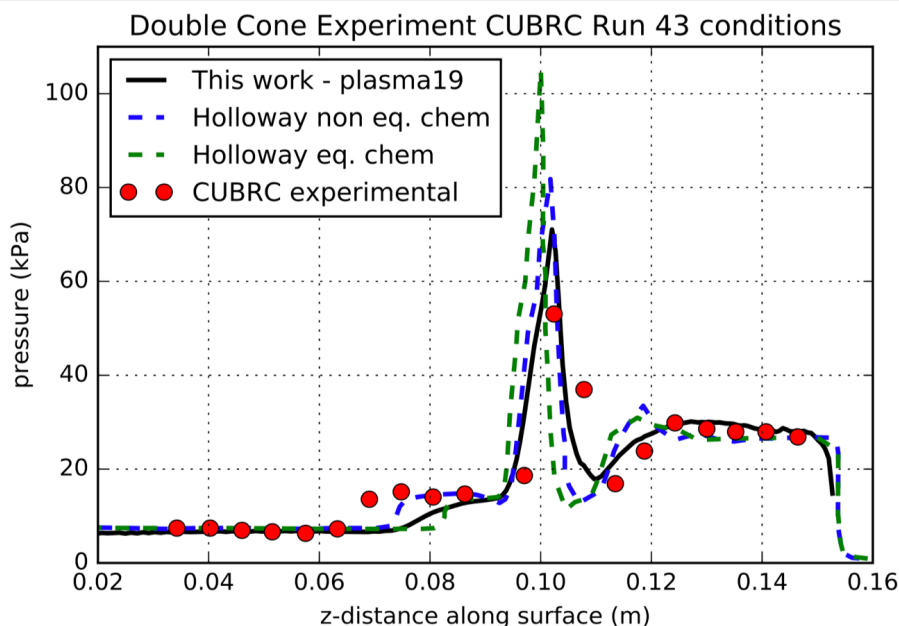


Fig. 5.54 Pressure trace along surface of double cone: left: CUBRC run 7 compared with experimental result and simulations of Nagata et al. [31] and Moss et al. [32], right: CUBRC run 43 compared with experimental result and simulations of Holloway [33] under different thermochemistry assumptions.

Whilst none of the models perfectly capture the position of the transmitted shock upstream of the separation region, the result of this work shows very good agreement with prevailing models which account for real gas effects. In fact the peak pressure and post-peak dip in pressure computed from this work are seen to match more closely with the experimental data. Properties along the secondary surface of the double cone are more critical for the ensuing MHD double cone test, since magnetic interaction dominates downstream of the kink.

It is also worth noting that peak pressure values are dependent upon precise location of experimental pressure probes along the surface, and peak p may not be captured at the exact probe locations.

5.7 Validation and performance comments

Collectively across the presented validation tests, the proposed numerical methodology is shown to be highly effective and able to capture the full physical phenomena resulting from each test configuration. The key functionality and efficacy aspects to highlight across these cases include:

- The modularised approach is efficient: the appropriate model can be selected for each test case to avoid overhead where, for example, viscous effects can be neglected, or ideal gas and plasma solutions would be indistinguishable.
- AMR is highly effective and efficient: the adaptive refinement implementation effectively captures the salient flow features as they evolve in time, meaning the solution maintains very high effective resolution at a fraction of the computational cost of a high resolution base mesh.
- MPI and scalability: running these test cases with MPI across 16 nodes (on a 16 core machine) achieves considerable speed up to a single core run. This speed up is scalable by increasing the number of nodes.
- Accuracy of the rigid body GFM: shown to be highly effectively for complex geometries both for the inviscid Euler model and for the viscous Navier-Stokes model, effectively capturing key BL dynamics and interactions, and without any numerical heating artefacts.
- Hypersonically stable: The new HLLC-HS solver is highly effective, and with generalised performance across several tests which are known to produce instabilities in the hypersonic flow regime.
- Accurate MHD system forcing dynamics: as validated by the standardised literature test for increase in shock stand-off distance.
- Accurate viscous effects: extensive validation of the NS model shows viscous effects are correctly captured both in the subsonic regime (off-design result for a compressible flow solver), as well as supersonic and hypersonic regimes.
- Real gas effects and plasma formation: though challenges prevail broadly in the case of modelling real gas chemistry in hypersonic flows, good agreement is obtained in terms of bulk fluid properties and in terms of plasma properties (e.g. N_e) as compared with existing models, for cases where experimental data is available.

One may have noticed the full system model: Navier-Stokes + resistive MHD was not validated in this section. Having validated each of the constituent components, the performance of the full system model - as applied to a complex test case - is the subject of

the next chapter. Since good quantitative agreement between experiment and simulation for hypersonic MHD flows remains a key research challenge in the literature, such investigation is treated in the Hypersonic MHD applications chapter.

Chapter 6

Hypersonic MHD applications

This chapter applies the developed model to realistic flight regimes and experimental conditions for hypersonic flows with imposed MHD effects.

The first study is placed within the context of a realistic atmospheric reentry condition with blunt body geometry. The study focusses on the role of the new 19-species air-plasma EoS applied to this flow regime, and draws comparisons to the commonly employed ideal gas EoS. The study seeks to examine the ways in which MHD affected flows are influenced by the thermochemistry modeling, and what differences this leads to in terms of MHD flow control predictions.

The focus of the Chapter then progresses from the simple blunt body geometry which produces a singular bow shock structure, to examine non-simple geometries, which produce complex shock interactions and multiple regions of elevated conductivity. This therefore produces a flow which exhibits complex fluid dynamic and magneto-dynamic behaviours when a magnetic field is applied. Numerical modelling of this flow configuration has remained a challenge due to the sensitivity of feature formation, the real gas modelling of weakly ionised plasmas, and their interplay.

Due to the complexity of this problem configuration, an experimental test case is examined in detail. Simulations are conducted to replicate the conditions of an experiment of a hypersonic flow over a double cone geometry with imposed magnetic field. These simulations bring together all of the elements of the developed numerical model: solution of the full Navier-Stokes resistive MHD model, closed with the plasma19X EoS, utilising numerical methods which capture strong shock interactions at high resolution over non-simple embedded geometries.

Building on from the validated results of the experimental test configuration, simulations are conducted to investigate varied geometric and magnetic field conditions. The purpose of these studies is to make predictions and gain insights about the fundamental flow physics.

This problem configuration is consequential for emerging aerospace technologies, such as the enticing proposal of replacing mechanical control surfaces on hypersonic vehicles with so-called *magnetic actuation*.

6.1 Spherical reentry vehicle with imposed B-field

This test case represents the classic application of MHD flow control in spacecraft reentry. The configuration follows many studies in the literature: a spherical rigid body representing the nose cone geometry, with an imposed dipole magnetic field generated from within the vehicle. A steady state is formed with elemental shock structure (a bow shock) forming around the vehicle. Determining the feasibility of MHD flow control is predicated on an accurate prediction of the increase in shock stand-off distance (shock enhancement effect) when the imposed magnetic field is activated. An increase in shock stand-off distance is associated with a decrease in heat flux to the vehicle (magnetic heat shielding), and aerodynamic control effects (e.g. drag enhancement).

6.1.1 Problem configuration and governing assumptions

A realistic test configuration is defined for a reentry vehicle at 40km altitude with a Mach 19 flow over a spherical body of 1.0 m radius. Equilibrium chemistry can be verified as suitable for this geometry and flight regime, with reference to the developed reentry thermochemistry map of Figure 3.4.

Free stream conditions:

$$M_\infty = 19.0, \rho_\infty = 4.0 \times 10^{-3} \text{ kg/m}^3, V_\infty = 6021.9 \text{ m/s}, \\ p_\infty = 287.0 \text{ Pa, Gas} = \text{Air}$$

The magnetic field is defined as a static dipole field, given by the analytic equation 6.5, centred at the sphere centre, and with a maximum absolute magnetic field strength of 1 Tesla outside the vehicle. The radial and z-components, as well as absolute field strength are shown in Figure 6.1.

Under these conditions, the peak electrical conductivity is calculated *a posteriori* from the plasma19X simulation as $\sigma_{max} = 180 \text{ S/m}$. Therefore the magnetic Reynolds number is 1.36, verifying the assumption low Re_m (order of 1 or less) of the governing model.

For the blunt body configuration at hypersonic velocity, the free stream Reynolds number is 1.27×10^6 and the boundary layer is extremely thin with no interaction with the outer inviscid flow. Therefore the inviscid MHD model is applied for these simulations.

This study seeks to compare the results computed by the plasma19X and ideal gas EoS: to investigate the role of real gas thermochemistry, specifically in relation to predicting MHD effects.

The plasma19X model directly computes electrical conductivity throughout the fluid domain. The ideal EoS however, requires a supplementary analytic approximation model. The standard analytic formulation with exponent $n = 2$ is adopted as per previous models [9], [54] and [20] where:

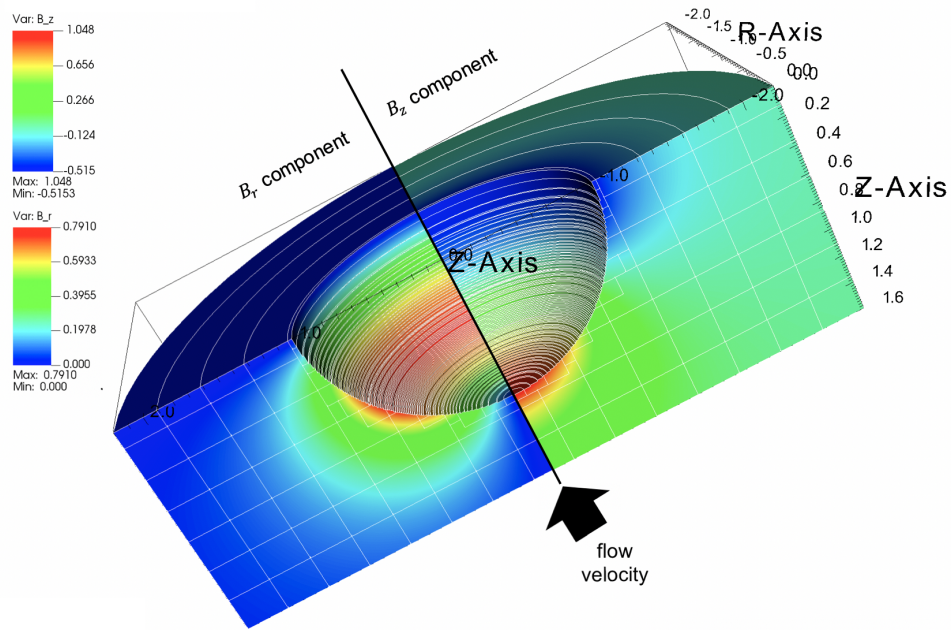


Fig. 6.1 3D rendering of the configured dipole magnetic field around the defined spherical geometry: radial and z-components depicted respectively over each half plane. Mesh AMR blocks shown at time = 0.

$$\sigma = \sigma_0 \left(\frac{T}{T_{max}} \right)^2 \quad (6.1)$$

where here σ_0 is taken to be 180 S/m in order to manually match the real computation of the plasma19X conductivity. The reference temperature T_{max} is determined from the base ideal gas simulation to be 18,540 K. This empirically renders the ideal gas approximation to be as close to the real gas chemistry model as can be achieved. However, these parameters would have remained unknown without being able to be manually fit to the plasma19X result.

Figure 6.2 compares the resultant conductivity profile of the selected square power law fit with appropriate σ_0 and T_{max} as compared with the base flow plasma19X result. The manually fit analytic model is shown to approximate the real gas conductivity profile well, despite the observed difference in shock layer width.

The simulation is run with a base resolution of 80×56 cells with 3 levels of AMR, resulting in an effective resolution of 291 cells/radius. It is essential to run the simulations with the HLLC-HS solver to eliminate the manifestation of carbuncle instability. Simulations are run until a steady state is achieved for the base case without magnetic field ($t_f = 0.002$ s, and approximately 700 base AMR level time steps). The simulation is run for approximately the same time/steps for the MHD affected test case, with \mathbf{B} -field activated from the initial time step.

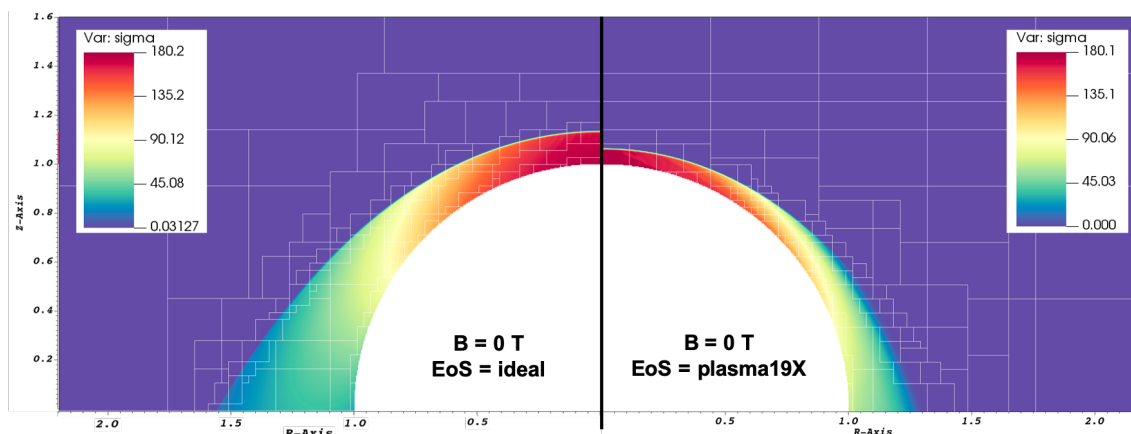


Fig. 6.2 Comparison of electrical conductivity profiles before the magnetic field is activated

6.1.2 Results

Computed flow-fields of the ideal gas and plasma19X models are compared. Figure 6.3 also shows the vast temperature over-prediction of the ideal gas model (factor of 2.85 over-prediction for the base flow case), and compares bow shock stand-off distances.

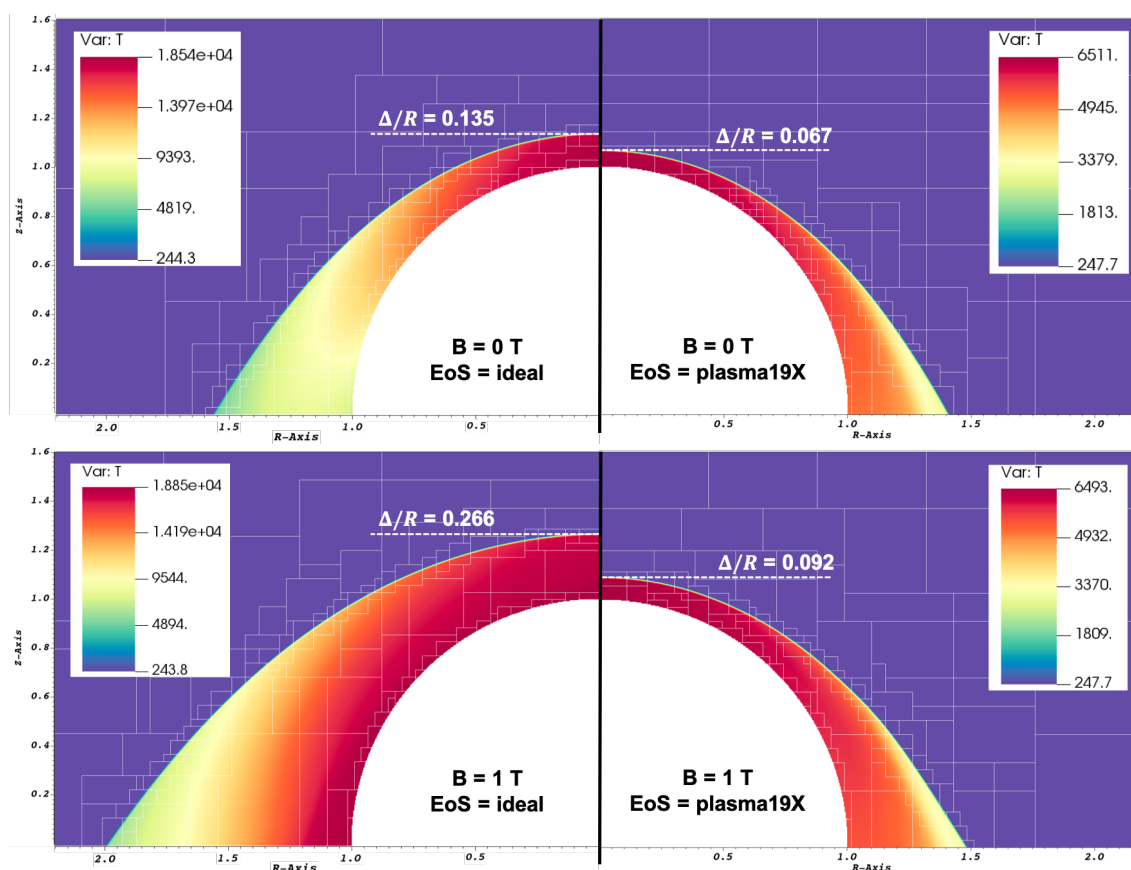


Fig. 6.3 Top) Temperature profiles at steady state in the absence of magnetic field for ideal gas and for plasma19X chemistry models. Bottom) Temperature profiles at steady state under imposed magnetic field of strength $B_0 = 1$ T.

Measurements	Ideal Gas Model	Plasma19X model
Base flow ($ B = 0$ T) normalised shock stand-off distance	0.135	0.067
$ B = 1$ T normalised shock stand-off distance	0.266	0.092
Shock enhancement (%)	97.0	37.3

Table 6.1 Comparison of MHD shock stand-off enhancement prediction for the ideal vs plasma19X gas models

Table 6.1 shows the shock stand-off measurements for cases with and without magnetic field for both gas models. While the ideal EoS predicts an increase of 97.0%, the plasma19X model predicts an increase of only 37.3%. This is a key difference for feasibility studies. We therefore examine the MHD phenomena driving the discrepancy.

The circumferential component of electric current density is given by:

$$\mathbf{J} = J_\theta = \sigma(u_z B_r - u_r B_z) \hat{\boldsymbol{\theta}} \quad (6.2)$$

and the comparison of computed electric current density is shown in Figure 6.4. The velocity of the conductive gas in the r-z plane passing through the magnetic field induces an electric current circumferentially around the vehicle. The dominant anti-clockwise current (around the z-axis) occurs at approximately 49.9° azimuthal height in the ideal gas result, and at approximately 59.6° azimuthal height in the plasma19X solution, and the regions differ notably in their size and distribution.

Figure 6.5 compares the magnitude and vector field of the shock layer Lorentz forcing. The r-z plane forcing components can be expanded as:

$$\mathbf{J} \times \mathbf{B} = \sigma(u_z B_r B_z - u_r B_z^2) \hat{\mathbf{r}} - \sigma(u_z B_r^2 - u_r B_z B_r) \hat{\mathbf{z}} \quad (6.3)$$

The Lorentz forcing comparison in fact reveals a greater peak magnitude in the plasma19X result than in the ideal gas result. It is important to additionally consider the directional vectors acting within the magnitude profile.

A better measure for interrogation of the Lorentz forcing dynamics in terms of consequent dynamic effect on the shock layer is to examine the magnetic interaction parameter (Q_{MHD}),

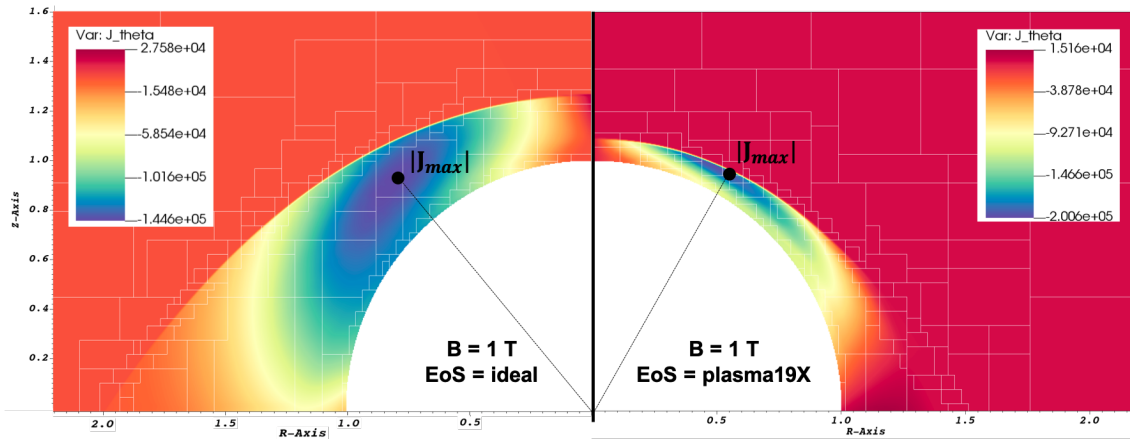


Fig. 6.4 Comparison of circumferential (θ -component) electric current density. NB: both simulations are run in the right half plane (plasma19X result as shown), whereas the ideal gas result is reflected across the z -axis of symmetry, however the electrical current is shown with its original sign/direction as per the right plane for mirrored comparison. Both peak negative currents circulate in the anti-clockwise direction around the z -axis.

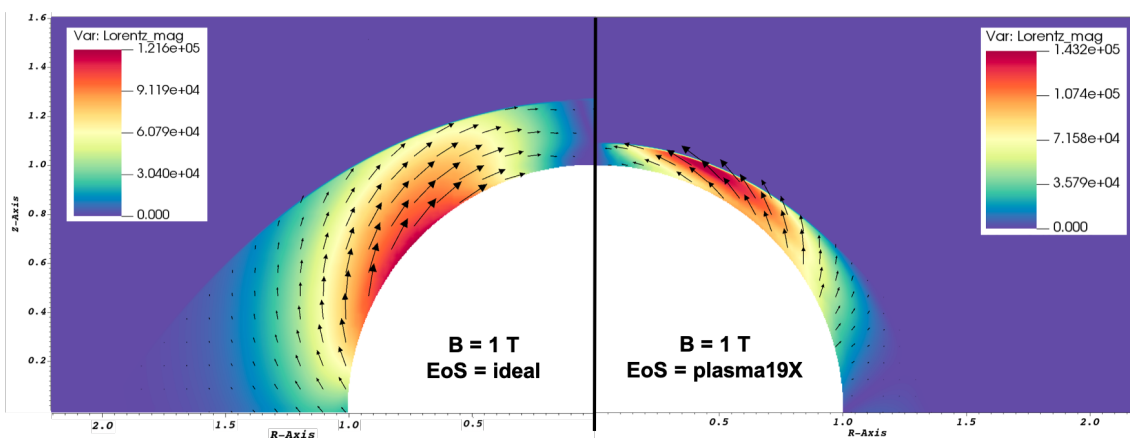


Fig. 6.5 Comparison of Lorentz forcing directional vectors (black arrows) and magnitude (colour map).

which considers the relative influence of magnetic forcing to the fluid inertial force. A comparison of magnetic interaction parameter along with the directional Lorentz forcing vectors is presented in Figure 6.6.

This comparison is more illuminating as it reveals the relatively larger region where Q_{MHD} is of the order of 10 or greater. Since the Lorentz forcing profiles have already been examined, this therefore indicates the effect is due to differences in computed total momentum. The differences can be seen most clearly by comparing plots of density and total velocity in Figure 6.7. As shown, the density is significantly higher within the more compressed plasma19X shock layer. Additionally, the ideal EoS computes a much larger region of low velocity around the body surface (closest to where the Lorentz forcing is dominant), therefore resulting in a stronger magnetic interaction effect over a larger fluid volume, which acts to more significantly augment the flow.

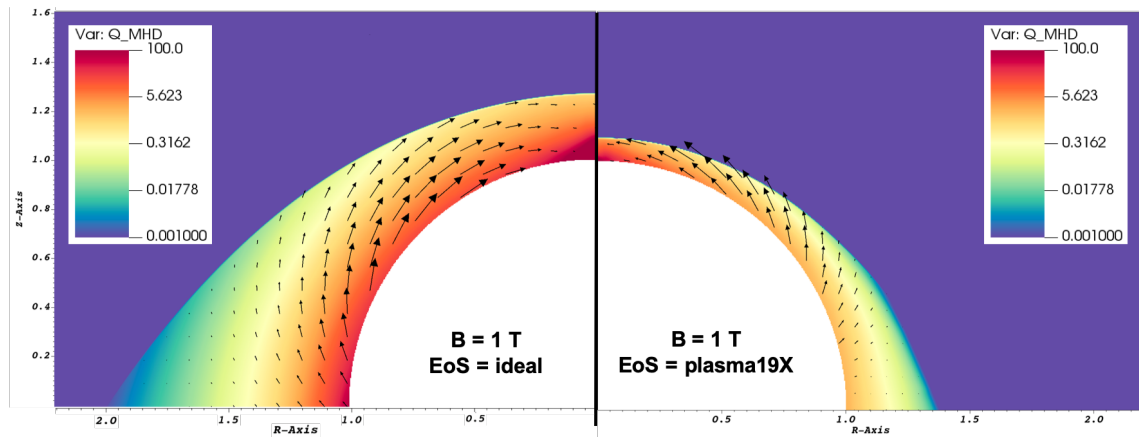


Fig. 6.6 Comparison of Lorentz forcing vectors (black arrows) and magnitude of the magnetic interaction parameter (colour map): $Q_{MHD} = (\sigma|\mathbf{B}|^2 R_0)/(\rho|\mathbf{u}|)$.

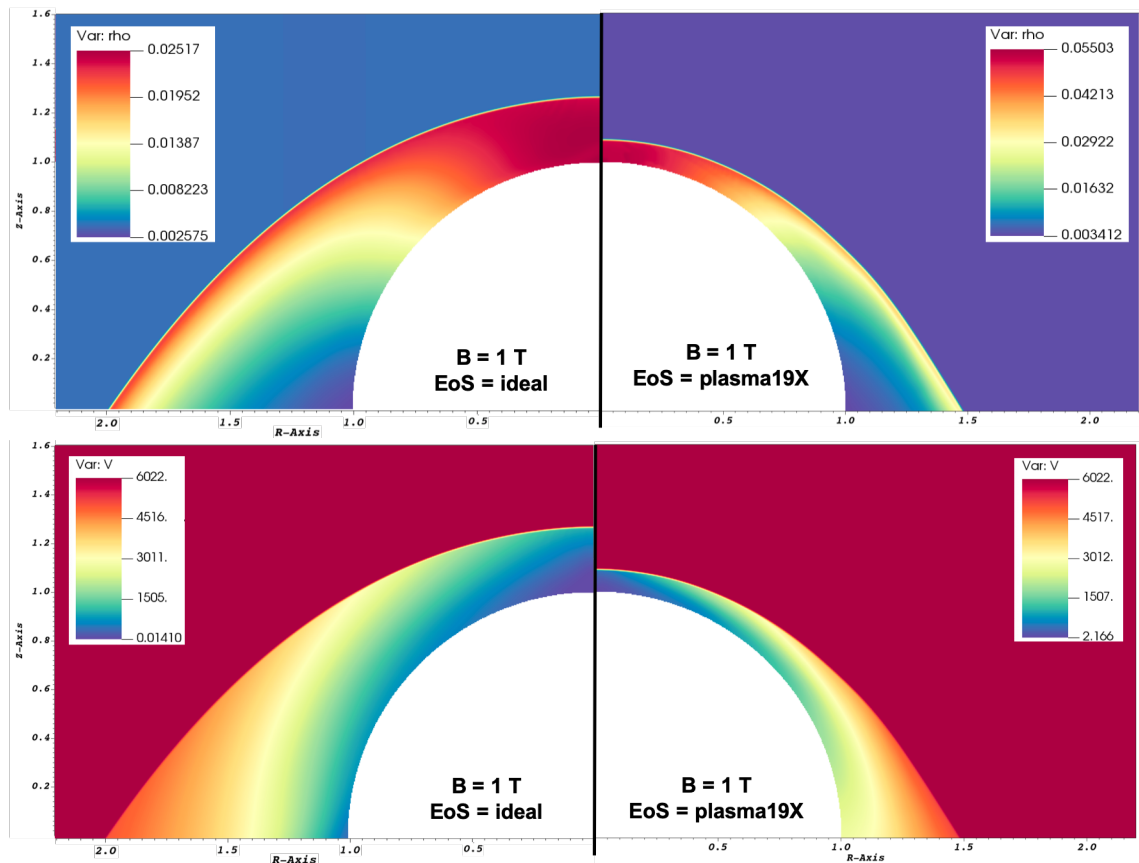


Fig. 6.7 Comparison of: top) density field, and bottom) total velocity profile for each EoS.

This result reveals some important insights about the MHD flow physics. Whilst several studies attempt to use an ideal EoS to investigate the effects of MHD forcing on reentry type flow regimes and geometries, even if the electrical conductivity profile is reasonably well matched by fitting parameters, the resultant flow effects are still unrealistic due to differences in the relative profiles of Lorentz forcing and momentum between an ideal gas model and

a real chemistry model. Such a difference is significant for MHD flow control feasibility studies.

The plasma19X model computes the real gas thermochemistry (including electrical properties) while achieving comparable computing time to the ideal gas law, due to the direct interpolation routine. Additional computing time is predominantly due to computation of additional properties, as they require resolving.

Electron number density (N_e) is a parameter of interest in characterising the weakly ionised plasma. Naturally, the electron concentration cannot be resolved within the simple ideal gas model, however under the advanced 19-species EoS, we are able resolve the electron number density in the temperature range of the shock layer. It can be seen in Figure 6.8 that free electrons are present in some concentration throughout the full shock layer. The peak value and profile remains near identical for the MHD affected case compared to the base flow. Ionisation reactions have occurred to produce a minimum number density of the order of 10^{18} m^{-3} and maximum density of the order of 10^{20} m^{-3} towards the stagnation region. Such information is of interest for studies of communications black-out during atmospheric reentry.

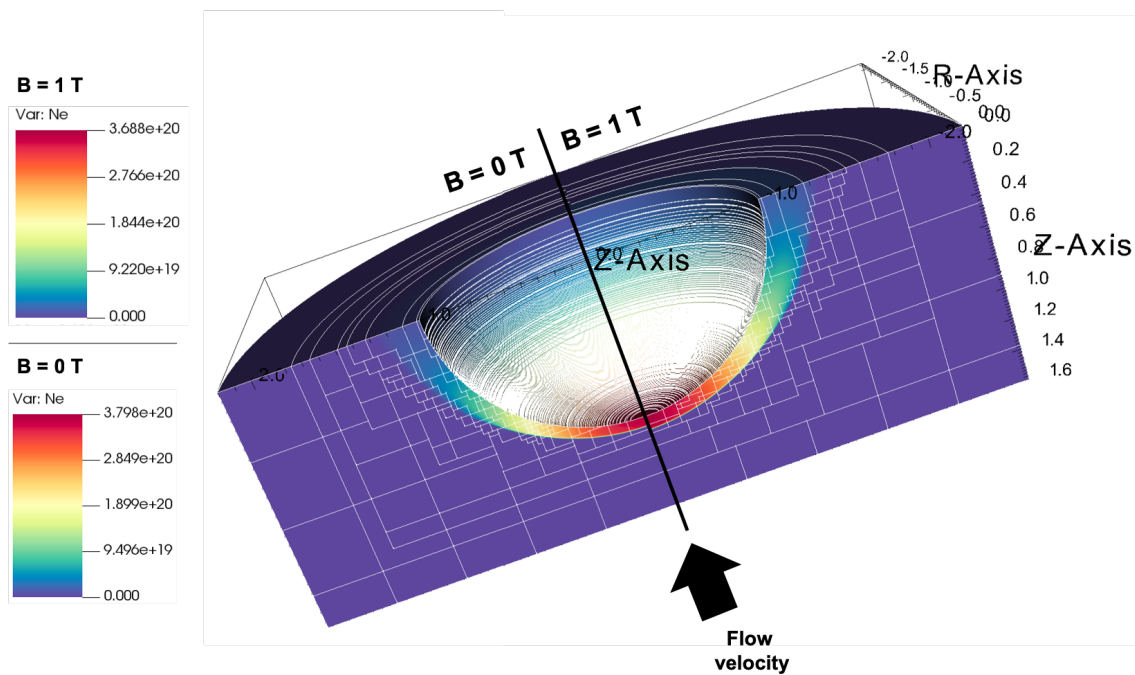


Fig. 6.8 Logarithmically scaled plot of electron number density N_e for the the $B_0 = 0 \text{ T}$ case (left) and the $B_0 = 1 \text{ T}$ case (right). 3D rendering to better represent true geometry and fluid profile.

6.2 Hypersonic double cone with imposed magnetic field

Experimental and numerical research for MHD control of hypersonic flows has generally focussed on simple geometries [160] which produce an elementary shock structure: such as the single bow shock formed around blunt bodies[161, 20] and the leading oblique shock formed over wedges[52, 162] and cones[163, 160]. In contrast, there is limited research which deals with MHD control of the weakly ionised plasma formed in high temperature regions from shock-shock and shock-boundary-layer interactions.

Extreme forces are experienced along the surfaces of hypersonic vehicles. Control flaps and surfaces require high power mechanical actuators and multiple moving parts to adjust surface angles dynamically during flight. MHD flow control presents the desirable possibility of replacing mechanical actuation of the control surface, however, such research is in the early stages [34].

In the case of multiple angled surfaces - which realistically represents a mechanical control surface, such as a flap or ramp - the coupled fluid dynamic and magneto-dynamic effects become complex. Shock wave boundary layer (SWBL) interactions lead to the formation of a separation region, and produces multiple ensuing shock interactions. With sufficient ionisation in the flow, the high conductivity low velocity regions which form within the steady state shock structure, are sensitive to manipulation via magnetic fields [26].

The double cone is considered a highly useful test geometry since the resultant flow exhibits all of the relevant features of common 3D internal engine geometries or aerodynamic control surfaces. Figure 1.3 from Chapter 1 depicts the comparison between shock structure control via imposed MHD effect and traditional mechanical surface actuation.

6.2.1 Experimental conditions

Wasai et al. [34] conducted an experiment on magnetohydrodynamic control of shock interactions over a $25^\circ/55^\circ$ double cone geometry in hypersonic flow where results were obtained to measure the MHD flow control effect on shock enhancement. Simulations of the experimental conditions have been conducted by Nagata et al. [31, 164].

The problem configuration is congruent to the CUBRC double cone experiments with model dimensions shown in Figure 6.9. A dipole magnetic field is initialised from within the model, with the dipole centre depicted in the figure, and a magnetic field strength of $B=0.36$ T is measured at the labelled reference point. The dipole magnetic field equation is therefore configured to match the experimental condition, with resultant $B_0 = 0.0001125$ T in the dipole equation 6.5. The computed magnetic field is shown in Figure 6.9. The value at the kink is approximately 0.53 T.

The experimental inflow test gas was pre-heated, and Wasai [34] and Nagata [164] consider it to have reached a state of thermochemical equilibrium, determining the initial (single) temperature and species composition as such. Of the 18 test runs conducted, flow

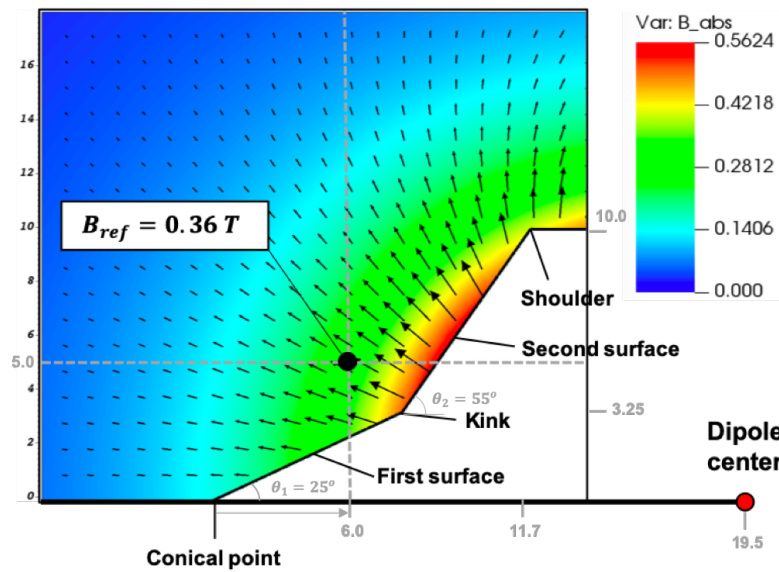


Fig. 6.9 Computed magnetic field from this work - configured to match the experimental condition. Key geometry points and features are labelled for reference. Dimensions in mm.

velocities were measured between 11.4-12.5 km/s [34], with a nominal value of 12.1 km/s used for simulations.

Test run conditions:

$$M = 5.6, V_{\infty} = 12.1 \text{ km/s}, T_{\infty} = 6110 \text{ K}, T_w = 300.0 \text{ K}, \\ \rho_{\infty} = 2.52 \times 10^{-3} \text{ kg/m}^3, p_{\infty} = 7.22 \text{ kPa}, \text{ Gas} = \text{Air}$$

The flow is characterised with the following parameters:

$$\text{Reynolds number} = 1.77 \times 10^3 \\ \text{Magnetic Reynolds number} = 0.2 \\ \text{Hall parameter} = 0.61$$

These parameters confirm the assumptions of the governing mathematical model: low magnetic Reynolds number, and negligible Hall effect (since additionally the model surface can be electrically insulative [34]). The Nagata et al. model makes the same assumptions [31].

The body fitted mesh of the Nagata simulations, vs embedded boundary Cartesian approach of this work is shown in Figure 6.10.

Simulations in this work are run with a base resolution of 80×64 cells in the (r,z) dimensions, with 4 levels of AMR, resulting in an effective resolution of 753 cells per model radius. The full system mathematical model (Navier-Stokes resistive MHD) is computed with the plasma19X EoS, with inviscid fluxes evaluated with the HLLC-HS solver with MUSCL (MinBee) extension, central differencing method for the viscous fluxes and two-step MHD source term integration procedure as per section 4.7.1. An initial start-up CFL of 0.1

is used for the first 5 time steps to handle the extremely strong start up shock reflection from the surface, after which a CFL=0.8 is adopted (slightly reduced from the standard 0.9 due to combined effects of non-ideal EoS and very strong shock interactions).

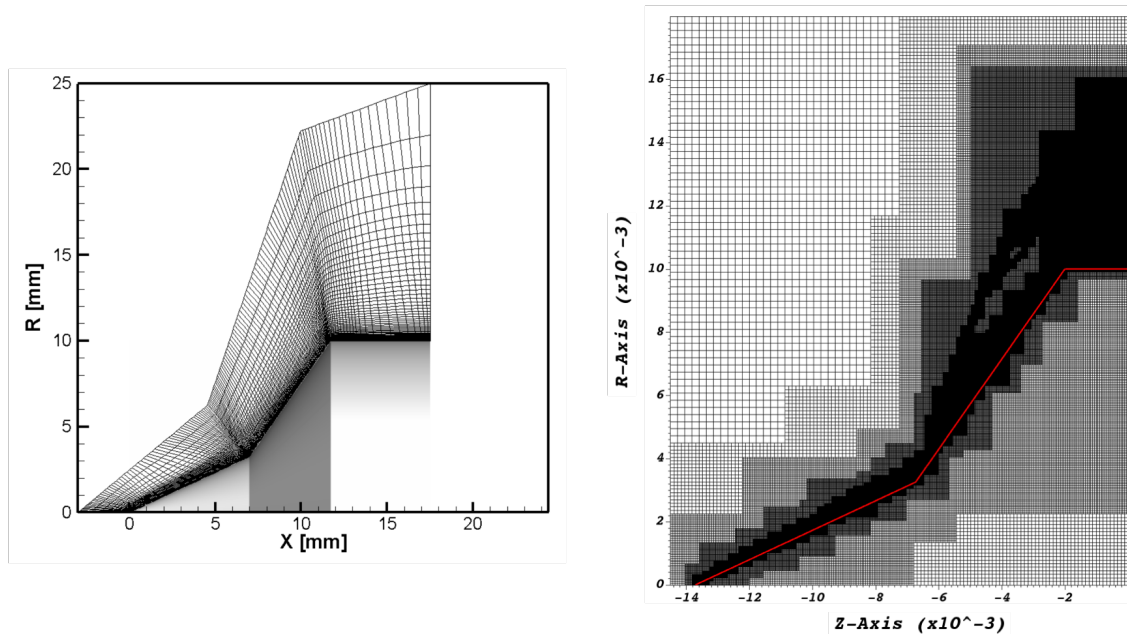


Fig. 6.10 Left) Body fitted mesh employed by Nagata et al. [31], compared with right) adaptively refined Cartesian mesh employed in this work - resolved at the steady state solution time step once the flow has formed around the embedded double cone (embedded boundary shown in red.)

Differences in the Nagata et al. numerical modelling include: 11 species non-equilibrium chemistry with supplementary electrical conductivity model ($\sigma = \frac{e^2 N_e}{m_e \nu}$), and a different flux solver in the time-explicit numerical update scheme (AUSM-DV scheme for the inviscid fluxes with MUSCL extension for 2nd order spatial accuracy). Most importantly, results of the Nagata et al. numerical simulations found that for a magnetic field strength matched with the experimental condition the MHD effect was un-observable in the computed steady state flow field solution. However, the experiment does in fact reveal a small but measurable increase in shock stand-off distance due to MHD flow control. By initialising the magnetic field strength in the numerical simulation to be much higher than that of the experiment, Nagata et al. were able to demonstrate the qualitative effect an imposed magnetic field has on the flow, which agrees with the qualitative effect observed in the experiment.

The computed pressure contours for different magnetic field strengths is shown in Figure 6.11. As can be seen, the result for the base case (no magnetic field) and for $B_{kink} = 1$ T (stronger field strength than the experiment) are close to indistinguishable.

The shock stand-off enhancement effect of this work can be visualised through the pressure contour plot of Figure 6.12. To show the effect of increasing the magnetic field strength (as per the Nagata simulations), a simulation is run with a stronger **B**-field: fixed at

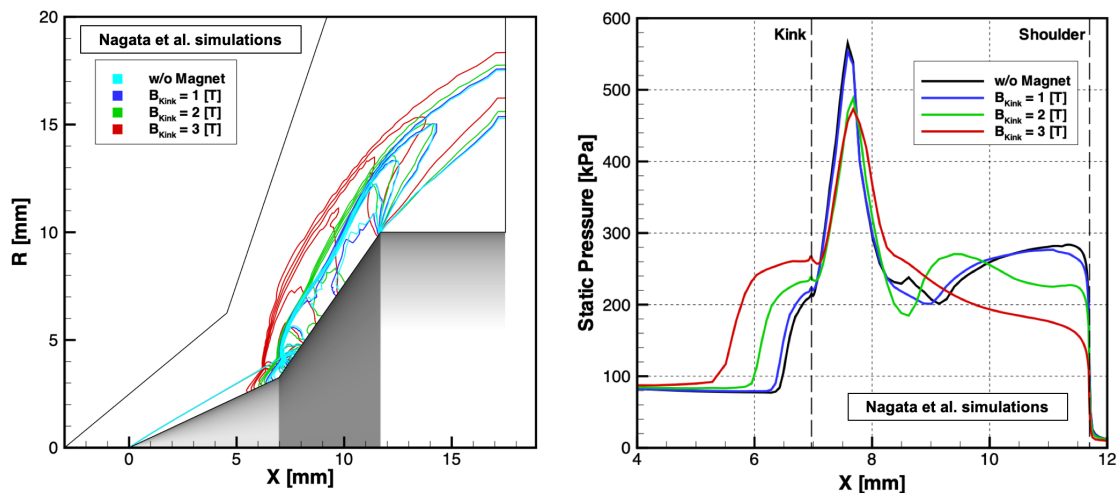


Fig. 6.11 Left) pressure contours computed by Nagata et al. [31] for different magnetic field strengths as measured at the kink point of the double cone, and right) corresponding pressure traces along surface (projected distance along the z-axis).

the same dipole centre location but scaled to a larger magnitude corresponding to 1.5 T at the reference point.

The MHD effect as depicted by the overlaid pressure contours for different magnetic field strength (Figure 6.12) agrees in terms of qualitative phenomenology with the simulations of Nagata et al. Specifically, we observe the MHD effect causes the shock layer over the second plane of the model to lift away from the surface, and for the stronger \mathbf{B} -field the shock wave becomes notably more bow shaped. The separation point moves upstream, and shock triple point becomes extended. The small but clearly observable magnetic augmentation of the shock position in the $B = 0.36$ T case demonstrates the importance of high resolution numerical methods to sharply capture the shock wave position. More diffuse numerical methods make the measurement of shock stand-off increase less precise. The diffuse shock front in the Nagata simulations (likely resulting from the accumulation of numerical diffusion at $CFL=0.001$ due to stiffness of chemically restricted fluid evolution) makes the measurement of difference in shock position less clear.

The pressure traces along the vehicle surface computed in this work are shown in Figure 6.13. In both models the pressure along the first plane rises, and the separation region expands significantly as \mathbf{B} -field strength increases. The peak pressure point is shifted downstream along the second surface and for the $B=1.5$ T case the pressure profile along the second surface takes on a rise-and-fall profile which is similar in behaviour to the comparably strong \mathbf{B} -field results in the Nagata simulations. The main difference in the surface pressure traces is the calculated peak pressures and the fact this increases for the stronger \mathbf{B} -field case in this work. Unfortunately there is no experimental data for surface pressure to validate against in these experiments.

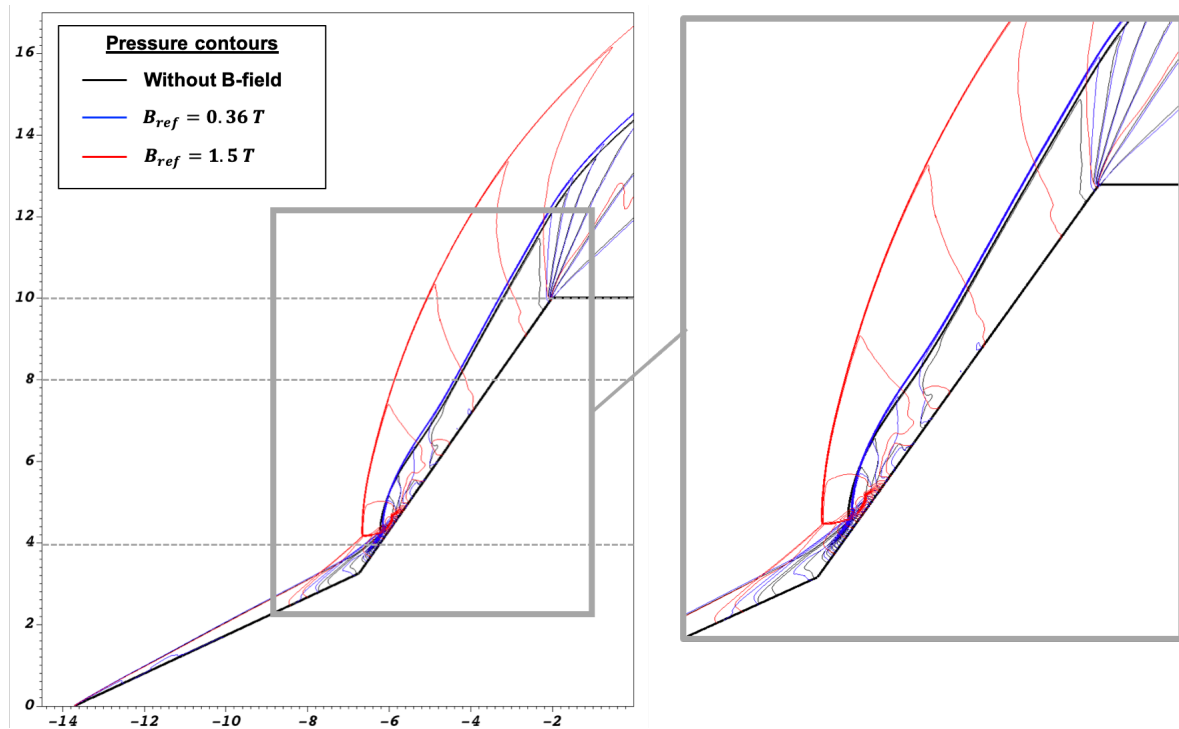


Fig. 6.12 Contours of pressure for the cases: without magnetic field, magnetic field initialised to experimental value $B_{ref} = 0.36$ T, and a stronger magnetic field of $B_{ref} = 1.5$ T intensity. Radial lines (along which property traces are taken) of 4 mm, 8 mm, 10 mm are marked.

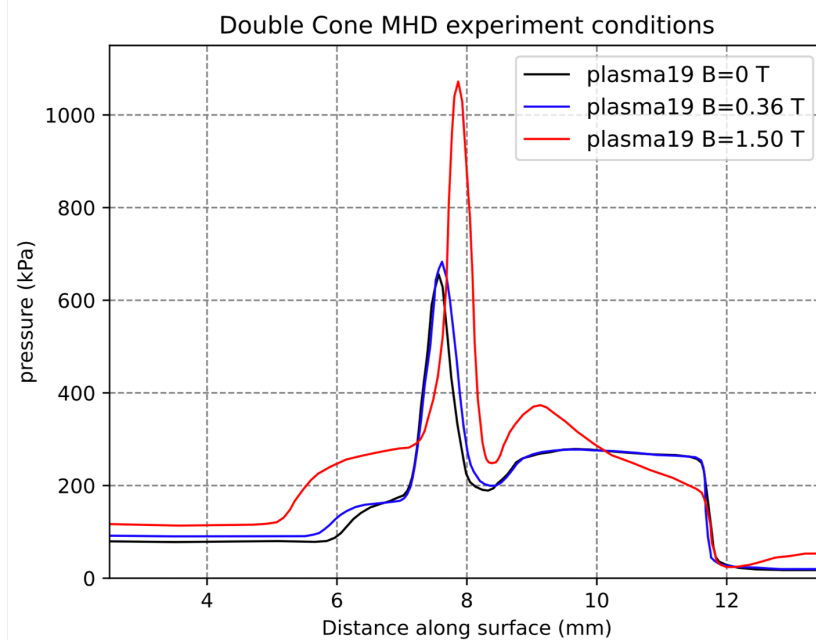


Fig. 6.13 Pressure trace along the surface of the model for the simulations of this work.

The Wasai et al. experiments conducted 18 test runs which varied in measured flow speed from 11.4 - 12.5 km/s. Therefore there is some variation in shock-stand-off results between test runs. In the experimental results, the increase in shock stand-off position is

observed via a brightness intensity rendering of the flow field with and without the imposed magnetic field (shown in Figure 6.14). The exact position of the shock-waves are difficult to determine from these rendered images alone. The experimental work therefore also resolves a property trace through lines parallel to the z-axis of symmetry at different radial distances ($r = 4\text{mm}$, 8mm and 10mm) along the model to determine shock position more precisely. These property traces along the different radial lines are shown in Figure 6.15, and the increase in leading shock position due to MHD effect of the imposed magnetic field can be measured from these graphs.

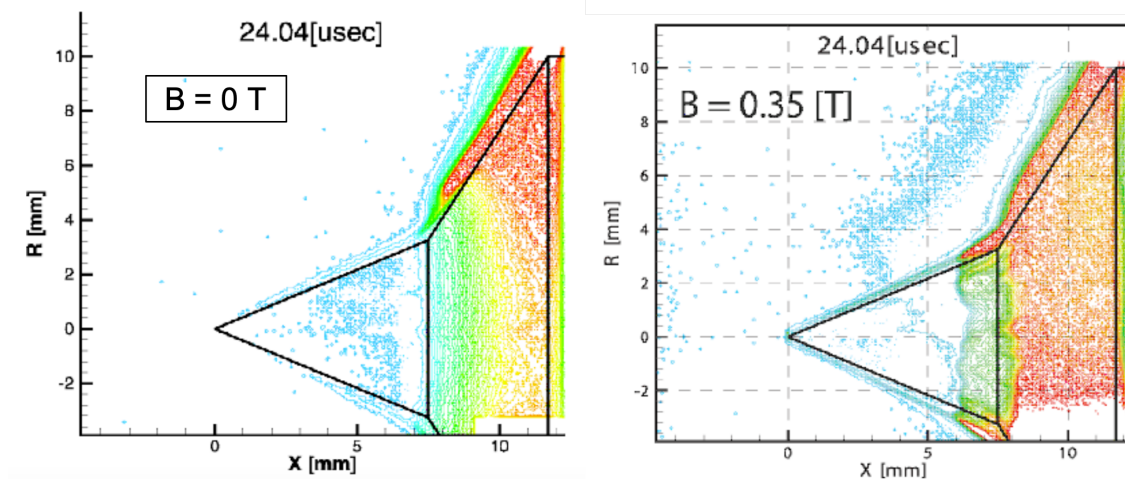


Fig. 6.14 Brightness intensity rendering of the flow field for $\mathbf{B}=0$ and \mathbf{B} at the test condition for a given test run. Image by Wasai et al. [34].

The leading shock position is measured to be where the property trace of brightness intensity first rises in value. Since multiple runs are presented in the one graph, the minimum offset and maximum off-set between the no- \mathbf{B} and $\mathbf{B} = 0.36$ T cases of all test runs is measured and a % increase in the shock stand-off distance is presented as the range of values in Table 6.2.

Whilst the measured brightness intensity relates most strongly with temperature, the rendering cannot be mapped directly onto any one property from the simulation for a number of reasons. The brightness intensity is measured as a 2D side view of the 3D experiment, which is different to the 2D planar cross section of the simulation. The depth of the fluid captured from the side-view also influences the total brightness intensity. While there is some uncertainty in the shock-front measurement, Table 6.2 offers a conservative estimate, and the Figure 6.15 directly shows the comparison of traces. Pressure is chosen as the property for comparison from the simulation results as it clearly shows the shock front position and retains a fairly steady value through the shock layer to the model surface - which offers a similar profile to the brightness intensity rendering. As per the discussed differences, the two-step profile of the numerical trace at $R=4\text{mm}$ shows how the trace passes through the separation shock (point at which stand-off enhancement is measured) and then a secondary

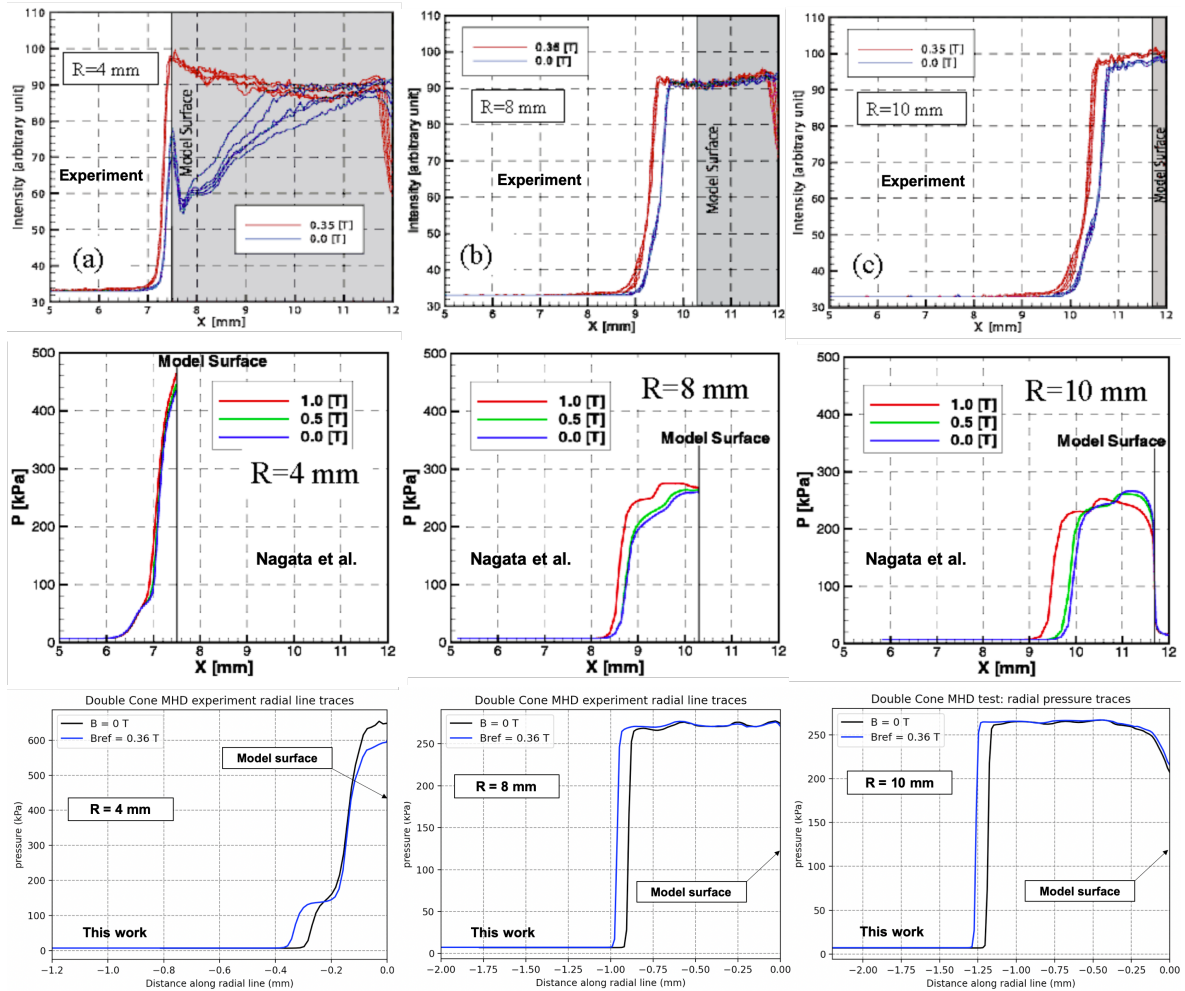


Fig. 6.15 Top) experimental result brightness intensity traces through radial lines 4 mm, 8 mm, and 10 mm, for a number of test runs by Wasai et al.[34]. Middle) pressure traces taken at the same radial lines from the numerical result of Nagata et al. [31]. Bottom) pressure traces taken at the same radial lines from the numerical result of this work. Experimental and Nagata traces are presented as total distance along the central z-axis (labelled X-axis in the experimental results), and simulation traces are shown more clearly as distance along the z-axis measured directly from the surface intersection point as $z=0$ for each case.

high pressure impingement point at the surface. This is a cross-sectional profile detail which cannot be captured by the 2D projected side view of the 3D flow from the experimental images.

The important conclusion from the experimental results is that there is a clearly observable MHD enhancement of shock-stand-off distance. Similarly, from the pressure traces along the radial lines, the clearly observable increase in stand-off distance is presented. In Table 6.2, the measured increase in leading shock stand-off distance from the simulations of this work is compared to the measured increase from the trace taken along the radial lines in the results published by Wasai et al. [34]. The results show an increase in shock stand-off within the banded measurement from the experimental results.

Radial distance	MHD shock stand-off enhancement: experiments (%)	MHD shock stand-off enhancement: simulations (%)
R = 4 mm	17.9 - 82.1	24.1
R = 8 mm	7.9 - 17.5	8.8
R = 10 mm	7.2 - 25.1	7.8

Table 6.2 Comparison of MHD shock stand-off enhancement (increase in leading shock distance from surface) for the experimental conditions with magnetic field strength $B_{ref} = 0.36$ T: experimental result by Wasai et al. [34] (as measured from experimental graphs), and computed result from the model of this work (as measured from computed pressure traces along radial lines shown in Figure 6.15).

Therefore the predictions of this work are quantitatively in-line with experimental measurements for matched magnetic field strength. Whereas previously, an MHD enhancement could not be measured at the matched experimental condition. The agreement in shock stand-off enhancement indicates that the model of this work is able to realistically capture the complex MHD flow control effect. This is a key result for the complex flow field: a hypersonic flow with SWBL interaction over the double cone model coupled with magnetic interaction.

The model (and specifically the advanced plasma EoS) permits us to investigate many other properties of interest in the weakly ionised plasma layer formed around the vehicle, both in the absence of, and under the influence of, the applied magnetic field. A key property driving the Lorentz forcing dynamics is computed electrical conductivity. Results are shown for the base flow case (without magnetic field) as compared with the $B_{ref} = 1.5$ T case (where MHD enhancement effects are more pronounced) in Figure 6.16.

A property of interest for studies of the communications blackout phenomena is electron number density (N_e). Figure 6.17 shows the computed electron distribution for the case with and without magnetic field activated. Regions of maximum and minimum electron density can be identified.

There are additional electromagnetic properties which result directly from the activation of the magnetic field. Figure 6.18 shows (for the $B_{ref} = 1.5$ T case) the induced electric current in the circumferential direction and the Lorentz force magnitude and directional vectors which informs the progression of shock structure phenomenology under MHD

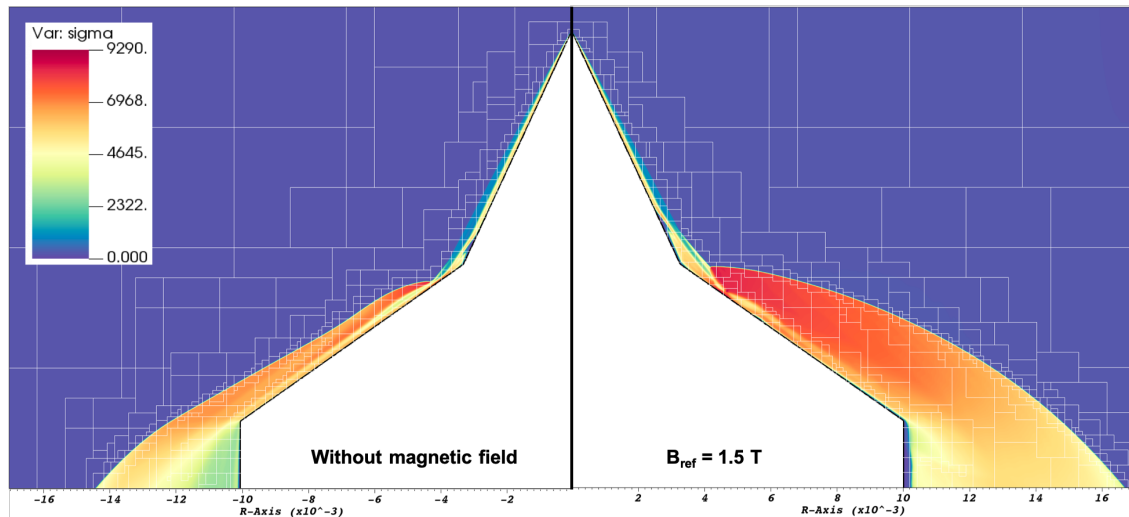


Fig. 6.16 Comparison of steady state solution for electrical conductivity (σ) without magnetic field (left plane) and for the case of applied magnetic field of strength $B_{ref} = 1.5$ T. Regions of mesh refinement are shown by white block borders.

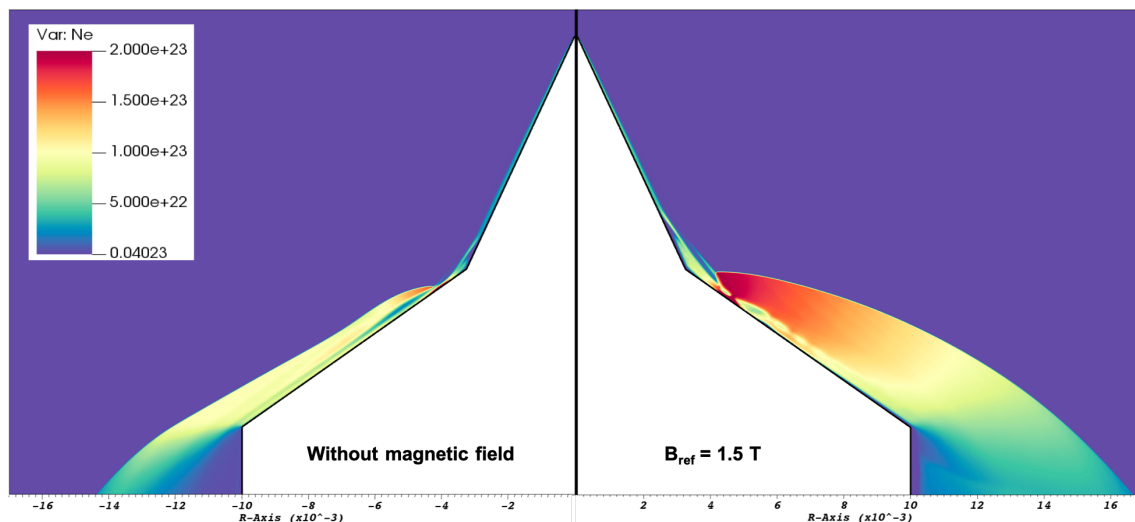


Fig. 6.17 Comparison of steady state solution for electron number density (N_e) without magnetic field (left plane) and for the case of applied magnetic field of strength $B_{ref} = 1.5$ T.

influence. The J_θ plot reveals a strong anticlockwise current flow in the supersonic regions of the flow structure and a weak clockwise current flow in the subsonic separation region.

The plot of Lorentz forcing magnitude and directional vectors in Figure 6.18 shows the proportionality of Lorentz force with electric current density, and also the angle at which forcing occurs relative to the vehicle surface and shock structure. The Lorentz force magnitude with directional vector plot shows peak magnetic forcing in the region of peak anticlockwise electric current flow. The directional vectors indicate why a notable movement in shock position is observed: in the region close to the shoulder Lorentz forcing occurs in a full 180° reversal of the free stream flow direction thereby directly decelerating the flow, while this angle turns to follow the second surface alignment, with forcing direction close

to parallel with the incline of second surface near the peak forcing region. This magnetic forcing which opposes the flow direction causes the Mach stem of the shock triple point to become extended and the shock wave to bow and expand outwards from the vehicle.

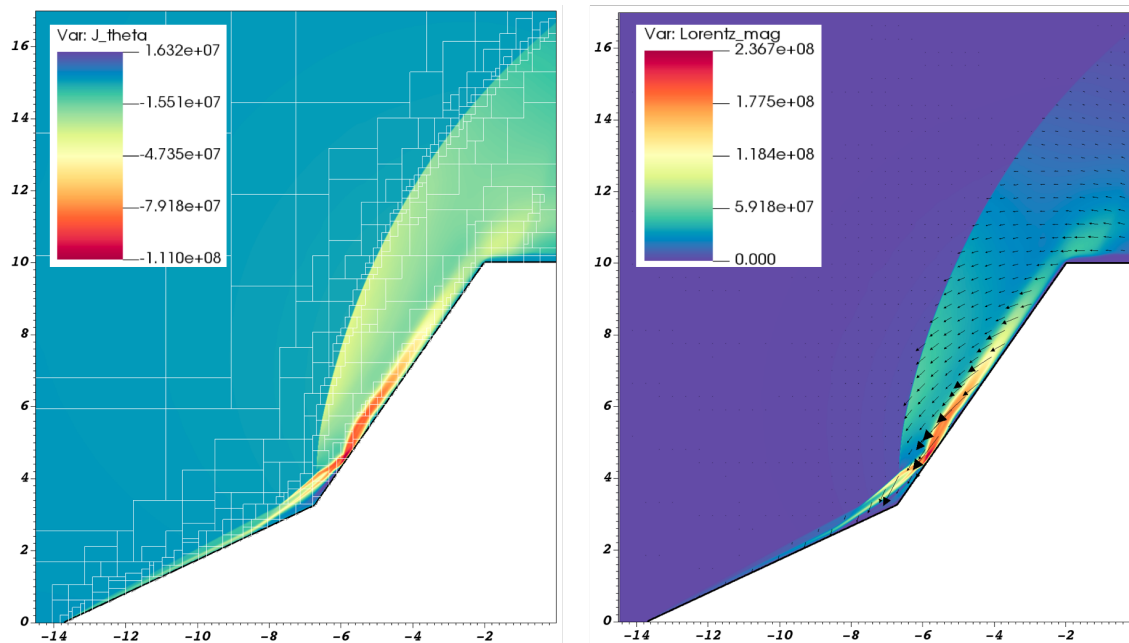


Fig. 6.18 Key electromagnetic properties- left: circumferential component of electric current density, and right: Lorentz forcing magnitude and directional vectors.

The computed Mach number for the $B_{ref} = 1.5$ T case is presented as a full 3D rendering in Figure 6.19 to give a holistic view of the resultant flow field.

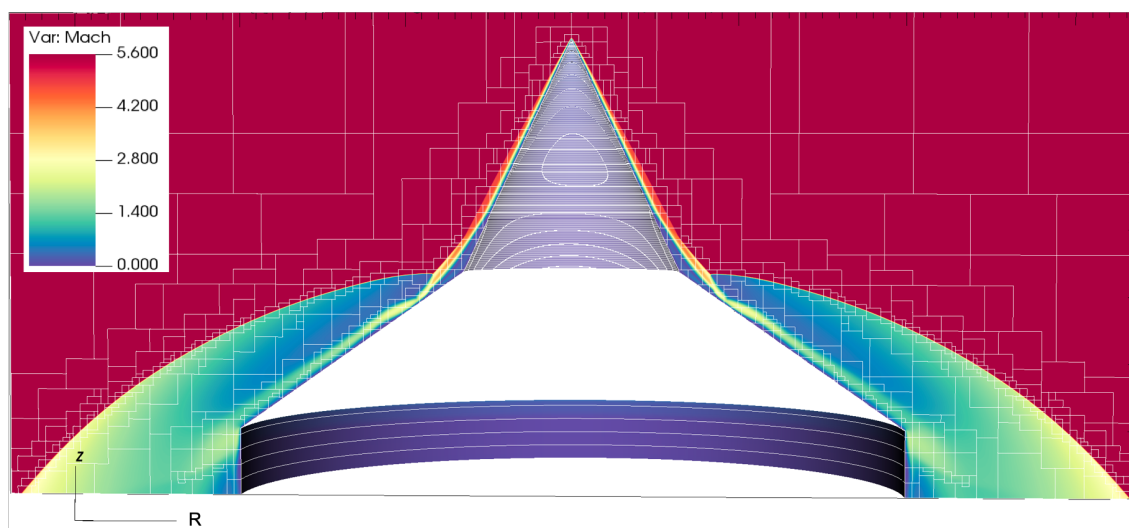


Fig. 6.19 Full 3D rendering of computed steady state Mach number for case of imposed magnetic field strength $B_{ref} = 1.5$ T.

6.2.2 LTE analysis

Determination of chemistry assumptions for this flow type is difficult.

Nagata et al. state that there is some uncertainty in the thermochemical model employed in their work (11 species non-equilibrium chemistry), and the fact that the base case flow (no magnetic field) shock layer width is over-predicted in their simulations is an indication that the fluid chemistry is not well matched. As can be seen from the radial property traces of Figure 6.15, the sharp rise in pressure (which shows the leading shock position) from the simulation results of this work aligns very well with the distance from the model surface where the brightness intensity is measured to rise - showing that the base flow shock layer width accurately computed in this work. This is one indicator that the thermochemistry is well matched in this work, though shock width alone is not conclusive.

LTE validity is primarily determined by the comparison of the rate of chemical reaction to the rate of fluid transport. Whilst the flow speed of the experiment is extremely high (12.1 km/s) the pre-heated free stream gas (6110 K) increases the rate of chemical reaction which promotes chemical equilibrium. Without explicitly resolving chemical reactions, the rate of reaction cannot be directly quantified, however the rate of fluid transport can be analysed. Specifically, in the case of quantifying MHD effects, a relevant consideration is that the system tends toward equilibrium specifically *where* the magnetic interaction is dominant. Therefore to assess the appropriateness of the LTE model for the MHD flow control double cone test case, the magnitude of magnetic interaction parameter (indicator of where the flow is magnetically affected by the imposed **B**-field) is compared with an indicative measure of fluid residence time (τ_r), defined as:

$$\tau_r = \frac{\text{vehicle length scale}}{\text{total velocity}} = \frac{L_0}{|\mathbf{v}|} \quad (6.4)$$

Where the velocity approaches a very low magnitude (such as subsonic and stagnation regions), and therefore the residence time is high, the flow can be assumed to be approaching equilibrium. Figure 6.20 shows the comparison of defined τ_r and magnetic interaction parameter Q .

As can be seen from the comparison in Figure 6.20, the regions with dominant magnetic interaction, predominantly producing the measured MHD effects, map very well with the regions where the flow is most expected to have equilibrated based on the residence time indicator τ_r .

This is an important relationship to draw: regions which tend to zero velocity, also tend towards equilibrium in terms of the chemical state, and correlate with the key regions of the flow structure where the Lorentz forcing magnitude vs flow momentum is high such that electromagnetic forcing affects the flow.

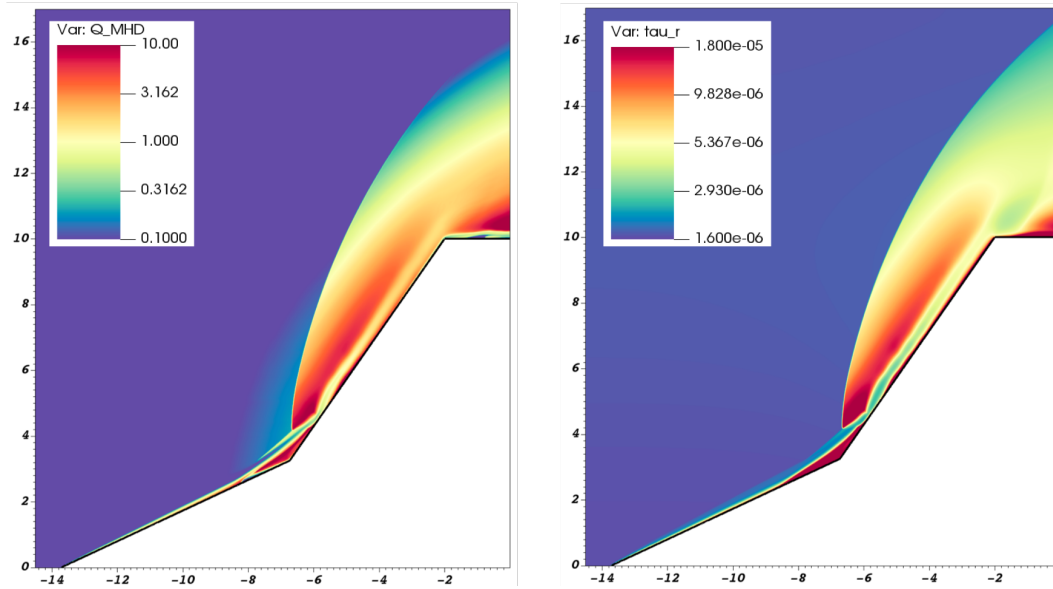


Fig. 6.20 Left) magnetic interaction parameter: $Q = (\sigma|B|^2 R_0)/(\rho|\mathbf{u}|)$, compared with right) residence time indicator of regions approaching equilibrium: $\tau_r = \frac{L_0}{|\mathbf{V}|}$

6.3 Studies of complex interactions in hypersonic flows with MHD effect

Since quantitative agreement with the experiment has been obtained in terms of MHD shock enhancement effect, the validated numerical model is now applied to varied configurations of the hypersonic double cone geometry with an imposed dipole magnetic field.

Within the motivating context of hypersonic flight control, even small changes in shock position can affect the flight dynamics. Previous MHD studies on simple geometries - blunt bodies, single cones and wedges - produce an elemental shock structure: bow shock or oblique shock. When the magnetic field is imposed upon the flow, this causes a *self-similar* MHD enhancement effect: congruent shock structure, but with a change of position. This type of shock enhancement can be effectively quantified through a singular measured variable: % increase in shock stand-off distance along the stagnation line for a blunt body, or, the increase in angle of an oblique shock wave for conical or wedge geometries. These studies demonstrate how, for hypersonic flows with complex shock interactions, the MHD affected flow is not only augmented in terms of shock position, but may exhibit *topological adaptations* in the fundamental flow structure. This has high consequence for predictions in flight control.

These studies seek to explore and explain the effects of magnetic field configurations, combined with variations in geometry, in terms of the causal mechanisms leading to:

1. Differences in magnitude of MHD enhancement effect
2. Topological adaptation of the fundamental flow structure

In this section, the coupled fluid-dynamic and magneto-dynamic flow physics which leads to quantitative and topological changes in the flow, seek to be better understood.

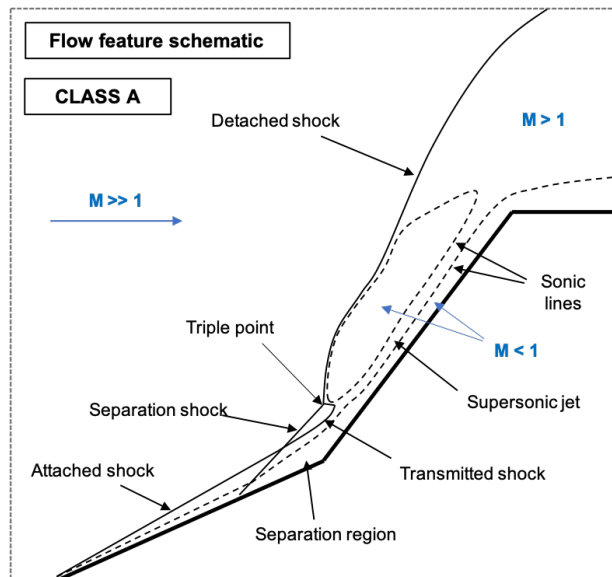


Fig. 6.21 Schematic of the known shock structure formed for the hypersonic flow over the previously studied hypersonic double cone test cases. All flow features are labelled, including sonic lines to depict the supersonic and subsonic regions of the flow. This flow structure is classified as CLASS A in the analysis to follow.

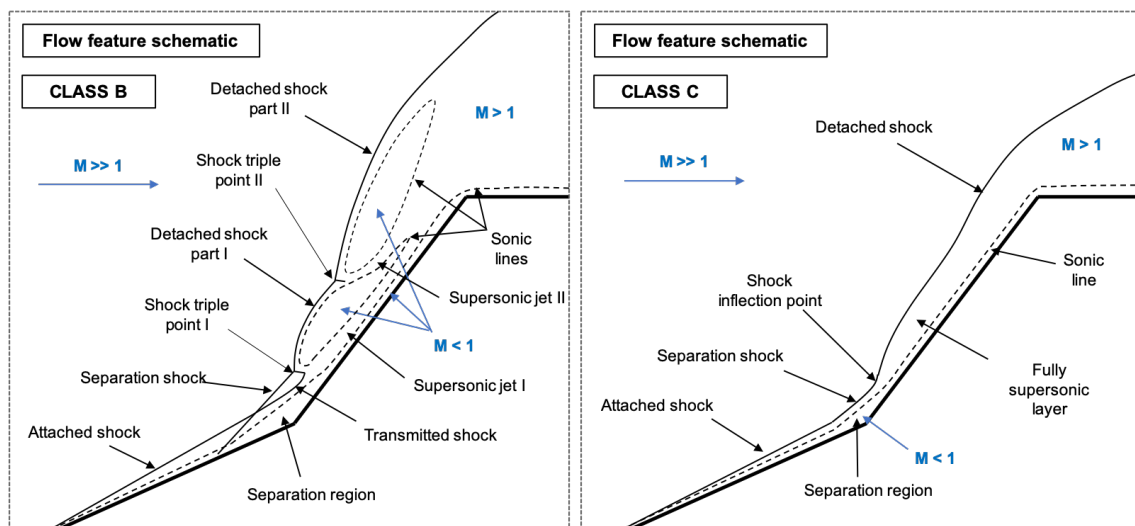


Fig. 6.22 Schematic of the flow structures CLASS B and CLASS C. All flow features are labelled, including sonic lines ($M=1$) to depict the supersonic and subsonic regions of the flow.

In relation to the surface actuation concept, the identification of topological changes in shock structure determines whether MHD actuation can *morphologically replicate* mechanical surface actuation effects.

To aid the subsequent analysis, a flow structure classification system is introduced. Since there are 3 identified emergent flow topologies within this work, they are classed A, B and C for the analysis of these studies. The definition and constituent flow features of each are given in Figures 6.21 and 6.22.

The classification system is not based on the singular shock interaction arising near the kink point, but the form of the *overall* shock structure as determined by the presence, absence or duplication of salient flow features. Specifically: the formation of shock triple points, and bounded subsonic regions. Therefore the topologies are delineated as classes, which consider *all* shock interactions (multiple may occur) within the total shock structure. This classification is highly relevant to the objective of assessing the shock structure's susceptibility to imposed MHD flow control, since the 3 classes show distinct differences in the bounded subsonic regions of the detached shock layer, which predominantly dictate the magnetic interaction and augmentation of the flow.

CLASS A represents the topology produced by hypersonic double cone tests in the CUBRC validation tests and in the MHD double cone experiment of the last section (6.2), where a single shock triple point, detached shock, and bounded subsonic region forms. CLASS B identifies flow structures where features surrounding the detached shock region ahead of the second surface become duplicated. Here a second shock triple point is associated with the formation of a second discrete subsonic region and a distinct secondary portion of the detached shock. CLASS C collectively identifies cases where the reflected flow over the second surface produces a shock inflection point, rather than a shock triple point, and no isolated subsonic region forms beyond the boundary layer and separation region.

6.3.1 Effect of conical surface angle

To first examine the effect of varying geometry on the base flow (no magnetic field), we conduct a parameter study of varied second surface angle (θ_2). Inclination of the second conical surface generically replicates the effect of a mechanical control surface.

It is identified from the previous studies that magnetic interaction is dominant in regions where the flow is at high temperature (high conductivity) and low velocity (low inertial forcing). Lorentz forcing has a linear dependency on $|u|$ (see equation 6.6) whereas fluid inertial forces scale with $|u|^2$. Therefore the magnetic interaction parameter: ratio of Lorentz forcing to fluid inertial forces is $Q_{MHD} \propto |u|^{-1}$. Increased flow stagnation and elevated electrical conductivity occur concurrently by increasing the angle of the second conical surface. We therefore conduct a parameter study with θ_2 surface angles of: 55° (experimental condition), 60° and 65° , where conditions are expected to *amplify* the shock enhancement effect once a magnetic field is introduced.

First the resultant steady state base flows are examined for each case: shown in Figure 6.24, As anticipated, increasing θ_2 creates larger regions of elevated electrical conductivity, and the formation of larger subsonic flow regions (depicted via the white sonic lines). Most

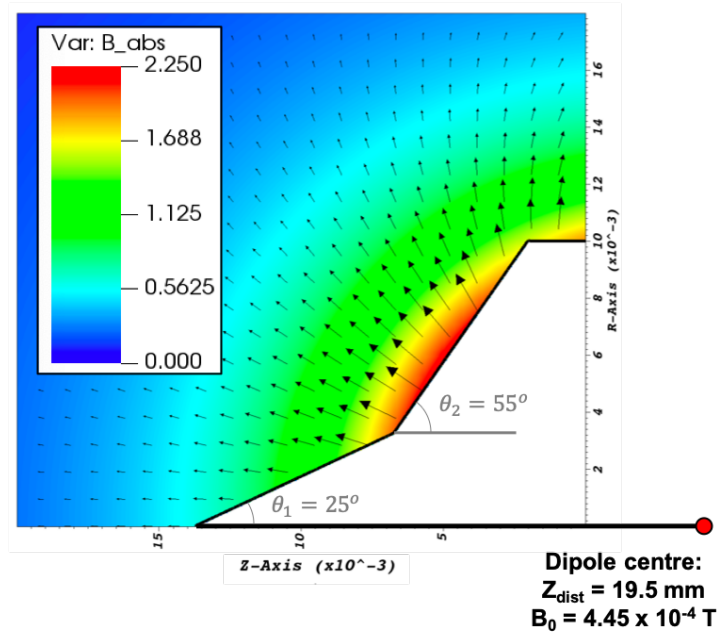


Fig. 6.23 Imposed dipole magnetic field configuration for the $\theta_2 = 55^\circ$ test case.

importantly, however, we observe the emergence of what can be identified as a new shock structure *class* (CLASS B) for the $\theta_2 = 65^\circ$ inclination case. As compared with CLASS A, CLASS B exhibits the emergence of a second shock triple point, which causes the formation of a second subsonic region within the detached shock region over the second surface. The constituent features are labelled in the schematic of Figure 6.22.

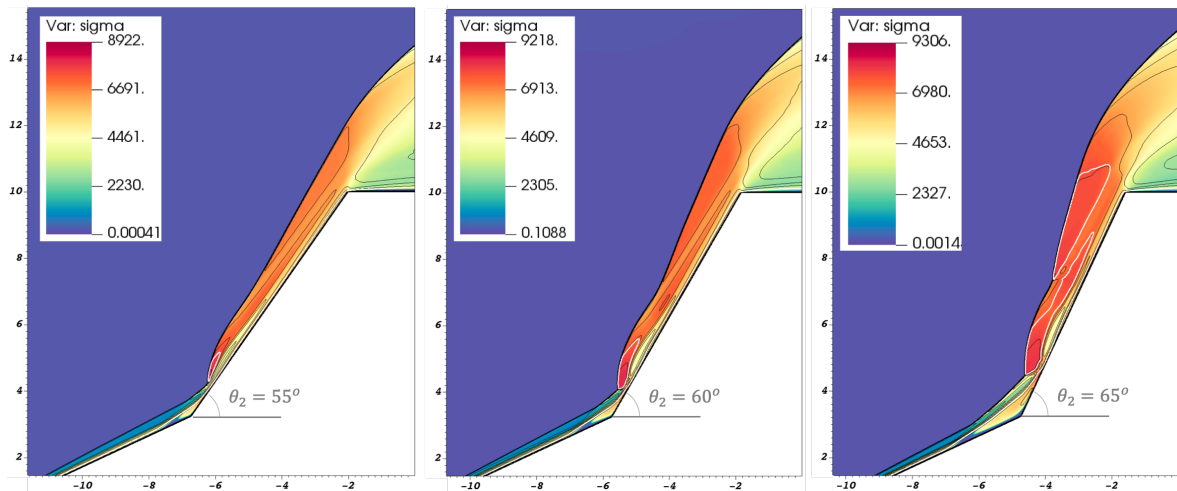


Fig. 6.24 Computed steady state electrical conductivity (colour-map) for the base case without magnetic field activation for each of the second surface angles. Mach number contours are overlaid in black with the $M=1.0$ sonic line contour additionally overlaid in white.

The dipole magnetic field is now activated to study the imposed MHD effect on the flow cases. For consistency with the experimental configuration of Section 6.2, the magnetic

field is configured to match the strong **B**-field case, with the dipole centre located at 19.5 mm from the conical point. The corresponding peak $|B|$ value in the fluid domain is 2.25 T, occurring partially along the second surface, as shown in Figure 6.23 (B_0 of equation 6.5 to produce this field is cited in figure).

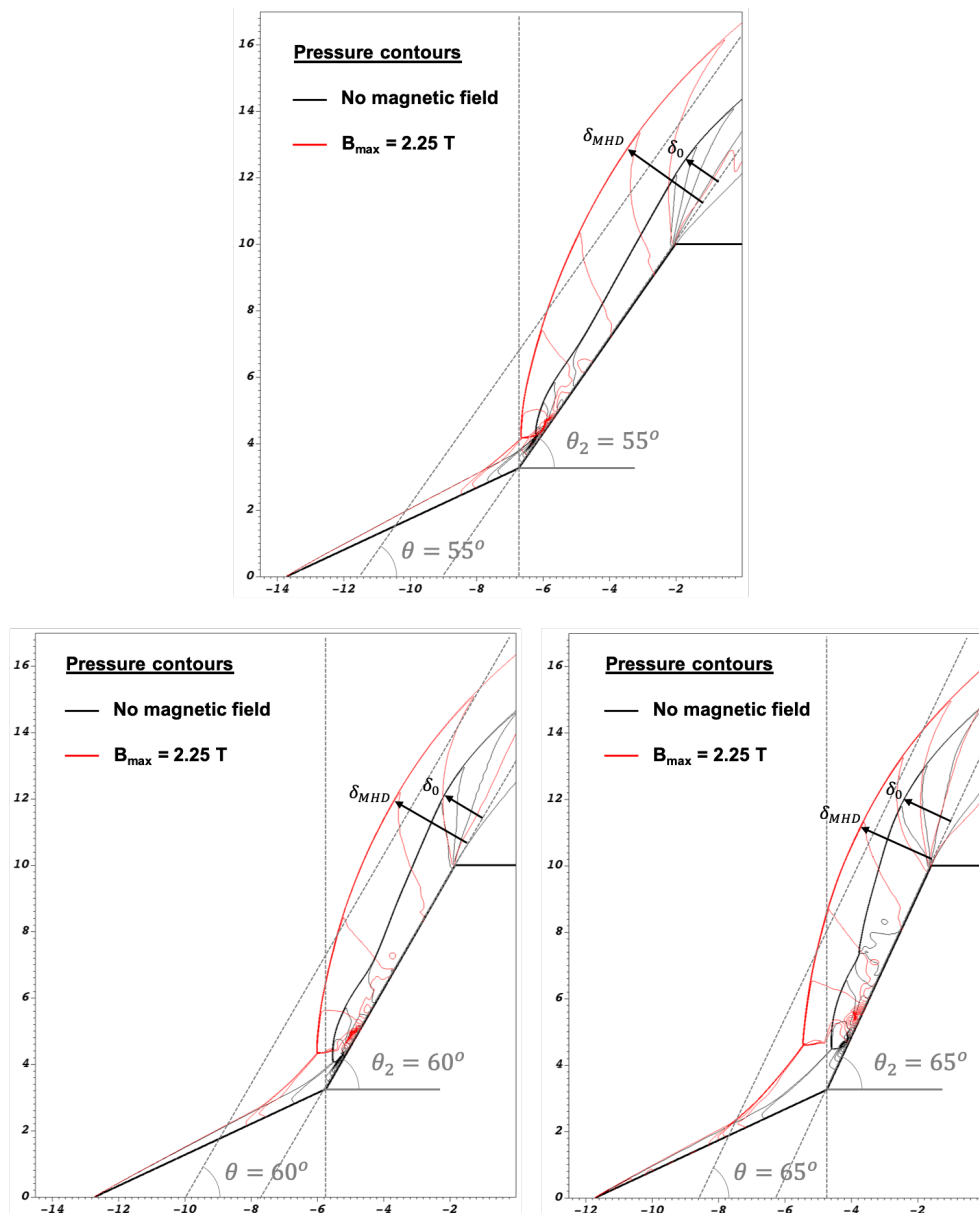


Fig. 6.25 Computed steady state pressure contours for different second conical surface angles. Guide lines are added for reference: one perpendicular to the z-axis of symmetry, intersecting through the kink point, and two tangential guide lines running parallel to the second surface incline, one at the surface and one offset 2 mm from the vehicle surface.

Varying the second surface angle affects both the maximum $|B|$ in the flow field and the angle of the **B**-field lines relative to the surface (and flow field). There is no perfect solution to isolate the effect of changed surface angle within the dipole magnetic field, given this is a complexly coupled problem. However, configurations can be achieved which closely control

Second conical surface angle: θ_2	Maximum perpendicular stand-off distance: δ_{MHD} (mm)	MHD shock stand-off enhancement (%)
55°	2.81	139.15
60°	2.55	91.73
65°	2.38	61.90

Table 6.3 Collated in the table is the measured peak stand-off distances for $B_{max} = 2.25$ T case, with computed MHD stand-off distance calculated as a % enhancement from the base case: $enhancement(\%) = \frac{\delta_{MHD} - \delta_0}{\delta_0} \times 100\%$.

B-field orientation and magnitude relative to the actuation surface. The selected approach is to maintain the dipole centre at $Z_{dist} = 19.5$ mm from the conical point, whilst fixing the shoulder point and kink point of the geometry along the r-axis, and extending along the z-axis as the θ_2 angle changes. This produces a magnetic field which is approximately congruent for each test case angle and B_0 is scaled to maintain precisely constant B_{max} of 2.25 T, in the flow field.

Figure 6.25 shows the steady state pressure contours for the base flow case as well as the enhanced shock structure of the MHD affected case for each conical surface angle. Reference lines are added to aid the analysis of MHD enhancement effect. Two classes of effects are observed as a result of the imposed magnetic field: (1) differences in the magnitude of shock enhancement effect between cases, and (2) alteration of the flow structure classification.

Notably, for the $\theta_2 = 65^\circ$ case, addition of the magnetic field is observed to alter the steady state flow topology from CLASS B classification to CLASS A. The magnetic enhancement of the separation region alters the fluid dynamics downstream along the second surface, while Lorentz forcing acts to bow the shape of the detached shock in all cases. Combined, the resultant steady state forms to become CLASS A under the imposed MHD effect.

With reference to the guide line running tangential to the second surface (off-set at 2mm), for increasing θ_2 values: all 3 inclined surface cases become more bow shaped and show a *decreasing* segmented arc which exceeds the tangential guide line. Measurement of shock stand-off and % enhancement from the base case is calculated by taking the peak stand-off distance perpendicular to the second surface tangential line for both the base case and MHD affected case. Values are compared in Table 6.3.

The base flow conditions depicted in Figure 6.24 indicate increased θ_2 promote conditions which would *amplify* the shock enhancement effect once a magnetic field is introduced. The counter-intuitive result which arises, is that the peak stand-off distance and % enhancement both diminish for increasing θ_2 . The MHD enhanced shock structure lifts maximally away, perpendicularly from the surface lines, for the case of minimum $\theta_2 = 55^\circ$.

The separation region, however, becomes significantly more enhanced with increasing surface angle. In the base case flow (without magnetic field activation), the separation region is larger, the more inclined the second surface. The subsequent expansion of the separation region due to magnetic interaction results in maximum enhancement for largest θ_2 .

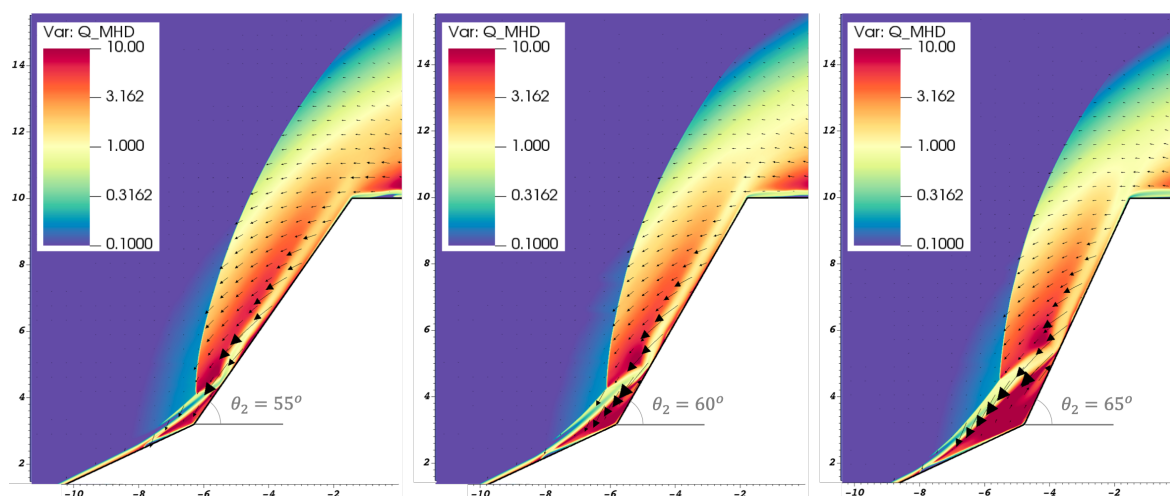


Fig. 6.26 Computed Q_{MHD} and Lorentz forcing vectors for each θ_2 surface angle.

A plot of magnetic interaction parameter (scaled logarithmically from 0.1-10) is compares the different conical surface angles in Figure 6.26. The significant expansion of the separation region can be explained by the strong magnetic interaction which is observed to occur in the high conductivity low velocity separation region near the kink. Expansion of the separation region causes the separation shock to become more detached and inclined relative to the first surface. This causes the jet stream to rise and reflect further along the second surface (peak surface pressure point). Enhancement of the separation region diminishes the volume of fluid within the detached bow shock region where peak Lorentz forcing and magnetic interaction occurs in this section of the flow field. The peak Lorentz forcing vectors shift from the subsonic detached shock region and towards the separation region as the surface angle increases. This coupled effect between the detached shock layer and the separation region leads to reduced stand-off distance in the upper bow shock region for increased θ_2 under MHD effect.

6.3.2 Magnetic path dependence

An important detail of the flow physics - critical to identify for the simulation set-up - is that the intermediate flow fields summatively influence the final steady state solution. This means the MHD affected solution exhibits temporal path-dependence.

For steady state MHD affected flows, it is identified that switching the magnetic field on once the solution has reached its base case steady state *is not equivalent* to the end steady state solution which forms summatively from a \mathbf{B} -field initialised at $t = 0$ s.

In a standard time-marched numerical simulation, the high Mach number free stream air is initialised to instantaneously impact the vehicle geometry and progressively converge to the steady state solution. This occurs in a similar manner to the test gas of a physical expansion tube experiment (although real experiments may have turbulent start-up air from the diaphragm rupture in the shock tunnel, but this is typically considered negligible). Changes to configuration mid-way through the simulation does not produce the same steady state solution as if the altered configuration was initialised from time = 0. This is found to be true for *changes to magnetic field configuration* as well as changes to geometric configuration.

This path dependence can be examined to better understand the result of the $\theta_2 = 65^\circ$ case. Figure 6.27 shows the time progression of shock structure by visualising the contours of the numerical Schlieren at different times from simulation start-up. Schlieren is selected as the parameter for visualisation to most clearly highlight the leading shock front.

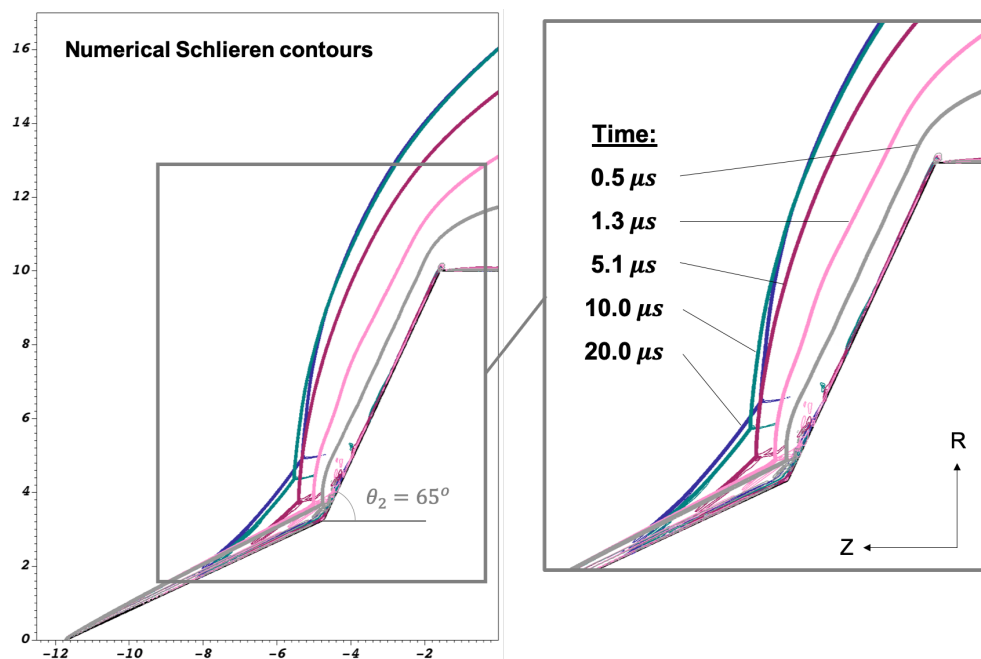


Fig. 6.27 Numerical Schlieren (density gradient) contours at different time stages of the evolution of the steady state for the case $\theta_2 = 65^\circ$ with magnetic field activated from $t = 0$ s.

The shock wave over the second surface begins largely parallel to the surface in the early time stages, before bowing outwards and away from the vehicle - demonstrating that no second triple point is generated along the path to the steady state solution. The path of motion of the shock triple point itself is particularly interesting - initial evolution of the point is upstream along the z-axis, before then more gradually moving outwards along the radial axis as the separation shock grows due to the magnetic interaction. The peak stand-off distance of the shock just downstream of the triple point in fact reaches its peak value earlier than the steady state shock-structure.

Due to the progressive Lorentz forcing activation from $t = 0$ s, the shock wave becomes more bow shaped from the first subsonic region, thereby reducing the angular force induced by the inclined plane, alleviating the moment leading to the split shock and second triple point formation. By activating the \mathbf{B} -field from $t = 0$ s, no second triple point emerges in the MHD affected flow case, and there is no added enhancement effect from a second subsonic, high conductivity region. The flow field does not *switch* from CLASS B to CLASS A, but forms progressively towards CLASS A in the magnetically influenced case.

This explains why the second subsonic region formed behind the emergent second shock triple point in the base flow case, does not lead to amplified enhancement in the MHD activated case.

6.3.3 Effect of magnetic field configuration

The study examines the effects of altered magnetic field configurations by varying the dipole centre location.

Moving the magnetic centre position along the z-axis maintains magnetic axisymmetry whilst altering the orientation of the magnetic field lines in the region where they emanate beyond the vehicle surface. Simply moving the dipole centre location with fixed B_0 in the dipole equation means the maximum \mathbf{B} -field strength interacting with the fluid also varies. Note that $|\mathbf{B}|$ diminishes cubically with radial distance from the dipole centre. To best isolate the effect of \mathbf{B} -field *orientation*, independent of \mathbf{B} -field *strength*, B_0 in the magnetic field equation (6.5 repeated below) is scaled such that the B_{max} in the fluid region is maintained at constant 2.25 T. The $B_{max} = 2.25$ T case at $Z_{dist} = 19.5$ mm corresponds to the $B_{ref} = 1.5$ T case of the previous sections. Figure 6.28 shows how the varied position of dipole centre changes the orientation of emerging field lines and the location of peak magnetic field strength.

$$\mathbf{B} = B_0 \left[\frac{3\mathbf{r}(\mathbf{r} \cdot \mathbf{m}) - r^2\mathbf{m}}{r^5} \right] \quad (6.5)$$

Figure 6.29 compares the steady state pressure profiles of the resultant MHD affected steady state flow field for the different dipole centre locations. Several interesting features arise: resultant shock structures exhibit dimorphic overall topologies between cases, which

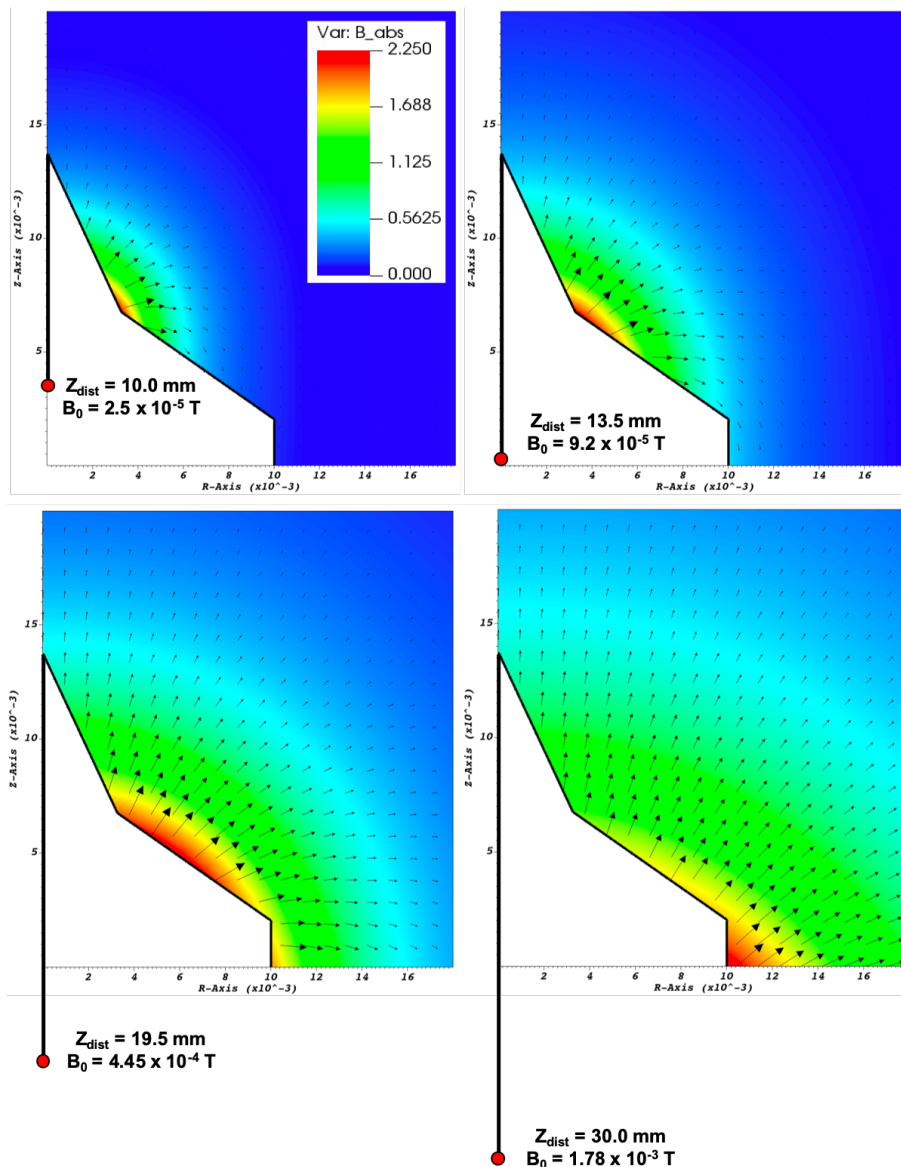


Fig. 6.28 Resultant magnetic fields from varied dipole centre locations: intensity colour plot (colour bar shown in left figure holds for all plots) with magnetic field directional vectors scaled by magnitude. Magnetic dipole centre shown, with calculated B_0 in order for maximum B-strength in the fluid region to be equivalent at 2.25 T across all cases.

has important consequences for the magnitude and characterisation of the shock enhancement effect.

Most critically, we observe that the $Z_{dist} = 30.0$ mm case leads to the emergence of the CLASS B flow structure (where the non-magnetic base flow was of CLASS A). Further, for the case where the magnetic field is at position $Z_{dist} = 10.0$ mm, we observe the emergence of a new classification of flow structure: CLASS C. The schematic for the TYPE C flow structure is given in Figure 6.22. The flow class is characterised by a shock inflection point, rather than the formation of a triple point, ahead of where the flow impinges on the second surface. This results in a fully supersonic post-shock layer within the detached shock region.

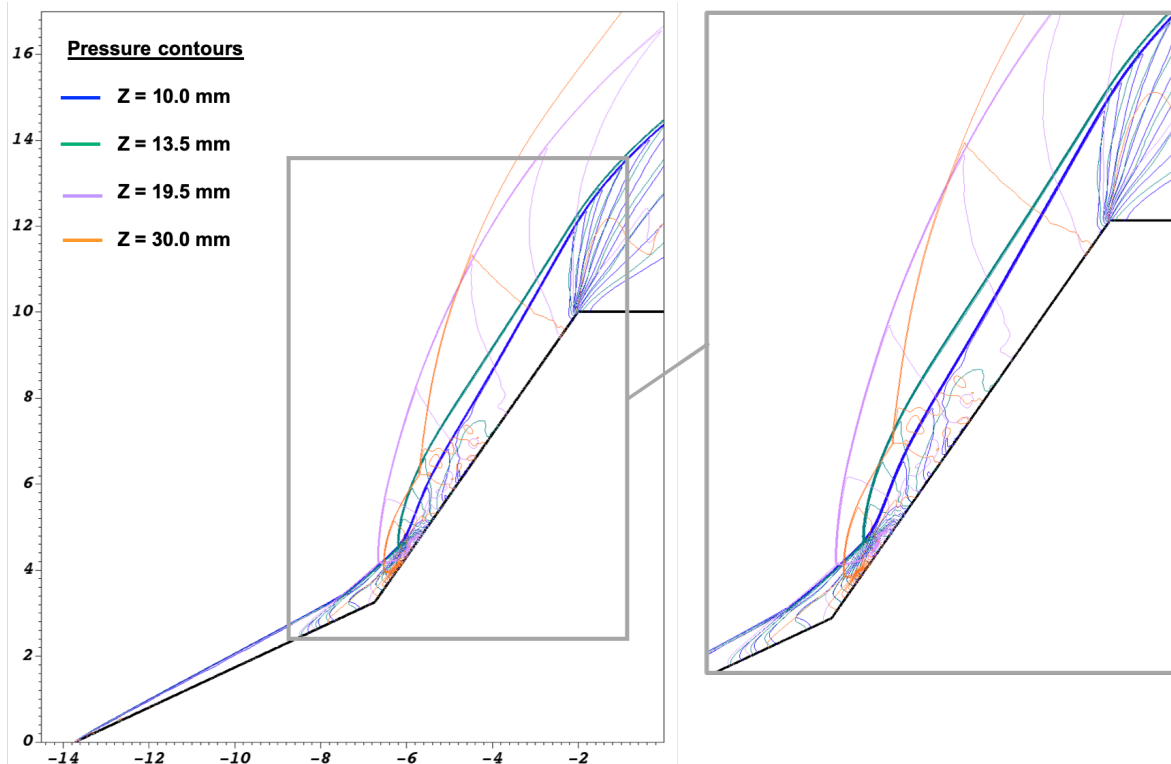


Fig. 6.29 Steady state pressure contours for each magnetic field location.

Examining the shock structures of Figure 6.29, the leading shock front over the second surface lifts away from the vehicle becoming broader above the shoulder for increasing Z_{dist} , until the $Z_{dist} = 30.0$ mm case, where we observe the emergence of the CLASS B flow structure. Since the shock wave splits midway along the second surface to form a second shock triple point, in the region centred at approximately the 6 mm radial line, the distance of the leading shock from the vehicle surface does not behave predictably with magnetic dipole position. Of the tested \mathbf{B} -field strength and dipole positions, the $Z_{dist} = 19.5$ mm case creates the largest shock enhancement effect over the region directly forward (z -direction) of the second surface. The detached shock part II of the $Z_{dist} = 30.0$ mm becomes more prominently enhanced in the region above the shoulder.

Also, notably, the emergent CLASS C flow structure of the $Z_{dist} = 10.0$ mm case results in a more suppressed shock structure. Compared to the base flow case, the detached shock remains closer to the second conical surface. Therefore, this magnetic field configuration could be considered to exhibit an MHD *diminishing* effect.

Focussing our attention on the separation region and surrounds, the position of the first triple point or shock reflection point (depending on the case) is not affected in a predictable way as the peak $|\mathbf{B}|$ location moves down the second surface. This is due to the complex interaction of the MHD effect, the SWBLI and separation region formation.

Analysis of the separation region (Figure 6.30) in conjunction with the magnetic interaction parameter and Lorentz forcing directional vectors (Figure 6.31) characterises some of

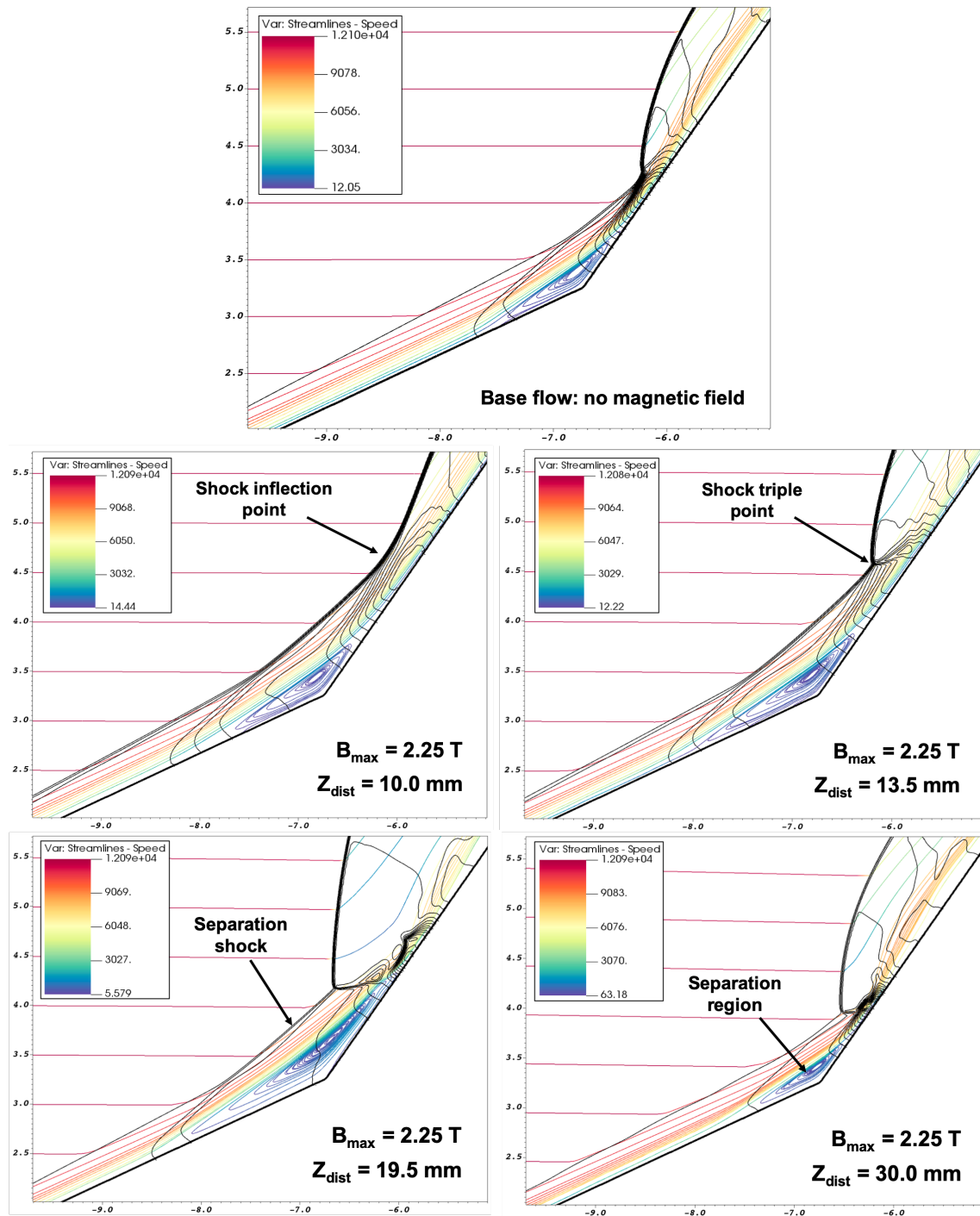


Fig. 6.30 Examining the effect of magnetic field location on separation region: steady state pressure contours in black with computed velocity streamlines (coloured by total velocity magnitude) shown for each magnetic dipole centre location.

the interdependent physical phenomena. With reference to these figures, an examination of the flow physics is given for each flow classification.

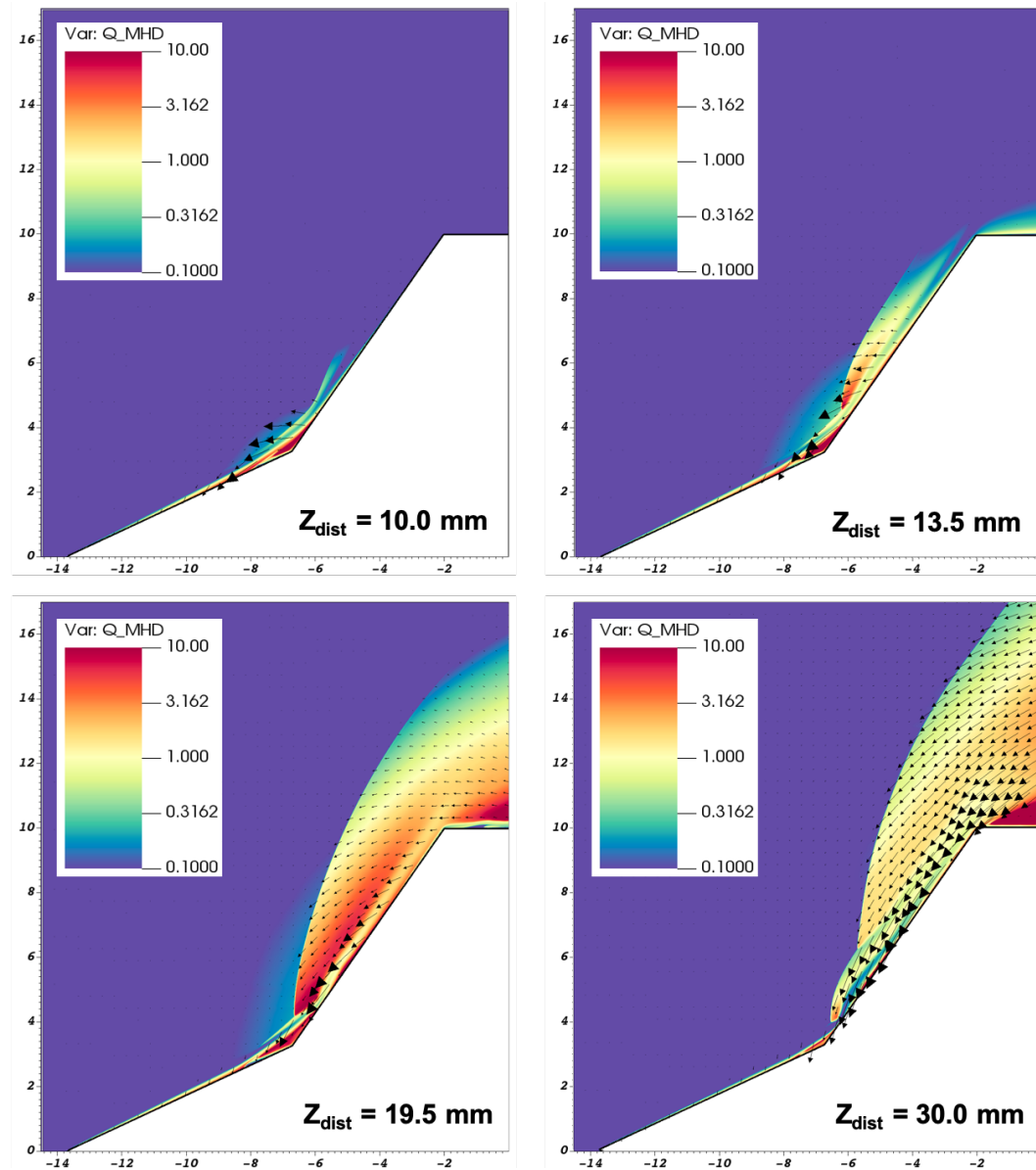


Fig. 6.31 Computed Q_{MHD} (logarithmically scaled between 0.1-10) and Lorentz forcing vectors (showing direction and relative magnitude) for each magnetic field location.

CLASS C flow structure: $Z_{dist} = 10.0$ mm case

As shown in the Q_{MHD} with Lorentz forcing vectors plot, the peak forcing and magnetic interaction both occur close to the kink point. MHD forced deceleration of the flow at the kink causes the separation region to enlarge (see leading pressure contours of the separation region have migrated upstream along the first surface) which causes the flow to be deflected away from the kink at an earlier separation point, resulting in a separated shock which becomes reflected by the second surface further downstream than the base case. Since the flow behind the separated shock is more tangentially aligned with the incline of the second surface (as compared with the base flow), the shock is weakly reflected without forming

a shock triple point. Absence of the triple point also eliminates the small subsonic region which forms just downstream of this shock feature (the subsonic region is retained in all the other flow cases).

Note that the colour-mapped streamlines reveal a much higher (and supersonic) velocity magnitude behind the shock reflection point than the shock triple point of the other test cases. Greater velocity magnitude in this region diminishes Q_{MHD} via two concurrent mechanisms: the non-stagnated gas results in a lower static temperature and thereby lower resultant electrical conductivity, while simultaneously the fluid maintains greater inertial force. These aspects dually act to diminish magnetic interaction. Recall that: $Q_{MHD} = (\sigma(p, T)|B|^2 R_0) / (\rho|\mathbf{u}|)$, and the flow exhibits both diminished $\sigma(T)$ and increased $|\mathbf{u}|$. Consequently, as there is almost no magnetic interaction downstream of the inflection point, there is no MHD forced deceleration to bow the shock wave. The shock position retains a flattened profile along the second surface. Therefore, counter-intuitively, the imposed \mathbf{B} -field actually serves to diminish the overall width of the shock layer over the second surface.

CLASS A flow structure: $Z_{dist} = 13.5$ and 19.5 mm cases

In the $Z_{dist} = 13.5$ mm test case, the peak magnetic field value is still located very close to the kink, however, in the previous $Z_{dist} = 10.0$ mm case the magnetic field lines were almost perpendicular to the z -axis at the kink, whereas in this dipole position the magnetic field lines emanate at approximately 40° away from the z -axis at the kink point, and the magnetic field diminishes more gradually at this radial distance from the dipole centre (refer to Figure 6.28). As a result, the Lorentz forcing vectors are also rotated. They now align to be almost direct deceleration vectors near the separation region (vectors run parallel to streamlines, forcing in the opposing direction to the fluid velocity), and the separation region becomes more enhanced in this test case.

Figure 6.30 shows the vortical streamlines of the separation region are notably enhanced from the base case flow (high Q_{MHD} can be seen in this region of high conductivity and low momentum) which in turn makes the separation shock more detached and lifts the flow reflection point further along the inclined second surface. For this magnetic field position, significantly greater Lorentz forcing originates along the second surface. Lorentz forcing augments the flow further outwards from the second surface resulting in the formation of a shock triple point and subsonic downstream region which further enhances magnetic interaction due to the low flow momentum and high conductivity. This could be considered a form of feedback effect. As a result we see a notably bowed shock structure lifted away from the second surface, predominantly in the region just downstream of the shock triple point. The position of the shock wave above the shoulder eventually converges closely with the $Z_{dist} = 10.0$ mm case, where magnetic interaction is weak or absent.

The $Z_{dist} = 19.5$ mm case exhibits the same primary dynamics. However, with peak $|B|$ shifted further down the second surface, the magnetic interaction and Lorentz forcing is

more significant in the detached shock region. This results in a more bowed shape of the detached shock and prolonged stem of the shock triple point. This creates the coupled effect of increasing the size of the subsonic high-conductivity region within the detached shock layer, which amplifies the total shock enhancement effect.

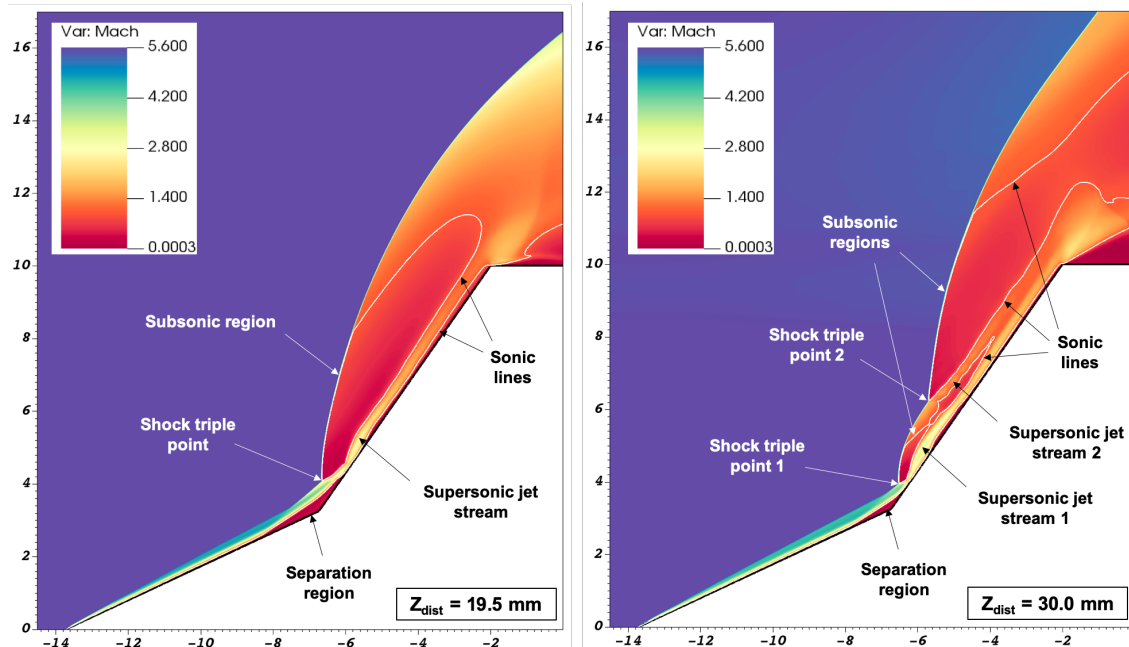


Fig. 6.32 Mach number plots of $Z_{dist} = 19.5$ mm and $Z_{dist} = 30.0$ mm cases, with sonic line ($M = 1$) contour and key features labelled.

CLASS B flow structure: $Z_{dist} = 30.0$ mm case

By placing the magnetic dipole centre far from the leading conical point, the peak $|B|$ emerges just above the vehicle shoulder, and the magnetic field diminishes more gradually in intensity. The region of the dipole magnetic field that interacts with the flow, exhibits field lines which are more homogeneously oriented (less variation in the angles of the \mathbf{B} -field vectors across the domain). The resultant flow field is very interesting for this test case. The Lorentz forcing acts to directly decelerate the flow velocity over the vast majority of the second surface shock layer (forcing vectors shown to almost directly oppose flow motion). The strong MHD deceleration forces which persist in the region around and above the shoulder creates a rotational pressure on the detached shock structure, which accumulates in angular force as the shock stand-off distance increases above the shoulder (the effective torque is enlarged by forcing from a greater displacement), ultimately leading to a split in the detached shock and a second shock triple point being generated. This significantly alters the resultant shock structure (formation of CLASS B from CLASS A base flow), as seen through the comparison of pressure contours (Figure 6.29).

A Mach number plot of the $Z_{dist} = 19.5$ mm and $Z_{dist} = 30.0$ mm cases are compared in Figure 6.32. The split shock structure has a number of consequences: a second supersonic jet stream forms within the detached shock layer, as well as a large second subsonic region forming downstream of the second shock triple point. The consequence of the shock splitting is that MHD enhancement effect is diminished (in terms of % increase in shock stand-off distance) along the first portion of the second surface, but is more pronounced above the shoulder. Precise prediction of magnetic dipole position and \mathbf{B} -field strength combinations which reach the angular force threshold for shock splitting would be of high importance for design in MHD flight control.

All cases

In terms of maximising the MHD enhancement effect for a given magnetic field strength, the orientation of the magnetic field lines are best optimised when oriented perpendicularly to the fluid flow direction, since:

$$\text{Lorentz Force} = \sigma \cdot (\mathbf{u} \times \mathbf{B}) \times \mathbf{B} \quad (6.6)$$

where σ is a scalar. The $(\mathbf{u} \times \mathbf{B}) = |u||B| \cdot \sin(\theta)$ term is maximised relative to u and B magnitudes when $\theta = 90^\circ$. There is no singularly clear \mathbf{B} -field orientation, however, to achieve this. The dipole configuration of \mathbf{B} has field lines which vary gradually in orientation, and the complex flow field exhibits velocities in many directions at different electrical conductivities. Moreover, the interaction between the flow-field and the MHD forcing affects the cumulative orientation of conductive flow velocity with the magnetic field lines, and so the base flow (without magnetic field) cannot clearly guide predictions of the resultant magnetically influenced flow. These coupled effects, among others, mean that the magnetically affected flow field can behave in counter-intuitive and unpredictable ways - as demonstrated through the cases simulated in this study.

6.3.4 Magnetic replacement of surface actuation - an outlook

In light of the complexity of the flow field coupled with MHD forcing effects, design for precise equivalence between magnetic interaction and mechanical surface actuation is a precarious task. However, an important result which can be drawn from these studies, is the identification of *classes* of configurations which produce *morphology equivalence* in terms of the flow structure.

Since the conditions leading the CLASS A flow structure have been extensively examined, here we demonstrate the two identified classes of cases where CLASS C and CLASS B flow structures emerge: drawing equivalence between surface inclination and magnetic field activation.

Firstly, we introduce the additional case where the second surface angle is *declined*. The base flow case (no magnetic field) is depicted in Figure 6.33, and demonstrates the formation of a CLASS C flow structure: a sonic line ($M=1$) contour is overlaid, demonstrating that only the boundary layer and separation region are subsonic. The remaining detached shock layer is fully supersonic, downstream of the shock inflection point.

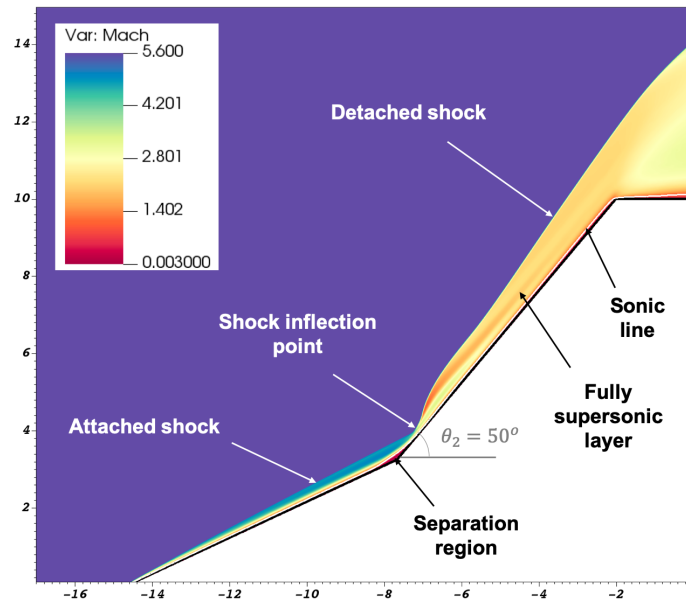


Fig. 6.33 Plot of Mach number for the base flow case with declined second surface angle at $\theta_2 = 50^\circ$. The steady state flow is of CLASS C exhibiting a shock inflection point and fully supersonic detached shock layer. The sonic line ($M=1$) is overlaid in white.

The numerical Schlieren images shown in Figure 6.34 exhibit two classes of equivalence. The declined second surface angle of $\theta_2 = 50^\circ$ and the magnetic dipole configuration of $Z_{dist} = 10$ mm produce flow topologies which can both be classified as CLASS C. This magnetic field configuration produces the same topology of a declined actuation surface which are characterised by a thin detached shock layer, and could both be considered to exhibit a shock layer *diminishing effect*.

The second Schlieren compares the computed flow field for the $B_{max} = 2.25$ T, $Z_{dist} = 30$ mm case from the dipole location parameter study, with the base flow (no magnetic field) of the $\theta_2 = 65^\circ$ case. As could be expected, both actions (magnetic and geometric) serve to augment the detached shock position further upstream. The particularly interesting result, is that both conditions produce a topological adaptation, resulting in the CLASS B flow structure. In both cases, the flow deceleration induces the formation of a second triple point (with second jet stream exhibiting a cascade of internal reflected shocks - seen weakly in the numerical Schlieren).

Whilst the same class of flow topology can be identified between cases, finer internal differences remain. The size of the separation regions and extent of the detached shock above the vehicle corner, differ between cases. Perfect matching would not be expected given the

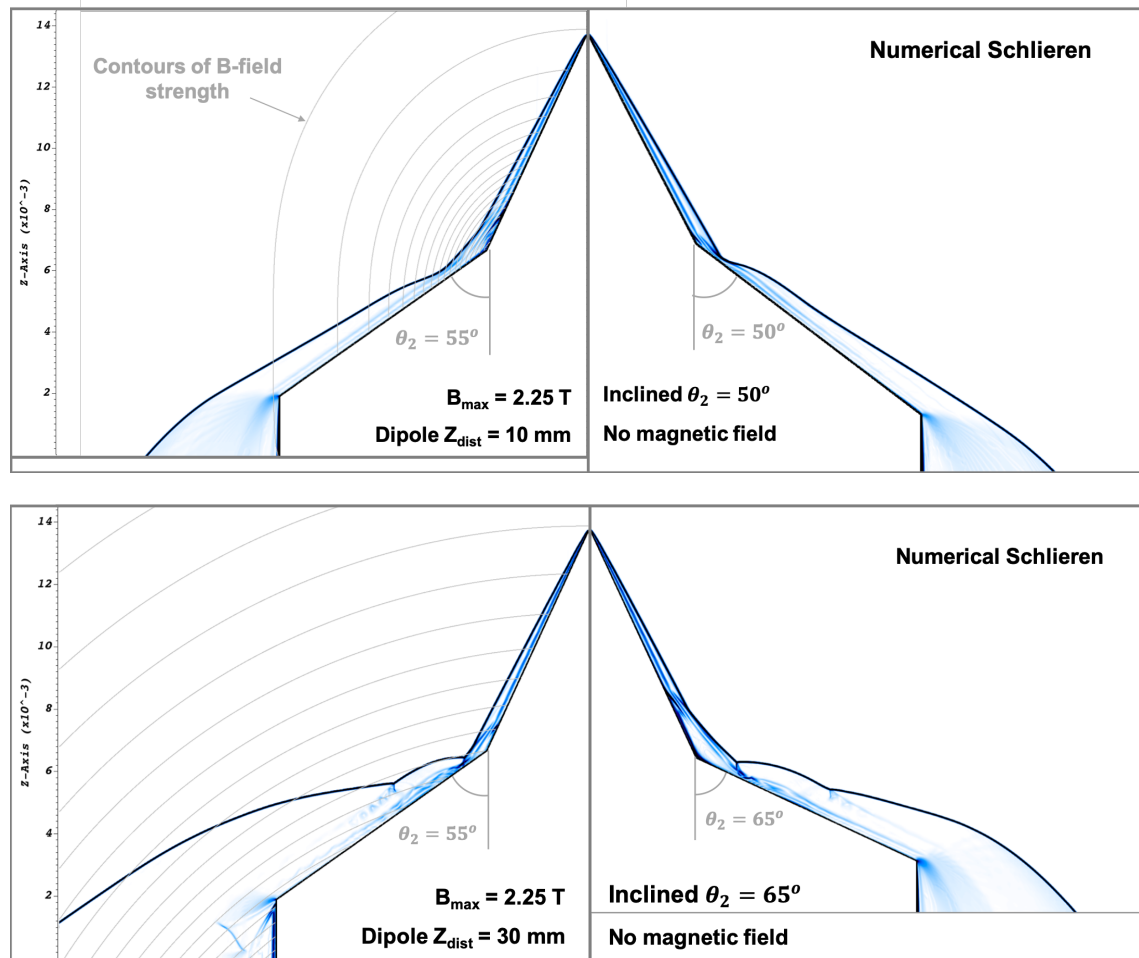


Fig. 6.34 Numerical Schlieren (density gradient) depicting two classes of emergent flow structures: Top) CLASS C, and Bottom) CLASS B. In each case an equivalence is drawn between: left) magnetic actuation effect, with contours of $|B|$ depicted in grey, and right) mechanical surface actuation via varied θ_2 angles of the geometry.

notable differences in the phenomenology of forcing dynamics. However, identification of equivalent structure *classes*, is extremely useful, since it provides a basis for quantitative analysis (regarding enhancement effects), which otherwise cannot be translated directly across classes of flow structures.

6.4 Conclusions

This chapter contains two aspects of importance: the *capabilities* of the developed numerical model to realistically simulate the hypersonic MHD applications, and the *insights* gained into the flow physics from the numerical studies.

The proposed combined numerical methodology presents a new approach to modelling the complex fluid-dynamic coupled with magneto-dynamic behaviour of the hypersonic flow

problems of this chapter. The role of plasma19X is crucial to capturing thermodynamic properties, direct electrical conductivity prediction, and resultant shock structures.

As previously investigated, a large portion of reentry trajectories take place within the equilibrium envelope. MHD studies have not traditionally been conducted in this altitude-velocity band due to: lack of availability of real flight data, the relatively lower temperatures and ionisation rate, and the challenges in electrical conductivity prediction in this regime. For a realistic reentry condition within the LTE valid regime, the effect of the EoS as compared with the commonly implemented ideal EoS shows significant differences in the flow predictions, for both the base flow properties and for MHD effects. In the ideal gas case, the electrical conductivity calculation can be considered independent of the base flow, however, for the plasma19X model, the electrical conductivity is strictly interdependent of the base flow. Even when the electrical conductivity is manually matched as a best fit analytic approximation to the real gas chemistry result, the resultant prediction of the MHD enhancement effect exhibits large differences between the two gas models. The implication is that MHD effects cannot be fully decoupled from the computed flow field, and therefore realistic thermochemistry is always critical for assessments of magnetic enhancement effects.

Moving from simple to complex shock structures, the double cone experiment with imposed magnetic field provides a key validation test for problems containing multiple shock interactions combined with MHD effects. Traditionally, producing quantitatively realistic results for this flow type has remained a challenge. Nagata and Wasai et al. attribute the differences between the experiment and their numerical results to uncertainty in the thermochemical model and to sensitivity of features around the separation bubble. The notable advances in this work pertain exactly to these identified aspects.

1. Regarding the EoS: as discussed in the previous chapters, the gas chemistry is critically linked to the prediction of electrical conductivity, which is crucial to accurately quantifying Lorentz forcing dynamics. The well matched base flow shock layer width of this work, as well as the MHD enhancement effect indicate that the plasma19X EoS makes improvements in the gas chemistry and resultant electrical transport properties. This is critical to the accuracy of the overall MHD model.
2. Regarding the sensitivity of separation region features: the combination of numerical methods used in the model of this work offer advantages. The embedded boundary approach permits the non-simple double cone shape to be easily defined, without causing any mesh skewing. The rigid body GFM approach was previously validated, and shown to be effective to capture the complex flow features which form around the kink and affect the overall shock structure. The other critical benefit of the combined embedded-boundary-AMR approach, is that the mesh is adaptively refined around the leading shock structure as its position evolves (body fitted meshes tend only to be highly refined in the boundary layer), which - combined with a spatially second

order numerical method - permits very high resolution of the shock front. This high resolution result is necessary to capture the detailed and sensitive regions of the flow, as well as to measure the relatively small enhancement effect of the experimental **B** case of the experiment.

The quantitative agreement obtained between simulation and experiment is a step forward for the study of hypersonic flows with multiple shock interactions under MHD influence.

In assessing the LTE validity - the pre-heated free stream conditions promote chemical reaction completion, however the post shock flow field is complex. One important relationship to draw is that the flow regions with highest fluid residence time map with the regions of highest magnetic interaction. This relationship supports the efficacy of LTE chemistry for studying MHD forcing effects.

Examination of the base flow case (no magnetic field) for increased second conical surface angle is shown to produce a new classification of flow topology - CLASS B - for sufficiently large θ_2 . This base flow exhibits conditions expected to amplify MHD interaction: formation of large subsonic regions of high electrical conductivity. However, activation of the imposed magnetic field reveals the opposite: peak shock stand-off distance enhancement is greatest for smallest θ_2 . Analysis of the flow field reveals that magnetic interaction (and resultant enhancement effect) dominates in the separation region. Expansion of the separation region diminishes the volume of fluid experiencing peak magnetic interaction in the detached shock layer, resulting in the coupled effect of increased enhancement of the separation shock with reduced enhancement of the detached shock, as θ_2 increases.

Notably, for the $\theta_2 = 65^\circ$ case, the base flow exhibits the CLASS B flow structure, whereas the magnetically influenced case converges to the CLASS A flow structure. Therefore, it is identified that application of an imposed magnetic flow can result in *topological adaptation* between the base flow and MHD affected flow. To the Author's knowledge, this is the first demonstration that an imposed magnetic field can serve to alter the flow structure *topology*, as well as position, within a steady state hypersonic flow field.

The numerical study of magnetic dipole centre location finds that the flow field is sensitive to magnetic field configuration. In fact, all 3 flow classes (A, B and C) can be produced, depending on dipole position. CLASS C exhibits what could be classified as an MHD diminishing effect, with the MHD interaction behaviour in the separation region leading to the formation of a shock inflection point instead of a shock triple point, which alters the downstream magneto-fluid dynamic behaviour in the detached shock region. The detailed flow physics for each topological flow class is described, revealing some of the key mechanisms of action.

The role of temporal path dependence was also identified for the case of magnetically influenced flow field evolution. While this is important for the purpose of correctly matching experiments, this could also be utilised more intentionally. Identifying transient or intermediate conditions of such flows could enable magnetic fields to be temporally activated

and deactivated in response to favourable flow feature formation. Such techniques could be leveraged to improve energy efficiency of on-board electromagnetic systems.

Taking a step back, computational models can be applied to conditions which have not been, or cannot be, experimentally investigated. As such, simulations are valuable for their predictive power, but should act in tandem with experiments. The validated model of this work can be used to investigate a wide range of different configurations, in order to propose new experiments to validate the observed effects. The complexity of the coupled fluid-magnetic interactions means that flow field effects are not always predictable - as found in this work. It would be valuable to conduct experiments to validate the MHD induced topological adaptation predicted by the simulations of this work.

A valuable extension to this work would be to conduct a large global sensitivity analysis - by varying many parameters over a wide multi-dimensional parameter space - to determine bounded multi-parameter problem configurations which lead to the emergence of each of the 3 identified flow structure classes. The obvious limitation to such a study is the large computational cost that would be required to run a sufficient number of test cases for a full global sensitivity analysis.

The most exciting result to emerge in this chapter, is the observed phenomenological similarity of a control surface effect with a magnetic interaction effect. The possibility of replacing mechanical actuation with magnetic flow control is an enticing prospect for hypersonic vehicle design. The identification of classes of equivalent shock structures is of high consequence for appraising the viability of emerging aerodynamic control technologies.

Chapter 7

New and emerging plasma technologies

The purpose of this Chapter is to demonstrate model *capabilities*, by applying the developed numerical model to another plasma-generation based application in aerodynamic flight control. Future investigations can examine the emergent flow *physics* in much greater detail. The intended scope of this study is simply to showcase the suitability and advantages of the numerical methodology, to highlight future research possibilities.

Plasma physics and aerospace engineering first came into contact in the context of atmospheric reentry plasmas in the mid 1900's. Since then, the coalescence of plasmas and aerospace technologies has ebbed and flowed, and gyrated, as emerging technologies were deemed feasible, infeasible, or superseded. One such technology breakthrough in the 1990's was the magnetohydrodynamic-bypass scramjet engine, which was able to accelerate the ionised flow out of the combustor to produce more thrust. In doing so, it also accelerated development and interest in aerospace plasma applications more broadly. Swiftly following the MHD by-pass engine, research interest took off in the areas of: remote energy deposition for flight vehicle drag reduction, flow control via near-surface plasma actuators, radiative heating based hypersonic wind tunnels, sonic boom mediation, and plasma enhanced ignition and combustion stability [26].

This Chapter applies the model of this work to new and emerging plasma technology concepts - specifically, remote energy deposition for aerodynamic control and for plasma enhancement in MHD flow control. With rapid advancement currently under way in laser technologies, it is expected in the near future that an efficient high-power and lightweight on-board laser system, such as a fiber laser system, will become available [76]. This opens up the possibility - sci-fi as it may sound - for laser energy deposition flow control technologies on-board of supersonic aerospace vehicles. New experimental and numerical research is being conducted to examine the feasibility and configuration of such prospective technologies.

The model of this work offers some key advantages when applied to these applications. The advanced plasma EoS can elucidate electromagnetic properties of thermally produced plasmas. The advanced geometry-meshing-AMR combination has high utility and

efficiency in tracking the complex transient flow features. When a plasma is generated with sufficiently high thermal energy, the model of this work presents a unique approach to the simulation of energy deposition plasma flows, and further, can permit the study of such flows under the influence of an applied magnetic field.

This Chapter should therefore be considered a pilot or preliminary study into the numerical modelling of remote energy deposition for emerging aerospace plasma applications.

7.1 Background

The viability of MHD flow control via an imposed magnetic field is foundationally influenced by the flow electrical conductivity. High enthalpy hypersonic regimes are able to ionise the flow sufficiently to drive a small electromagnetic effect, however supersonic regimes do not typically produce sufficient electrical conductivity. Therefore several methods have been proposed and studied to elevate the electrical conductivity of supersonic flow - either to supplement magnetic flow control, or for aerodynamic control of its own. Therefore such concepts are of emerging research interest.

There are many different techniques to generate and enhance the plasma, including: surface plasma actuators, plasma arcs, laser pulse methods, microwave energy deposition, electron beams and electrical discharges, all of which can be classified as energy deposition methods. Many such methods have been investigated experimentally and numerically [38, 74], and as summarised in the extensive survey by Knight [75].

Joule heating can be classified as the class of methods which deposit thermal energy due to air resistivity when electric, microwave or laser discharges are applied to the flow [74]. In the case of laser energy deposition, active flow control is enacted either due the blast wave generated at the source of energy deposition, or by the localised heating of the fluid. Zheltodov and Pimminov [37] note that such Joule heating methods can be utilised to achieve desirable properties including lift and drag control.

The relationship between the thermochemistry model and electrical transport properties has been found to be critical in the earlier chapters of this thesis. A few recent studies have investigated the effect of the real gas model in the simulation of plasma generation via laser energy deposition [165, 166]. However, the effects in terms of electromagnetic gas properties and subsequent MHD effects have scarcely been investigated. Numerical studies have examined the feasibility of electrical surface actuation (electrodes used to ionise regions of the boundary layer) combined with imposed magnetic fields to generate MHD control effects [72, 70], however these studies employ an ideal gas with finite conductivity approximation. Presently, flows with plasmas generated via laser energy deposition, combined with imposed magnetic field effects are yet to be reported upon.

Plasma generation via energy deposition can be leveraged for the purpose of elevating the conductivity of the flow for improved magnetic control viability. In this case, the properties

of electrical conductivity and electron number density are of interest. The model of this work is able to be directly applied to the simulation of plasmas formed by remote energy deposition, the computation of electrical properties, and possible influence of such plasmas via an imposed magnetic field. The plasma19X EoS is central to this capability, and the dynamic AMR has high utility for maintaining high effective resolution over a temporally evolving flow field.

7.2 Laser energy deposition modelling

The use of microwave and laser energy deposition has been demonstrated both experimentally and numerically to have effects of interest on high speed flows, including: drag reduction, lift and moment control, as well as, suppression of instabilities, alterations to shock wave boundary layer interaction and location of separation regions. Therefore, microwave and laser energy deposition methods have been investigated actively in recent years.

Experimental investigations of the phenomena associated with plasma generation via laser energy deposition has been conducted by Borzov et al. (1994) [167], Tretyakov et al. (1996) [168], and more recently by Adलगren et al. (2001, 2005) [169, 36]. The experiments of Adलगren et al., and the high quality Schlieren images produced therein, have been seminal for validation of numerical models, and as such, several authors have numerically simulated the Adलगren experiments.

In terms of the numerical modelling, choices include: (1) whether to model directly the physics of the laser energy absorption process and initial plasma generation, or, whether to adopt a simple parameter based cross-sectional initialisation where the plasma is considered to be instantaneously generated for a defined bounded volume of plasma, (2) whether to treat the flow as an ideal gas or to model the real gas thermochemistry, (3) whether to treat the system as inviscid and compute with the Euler equations, or to model the full Navier-Stokes equations.

In consideration of (1): modelling the actual energy absorption process, local radiative heat transfer and ionization leading to plasma generation has the benefit of self-consistent experimental inputs i.e. the exact specification of the laser beam (wavelength, focal length, focussing lense diameter, pulse duration, etc) defines the initialisation. This therefore removes empiricism, parameter fitting, and generalisations. The process of plasma generation via an optically focussed laser takes place on the time-scale of the order of nanoseconds. Direct simulation renders the problem as temporally highly multi-scale as the supersonic flow evolution and macroscopic dynamics evolve on the time scale of the order 10^2 microseconds. Direct modelling of the energy absorption and ionization process necessitates that non-equilibrium chemistry be considered, since reactions take place on a time-scale commensurate to that of the laser pulse duration. Alberti et al. [165] model the detailed plasma-generation method directly, by accounting for non-equilibrium chemistry and adopt-

ing a coupled multi-photon ionization and Bremsstrahlung radiation model. They find that plasma temperatures reach an extreme peak of approximately 250,000 K halfway during the pulse and then relaxes toward much lower values by the time the laser is turned off. By the time the laser energy absorption process has completed, on the time-scale of bulk fluid dynamics (several microseconds), the flow has almost certainly equilibrated. Therefore most models adopt a simple parameter-based cross-sectional energy deposition fit, where a highly energetic gas is initialised instantaneously in the flow domain, within a bounded volume of consistent total energy (matched with the calculated total laser deposition energy of the experiment). Whilst this relies on some degree of empiricism and parameter fitting, it has the advantage of far greater computational expediency where time-scale need not be restricted below the bulk fluid dynamic time-evolution when accounting for an instantaneous plasma initialisation.

A widely used relation for the numerically initialised energy deposition from a laser pulse is given by [37], which defines a Gaussian weighted ellipsoid:

$$q(t, x, y) = q_0 \cdot g(t) \cdot \exp \left[-k \left(\left(\frac{x - x_0}{r_r} \right)^2 + \left(\frac{y - y_0}{r_z} \right)^2 \right) \right] \quad (7.1)$$

where k controls the Gaussian variance of the energy profile, (x_0, y_0) is the centre point of the deposition location, r_r and r_z are the semi-major and semi-minor axes of the ellipsoid in the r - z plane. q_0 is the energy density over the bounded volume, which for an ellipsoid is given by:

$$q_0 = \frac{\eta E_0 C_p (\gamma - 1)}{\frac{4}{3} \pi r_r^2 r_z R} \quad (7.2)$$

where E_0 is the total laser energy, η is the energy conversion efficiency and R is the gas constant for air.

$g(t)$ is the time deposition function, which, given that the energy deposition is treated as instantaneous (initialised within a single time step), $g(t)$ is given by the simple step function:

$$g(t) = \begin{cases} 1, & \text{if } t = t_i \\ 0, & \text{otherwise} \end{cases}$$

where t_i is the time of the instantaneous deposition (singular or multiple).

In consideration of (2) ideal or real gas treatment of the ensuing flow: a recent study by Kianvashrad and Knight compared the results of laser energy deposition for a thermally perfect model (which does not consider any thermochemistry), and for a large 23-species real gas model. The important conclusion was that both models gave “essentially identical results” [170] in terms of the bulk fluid dynamics and aerodynamic properties (pressure and density profiles, and computed drag forces). The extensive review by Russell [74] similarly notes that, for the purpose of capturing the macroscopic flow dynamics, an ideal gas model is sufficient,

and far more computationally expedient. However, the more computationally intensive real gas model is able to elucidate additional information, such as species composition in the plasma. For flows with peak temperatures below approximately 550 K, there is negligible difference in temperature and internal energy predictions, however, differences emerge in more thermally energetic flows. This is consistent with the EoS analysis previously in Chapter 3. Use of simple or complex EoS therefore depends on peak energies and which properties are of interest.

Finally, in regards to (3) inviscid or viscous modelling of the flow: a number of studies have compared the results of Euler vs full Navier-Stokes flows. Both model produce essential identical transient flow features, and only very small differences can be observed when directly comparing property traces near the model surface.

7.2.1 Numerical modelling considerations

The only required extension to the numerical model pertains to the instantaneous energy initialisation. Some consideration is required in relation to the instantaneously defined sharp property gradients near the location of energy deposition, and the AMR framework.

Firstly, one must consider the physical definition of the energy deposition (ED). Considering the total energy is composed of an internal and kinetic energy component: $E = \rho e + \frac{1}{2}\rho|\mathbf{u}|^2$, Joule heating methods raise the thermal energy of the system, therefore the numerical implementation must be consistent with raising the total thermal energy in the bounded volume V by:

$$E_0 = \int_V (\rho e) dV \quad (7.3)$$

thereby without affecting the momentum in the 0^{th} time-step of energy deposition. This can be enforced by implementing the ED in terms of primitive variables, noting that: $e = \frac{p}{\rho(\gamma-1)}$, then for the general form of an ellipsoid with Gaussian profile for the energy distribution, the ED at cell (i, j) can be implemented as an instantaneous pressure rise of:

$$\Delta p_{i,j} = \left(\frac{E_0 \cdot (\gamma - 1)}{\frac{4}{3}\pi r_z r_r^2} \right) \cos\left(\frac{(x_i - x_0)}{r_r} \cdot \frac{\pi}{2}\right) \cos\left(\frac{(y_i - y_0)}{r_z} \cdot \frac{\pi}{2}\right) \quad (7.4)$$

where (x_0, y_0) is the centre coordinate of the ellipsoid.

Considering now the AMR implementation: the computed flux from the direct energy deposition initialised at the 0^{th} time step affects the conservative variables (including ρ) in the 1^{st} time step post ED. This therefore influences adaptive refinement (refined based on $\nabla\rho$) at the 2^{nd} step. Introducing fine mesh patches over an existing strong property discontinuity results in small numerical oscillations at the patch boundaries. Additionally, the bounded volume deposition site typically in the freestream tends to consist of the coarsest mesh (base) level.

Therefore, the approach proposed is to pre-emptively define the refinement *before* the pressure-based ED step. This ensures high resolution in the ED location prior to initialisation. The additional refinement condition is added:

Algorithm 5 ED adaptive refinement tagging condition

```

while  $n\_pulses < n\_total\_pulses$  do
  if ED_time < current_time +  $\Delta t$  then
    for each cell in domain do
      if  $\left(\left(\frac{x-x_0}{r_r}\right)^2 + \left(\frac{y-y_0}{r_z}\right)^2\right) \leq 1$  then
         $\rightarrow$ tag cell()
      end if
    end for
  end if
   $\rightarrow$  count ED n_pulses
   $\rightarrow$  compute next ED_time
end while
  
```

A very important consideration is that stable Δt is computed at the 0^{th} mesh level, and hierarchically refined cells are sub-cycled at the integer fraction of the level 0 stable Δt . The AMReX procedure for time stepping over the AMR levels is depicted in Figure 7.1.

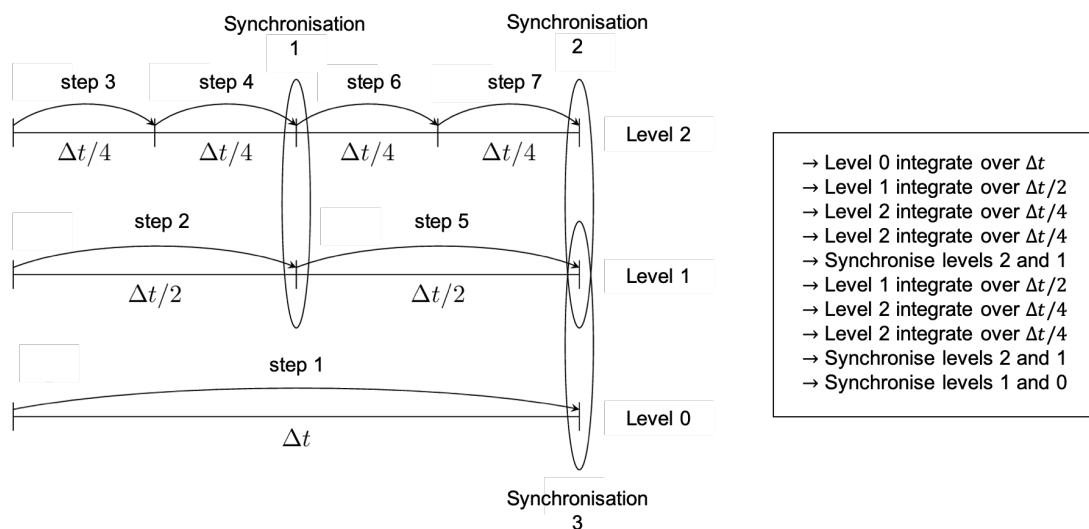


Fig. 7.1 Multi-level procedure for time-step sub-cycling, depicted for 2 AMR levels. Chronological steps listed. Synchronisation steps between level integrations ensure that flux conservation is maintained between the finer cells and adjacent coarse cells. This is termed *re-fluxing* where the coarse data (lower accuracy) is modified in line with the fine data solution at the coarse-fine boundary. This figure is adapted from an image by A. Meyers, AMReX developer [35].

It is also necessary to consider at what step within the overall algorithm to instantaneously deposit the energy. Since the high temperature plasma temperature will instantaneously elevate the maximum acoustic speed in the domain, the new stable Δt must be computed to

include the new plasma region before the next finite volume update, otherwise the model becomes numerically unstable. In the AMR context, if the ED takes place on a sub-cycled level, where Δt has been determined at the 0^{th} level without the high temperature ED zone then, again, the method becomes unstable.

Therefore, within the AMR framework, the instantaneous ED must take place on the highest level of refinement *after* the final time sub-cycle, and *before* the next Δt calculation. This requires tracking of the sub-cycles with ED on the condition: `level == max_level` **and** `sub_cycle == max_sub_cycle` where:

$$\text{Total sub cycles} = \sum_{level=0}^{max_level} R^{level} \quad (7.5)$$

where R is the refinement factor.

For test cases with flows over blunt bodies the HLLC-HS solver is employed to stabilise any transverse wave instabilities which form at high resolution. With the MUSCL extension, the method is 2nd order in time as well as space, and the AMR functionality is particularly useful for capturing the dynamic transient flow features which emerge from the ED.

7.2.2 Validation: single pulse laser energy deposition over a blunt body

The seminal experiments by Adelgren et al. [36] are very useful for validation of numerical models of laser energy deposition due to the high quality Schlieren images produced at defined time frames after laser energy deposition. The experiments are of a Mach 3.45 flow over a spherically blunted cylinder, with laser beam depositing energy at a point along the upstream centreline once a steady state shock has formed around the model. The geometric configuration is a sphere of radius 12.7 mm with cylindrical aft body, and laser deposition location of 25.4 mm (1 diameter) upstream of the sphere surface. The free-stream properties are given as:

Experimental conditions:

$$\begin{aligned} M &= 3.45, Re_D = 5.0 \times 10^5, V_\infty = 611.4 \text{ m/s}, T_\infty = 77.8 \text{ K} \\ \rho_\infty &= 0.587 \text{ kg/m}^3, p_\infty = 13100 \text{ Pa}, E_0 = 283 \text{ mJ}, \text{Gas} = \text{Air} \end{aligned}$$

We are interested in comparing the numerical Schlieren result of the model to the high quality experimental Schlieren images captured for the full flow field. Results show the utility of the AMR technique to efficiently capture the complex transient features at high local resolution. The simulation is run with a base resolution of 38 cells per model radius in the half plane, with 3 levels of AMR, therefore with effective resolution of 304 cells/radius.

Simulations are run both for the full plasma 19X Navier-Stokes model and the Euler model closed with ideal gas EoS. Numerical Schlierens are difficult to differentiate between the two simulations. Figures 7.3 and 7.4 show the numerical Schlieren produced for the ideal Euler result (for the purpose of direct comparison with the ideal Euler model of Zheltovodov

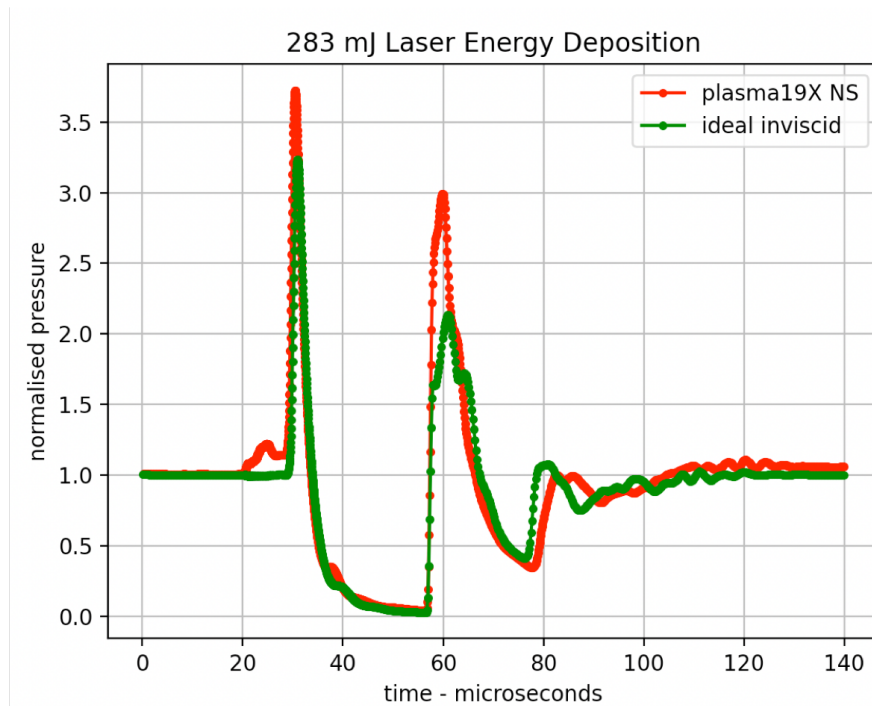


Fig. 7.2 Pressure over time, sampled at the stagnation point at the front of the spherical leading surface: comparing result of the full Navier-Stokes simulation closed with plasma19X EoS, and the inviscid Euler simulation closed with ideal gas EoS.

et al.). A pressure trace taken at the stagnation point at the geometry surface shows only very small differences computed by the two models. The pressure trace (Figure 7.2) also aids the analysis of the surface dynamics.

Analysis of the pressure traces combined with Schlieren images reveals the following flow dynamics: The experiment demonstrates a laser generated blast wave expanding and advecting from the site of the deposition. This results in a sharp pressure rise as the blast wave expands, propagates and impinges on the model surface. This is followed by a period of decreased surface pressure due to the expansion region behind the blast wave, followed by a series of re-compression and expansion events at the centreline stagnation point due to transmitted and reflected shock behaviours. Notably, when the plasma region contacts the model surface, the bow shock begins to lense upstream and toroidal vortices are formed as a result of the Meshkov-Richtmeyer instability.

Results of the simulations reveal very high suitability of the model to capture the time-accurate dynamics of laser pulse and blast wave interaction with the settled bow shock (all key features can be matched with experimental images). The AMR is particularly effective in tracking the shock-wave and vortical features, and the parameter-based cross-sectional energy deposition fit for the plasma initialisation described in section 7.2.1 is also shown to accurately represent the macroscopic fluid profile, and ensuing dynamics.

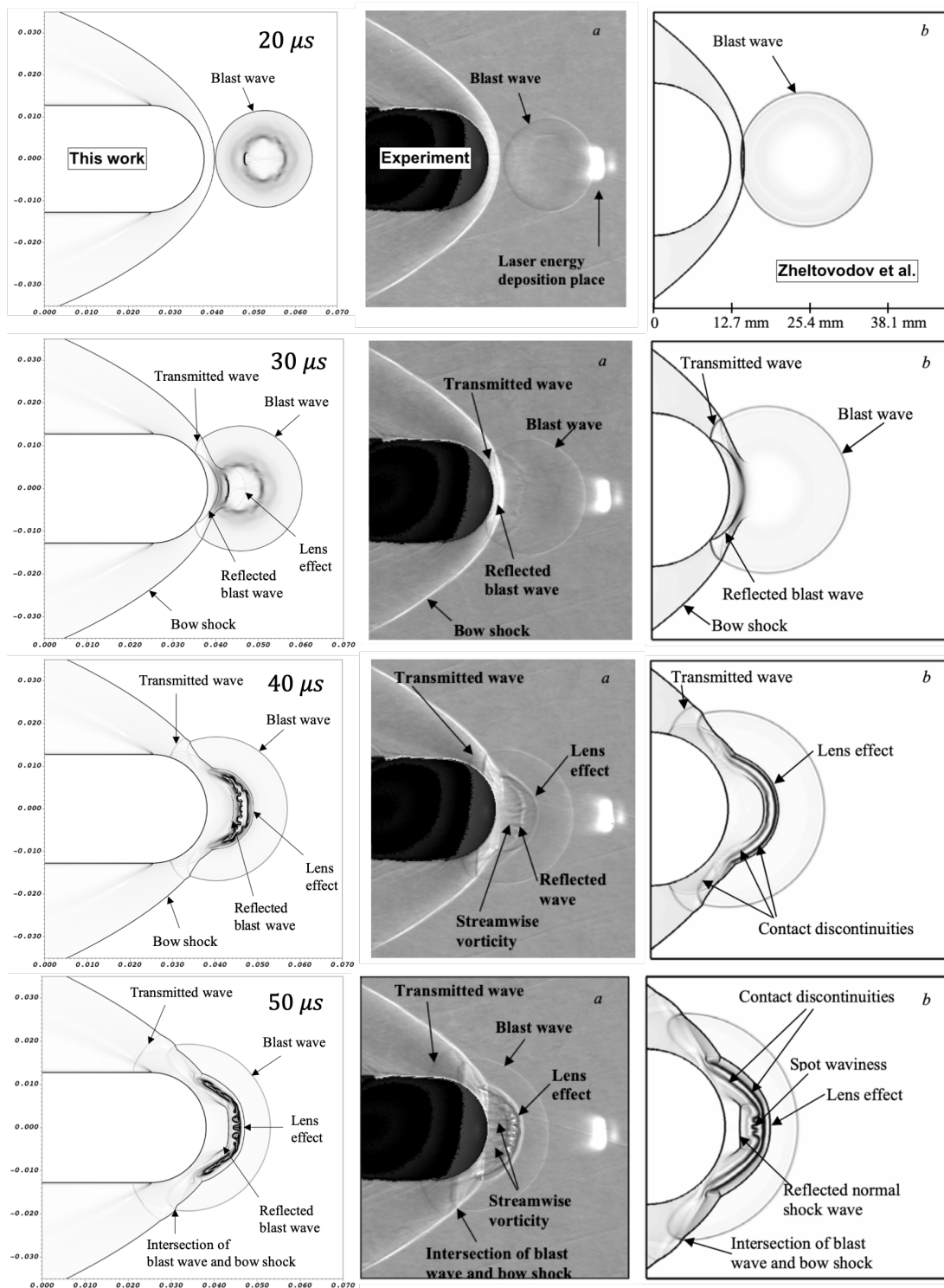


Fig. 7.3 Numerical Schlieren result of this work (left column), compared with experimental Schlieren image from Adelgren et al. [36] (middle column), and the numerical results of Zheltovodov et al. [37] (right column) at equivalent times post single laser energy deposition: $20\mu\text{s} - 50\mu\text{s}$

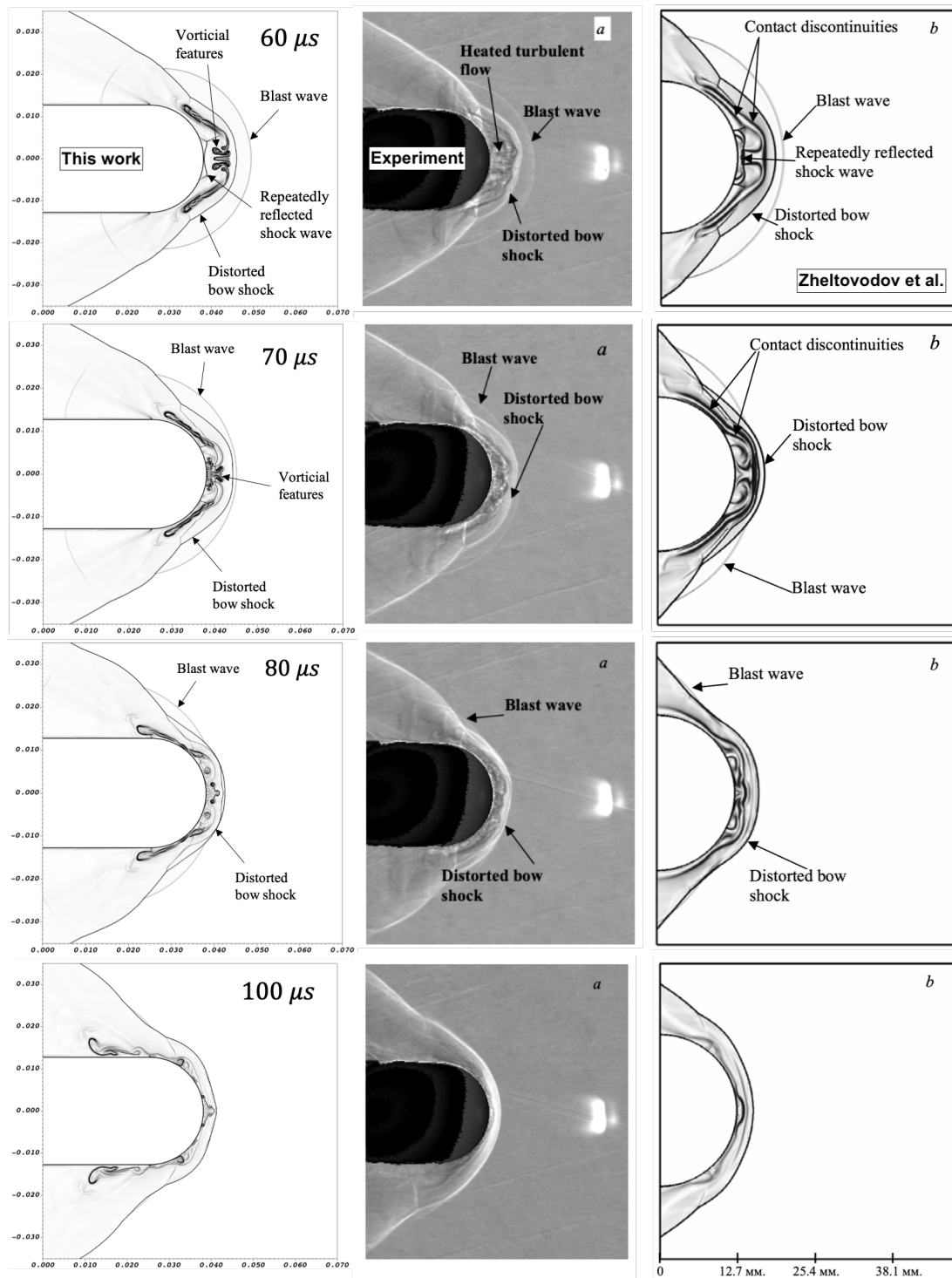


Fig. 7.4 Numerical Schlieren result of this work (left column), compared with experimental Schlieren image from Adelgren et al. [36] (middle column), and the numerical results of Zheltovodov et al. [37] (right column) at equivalent times post single laser energy deposition: 60 μs – 100 μs

7.2.3 Validation: double pulse laser energy deposition over blunt body

In the case of repeated laser pulses, when the frequency is sufficiently high that the generated blast waves from the energy deposition interact, the dynamics of the laser heated bubbles exhibit interesting interaction dynamics before impacting the blunt body. Schülein et al. [171] conducted experiments which demonstrated the intricate interaction of double laser pulses. They also produced simulations of this effect to better elucidate the physics of the resultant flow formations.

Experimental conditions:

$$M = 2.0, Re_D = 1.54 \times 10^6, V_\infty = 571.0 \text{ m/s}, T_\infty = 270 \text{ K}$$

$$\rho_\infty = 0.8136 \text{ kg/m}^3, p_\infty = 47368.4 \text{ Pa}, E_0 = 333 \text{ mJ}, \text{ Gas} = \text{Air}$$

The geometry is a sphere with radius 30 mm, blunted at the leading surface where the optical lens is located (radial distance perpendicular to blunted surface = 29.58 mm). The point of laser energy deposition is 76 mm upstream of the leading surface, and the time between repeated pulses is $\Delta t = 20 \mu\text{s}$.

Since peak temperatures in the laser-generated heat bubble exceed 900 K and it is the high temperature low density regions which create suction effects between repeated pulses, the simulation is run with the real gas chemistry EoS plasma19X, and viscous effects are also accounted for. Resolution is approximately equivalent to the single laser pulse case, with 3 AMR levels and effective resolution of 300 cells/radius.

The numerical Schlieren produced from this work is compared to experiment and simulations of Schülein et al. in Figure 7.5.

Results show that the instantaneous energy deposition via the bounded volume approximation of equation 7.1 is effective not only for a single laser pulse, but to in fact capture the interaction of consecutive laser pulses which interact with one another. Whilst the time between repeated instantaneous energy depositions is fixed ($20 \mu\text{s}$) there is some empiricism involved in the radius of the Gaussian deposition. Very good similarity between experiment and simulation is found for a spherical deposition with radius of approximately 2 mm. The Gaussian pressure distribution is fit in each case to maintain fixed defined $E_0 = 333 \text{ mJ}$.

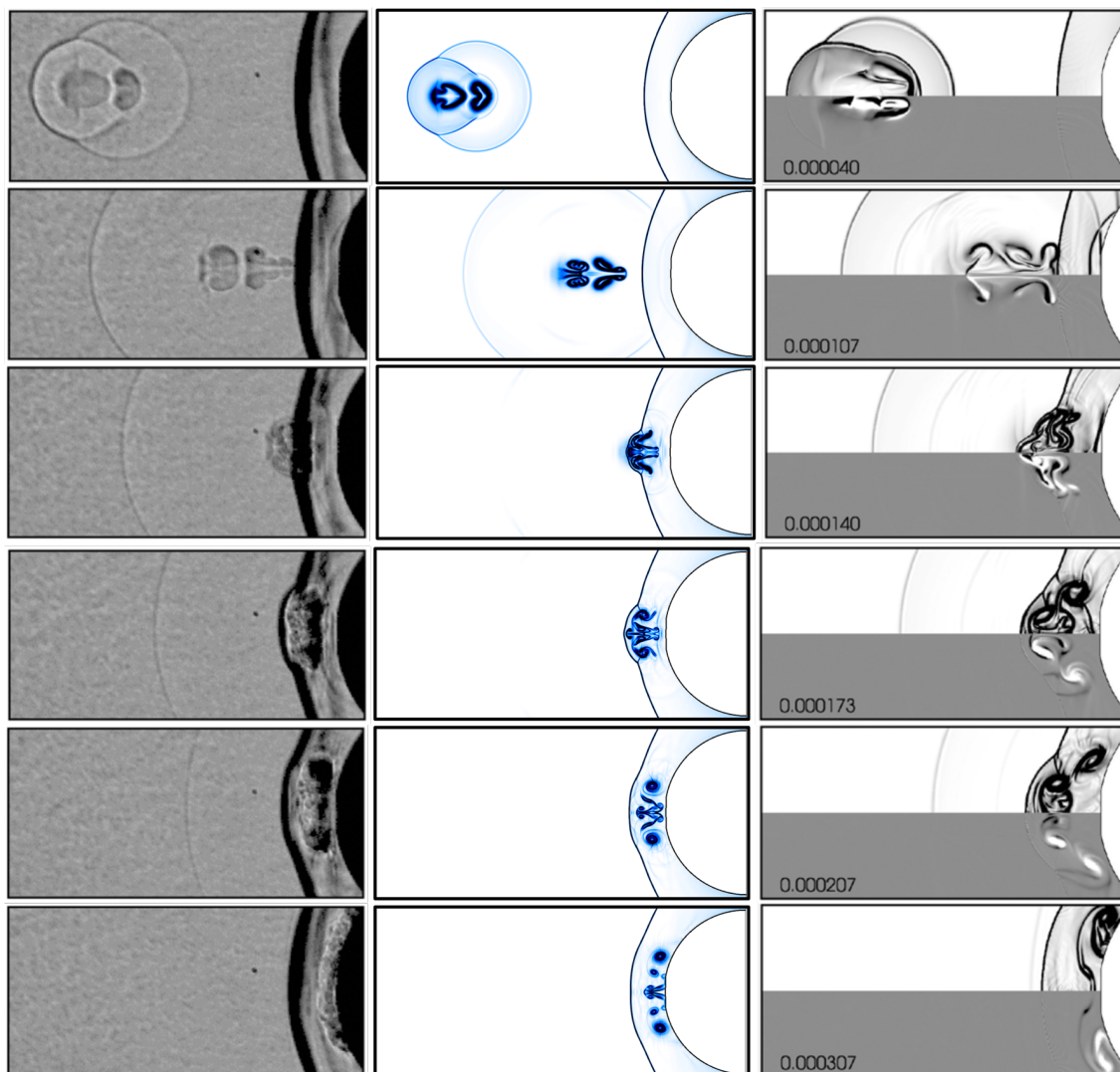


Fig. 7.5 Experimental Schlieren from Schülein et al. experiments (left column) compared with numerical Schlieren result of this work (middle column), and the numerical results of Schülein et al. [37] (right column) at equivalent times post double pulse laser energy deposition.

7.3 Plasmoid generation via magnetocompressor

Another method of direct energy deposition was recently studied experimentally and numerically by Znamenskaya et al. [38] in their 2019 paper: “Supersonic Flow past a Blunt Cone under the Action of Plasma Formation”. In the experiment a magnetoplasma compressor was able to generate a ‘plasmoid’ in a high pressure bounded volume. High speed shadowography shows the plasmoid to interact in a complex manner with the previously steady Mach 3.1 flow around the blunted cylinder, initiating a cascade of unsteady shock wave interactions as the plasmoid expands and passes over the shocked flow.

The accompanying simulations of Znamenskaya et al. [38] model the plasmoid through instantaneous initialisation of a higher pressure bounded volume of radius r_0 where the internal pressure (p_i) can be calculated as:

$$p_i = \frac{(\gamma - 1)E_0}{\frac{4}{3}\pi r_0^3} + p_\infty \quad (7.6)$$

The simulation of this work is configured to match the dimensional set-up of the experiment, and Mach number of 3.1. The initial conditions are therefore set to:

Simulation initial conditions:

$$M = 3.1, V_\infty = 1054.91 \text{ m/s}, T_\infty = 288.2 \text{ K},$$

$$\rho_\infty = 0.01225 \text{ kg/m}^3, p_\infty = 1013.25 \text{ Pa}$$

$$E_0 = 282.8 \text{ mJ}, \text{ Gas} = \text{Air}$$

Simulations show a steady state definitively reached by 110-130 μs , which is in very good agreement with the steady state reached in the experiment. Therefore the instantaneous energy deposition is initialised in the simulation to occur at $t = 130 \mu\text{s}$. Under these supersonic transient flow conditions, the effect of viscosity is negligible. Znamenskaya et al. use an Euler model closed by ideal gas law, and so for the purpose of first validating against their results we present the results of the inviscid, ideal simulation, to ensure all key shock features are captured and consistent with the literature result.

The literature result of Znamenskaya et al. as compared with the results of this work (both as ideal Euler models) is shown as model verification through Figures 7.6 and 7.7 for the unsteady progression of the plasmoid. For this work, a base resolution is 128×256 cells with 2 levels of factor 2 AMR. The inviscid fluxes are solved with the HLLC-HS solver as this problem is susceptible to carbuncle instabilities.

The results of this work show very good agreement with the previous solution, with all same key wave features captured in the model of this work.

Examination of the simulation results shows the energy source shock wave passing over the steady state bow shock of $M=3.1$. This interaction produces complex unsteady shock interactions and new shock wave generation in the front region ahead of the blunted cone. First frame represents the steady state flow solution reached before 130 μs . At $t = 130 \mu\text{s}$ the direct energy deposition is initialised: $t = 130.619 \mu\text{s}$ shows the solution only a few time steps post-initialisation. The initial stages of expansion and propagation of the plasmoid over the flow state is shown over time $t = 134-192 \mu\text{s}$ before the flow settles completely to the original steady state at $t = 244 \mu\text{s}$. All wave features produced match exactly with the solution of Znamenskaya et al. [38].

A fundamental consequence of producing a plasmoid via energy deposition is the elevation of flow conductivity and electron number density, as described. However, in a model closed via the ideal gas law, only an approximation of resultant conductivity and N_e can be achieved via supplementary analytical equations, as discussed in the previous

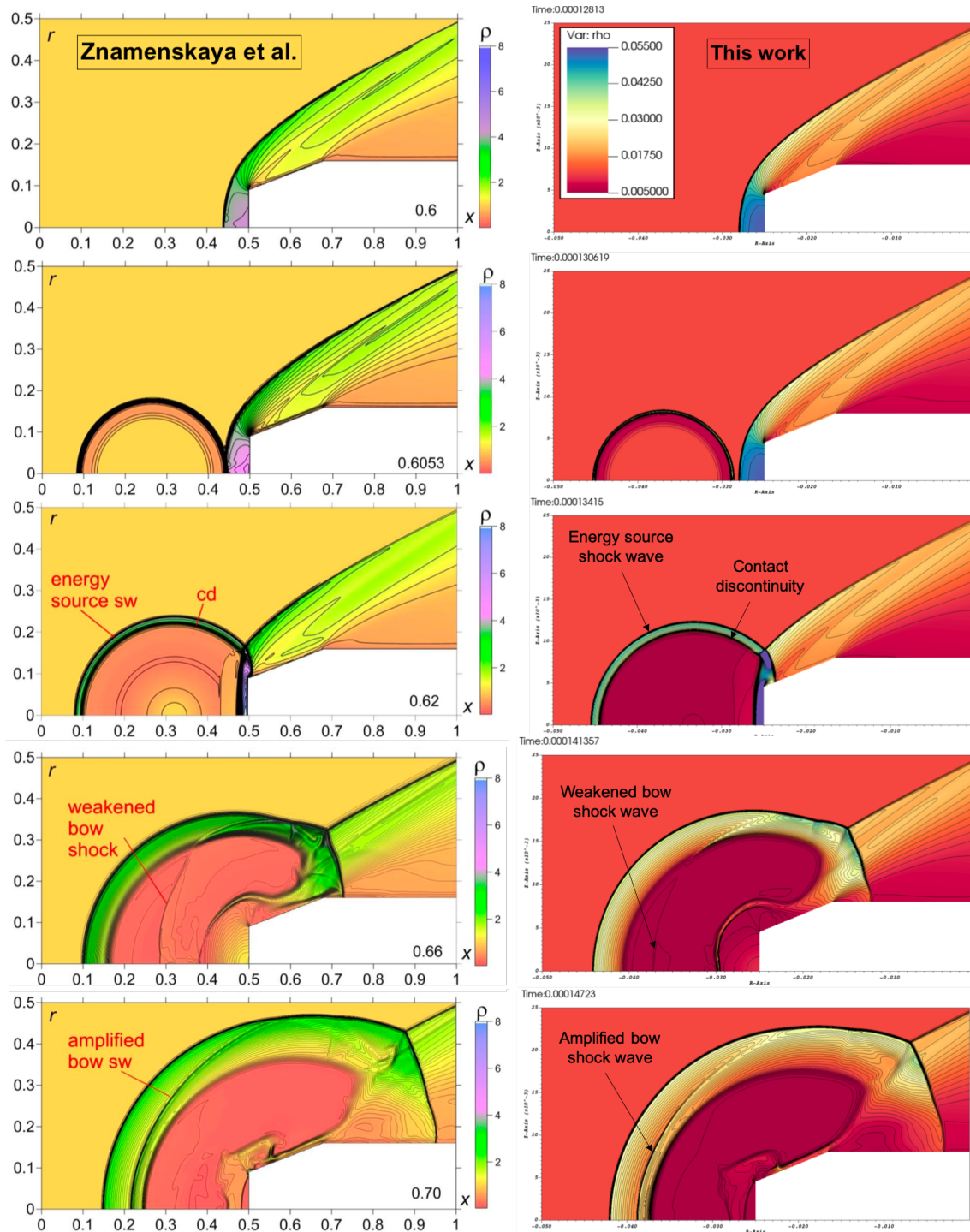


Fig. 7.6 Left) result of Znamenskaya et al. [38]. Plot of normalised density with contours, normalised time also shown. Ideal Euler model. Key features labelled (SW: shock wave, and CD: contact discontinuity). Right) Results of this work: ideal Euler model. Plot of density with contours (dimensional), at close to equivalent time frames as the Znamenskaya et al. result.

sections. The results of the previous reentry test cases showed such approximations led to significant differences in conductivity prediction. Therefore, accurate prediction of such

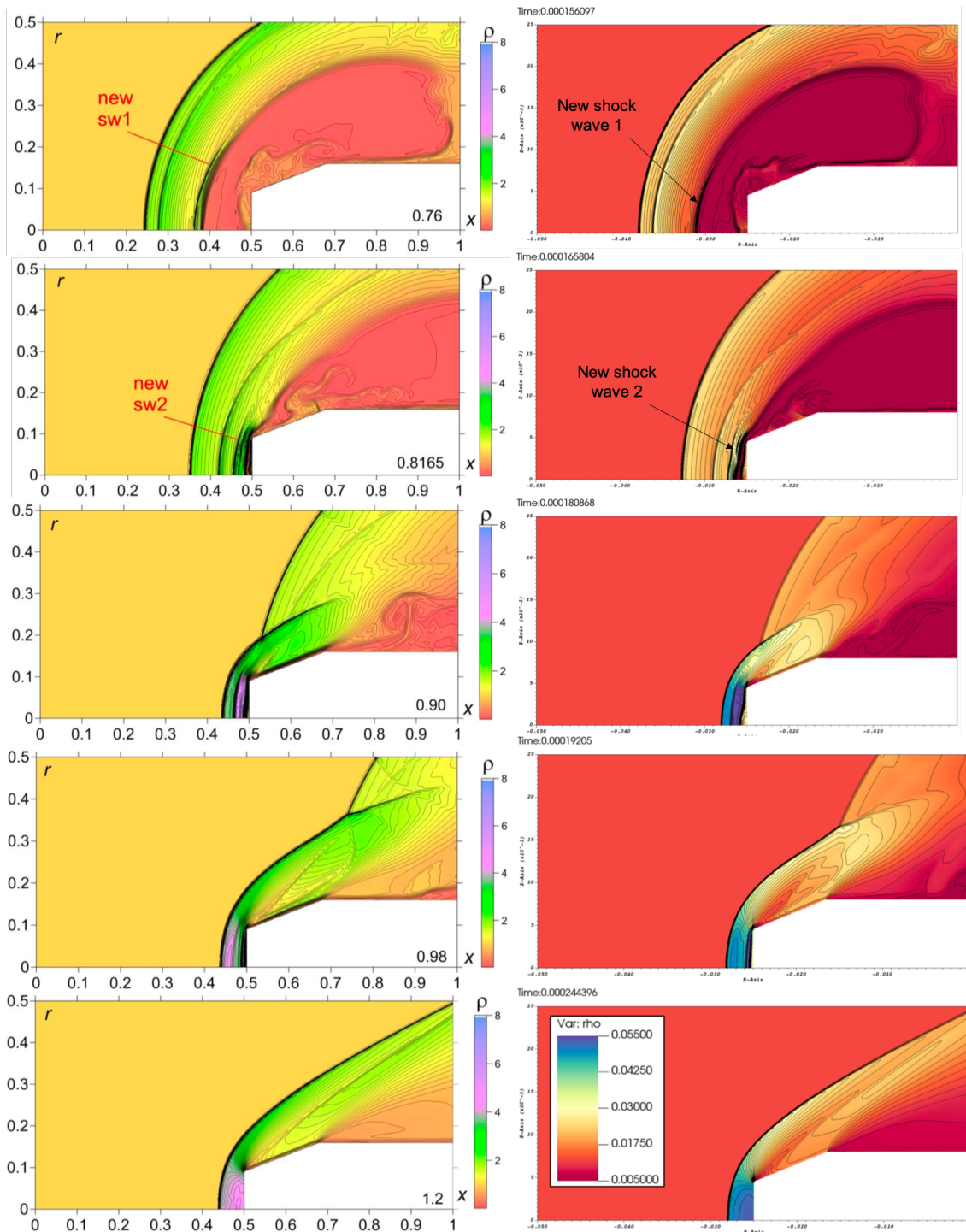


Fig. 7.7 Left) result of Znamenskaya et al. [38] (non-dimensional). Right) Results of this work: ideal Euler model. Plot of density with contours (dimensional), at close to equivalent time frames, as the simulation evolves.

properties is key to electrical properties of plasma generation methods - for applications where electron density and conductivity must be quantified. The plasma19X model of this work permits the direct and realistic computation of such properties.

The unsteady progression of electrical conductivity as computed by the plasma19X model is shown in Figure 7.8.

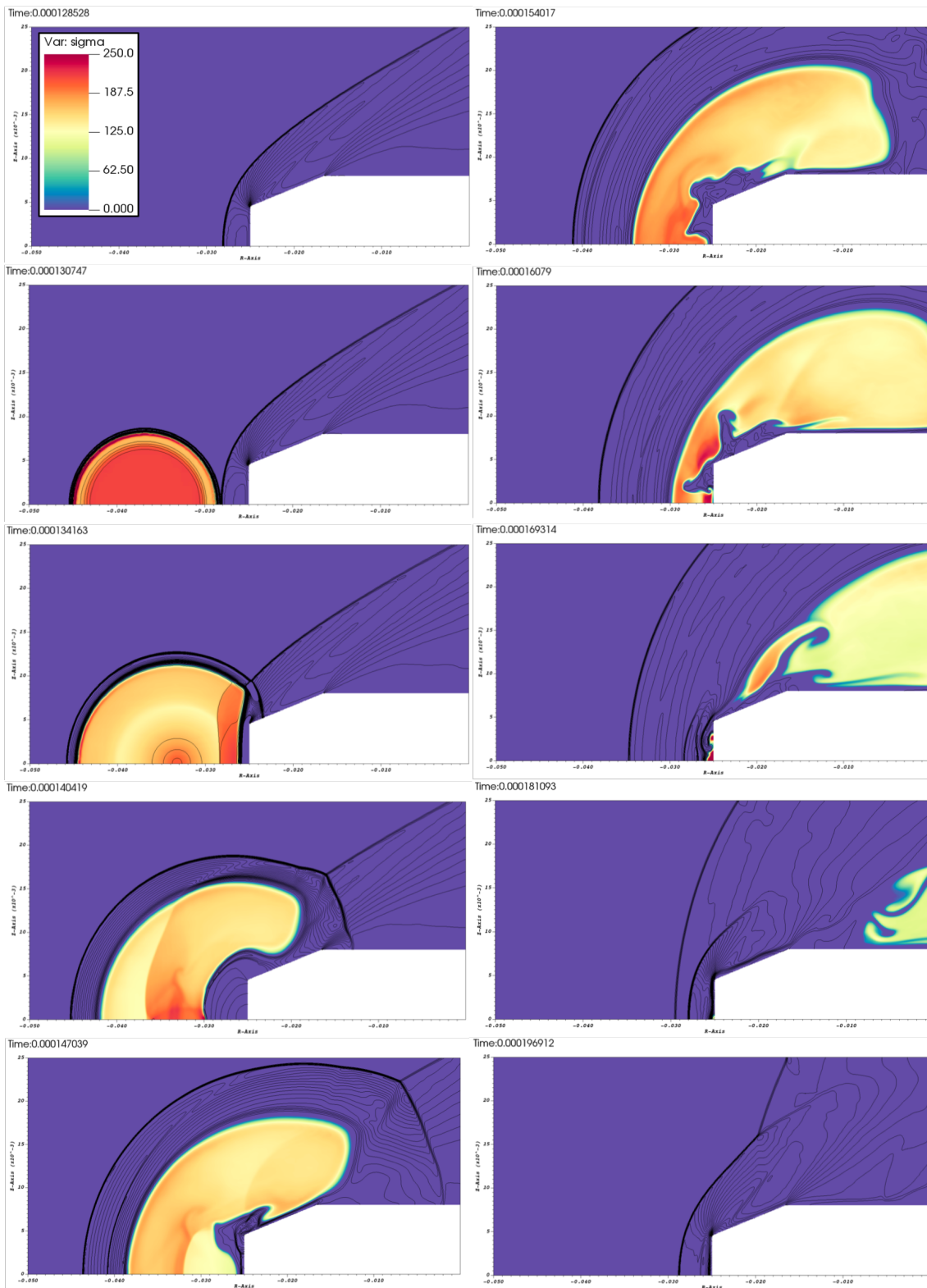


Fig. 7.8 Results of this work: inviscid plasma19X model. Colour plot of electrical conductivity. With contours of density to show the shape of the bulk fluid flow.

The density contours of the plasma19X simulation enables one to draw comparison with the density field evolution of previous ideal gas solution. The colour field shows electrical conductivity computed directly from plasma19X EoS. The first frame shows the steady state achieved by $130 \mu s$, just before the plasmoid is instantaneously initiated. Subsequent time-steps show the early stages of plasmoid expansion and unsteady interaction with the initial bow shock. The density contours show that the phenomenological evolution remains very similar between the ideal gas model and the plasma19X model. Progression of the conductive plasma region through the domain reveals importantly the way the plasma region separates between $t = 160-170 \mu s$, forming small localised regions in front of the blunted cylinder. Such behaviour is unknown from the ideal gas model. It also reveals the duration of which the conductive plasma region remains in the domain - the flow becomes fully non-conductive again (plasma region exits the domain) well before the flow re-settles to its initial steady state.

At any one of these time steps, the distribution of electrons can be determined, as shown in Figure 7.9.

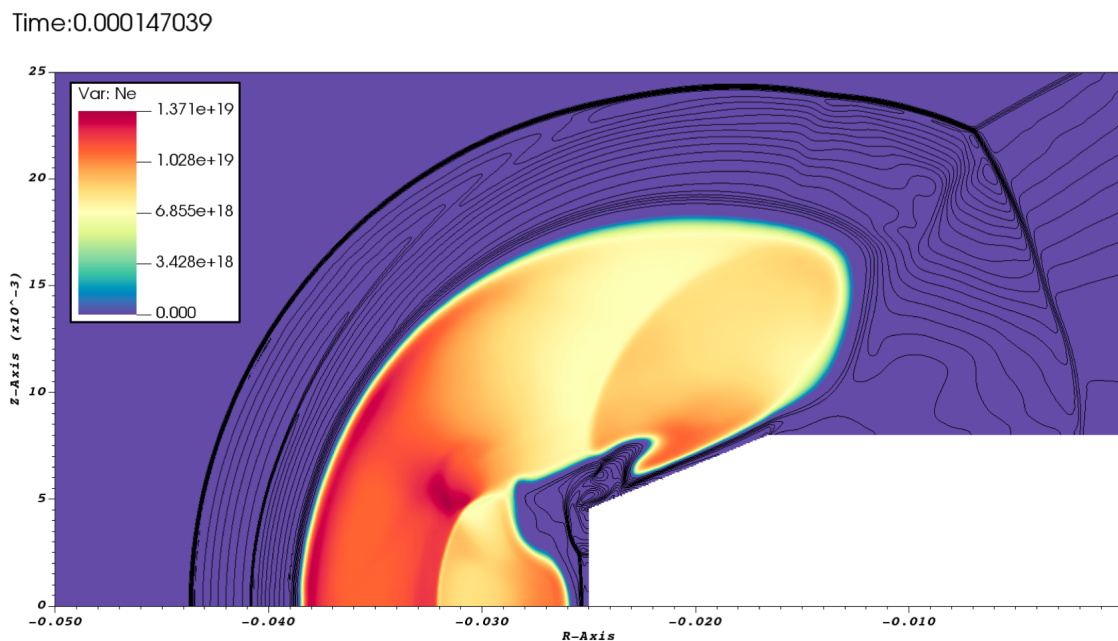


Fig. 7.9 Plot electron number density through plasmoid region, with density contours depicting broader flow structure.

The 2D axi-symmetric plane represents the 3D dynamics of the blunted cone geometry, the full rendering of which is depicted for the temperature field in Figure 7.10. This offers a more realistic visualisation of the full 3D dynamics at play, and shows the utility of the AMR in dynamically maintaining high effective resolution.

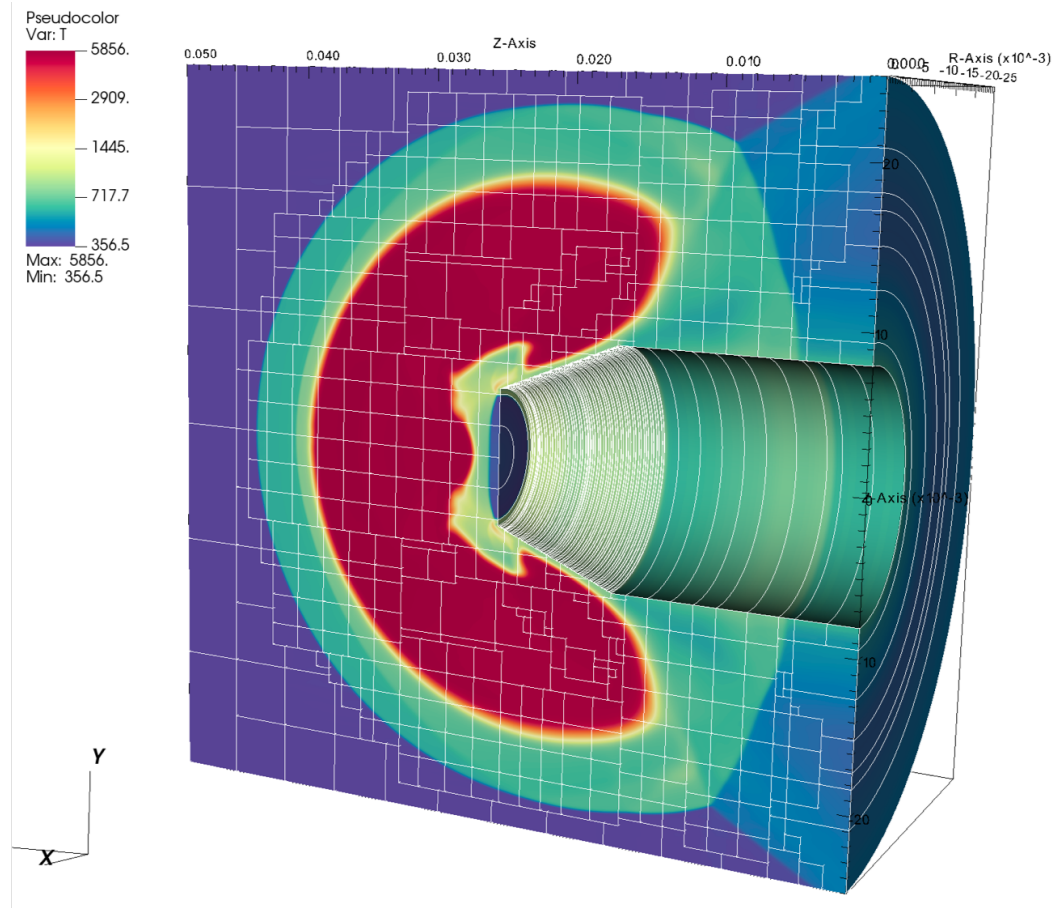


Fig. 7.10 3D rendered plot of temperature field midway through plasmoid evolution.

7.4 Plasma generation combined with MHD flow control

Bringing all of the model elements together, the following open research question is explored for remote energy deposition: can an imposed magnetic field dynamically affect a high speed plasma? Studies of MHD affected flows have thus far only been applied to steady state flow cases. This particular transient plasmoid configuration has not been experimentally tested. However, MHD combined with remote energy deposition has been paired in other combinations (i.e. surface plasma actuators) and similarly has the potential for practical utility in aerodynamic flow control as technologies mature. Simulations of this set-up can be valuable in proposing configurations of future experiments.

Each element of physics involved has been individually validated, and are now brought together in this test case. For an MHD effect to be feasible, the thermal energy deposition must produce a plasma of sufficiently high temperature. We therefore adopt the problem set-up of the magneto-compressor generated plasmoid of the last section, where experimentally produced temperatures are known to be sufficiently high to produce a conductive plasma region. A strong magnetic field strength of 5 Tesla is initialised in the fluid region. The amount of energy deposition is also approximately the same as the plasmoid experimental

case, such that it remains in the bounds of practical feasibility. Therefore, the initial conditions are as follows:

Simulation initial conditions:

$$\begin{aligned} M &= 3.1, V_\infty = 1054.91 \text{ m/s}, T_\infty = 288.2 \text{ K}, \\ \rho_\infty &= 0.01225 \text{ kg/m}^3, p_\infty = 1013.25 \text{ Pa} \\ E_0 &= 300.0 \text{ mJ}, \text{ Gas} = \text{Air} \end{aligned}$$

The geometry remains to be a blunted cone, as per the previous simulations and experiment, however dimensions are adjusted such that its boundary permits a more consistent magnetic field strength around the surface (since the absolute strength of the dipole magnetic field diminishes spherically from the dipole centre). Put simply, the rectangular bunted cone is adjusted to be more square-like within the circular \mathbf{B} -field.

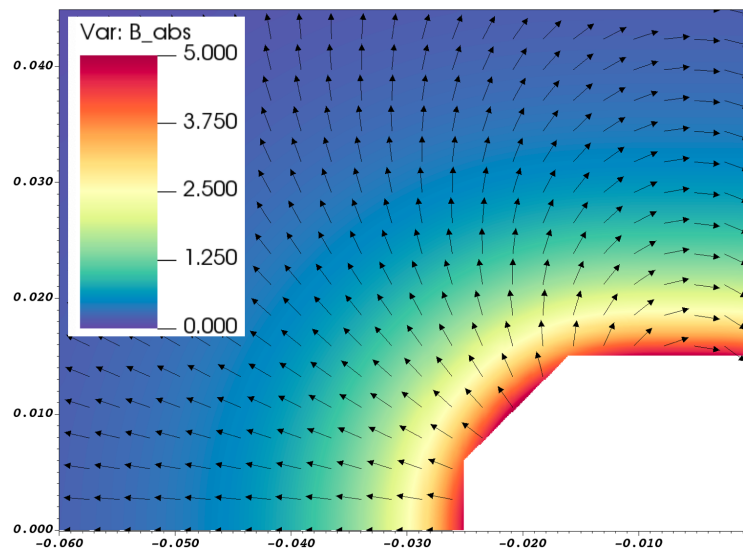


Fig. 7.11 Static dipole magnetic field - absolute magnitude shown (colour map) with field line vectors shown in black. Rigid body geometry shown in white.

The simulation is run using the full system model: Navier-Stokes + resistive MHD, closed with the plasma19X EoS. The geometry and static imposed magnetic field are shown in Figure 7.11. The simulation is run with a base resolution of 128×192 cells with 2 levels of AMR. The inviscid fluxes are solved with the HLLC-HS solver as this problem is still susceptible to carbuncle instabilities, since viscous fluxes are very weak.

The flow structure has reached a steady state by $130 \mu\text{s}$ after simulation initialisation. Due to the slightly altered geometry, the base flow structure differs marginally from the previous test case. The plot of steady state density field is depicted in Figure 7.12. The flow still exhibits expansion fan features around the blunted cone corners, but the detached shock is slightly concave rather than bowed ahead of the conically inclined portion of the geometry.

Simulation results are shown for time sequences following plasma initialisation, with comparison between the base flow (no magnetic field) and the magnetically affected flow

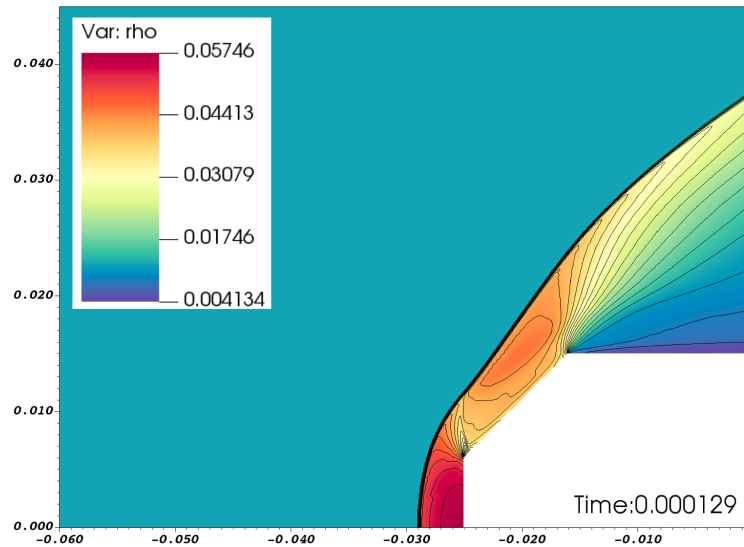


Fig. 7.12 Steady state density field at $130 \mu s$ after simulation initialisation, with black density contours superimposed for shape visualisation.

solution (with \mathbf{B} -field initialise as shown). In order to show the shape of the bulk fluid evolution as well as more detailed internal plasma forms, density contours are shown (this time in white), and the fluid electrical conductivity is shown by the colour plot, with black contours overlaid to better depict internal plasma form.

From inspection of the simulation results, it is clear that MHD effects exert an influence on the transient plasmoid. Using the insights gained from the MHD studies of Chapter 6, the low density high conductivity region which characterises the plasmoid is most susceptible to magnetic interaction, especially as the plasma region nears the model surface where the magnetic field is strongest. However, even in the magnetic dipole far-field where the plasmoid is initialised, since electrical conductivity is extremely high in the early stages post-deposition, the expanding plasmoid is mildly distorted even $5 \mu s$ after initialisation, as seen in the first comparative frames of Figure 7.13.

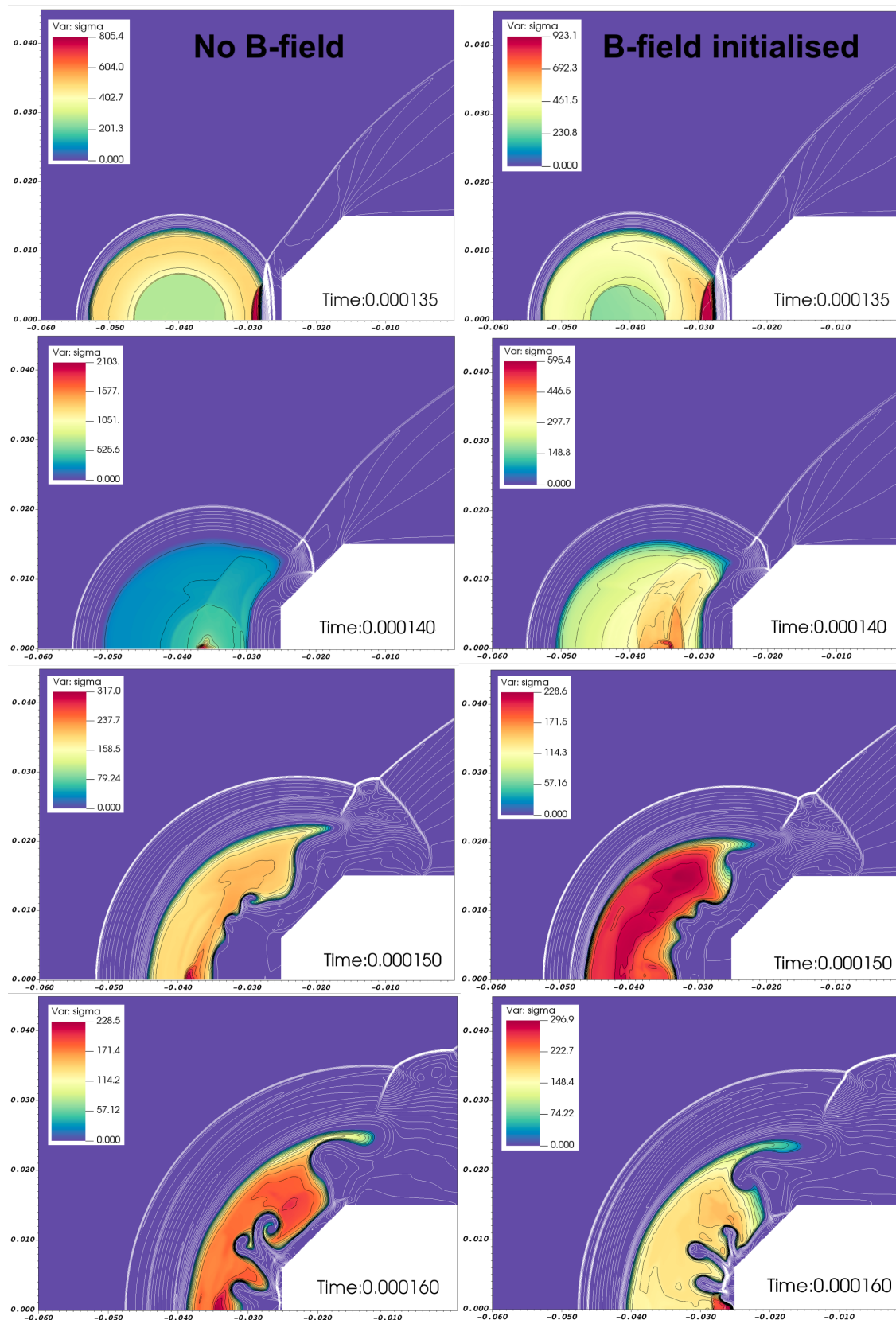


Fig. 7.13 Comparison of: left) base flow case (no magnetic field) with right) MHD affected case (magnetic field initialised). Evolution of density field (25 white contour lines), and generated plasma region shown via a colour plot of conductivity (colour map re-scaled for each time progression), with internal detail depicted through 15 overlaid black conductivity contour lines. Evolved solution over 135-160 μs after simulation initialisation

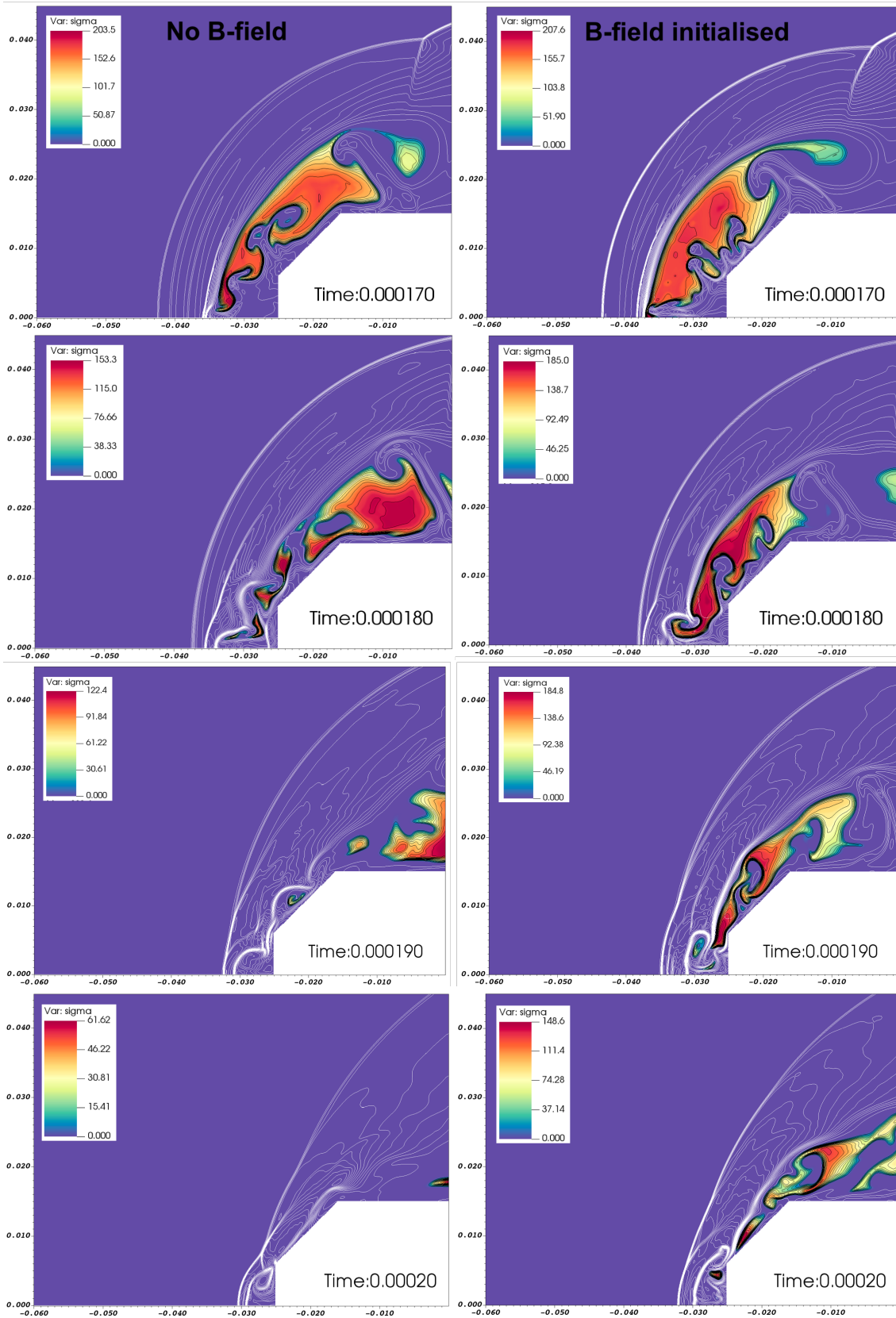


Fig. 7.14 Comparison of: left) base flow case (no magnetic field) with right) MHD affected case (magnetic field initialised). Evolution of density field (25 white contour lines), and generated plasma region shown via a colour plot of conductivity (colour map re-scaled for each time progression), with internal detail depicted through 15 overlaid black conductivity contour lines. Evolved solution over 170-200 μs after simulation initialisation

An interesting feature of the internal plasmoid behaviour is the effect of fluid motion on electric current direction. Regions of internal wave reflections, and even portions of rarefaction regions, where velocities are highly multi-directional within the plasma, the induced electric current exhibits regions of localised inversion. Observe in Figure 7.15 the circumferential electric current density contains both positive and negative values. This results in a corresponding inversion effect on the Lorentz Forcing directional vectors. Whilst these small localised regions emerge as shown at 135 and 150 μs , the dominant effect for the vast majority of the plasmoid evolution, is a Lorentz force acting approximately 90° counter-clockwise to the magnetic field lines, therefore decelerating the progression of the plasma region through the domain.

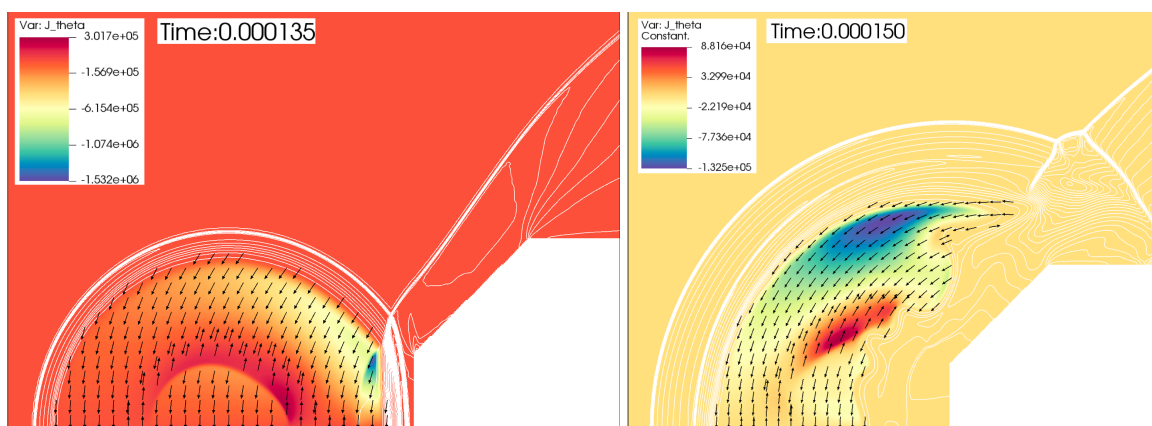


Fig. 7.15 For the magnetically affected case: plots of induced circumferential (\mathbf{J}_θ) electric current density, with Lorentz forcing directional vectors (direction only, magnitude not indicated), for the two time stages: 135 μs and 150 μs after simulation initialisation.

The dominant effects of the imposed magnetic field are:

1. A notable *deceleration* of the bulk plasma motion through the domain
2. Differences in the finer detail of the plasmoid form, as the simulation evolves
3. A propagation effect from the magnetically influenced plasma to the features of the enveloping non-conductive fluid

In terms of addressing the open research question for this test: yes, the imposed magnetic field is found to influence the behaviour of a transient plasmoid. The most dominant effect is a bulk deceleration, characterised by the longer duration of the plasma region transiting the domain. Notably, though only the high conductivity plasma region is able to be magnetically affected, augmentation of the internal plasma region propagates an effect to the surrounding non-conductive fluid structure, as observed in the surrounding density contours.

The end phases of the flow evolution, where the plasmoid region has exited the domain (or very nearly exited the domain in the \mathbf{B} -field case), remain to exhibit differences, not only in the time-scale of evolution but in the morphology of the flow field. An additional

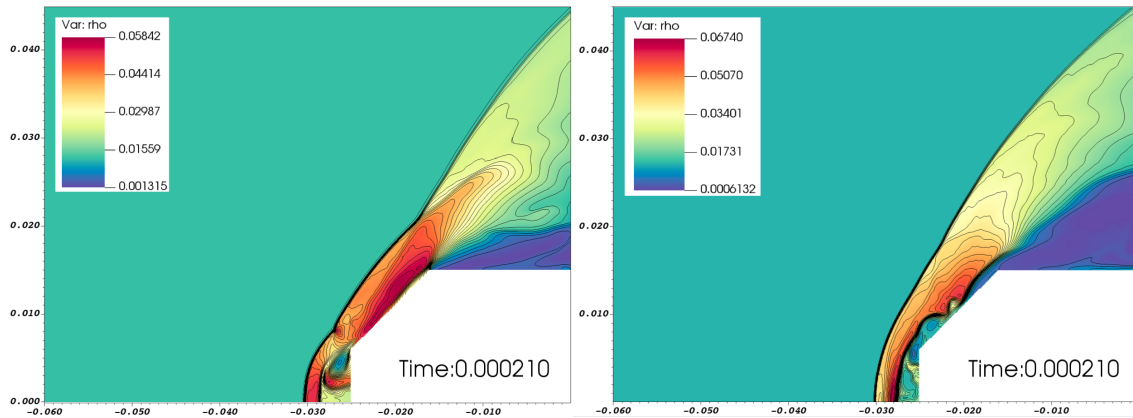


Fig. 7.16 Density field at $130 \mu s$ after simulation initialisation, with black density contours superimposed for shape visualisation. Left) no magnetic field, right) with magnetic field.

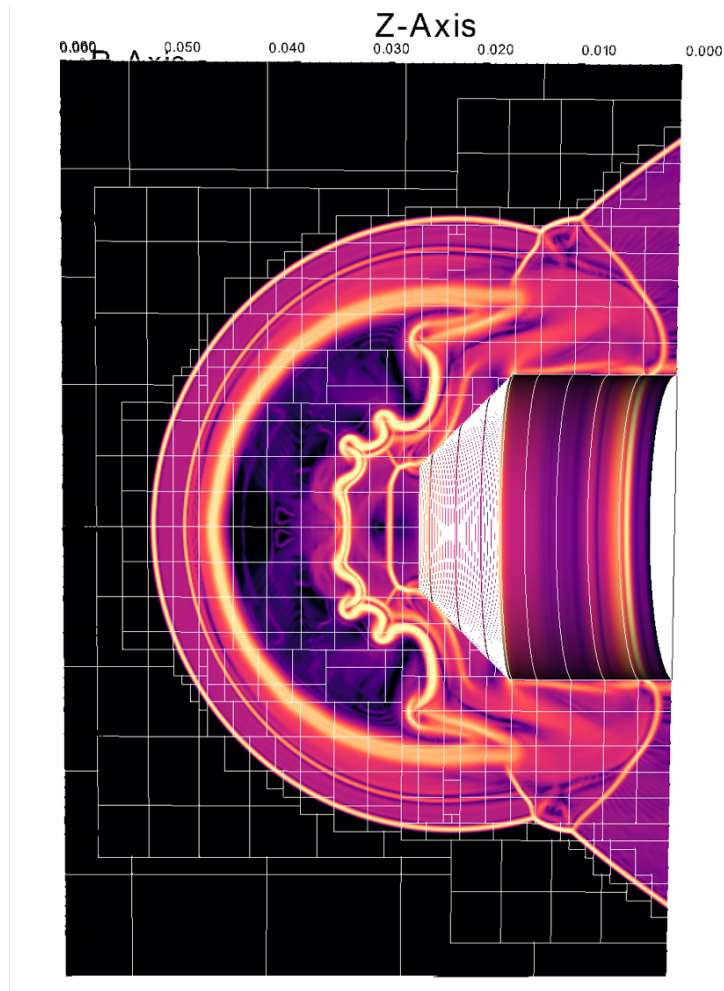


Fig. 7.17 3D revolved rendering of 2D axisymmetric result: numerical Schlieren scaled (function of density gradient) to depict more complex wave structures at play. Time progression shown: $153 \mu s$. The borders of AMR refinement blocks are overlaid in white.

time step is shown for $210 \mu s$, with density field visualised for comparison in Figure 7.16. The energy source shock wave has clearly progressed further through the flow domain. A

vortical shock feature remains ahead of the front surface of the base flow case, compared to a straighter, more prolonged shock up the conical surface in the MHD case. This demonstrates how the MHD control of the plasma has propagated an effect into the non-conductive fluid region. In both cases, the flow ultimately settles to the original steady state of Figure 7.12, however, this takes longer for the MHD affected case.

To provide a final visualisation to more realistically depict the 2D axisymmetric flow field, in its full 3D form, Figure 7.17 renders a numerical Schlieren to reveal more detailed wave interactions. The AMR mesh block borders depicted in this image highlight the utility of the adaptive refinement (computed based on density gradient) which maintains high effective resolution throughout the evolution of the simulation.

7.5 Model summary

The pilot studies of this chapter demonstrate the suitability of the combined numerical methodology and plasma19X EoS of the model, to explore a class of aerospace plasma problems involving remote energy deposition. The temporally dynamic feature tracking of the AMR was shown to be especially effective in the series of validation tests presented in this chapter. Results for single and double laser pulse showed good agreement with the Schlieren visualisations obtained from experiments.

The plasma19X EoS has advantages over the simple ideal gas EoS in the direct and realistic computation of electric properties of a plasma produced, when the energy deposition is sufficient to ionise the flow. Properties such as electron number density and electrical conductivity can be predicted directly.

This permits the combination of all elements of the developed numerical model to explore the open question: can a transient plasma generated through remote energy deposition, be influenced by an imposed magnetic field? The preliminary results of this work indicate that an MHD effect is observed to: decelerate the flow, alter the form of the finer features, and propagate altered flow effects to the enveloping non-conductive fluid.

The purpose of this study was to demonstrate model *capabilities* to enable further studies of such classes of aerospace plasma control problems. Future investigations can examine the emergent flow physics in much greater detail, including the effect of varying many of the parameters at play. Energy deposition and MHD effects are both methods which can alter aerodynamic (drag and moment control) and surface properties of the flow. Combining the two opens further possibilities for these objectives. Studying them in unison could lead to practical designs where desirable effects are maximised, for minimised system complexity, weight, and resources. Many different possibilities are emerging as new technologies mature. Computational models are a powerful tool for their exploration.

Chapter 8

Conclusions and future outlook

There are many ways to write a single algorithm, and there are very many algorithms combined to solve a complex problem. Advancements in individual numerical methods and combined numerical methodologies are cornerstone to the advancement of the fields of fluid dynamics and magnetohydrodynamics, which underpin many active areas of research in modern physics. This thesis is concerned with advances in combined numerical methodologies for application to complex magnetohydrodynamic flows, to enable meaningful physical investigations.

The central dilemma in the simulation of magnetohydrodynamic phenomena in the hypersonic regime is the balance at play between the physical complexity of the system and computational tractability. Therefore, advances in numerical modelling must wholly incorporate: the problem specific mathematical modelling as well as the development of advanced numerical algorithms and their efficient implementation, in order to effectively apply the numerical model to applications of interest in aerospace plasma research.

This chapter summarises the steps taken, and contributions made, in the development of a new computational model designed primarily for the simulation of plasmas formed, and magnetically controlled, in hypersonic flows. The Chapter also highlights utility of the model to elucidate new insights into the complex phenomena at play.

Undertaking any major research project uncovers many avenues for extension and future work. The key recommendations for extensions and possibilities for further developments are detailed in this Chapter. Finally, it is worthwhile to contextualise the research in terms of applications and implications within a broader research context.

8.1 Thesis summary

The complete form of MHD system equations is comprised of six coupled, multi-dimensional, non-linear PDEs. The overall numerical model is aimed to achieve a high degree of generality, such that very many different types of fluid dynamics problems can be simulated: from inviscid to viscous, transient to steady state, simple gas to real gas effects, non-magnetic

to MHD affected, or any combination of the above. Therefore a modularised approach was devised whereby a set of sub-models was derived based on specific assumptions and reductions in order to efficiently simulate the dominant physics of a prescribed problem of interest.

Firstly though, a number of system reductions could be applied to all models via a careful order of magnitude analysis which considered the fluid dynamic property bounds and the electrodynamic property bounds of *all problems* addressed in this work. This results in the so called full-system sub-model of the model hierarchy. The electrodynamic assumptions and fluid dynamic assumptions which underpin this model are carefully assessed and clearly stated. A magnetic field reduction of the full system model results in the defined Navier-Stokes model, while the outlined transport property reduction of the full system model results in the Inviscid MHD model. Combining both reductions recovers the simplest form of the system model described by the Euler equations. All defined sub-models can be closed with either a simple ideal gas equation of state or the advanced plasma19X equation of state, adopted and extended in this work. The modularised design of the overall numerical model means that a high degree of generality is achieved (wide array of fluid dynamic problems can be simulated) without comprising in any significant way on solution efficiency.

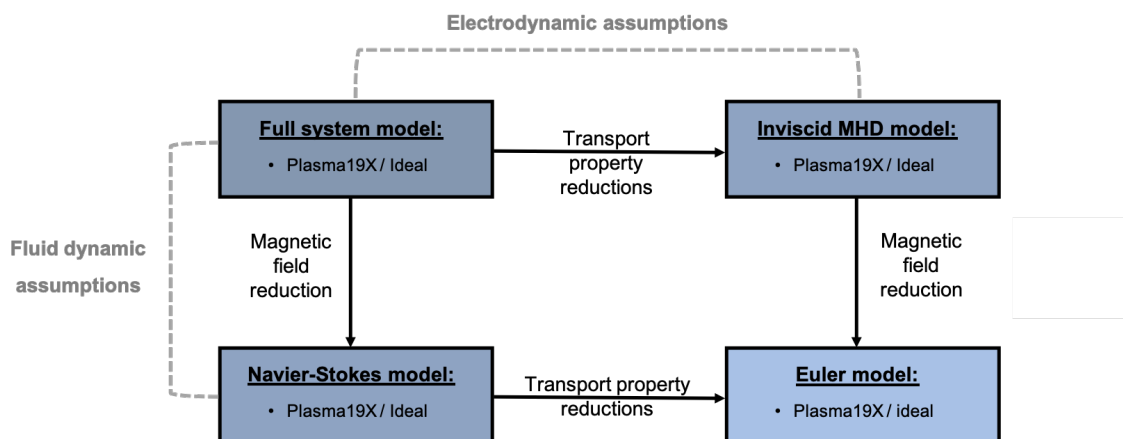


Fig. 8.1 Modularised approach: map of mathematical sub-models, governing assumptions, and reductions.

The equation of state plays a critical role for the simulation of plasmas formed in hypersonic flows. The choice of a non-equilibrium, equilibrium or ideal gas based EoS depends on several interrelated considerations. A theme of this thesis is the identification of assumption abiding regimes which permit advances in the numerical modelling of classes of plasma problems. It is identified that a large portion of atmospheric reentry vehicle trajectories, and scramjet flight conditions, occur within the equilibrium valid regime, however the regime has scarcely been studied in terms of MHD applications due to limitations in the accuracy and efficiency of electrical conductivity modelling [78]. The advanced plasma19X EoS for equilibrium air-plasmas (originally developed by Träuble et al. [84])

offers significant improvements for the computation of thermodynamic and electric transport properties of air, across a wide temperature band, as compared to prevailing gas chemistry models. However, in order to apply the 19 species gas chemistry model to the regime of this work, substantive extensions were required. A physical basis for property extension, based on effective adiabatic index extrapolation along isotherms, was devised and assessed in this thesis in order to extend the bulk thermodynamic properties to a lower density and pressure range required for atmospheric reentry conditions.

The more precise and extended values for electron molar fraction and number density were generated from scratch following the extended theory by D'Angola [124]. Collectively this creates a 19-species equilibrium air-plasma EoS which can be applied for the first time to problems in atmospheric reentry and other hypersonically formed plasmas. Specifically, the improvement in computed electrical conductivity is highlighted, since this most significantly underpins the accuracy of full-field MHD effects.

The efficiency of the EoS computation is critical to the efficiency of the overall code. The look-up table approach for tabulated (pre-computed) equilibrium gas chemistry models is significantly faster than the large set of system of equations which must be solved in the non-equilibrium regime. However, performance of the search and interpolation routines for equilibrium models can vary widely in computational cost. This work proposes precise restructuring of the property vectors such that exact logarithmically spaced data permits a direct search method based on logarithmic interpolation between known vector bounds and data density. This method, proposed in this thesis, reduces the cost of search convergence from $O(\log_2(N))$ to $O(0)$. Once the look-up table properties which bound the search-value are identified, a precise value is traditionally computed via bilinear interpolation. It is identified in this work that bilinear interpolation on a bi-logarithmically distributed property space can result in a moderate degree of property creep in the overall hydrodynamic simulation, especially in the case of steady state simulations which often converge slowly over many iterations. This issue is corrected for via the coefficient based bi-logarithmic interpolation method proposed in this work.

Development of the numerical model involved a unique combination of numerical methods, implemented within the state-of-the-art meshing framework AMReX. A general theme of Chapter 4 on numerical model development, is the special consideration of the ways in which standard numerical methods work in combination, especially in regard to how methods are implemented in the Cartesian, hierarchical, and parallelised AMR framework, with defined sub-cycling routines across refinement levels. Even well established methods for compressible flow solvers often required careful adjustments and extensions when implemented in unison and within AMReX. More complicated aspects of the numerical solver (e.g. the hypersonically stable inviscid flux solver) required some more inventive adjustments to conventional methods.

Given the underlying Cartesian mesh with hierarchical AMR, geometry was implemented as an embedded boundary whole cell Riemann-based rigid body GFM, to handle strong shock-boundary interactions. Pairing this with robust approximate Riemann solvers for the inviscid flux computation yielded an effective method for high Mach number compressible flows over arbitrarily complex geometries. The base inviscid flux solver was the HLLC solver with 2nd order (space and time) MUSCL extension. However, for very high Mach number flows over blunt body surfaces, the Carbuncle instability was known to manifest. A new hypersonically stable solver was proposed in this dissertation, based on weighted linear combinations of HLLC and HLL star-state fluxes, with an automated weighting calculation which is robust within an AMR framework (liberating the method from manual tuning parameters). This proposed solver was shown to have very good generalised performance over standardised tests (presented in Chapter 5).

The viscous and thermal conductivity terms of the Navier-Stokes system are computed via the second order central differencing method. Special care is taken regarding the order of operations and sequential boundary construction for the operator-split and dimensionally split flux updates within the rigid body GFM implementation. With the addition of viscous fluxes to the system, stability analysis is conducted for the Δx vs Δx^2 dependance of stable Δt . Considering the algorithmic time-stepping procedure over hierarchical refinement levels, a new N_MAX (finest) level projected stability condition is proposed, enacted at the 0th (coarsest) level of flux computation, which preserves stability for sub-cycling routines over all higher levels.

Finally, integration of the MHD forcing terms is conducted with special care, proposing a 2-step momentum integration in order to conserve internal energy self-consistently. For the known magnitude bounds of parameters in system equations, the computed stable time-step restricted by the hyperbolic flux will almost certainly satisfy the stability requirement of the MHD source term integration, based on a problem-specific order of magnitude stability analysis.

Given the unique combination of methods contained within the system model, extensive validation is paramount. The broad set of validation tests presented in Chapter 5 were selected to ensure that every aspect of the implementation was validated against known solutions, other simulations, and where possible, against experiments.

Across Chapters 1-5, the theory, mathematical modelling and numerical modelling were developed and validated. Chapters 6 and 7 then apply the model to aerospace plasma research problems of interest.

The first study looked at the role of the plasma19X EoS on MHD effect prediction, as compared with the commonly implemented ideal gas model (with supplementary conductivity approximation). The study revealed a significant over-prediction of shock enhancement effect by the ideal gas model, and interrogation of simulation parameters revealed the diverging property phenomenology driving such a difference. A key finding was that, even

when the electrical conductivity profile is manually fit to very well approximate the real gas case, the MHD interaction effect - which depends upon both the fluid dynamics and electrodynamics of the flow - still diverges significantly in the prediction of magnetically influenced shock enhancement. Therefore, real gas modelling of the weakly ionised plasma is centrally important to the study of imposed MHD effects.

Wasai et al. conducted a key experimental study of a high enthalpy hypersonic flow over a double cone geometry, with applied magnetic field, and was able to measure an MHD enhancement effect. The flow physics is complex in this experiment. The design of the model of this work is highly suitable for the simulation of the experimental condition, due to *all combined facets* of the developed numerical model of this dissertation: full Navier-Stokes resistive MHD governing system with advanced air-plasma EoS, effective embedded boundary methods for non-simple geometries, robust numerics for capturing strong shocks, and their interactions, at high resolution, in the hypersonic regime, with imposed MHD Lorentz forcing dynamics. Whilst previous numerical modelling was able to produce qualitative similarities with the experimental results, quantitative agreement remained illusive. The ability of the model of this work to produce results which are quantitatively in-line with the experimental measurement, is an important step forward. With this result as validation, the model could be used to conduct parameter studies and investigate more fundamental aspects of the flow physics.

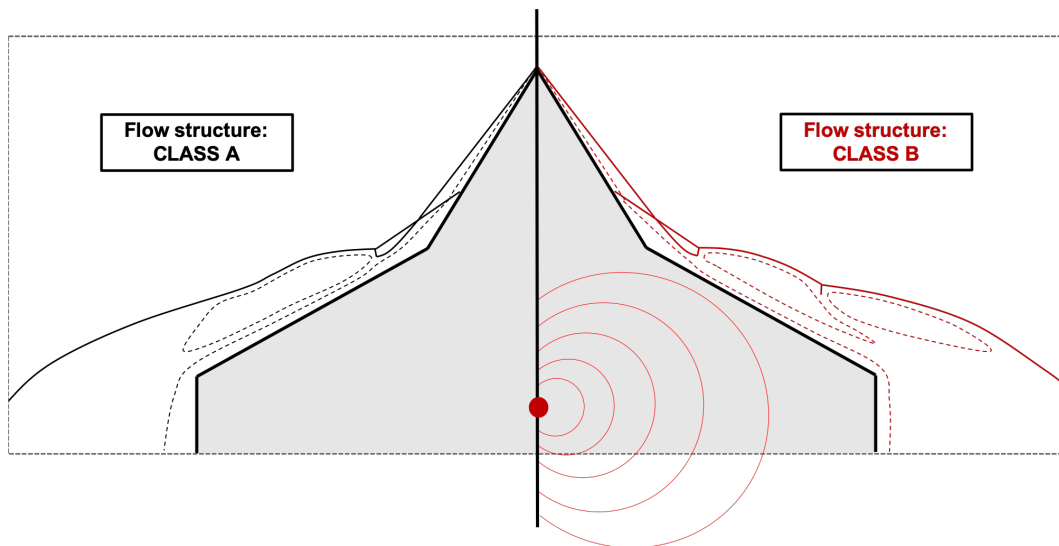


Fig. 8.2 Diagram depicting the topological adaptation which can arise due to imposed MHD effects - as identified for certain geometric and magnetic field problem configurations.

Studies which examined the effect of surface inclination angle and magnetic field configuration revealed detailed, and at times counter-intuitive, flow field effects. The simulations are able to predict geometric and magnetic conditions which both amplify and diminish the MHD enhancement effect, across different regions of the shock structure. Coupled interactions between magnetic enhancement of the separation region and the detached shock

layer plays an important role in the resultant flow formation. A deeper examination of temporal path dependency (cumulative Lorentz forcing as well as fluid dynamic forces) shows how the magnetically influenced flow field evolves, and why the base flow case is not always a useful predictor of the emergent flow field under imposed magnetic field activation. Perhaps the most interesting result of these studies, is the identification that: imposed MHD effects may not only alter the shock position, but may lead to a dimorphic flow structure. The analysis in this thesis identifies three flow classifications, and predicts conditions under which they form.

Figure 8.2 illustrates the conventional CLASS A flow structure, and its comparative adaptation to the CLASS B classification which may occur under certain imposed magnetic field configurations. This *topological adaptation* is a newly predicted and classified MHD control effect. Identification of divergent flow structures is particularly important in the context of hypersonic flight control. The salient technology consequence of these studies is the possibility of replacing mechanical surface actuation in hypersonic flows, with magnetic actuation. Conditions are able to be identified which produce topological equivalence between surface inclination and magnetic interaction.

The developed numerical model of this dissertation has specific capabilities for modelling air plasmas in compressible flows, as well as a high degree of generality for simulating different flow types (suitable for steady state as well as transient flows, effective over a wide Mach number range and for inviscid or viscous flows). Therefore Chapter 7 applies the model to a different research area of interest: plasmas formed via remote energy deposition in supersonic flows. The only adjustment required of the model, is the implementation of an instantaneous bounded volume of high energy gas which is initialised on the highest refinement level (requiring a simple temporal sub-cycling tracking routine).

Examining Joule heating methods and plasmas formed via laser energy deposition, experiments of single and double laser energy deposition were used as validation test cases. In these tests, the high utility of AMR is demonstrated. The transient flow was captured with high effective resolution as shock features moved dynamically across the domain. The results captured the bubble impact dynamics with higher resemblance to experiment as compared with the fixed meshes of other works. In the case of a plasmoid formed via magneto-compressor, the plasma19X EoS was able to elucidate key electromagnetic properties of the formed plasma. Drawing together all the elements of the developed model, a theoretical test problem is explored: what effect can an imposed magnetic field exert on a a supersonic plasma, dynamically transiting the flow domain? This should be considered a pilot study, with the purpose of demonstrating numerical model *capabilities* for application to wider aerospace plasma problems in the future.

To affirm the original hypothesis, one may conclude from the dissertation: advances in numerical modelling techniques, combined with an advanced EoS, permits the realistic and

efficient simulation of hypersonically formed plasmas. Further, this enables new and useful predictions about the control of such flows by applied magnetic fields.

8.2 Proposed future work

Through the development and application of the numerical model of this thesis, one becomes keenly aware of the avenues for extension and future work. Some key recommendations are listed.

Extension to Cartesian 3D

Extending the mathematical formulation and numerical model to be fully 3-dimensional in a Cartesian coordinate system, would open up a range of possibilities for numerical studies. In terms of key applications of interest - reentry capsules and scramjets do not tend to fly with their central axis perfectly tangentially aligned to the trajectory. Rather they fly at a small angle of attack to produce lift or drag. Whilst most experimental tests are conducted with axisymmetric alignment, which is useful for the 2D axisymmetric model validation of this work, extending predictions to realistic flight conditions across a broad portion of trajectories, would require a fully 3D model.

One motivating technology application of this work has been control surface actuation (mechanical and magnetic). Real aerodynamic control surfaces are not represented by a full axisymmetric conical surface, but rather, planar flaps and surfaces. The 2D axisymmetric conical surface is still highly relevant for analysis, but 3D simulations with discrete surfaces could prove useful in the future for more tailored vehicle types.

Extension to 3D is also beneficial to alleviate the constraint of axisymmetric magnetic field alignment. This permits many different magnetic field orientations, or multiple super positioned magnetic fields to be simulated. Another important consequence of 3D MHD flows is possible influences of Hall effect driven 3D flow effects, which will be discussed in the next section on Hall current extension.

In terms of the numerical implementation - the existing model design naturally lends itself to expansion to 3D. AMReX is already configured to handle 3D mesh generation, and the dimensionally split solution strategy of this work means that the third Cartesian dimension can be computed and integrated simply through an additional finite volume update flux integration, following the same order of operations as the 2D case. The major drawback of the extension to 3D is the significant increase in computational cost, which is discussed in the HPC recommendations.

Extension of Ohm's Law for Hall current

The most natural extension to the physics of hypersonically formed plasmas, is the inclusion of the Hall effect. If the wall conductivity is not regarded as a perfect insulator, then the Hall effect should no longer be neglected. If the product of fluid conductivity and magnetic field strength ($|\sigma| \cdot |B|$) is sufficiently high, then inclusion of the Hall effect causes the fluid's conductivity to become anisotropic.

When Ohm's law is expanded to account for the Hall current contribution, we obtain:

$$\mathbf{J} = \sigma(-\nabla\phi + \mathbf{u} \times \mathbf{B}) - \beta(\mathbf{J} \times \mathbf{B}) \quad (8.1)$$

where β is the Hall parameter. Equation 8.1 can be rewritten in tensorial form:

$$\mathbf{J} = \tilde{\sigma}(-\nabla\phi + \mathbf{u} \times \mathbf{B}) \quad (8.2)$$

with:

$$\tilde{\sigma} = \frac{\sigma}{D} \begin{bmatrix} B^2 + \beta^2 B_x^2 & \beta(\beta B_x B_y - BB_z) & \beta(\beta B_x B_z + BB_y) \\ \beta(\beta B_y B_x + BB_z) & B^2 + \beta^2 B_y^2 & \beta(\beta B_y B_z - BB_x) \\ \beta(\beta B_z B_x - BB_y) & \beta(\beta B_z B_y + BB_x) & B^2 + \beta^2 B_z^2 \end{bmatrix} \quad (8.3)$$

where $D = B^2(1 + \beta^2)$ and the Hall Parameter is a function of electrical conductivity and magnetic field strength:

$$\beta = \frac{\sigma B}{eN_e} \quad (8.4)$$

The solution of ϕ in the divergence-free current density equation becomes the following 2^{nd} order elliptical PDE:

$$\nabla \cdot \mathbf{J} = \nabla \cdot [\tilde{\sigma}(-\nabla\phi + \mathbf{u} \times \mathbf{B})] \quad (8.5)$$

If the surface boundary condition on electric potential is not constrained to $\phi = 0$ (insulated condition) then a non-zero solution for fluid electric potential is obtained. A non-zero property field for ϕ drives electric current in the r-z plane which induces Lorentz forcing in the θ or z dimension (depending on coordinate system). This therefore induces fluid momentum in the θ or z dimension which has a strong coupled feedback effect on the solution for ϕ and computed Lorentz forcing dynamics. For example, where previously under the generalise Ohm's law:

$$J_\theta = -\sigma(u_r B_z - u_z B_r) \hat{\theta} \quad (8.6)$$

under the Hall effect the circumferential electric current density expands to:

$$J_\theta = \frac{\sigma}{1 + \beta^2} [-\beta(E_z B_r - E_r B_z) + (u_r B_z - u_z B_r) - \beta u_\theta B] \hat{\theta} \quad (8.7)$$

and additional J_r and J_z components emerge with similar complexity.

Analytic solution of ϕ can no longer be obtained, and the electric potential must be solved numerically. Numerical solution of the elliptic PDE requires different solution methods to the other hyperbolic PDEs of the system (or hyperbolic-parabolic for the Navier-Stokes equations). Consequences for parallelisation are discussed in the HPC section to follow. In the case of elliptic partial differential equations, solution methods typically require large matrices with iterative operations over the full domain to propagate boundary conditions, i.e. due to the numerical domain of dependence of elliptic PDEs as the full computational domain. The elliptic PDE is coupled with the system via σ , \mathbf{u} and \mathbf{B} terms. Solution of the Hall-MHD equations therefore requires coupled solution methods which solve iteratively for ϕ at intermediate time steps. This adds significant computational complexity to the system solution.

Internal wall conductivity model

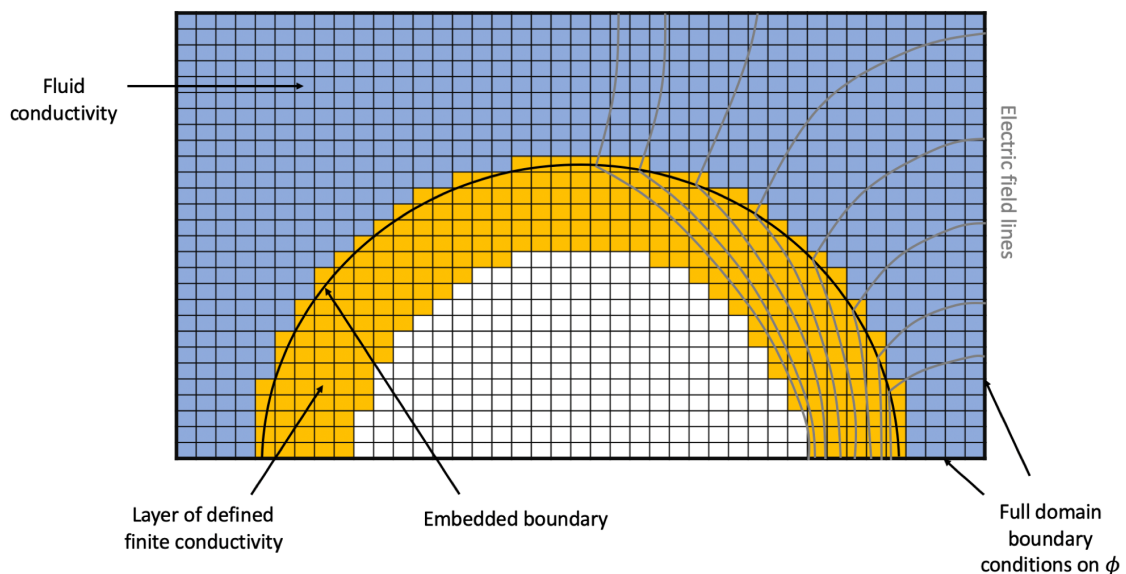


Fig. 8.3 Coarse depiction of the full domain discretisation, whereby, a layer of finite conductivity is defined for the material substrate. Electric boundary conditions can be defined on the full domain boundary for ϕ .

Since the interior of the geometry is fully discretised, this opens up a major opportunity for future development: the addition of an internal wall conductivity model. Mentioned above, the treatment of wall conductivity effects the electrodynamic field solution via the Hall effect. The surface is typically treated as perfectly insulated or perfectly conductive via simple Dirichlet and Neumann conditions on ϕ at the boundary. However, real materials are

not typically perfect conductors or insulators. The internal discretisation of the geometry through the GFM permits a finite conductivity (constant or varied) to be explicitly defined, which could offer improvements over simplified boundary conditions on ϕ . The concept is depicted in Figure 8.3.

By solving for electric potential through the fluid portion and conductive rigid body portion of the domain, the coupled fluid-dynamic and electrodynamic effects could be better realised. However, to be able to conduct such research, major improvements would first need to be made for the practical solution of the tensor form of elliptic PDE for extended Ohm's law. This could be a major challenge considering the steep discontinuities in the σ -field resulting from shock waves and the sharp transition from fluid to solid material conductivity at the surface. This would prove a challenging research problem, though it could potentially offer important insights into the electrodynamic feedback effects for conductive real materials embedded in weakly ionised plasmas.

High performance computing

Simulations of this work were run on a 16 core (2.4 GHz) machine, with the 2D double cone tests (the most expensive simulations of this work) taking a maximum of approximately 6-8 hours computing time. If this work were to be extended to 3D simulations of equivalent resolution, an upgrade in computational hardware is strongly recommended for practical computing time. A benefit of the AMReX framework is that the model is already highly scalable. The division of the mesh into massively parallelised sub-blocks means that speed up is possible for the number of cores which are accessible.

It should be noted that this parallelism is possible due to the hyperbolic and parabolic nature of the equations being computed, and their time-explicit numerical integration scheme, whereby solutions evolve deterministically from the previous time-step solution, lending itself to parallelisable sub-blocks for simultaneous solution. Whilst AMReX has developed clever in-built routines for parallelised solution methods for elliptic PDEs, these routines are presently limited to set forms of classical elliptic PDEs and still under development for multiple AMR levels. The form of elliptic PDE for Ohm's law which incorporates Hall effect, is a tensorial form of the Poisson equation. This form of equation is currently unsupported by in-built AMReX routines, and its parallelisation may not be robust for systems with strong property discontinuities, such as conductivity field for a fluid solution with strong shocks.

AMReX development is also presently under way to utilise GPU computing. Taking advantage of this by running large simulations on modern graphics processing unit clusters could offer critical gains in computing speed.

Further physical investigations

Utilising the existing model, there are many choices for parameter studies and physical investigations. Very many different geometries could be simulated, various combinations of

single/multiple magnetic field orientations and strengths, at various free stream conditions and Mach numbers. Something to consider at all times is the extent of validity of the thermochemical assumption for the combination of geometry and flow condition. If a full non-equilibrium chemistry model were to be implemented, a wider range of flight conditions (e.g. much higher altitudes for atmospheric reentry applications) could be explored. However, application of a non-equilibrium gas model at, or near to, equilibrium flight conditions will render the simulation as highly numerical stiff. Even at highly non-equilibrium conditions the computational complexity (and cost) of the simulation is significantly higher due to the tracking of individual species conservation equations and chemical reaction source terms.

Alternate numerical methods

Some suggestions for different or extended numerical methods would include: cut-cell methods for the embedded boundary, such as that recently developed for dimensionally split compressible Navier-Stokes equations by Gokhale [134]. This would add complexity to the model, but would have the benefit of smoother resolution of properties at the surface, which may become more important were electrodynamic boundary interactions to be incorporated.

The model of this work was designed for high generality- specifically the same model is able to capture temporally dynamic transient flows as well as flows which form a steady state. If the code were to be modularised further, or with a different delineation of sub-models to the map of Figure 8.1, steady state and transient flow models could be made distinct, with implicit methods or convergence acceleration techniques applied for the solution of steady state flows.

Coupled considerations

Taking a step back to look from a wider view of the thesis, an important theme is the interplay between the physics at hand, the numerical methods to solve the system equations and computing frameworks and architectures effective for these methods. No singular component can be considered independently. Design of an effective methodology must carefully balance all aspects of model development. The same applies to the recommended extensions. There is an inextricable coupling between the extension of physics (e.g. Hall effect, chemistry, flow asymmetry), the nature of numerical solution methods of the physics (coupled elliptic solution methods, dimensionally split 3D algorithms, efficient and stable chemical source term integration, implicit methods), and suitable computing frameworks and hardware (parallelism for elliptic PDEs, scalability of solution, computational speed-up with GPU computing for large 3D simulations).

8.3 Applications and implications

Many of the technology concepts explored in this thesis are yet to be realised in real flight tests. High enthalpy shock tunnel testing in combination with numerical simulation are essential first steps to achieving real flight technological maturity. Advances in numerical modelling are not only critical to real flight simulation, they also play an important role in the design of experiments themselves. It is interesting to consider the dual-directionality with which simulation and experiment inform each other. The relationship is depicted in Figure 8.4.

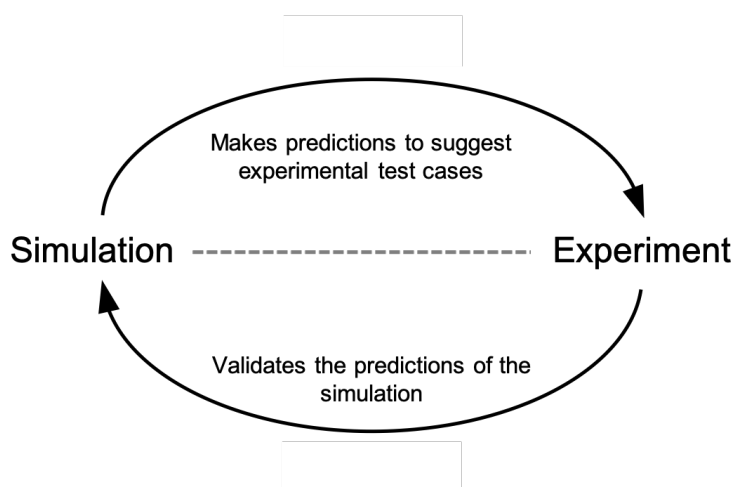


Fig. 8.4 The way in which simulation and experiment reciprocally interact.

The numerical studies of the key applications chapters of this thesis show the complex flow physics which can be elucidated from an examination of the simulations results. Often the computed flow field is found to be counter-intuitive or unpredictable from initial conditions. The role of experiments for validation is essential. However, the role of simulations for suggesting experiments is similarly instrumental.

Within the context of hypersonic flight control, even small alterations of shock position can have a large effect on the flight dynamics. The small, but measurable, MHD enhancement effect observed in experiments offer incentive for further development in magnetic actuation technologies. The quantitative agreement between simulation and experiment for the MHD influenced hypersonic double cone, gives credence to the utility of the developed numerical model to make meaningful predictions. The practical implications of these studies include: conductive flows with shock interactions of this type are shown to be sensitive to both magnetic field strength and configuration. Both need to be considered carefully, and in unison, for realistic design and for the practical design objective of minimising energy input (and on-board weight) for the magnetic field generation.

The extended numerical studies of this dissertation make a particularly interesting prediction. It was demonstrated how, an imposed magnetic field, can not only augment the shock position, but can produce a *topological adaptation* to the fundamental shock structure.

Predicting such behaviours would be paramount in the context of magnetically controlled hypersonic flight dynamics. It would therefore be of value to experimentally replicate this numerically predicted flow effect.

The concepts of magnetic heat shielding, or local electron number density reduction for communications blackout, are enticing proposals. However, both remain to be tested in a real atmospheric reentry flight. Similarly, concepts in MHD inlet control, and surface actuation, for scramjets and access to space vehicles remain a theoretical musing of the modern propulsion engineer. Elevating flow conductivity will be important for the practical utility of such technologies. Several of the numerical studies of this work considered a pre-heated free stream (as per experiment), however, an alternative for real-flight applications is to seed the flow with other species of low ionisation potential, as is the subject of emerging studies [60, 70].

With continued advances in material science, superconducting magnets, and on-board laser deposition systems, many more viable engineering technologies are likely to mature and emerge. The pilot studies into remote energy deposition in this dissertation, are a window into numerical explorations of plasma generation methods via remote energy deposition.

The numerical model developed in this thesis may usefully inform experimental design, with an ongoing feedback loop to approach real flight condition design. The wide parameter space for viable tests, and phenomena of interest, can be narrowed to best apportion experimental resources.

Access to space, return from space, and hypersonic flight vehicles are technologies of growing focus in today's world. Numerical simulation capabilities will remain to be at the heart of such research. The central tenets of this dissertation - advances in numerical methodologies, realistic and efficient simulation of hypersonically formed plasmas, and their combined basis to numerically explore the flow physics - aims to contribute to the larger research effort in aerospace plasma applications.

References

- [1] D. G. Fletcher. Fundamentals of hypersonic flow - aerothermodynamics. *Von Karman Institute*, 2004.
- [2] Q. Niu, Z. Yuan, S. Dong, and H. Tan. Assessment of nonequilibrium air-chemistry models on species formation in hypersonic shock layer. *International Journal of Heat and Mass Transfer*, 127:703–716, 2018.
- [3] T. Fujino and M. Ishikawa. Numerical simulation of control of plasma flow with magnetic field for thermal protection in earth reentry flight. *IEEE Transactions on Plasma Science*, 34(2), 2006.
- [4] J. D. Anderson. Hypersonic and high temperature gas dynamics. *New York: McGraw-Hill*, 1989.
- [5] R. Savino, D. Paterna, M. De Stefano Fumo, and M. D’Elia. Plasma-radiofrequency interactions around atmospheric re-entry vehicles: Modelling and arc-jet simulation. *The Open Aerospace Engineering Journal*, 3:76–85, 2010.
- [6] E. I. Asinovsky, A. V. Kirillin, E. P. Pakhomov, and V. I. Shabashov. Experimental investigation of transport properties of low-temperature plasma by means of electric arc. *Proceedings of the IEEE*, 59(4):592–601, 1971.
- [7] P. W. Schreiber, A. M. Hunter, and K. R. Benedetto. Electrical conductivity and total emission coefficient of air plasma. *AIAA Journal*, 11(6):815–821, 1973.
- [8] J. M. Yos. Transport properties of nitrogen, hydrogen, oxygen, and air. *AVCO/RAD-TM*, 63(7), 1963.
- [9] H. Otsu, D. Konigorski, and T. Abe. Influence of hall effect on electrodynamic heat shield system for reentry vehicles. *AIAA Journal*, 48(10), 2010.
- [10] W. B. Bush. Magnetohydrodynamic-hypersonic flow past a blunt body. *Journal of the Aerospace Sciences*, 25(11):685–690, 1958.
- [11] Y. Weng and M. J. Kushner. Method for including electron-electron collisions in monte carlo simulations of electron swarms in partially ionized gases. *Physical Review A*, 42(10):6192, 1990.
- [12] A. Villa, R. Malgesini, and L. Barbieri. A multiscale technique for the validation of a numerical code for predicting the pressure field induced by a high-power spark. *Journal of Physics D: Applied Physics*, 44(165201), 2011.
- [13] C. G. Harper. Looking across the river cam towards cloister court at queen’s college, showing the mathematical bridge. *Harper Collection*, 1892-1933.

- [14] S. Kamkar, A. Jameson, A. Wissink, and V. Sankaran. Automated off-body cartesian mesh adaption for rotorcraft simulations. *49th AIAA Aerospace Sciences Meeting including the New Horizons Forum and Aerospace Exposition*, 2011.
- [15] F. Dias and C. Xisto. Numerical computations of mhd flow on hypersonic and re-entry vehicles. *Proceedings of the ASME 2018, IMECE*, 2016.
- [16] E. F. Toro. Riemann solvers and numerical methods for fluid dynamics: a practical introduction. *Springer Science and Business Media*, 2013.
- [17] S. Sivier, E. Loth, J. Baum, and R. Löhner. Vorticity produced by shock wave diffraction. *Shock Waves*, 2(1):31–41, 1992.
- [18] S. K. Sambasivan and H. S. UdayKumar. Ghost fluid method for strong shock interactions part 2: Immersed solid boundaries. *AIAA Journal*, 27(12), 2009.
- [19] T. Fujino, Y. Matsumoto, J. Kasahara, and M. Ishikawa. Numerical analysis of reentry trajectory coupled with magnetohydrodynamics flow control. *Journal of Spacecraft and Rockets*, 45(5), 2008.
- [20] J. Poggie and D. V. Gaitonde. Magnetic control of flow past a blunt body: Numerical validation and exploration. *Physics of Fluids*, 14(1720), 2001.
- [21] N. Gokhale. A dimensionally split cartesian cut cell method for computational fluid dynamics. *PhD Thesis, University of Cambridge*, 2018.
- [22] J. D. Anderson. Computational fluid dynamics: An introduction. *Von Karman Institute, Springer Berlin Heidelberg*, 1992.
- [23] G. Degrez, C. H. Boccadoro, and J. F. Wendt. The interaction of an oblique shock wave with a laminar boundary layer revisited: An experimental and numerical study. *Journal of Fluid Mechanics*, 177:247–263, 1987.
- [24] D. Graves, P. Colella, D. Modiano, J. Johnson, B. Sjogreen, and X. Gao. A cartesian grid embedded boundary method for the compressible navier–stokes equations. *Communications in Applied Mathematics and Computational Science*, 8(1):99–122, 2013.
- [25] R. Savino, M. E. D’Elia, and V. Carandente. Plasma effect on radiofrequency communications for lifting reentry vehicles. *Journal of Spacecraft and Rockets*, 52(2):417–425, 2015.
- [26] J. S. Shang and S. T. Surzhikov. Plasma dynamics for aerospace engineering. *Cambridge University Press*, 2018.
- [27] M. Kundrapu, J. Loverich, K. Beckwith, and P. Stoltz. Modeling radio communication blackout and blackout mitigation in hypersonic vehicles. *Journal of Spacecraft and Rockets*, 52(3), May–June 2015.
- [28] R. N. Gupta, J. M. Yos, R. A. Thompson, and K. P. Lee. A review of reaction rates and thermodynamic and transport properties for an 11-species air model for chemical and thermal nonequilibrium calculations to 30000 k. *NASA*, 1990.
- [29] C. Park. Nonequilibrium hypersonic aerothermodynamics. *Wiley and Sons, New York, Chichester*, 1990.

- [30] T. Ozawa, J. Zhong, and D. A. Levin. Development of kinetic-based energy exchange models for noncontinuum, ionized hypersonic flows. *Physics of Fluids*, 20(4):046102, 2008.
- [31] Y. Nagata, K. Yamada, and T. Abe. Numerical investigation of the electrodynamic flow control around the double-cone configuration. *49th AIAA Aerospace Sciences Meeting including the New Horizons Forum and Aerospace Exposition*, page 899, 2011.
- [32] J. N. Moss and G. A. Bird. Direct simulation monte carlo simulations of hypersonic flows with shock interactions. *AIAA Journal*, 43(12):2565–2573, 2005.
- [33] M. E. Holloway, K. M. Hanquist, and I. D. Boyd. Assessment of thermochemistry modeling for hypersonic flow over a double cone. *Journal of Thermophysics and Heat Transfer*, 34(3):538–547, 2020.
- [34] K. Wasai, H. Makino, Y. Nagata, K. Hiraoka, K. Yamada, and T. Abe. Electrodynamic control of shock interactions in a $25^\circ/55^\circ$ double cone model in hypersonic flow. *48th AIAA Aerospace Sciences Meeting Including the New Horizons Forum and Aerospace Exposition*, 2010.
- [35] W. Zhang, A. Almgren, V. Beckner, J. Bell, J. Blaschke, C. Chan, M. Day, B. Friesen, K. Gott, D. Graves, et al. Amrex: a framework for block-structured adaptive mesh refinement. *Journal of Open Source Software*, 4(37):1370–1370, 2019.
- [36] R. G. Adelgren, G. S. Elliott, D. D. Knight, A. A. Zheltovodov, and T. J. Beutner. Control of edney iv interaction by pulsed laser energy deposition. *AIAA*, 43(2):256–269, 2005.
- [37] A. Zheltovodov, E. Pimonov, and D. Knight. Energy deposition influence on supersonic flow over axisymmetric bodies. *45th AIAA Aerospace Sciences Meeting and Exhibit*, 2007.
- [38] I. Znamenskaya, V. Chernikov, O. Azarova, and D. Naumov. Supersonic flow past a blunt cone under the action of plasma formation. 2019.
- [39] M. Al-Marouf and R. Samtaney. A versatile embedded boundary adaptive mesh method for compressible flow in complex geometry. *Journal of Computational Physics*, 337:339–378, 2017.
- [40] E. Berger and R. Wille. Periodic flow phenomena. *Annual Review of Fluid Mechanics*, 4(1):313–340, 1972.
- [41] N. Gokhale, N. Nikiforakis, and R. Klein. A dimensionally split cartesian cut cell method for hyperbolic conservation laws. *Journal of Computational Physics*, 364:186–208, 2018.
- [42] N. Mehra, R.K. Singh, and S.C. Bera. Mitigation of communication blackout during reentry using static magnetic field. *Progress in Electromagnetics Research*, 63:161–172, 2015.
- [43] K. J. H. Phillips. Guide to the sun. *Cambridge University Press*, pages 47–53, 1995.
- [44] A. Rodriguez and C. Snapp. Nasa reports: Engineering innovations- thermal protection systems. *NASA Reports*, pages 182–199, 2010.

- [45] K. Li, J. Liu, and W. Liu. Mechanism analysis of magnetohydrodynamic heat shield system and optimization of externally applied magnetic field. *Acta Astronautica*, 133:14–23, 2017.
- [46] S. Kranc, M. C. Yuen, and A. B. Cambel. Experimental investigation of magnetoaerodynamic flow around blunt bodies. *NASA report*, (No.35):CR-1393, 1969.
- [47] I. V. Adamovich. Plasma dynamics and flow control applications. *Encyclopedia of Aerospace Engineering*, 2010.
- [48] K. Matsuda, A. and Wakatsuki, Y. Takizawa, M. Kawamura, H. Otsu, D. Konigorski, S. Sato, and T. Abe. Shock layer enhancement by electro-magnetic effect for spherical blunt body. *37th AIAA Plasmadynamics and Lasers Conference*, page 3573, 2006.
- [49] M. Keidar, M. Kim, and I. D. Boyd. Modeling of electromagnetic manipulation of plasmas for communication during reentry flight. *Journal of Spacecraft and Rockets*, 45(3), 2008.
- [50] R. W. Porter and A. B. Cambel. Hall Effect in Flight Magnetogasdynamics. *AIAA Journal*, 5, 1967.
- [51] A. Gulhan, B. Esser, U. Koch, F. Siebe, J. Riehmer, and D. Konigorski. Experimental verification of heat flux mitigation by electromagnetic fields in partially-ionized-argon flows. *Journal of Spacecraft and Rockets*, 46(2), 2009.
- [52] V. Bityurin, A. Bocharov, J. Lineberry, and C. Suchomel. Studies on mhd interaction in hypervelocity ionized air flow over aero-surfaces. *34th AIAA Plasmadynamics and Lasers Conference*, page 4303, 2003.
- [53] V. A. Bityurin and A. N. Bocharov. Magnetohydrodynamic interaction in hypersonic air flow past a blunt body. *Fluid Dynamics*, 41(5):188–203, 2005.
- [54] A. Matsuda, H. Otsu, M. Kawamura, D. Konigorski, Y. Takizawa, and T. Abe. Model surface conductivity effect for the electromagnetic heat shield in re-entry flight. *Physics of Fluids*, 20(127103), 2008.
- [55] T. Fujino, Y. Matsumoto, J. Kasahara, and M. Ishikawa. Numerical Studies of Magnetohydrodynamic Flow Control Considering Real Wall Electrical Conductivity. *Journal of Spacecraft and Rockets*, 44(3), 2007.
- [56] K. Li, J. Liu, and W. Liu. Numerical analysis of hall effect on the performance of magnetohydrodynamic heat shield system based on nonequilibrium Hall parameter model. *Acta Astronautica*, 130:15–23, 2017.
- [57] K. Li, J. Liu, and W. Liu. Thermal protection performance of magnetohydrodynamic heat shield system based on multipolar magnetic field. *Acta Astronautica*, 136:248–258, 2017.
- [58] H. Otsu, K. Matsushita, K. Detlev, I. Funaki, and T. Abe. Reentry Heating Mitigation by Utilizing the Hall Effect. *35th AIAA Plasmadynamics and Lasers Conference*, (2004-2167), 2004.
- [59] M. Kim, I. D. Boyd, and M. Keidar. Electromagnetic reduction of plasma density during atmospheric reentry and hypersonic flight. *Journal of Spacecraft and Rockets*, 47(1), 2010.

- [60] M. Kim. Active plasma layer manipulation scheme during hypersonic flight. *Aerospace Science and Technology*, 35:135–142, 2014.
- [61] D. L. Liu, X. P. Li, Y. M. Liu, K. Xie, and B. W. Bai. Attenuation of low-frequency electromagnetic wave in the thin sheath enveloping a high-speed vehicle upon re-entry. *Journal of Applied Physics*, 121(7):074903, 2017.
- [62] D. D. Morabito. The spacecraft communications blackout problem encountered during passage or entry of planetary atmospheres. *IPN progress report*, pages 42–150, 2002.
- [63] V. A. Bitiyurin and A. N. Bocharov. Mhd flow control in hypersonic flight. *AIAA/CIRA 13th International Space Planes and Hypersonics Systems and Technolo*, 2005.
- [64] V. Bitiyurin, A. Klimov, S. Leonov, A. Bocharov, and J. Lineberry. Assessment of a concept of advanced flow/flight control for hypersonic flights in atmosphere. *9th International Space Planes and Hypersonic Systems and Technologies Conference*, page 4820, 1999.
- [65] A. Kuranov and E. Sheikin. Mhd control by external and internal flows in scramjet under ajax concept. *41st Aerospace Sciences Meeting and Exhibit*, page 173, 2003.
- [66] E. Sheikin and A. Kuranov. Mhd controlled inlet for scramjet with various configurations of magnetic field. *42nd AIAA Aerospace Sciences Meeting and Exhibit*, page 1195, 2004.
- [67] M. Shneider, S. Macheret, and R. Miles. Comparative analysis of mhd and plasma methods of scramjet inlet control. *41st Aerospace Sciences Meeting and Exhibit*, page 170, 2003.
- [68] M. N. Shneider, S. O. Macheret, and R. B. Miles. Analysis of magnetohydrodynamic control of scramjet inlets. *AIAA Journal*, 42(11):2303–2310, 2004.
- [69] M. N. Shneider and S. O. Macheret. Modeling of plasma virtual shape control of ram/scramjet inlet and isolator. *Journal of Propulsion and Power*, 22(2):447–454, 2006.
- [70] S. O. Macheret, M. N. Shneider, and R. B. Miles. Scramjet inlet control by off-body energy addition: a virtual cowl. *AIAA Journal*, 42(11):2294–2302, 2004.
- [71] J. S. Shang, S. T. Surzhikov, R. Kimmel, D. Gaitonde, J. Menart, and J. Hayes. Mechanisms of plasma actuators for hypersonic flow control. *Progress in Aerospace Sciences*, 41(8):642–668, 2005.
- [72] G. Gong, Y. Li, Y. Wang, and P. Kuang. Investigation on wedge shock wave control by surface mhd actuation. *AIP Advances*, 10(5):055212, 2020.
- [73] H. Jiang, J. Liu, S. Luo, J. Wang, and W. Huang. Hypersonic flow control of shock wave/turbulent boundary layer interactions using magnetohydrodynamic plasma actuators. *Journal of Zhejiang University-SCIENCE A*, 21(9):745–760, 2020.
- [74] A. Russell, H. Zare-Behtash, and K. Kontis. Joule heating flow control methods for high-speed flows. *Journal of Electrostatics*, 80:34–68, 2016.
- [75] D. Knight. Survey of aerodynamic drag reduction at high speed by energy deposition. *Journal of Propulsion and Power*, 24(6):1153–1167, 2008.

- [76] V. Malka, J. Faure, Y. A. Gauduel, E. Lefebvre, A. Rousse, and K. T. Phuoc. Principles and applications of compact laser-plasma accelerators. *Nature Physics*, 4(6):447–453, 2008.
- [77] D. D’Ambrosio and D. Giordano. Electrodynamical fluid dynamics for aerospace applications. part i: Classification and critical review of physical models. *AIAA*, pages 1–14, 2004.
- [78] N. J. Bisek. Numerical study of plasma-assisted aerodynamic control for hypersonic vehicles. *PhD Thesis, Department of Aerospace Engineering, The University of Michigan*, 2010.
- [79] G. V. Candler, P. K. Subbareddy, and J. M. Brock. Advances in computational fluid dynamics methods for hypersonic flows. *Journal of Spacecraft and Rockets*, 52(1):17–28, 2015.
- [80] S. D. Kim, B. J. Lee, H. J. Lee, and I. S. Jeung. Robust hllc riemann solver with weighted average flux scheme for strong shock. *Journal of Computational Physics*, 228(20):7634 – 7642, 2009.
- [81] G. Candler, D. Mavriplis, and L. Trevino. Current status and future prospects for the numerical simulation of hypersonic flows. *47th AIAA Aerospace Sciences Meeting Including the New Horizons Forum and Aerospace Exposition*, page 153, 2009.
- [82] M. MacLean, M. Holden and A. Dufrene. Comparison between cfd and measurements for real-gas effects on laminar shock wave boundary layer interaction, 1. *Oral Presentation*, 2014.
- [83] J. Hao, J. Wang, and C. Lee. Numerical simulation of high-enthalpy double-cone flows. *AIAA Journal*, 55(7):2471–2475, 2017.
- [84] F. Träuble. Multi-physics modelling of solid-plasma interaction. *Centre for Scientific Computing, Department of Physics, University of Cambridge*, 2018.
- [85] A. D’Angola, G. Colonna, C. Gorse, and M. Capitelli. Thermodynamic and transport properties in equilibrium air plasmas in a wide pressure and temperature range. *The European Physical Journal D*, 46:129–150, 2008.
- [86] G. Colonna. Improvements of hierarchical algorithm for equilibrium calculation. *Computer physics communications*, 177(6):493–499, 2007.
- [87] M. Capitelli, G. Colonna, C. Gorse, and A. D’Angola. Transport properties of high temperature air in local thermodynamic equilibrium. *The European Physical Journal D-Atomic, Molecular, Optical and Plasma Physics*, 11(2):279–289, 2000.
- [88] K. Sverdrup, A. Almgren, and N. Nikiforakis. An embedded boundary approach for efficient simulations of viscoplastic fluids in three dimensions. *Physics of Fluids*, 31(9):093102, 2019.
- [89] W. Schröder. Notes on numerical fluid mechanics and multidisciplinary design. *Springer-Nature*, 2021.
- [90] J. A. Carlson, A. Jaffe, and A. Wiles. The millennium prize problems. *Citeseer*, 2006.
- [91] J. P. Goedbloed and S. Poedts. Principles of magnetohydrodynamics: with applications to laboratory and astrophysical plasmas. *Cambridge University Press*, 2004.

- [92] O. U. Khan, K. A. Hoffmann, and J. Dietiker. Computational aspects of high-speed flows with applied magnetic field. *IEEE Transactions on Magnetics*, 42(3):389–397, 2006.
- [93] T. Yoshino, T. Fujino, and M. Ishikawa. Possibility of thermal protection in earth re-entry flight by mhd flow control with air-core circular magnet. *Transactions on Electrical and Electronic Engineering*, (4):510–517, 2009.
- [94] N. Hall. Kinetic theory of gases. *NASA Glenn Research Centre*, 2015.
- [95] F. Träuble, S. T. Millmore, and N. Nikiporakis. An improved equation of state for air plasma simulations. *Physics of Fluids*, 33(3):036112, 2021.
- [96] T. Benson. Real gas effects. *NASA Glenn Research Centre*, 2014.
- [97] T. A. Edwards. Fluid/chemistry modeling for hypersonic flight analysis. *Computers & Mathematics with Applications*, 24(5-6):25–36, 1992.
- [98] J. R. Maus, B. J. Griffith, K. Y. Szema, and J. T. Best. Hypersonic mach number and real gas effects on space shuttle orbiteraerodynamics. *Journal of Spacecraft and Rockets*, 21(2):136–141, 1984.
- [99] F. Chalot and T. J. Hughes. A consistent equilibrium chemistry algorithm for hypersonic flows. *Computer Methods in Applied Mechanics and Engineering*, 112(1-4):25–40, 1994.
- [100] W. A. Wood and R. A. Thompson. Combined laura-ups hypersonic solution procedure. No. *NASA-TM-107682*, 1993.
- [101] Y. Hu, H. Huang, and Z. Zhang. Numerical simulation of a hypersonic flow past a blunt body. *International Journal of Numerical Methods for Heat & Fluid Flow*, 2017.
- [102] O. Ekici, O. A. Ezekoye, M. J. Hall, and R. D. Matthews. Thermal and flow fields modeling of fast spark discharges in air. *Journal of Fluids Engineering*, 129:55–65, 2007.
- [103] K. Sawada and E. Dendou. Validation of hypersonic chemical equilibrium flow calculations using ballistic-range data. *Shock Waves*, 11(1):43–51, 2001.
- [104] M. N. Plooster. Shock waves from line sources. numerical solutions and experimental measurements. *The physics of fluids*, 13(11):2665–2675, 1970.
- [105] S. Gordon and B. J. McBride. Computer program for calculation of complex chemical equilibrium compositions and applications. part 1: Analysis. *NASA Lewis (now Glenn) Research Center*, 1994.
- [106] D. R. Cruise. Notes on the rapid computation of chemical equilibria. *The Journal of Physical Chemistry*, 68(12):3797–3802, 1964.
- [107] L. Mottura, L. Vigevano, and M. Zaccanti. An evaluation of roe’s scheme generalizations for equilibrium real gas flows. *Journal of Computational Physics*, 138(2):354–399, 1997.
- [108] G. Colonna and A. D’angola. A hierarchical approach for fast and accurate equilibrium calculation. *Computer physics communications*, 163(3):177–190, 2004.

- [109] S. Gordon and B. J. McBride. Thermodynamic data to 20,000 k for monatomic gases. *NASA*, 1999.
- [110] B. J. McBride and S. Gordon. Computer program cea (chemical equilibrium with applications). *NASA Lewis (now Glenn) Research Center*, 1985-2020.
- [111] M. G. Dunn and S. W. Kang. Theoretical and experimental studies of reentry plasmas. *NASA CR-2232*, 1973.
- [112] C. Park. Review of chemical-kinetic problems of future nasa missions. i-earth entries. *Journal of Thermophysics and Heat transfer*, 7(3):385–398, 1993.
- [113] J. Hao, J. Wang, and C. Lee. Numerical study of hypersonic flows over reentry configurations with different chemical nonequilibrium models. *Acta Astronautica*, 126:1–10, 2016.
- [114] JAXA. About orbital re-entry experiment (orex) - report. *Japan Aerospace Exploration Agency*, 2003.
- [115] Y. P. Raizer and J. E. Allen. Gas discharge physics. *Springer*, 1, 1991.
- [116] M. Turner, C. Hawk, and R. Litchford. Three-dimensional numerical modeling of the magnetohydrodynamic augmented propulsion experiment. *46th AIAA Aerospace Sciences Meeting and Exhibit*, page 1072, 2008.
- [117] R. S. Devoto. The transport properties of a partially ionized monatomic gas. *PhD Dissertation, Stanford University, Stanford, CA*, 1965.
- [118] H. K. Cheng and G. Emanuel. Perspective on hypersonic nonequilibrium flow. *AIAA journal*, 33(3):385–400, 1995.
- [119] G. Krishnamoorthy and L. E. Clarke. Computationally efficient assessments of the effects of radiative transfer, turbulence radiation interactions, and finite rate chemistry in the mach 20 reentry f flight vehicle. *Journal of Computational Engineering*, 2016, 2016.
- [120] A. Lani, J. Molnar, D. V. Abeele, P. Rini, T. Magin, and G. Degrez. Numerical study of elemental demixing in atmospheric entry flow regimes near local thermodynamic equilibrium. *European Conference on Computational Fluid Dynamics*, 2006.
- [121] G. V. Candler. Annual review of fluid mechanics: Rate effects in hypersonic flows. *Annual Review of Fluid Mechanics*, pages 379–402, 2019.
- [122] H. M. Damevin and K. A. Hoffmann. Numerical simulations of magnetic flow control in hypersonic chemically reacting flows. *Journal of Thermophysics and heat Transfer*, 16(4), 2002.
- [123] M. Capitelli, G. Colonna, and A. D’Angola. Fundamental aspects of plasma chemical physics. *Springer*, 66, 2012.
- [124] A. D’Angola, G. Colonna, C. Gorse, and M Capitelli. Thermodynamic prop- erties of high temperature air in local thermodynamic equilibrium: Ii accurate analytical expression for electron molar fractions. *The European Physical Journal D*, 65:453–457, 2011.

- [125] K. Sverdrup. High performance simulations of yield stress fluids in a structured adaptive mesh refinement framework with embedded boundaries. *PhD Thesis, University of Cambridge*, 2019.
- [126] J. Tu, G. H. Yeoh, and C. Liu. Chapter 4 - cfd mesh generation: A practical guideline. *Computational Fluid Dynamics (Third Edition)*, pages 125–154, 2018.
- [127] M. Bern and P. Plassmann. Chapter 6 - mesh generation. *Handbook of Computational Geometry, North-Holland*, pages 291–332, 2000.
- [128] A. Harten, P. D. Lax, and B. van Leer. On upstream differencing and godunov-type schemes for hyperbolic conservation laws. *SIAM Rev.*, 25(1):35 – 61, 1983.
- [129] J. Sitaraman, A. Katz, B. Jayaraman, A. Wissink, and V. Sankaran. Evaluation of a multi-solver paradigm for cfd using unstructured and structured adaptive cartesian grids. *46th AIAA Aerospace Sciences Meeting and Exhibit*, page 660, 2008.
- [130] S. Brahmachary, G. Natarajan, V. Kulkarni, and N. Sahoo. A sharp-interface immersed boundary method for high-speed compressible flows. *Immersed Boundary Method. Springer, Singapore*, 2016.
- [131] P. Colella, D. T. Graves, B. J. Keen, and D. Modiano. A cartesian grid embedded boundary method for hyperbolic conservation laws. *Journal of Computational Physics*, 211(1):347–366, 2006.
- [132] X. Y. Hu, B. C. Khoo, N. A. Adams, and F. L. Huang. A conservative interface method for compressible flows. *Journal of Computational Physics*, 219(2):553–578, 2006.
- [133] W. P. Bennett, N. Nikiforakis, and R. Klein. A moving boundary flux stabilization method for cartesian cut-cell grids using directional operator splitting. *Journal of Computational Physics*, 368:333–358, 2018.
- [134] N. Gokhale, N. Nikiforakis, and R. Klein. A dimensionally split cartesian cut cell method for the compressible navier–stokes equations. *Journal of Computational Physics*, 375:1205–1219, 2018.
- [135] R. Yamashita, L. Wutschitz, and N. Nikiforakis. A full-field simulation methodology for sonic boom modeling on adaptive cartesian cut-cell meshes. *Journal of Computational Physics*, 408:109271, 2020.
- [136] H. Forrer and R. Jeltsch. A higher-order boundary treatment for cartesian-grid methods. *Journal of Computational Physics*, 140(2):259–277, 1998.
- [137] M. D. de Tullio, P. De Palma, G. Iaccarino, G. Pascazio, and M. Napolitano. An immersed boundary method for compressible flows using local grid refinement. *Journal of Computational Physics*, 225(2):2098–2117, 2007.
- [138] R. P. Fedkiw, T. Aslam, B. Merriman, S. Osher, et al. A non-oscillatory eulerian approach to interfaces in multimaterial flows (the ghost fluid method). *Journal of computational physics*, 152(2):457–492, 1999.
- [139] J. J. Quirk. A contribution to the great riemann solver debate. *Upwind and High-Resolution Schemes, Springer Berlin Heidelberg*, pages 550–569, 1997.
- [140] M. S. Liou. Mass flux schemes and connection to shock instability. *Journal of Computational Physics*, 160(2):623 – 648, 2000.

- [141] J. M. Moschetta, J. Gressier, J. C. Robinet, and G. Casalis. The carbuncle phenomenon: A genuine euler instability? *Godunov Methods: Theory and Applications, Springer US*, pages 639–645, 2001.
- [142] B. van Leer. The development of numerical fluid mechanics and aerodynamics since the 1960s: Us and canada. *100 Volumes of 'Notes on Numerical Fluid Mechanics', Springer*, pages 159–185, 2009.
- [143] S. Zhijun, Y. Wei, and Y. Guangwei. A robust hllc-type riemann solver for strong shock. *Journal of Computational Physics*, 309:185 – 206, 2016.
- [144] R. Tramel, R. Nichols, and P. Buning. Addition of improved shock-capturing schemes to overflow 2.1. *19th AIAA Computational Fluid Dynamics*, page 3988, 2009.
- [145] S. Sangeeth and J.C. Mandal. A simple cure for numerical shock instability in the hllc riemann solver. *Journal of Computational Physics*, 378:477 – 496, 2019.
- [146] M. Pandolfi and D. D'Ambrosio. Numerical instabilities in upwind methods: Analysis and cures for the “carbuncle” phenomenon. *Journal of Computational Physics*, 166(2):271 – 301, 2001.
- [147] J. M. Simmons. Measurement techniques in high-enthalpy hypersonic facilities. *Experimental Thermal and Fluid Science*, 10(4):454–469, 1995. Experimental methods in Thermal and Fluid Science.
- [148] P. Woodward and P. Colella. The numerical simulation of two-dimensional fluid flow with strong shocks. *Journal of Computational Physics*, 54(1):115 – 173, 1984.
- [149] R. J. Hakkinen, I. Greber, L. Trilling, and S. S. Abarbanel. The interaction of an oblique shock wave with a laminar boundary layer. *No. NASA-MEMO-2-18-59W*, 1959.
- [150] R. W. MacCormack. A numerical method for solving the equations of compressible viscous flow. *AIAA journal*, 20(9):1275–1281, 1982.
- [151] National Oceanic, Atmospheric Administration, United States. National Aeronautics, Space Administration, United States Committee on Extension to the Standard Atmosphere, and Department of the Air Force. U.s. standard atmosphere, 1976. *National Oceanic and Atmospheric Administration*, 1976.
- [152] R. P. Starkey. Hypersonic vehicle telemetry blackout analysis. *Journal of Spacecraft and Rockets*, 52(2):426–438, 2015.
- [153] G. V. Candler and R. W. MacCormack. Computation of weakly ionized hypersonic flows in thermochemical nonequilibrium. *Journal of Thermophysics and Heat Transfer*, 5(3):266–273, 1991.
- [154] E. Josyula and W. F. Bailey. Governing equations for weakly ionized plasma flowfields of aerospace vehicles. *Journal of spacecraft and rockets*, 40(6):845–857, 2003.
- [155] R. George and R. K. Gupta. Viscous shock layer method to predict communication blackout during re-entry phase. *Defence Science Journal: Defence Scientific Information & Documentation Centre*, 61(4):364, 2011.
- [156] Y. X. Sha, H. L. Zhang, X. Y. Guo, and M. Y. Xia. Analyses of electromagnetic properties of a hypersonic object with plasma sheath. *IEEE Transactions on Antennas and Propagation*, 67(4):2470–2481, 2019.

- [157] M. Holden, T. Wadhams, I. Boyd, and W. L. Wang. Cfd validation for hyperconic flight: Hypersonic double-cone flow simulations. *40TH AIAA Aerospace Sciences Meeting and Exhibit, Reno, NV*, pages 14–17, 2002.
- [158] J. Hao and C. Y. Wen. Numerical investigation of oxygen thermochemical nonequilibrium on high-enthalpy double-cone flows. *International Journal of Heat and Mass Transfer*, 127:892–902, 2018.
- [159] F. Y. Zuo and S. L. Hu. Thermochemical non-equilibrium effects on aerothermodynamic prediction of laminar double-cone flow. *Acta Astronautica*, 2021.
- [160] D. Baccarella, A. Passaro, A. Cristofolini, C. Borghi, G. Neretti, and E. Trifoni. Mhd flow control experiment in air: Test article design. *17th AIAA International Space Planes and Hypersonic Systems and Technologies Conference*, page 2355, 2011.
- [161] J. F. Coakley and R. W. Porter. Time-dependent numerical analysis of mhd blunt body problem. *AIAA Journal*, 9(8):1624–1626, 1971.
- [162] J. Lineberry and V. Biturin. Experimental and theoretical study of mhd interaction in hypersonic ionized air flow over a wedge. *42nd AIAA Aerospace Sciences Meeting and Exhibit*, page 1194, 2004.
- [163] S. Bobashev, T. Erofeev, A. and Lapushkina, N. Mende, S. Poniaev, V. Sakharov, R. Vasilieva, and D. Van Wie. Recent results on mhd flow control at ioffe institute. *14th AIAA/AHI Space Planes and Hypersonic Systems and Technologies Conference*, page 8012, 2006.
- [164] Y. Nagata, K. Yamada, and T. Abe. Hypersonic double-cone flow with applied magnetic field. *Journal of Spacecraft and Rockets*, 50(5):981–991, 2013.
- [165] A. Alberti, A. Munafò, C. Pantano, and M. Panesi. Self-consistent computational fluid dynamics of supersonic drag reduction via upstream-focused laser-energy deposition. *AIAA journal*, 59(4):1214–1224, 2021.
- [166] N. Kianvashrad and D. Knight. Non-equilibrium effects of interaction of laser discharge with hemisphere-cylinder in supersonic flow. *2018 Flow Control Conference*, page 3757, 2018.
- [167] V. Y. Borzov, V. M. Mikhailov, I. V. Ribka, N. P. Savischenko, and A. S. Yuriev. Experimental investigation supersonic flow over obstacle at energy deposition in undisturbed stream. *IFZh (Engineering Physical Journal)*, 66(5):515–520, 1994.
- [168] P. K. Tretyakov, A. F. Garaninh, V. L. Kraynev, A. V. Tupikin, and V. I. Yakovlev. Investigation of local laser energy release influence on supersonic flow by methods of aerophysical experiments. *Proc: International Conference on the Methods of Aerophysical Research*, pages 200–204, 1996.
- [169] R. G. Adelgren, G. S. Elliott, D. D. Knight, A. A. Zheltovodov, and T. J. Beutner. Energy deposition in supersonic flow. *AIAA*, (2001-0885):33, 2001.
- [170] N. Kianvashrad and D. D Knight. Non-equilibrium effects of interaction of laser discharge with hemisphere-cylinder in supersonic flow. *2018 Flow Control Conference*, page 3757, 2018.
- [171] E. Schülein, A. Zheltovodov, E. Pimonov, and M. Loginov. Experimental and numerical modeling of the bow shock interaction with pulse-heated air bubbles. *International Journal of Aerospace Innovations*, 2(3):165–188, 2010.

Appendix A

Computing electron molar fraction and number density - tables of coefficients

Tables of coefficients for the polynomial expansion of equations contained in section 3.2.4.

	β_0	β_1	β_2	β_3	β_4	β_5	β_6
δ_0	-1.453520e+002	-2.449447e+000	-1.115521e-001	4.815904e-002	4.816233e-003	-4.844801e-004	-6.055194e-005
δ_1	1.369547e-001	2.858663e-003	3.205470e-005	-8.338958e-005	-5.701341e-006	8.585860e-007	8.583472e-008
δ_2	-6.345758e-005	-1.679107e-006	4.450866e-008	4.948604e-008	2.313164e-009	-5.251591e-010	-4.461556e-011
δ_3	1.617445e-008	4.919459e-010	-2.922150e-011	-1.375302e-011	-4.284662e-013	1.504247e-013	1.156213e-014
δ_4	-2.299085e-012	-7.370074e-014	6.536403e-015	1.931609e-015	3.938597e-017	-2.191122e-017	-1.631548e-018
δ_5	1.702203e-016	5.392941e-018	-6.228118e-019	-1.322524e-019	-1.891956e-021	1.569686e-021	1.216511e-022
δ_6	-5.100309e-021	-1.529637e-022	2.147344e-023	3.497704e-024	4.747413e-026	-4.387925e-026	-3.786008e-027

		α_0	α_1	α_2	α_3
σ_0	c_0	8.047945e+003	2.117097e+002	-6.978618e+000	
	Δ_0	5.000000e+001	6.863114e-002		
σ_1	$\log a_1$	-3.897330e-001	4.088303e-003	2.004021e-003	6.989005e-004
	$\log c_1$	9.510842e+000	6.332838e-002	5.805702e-004	-6.640588e-005
	$\log \Delta_1$	7.970326e+000	1.336309e-001	3.159430e-003	3.346003e-004
σ_m	$\log c_m$	6.343867e+000	1.473478e+000	-2.628976e-001	2.653667e-002
	$\log \Delta_m$	1.029159e+001	3.502366e-002	-1.043994e-002	-7.498040e-004
σ_2	$\log a_2$	-1.599518e+000	-3.681243e-002	-1.499672e-002	-4.875898e-003
	$\log c_2$	1.025313e+001	6.613035e-002	2.106960e-003	1.249059e-004
	$\log \Delta_2$	8.461864e+000	1.033435e-001	-6.800325e-003	-2.171111e-003
$a_3 = a_{3b} - a_2 - a_1$	$\log a_{3b}$	-3.465436e-001	-2.831472e-003	-1.021467e-003	-7.753035e-005
σ_3	$\log c_3$	1.009244e+001	5.691765e-002	2.642057e-003	3.297719e-005
	$\log \Delta_3$	9.041428e+000	9.809302e-002	1.899235e-003	-1.329754e-004
γ_4	$\log a_4$	-5.123507e+000	3.850431e-001	6.380724e-003	-1.088865e-002
	$\log c_4$	9.247533e+000	1.007851e-001	-1.058914e-002	9.089247e-004
	$\log \Delta_4$	8.132477e+000	9.307459e-002	-5.524780e-003	2.540886e-004

		α_4	α_5	α_6	α_7
σ_1	$\log a_1$	6.796657e-005	-1.460238e-006		
	$\log \Delta_1$	5.512825e-005			
σ_m	$\log c_m$	-1.170989e-003			
	$\log \Delta_m$	1.464646e-004	1.031691e-005	-3.878009e-007	
	$\log a_2$	-9.278204e-005	8.792226e-005	1.273088e-005	
σ_2	$\log c_2$	-3.254728e-006	-1.073094e-006	-4.149968e-007	-4.918145e-008
	$\log \Delta_2$	8.042855e-005	3.126866e-005	3.548083e-006	1.732832e-007
σ_3	$\log \Delta_3$	-2.357106e-005			
γ_4	$\log a_4$	1.189765e-003			
	$\log \Delta_4$	1.232437e-004			